Inferring Crystal Strain Distributions from X-ray Diffraction Data

Analytical and Computational Advances

Henningsson, Axel

2023

Citation for published version (APA):
Henningsson, A. (2023). *Inferring Crystal Strain Distributions from X-ray Diffraction Data: Analytical and Computational Advances*. Solid Mechanics, Faculty of Engineering, Lund University.

Total number of authors:
1

LUND UNIVERSITY

PO Box 117
221 00 Lund
+46 46-222 00 00

LUNDS UNIVERSITET

INFERRING CRYSTAL STRAIN DISTRIBUTIONS FROM X-RAY DIFFRACTION DATA:

ANALYTICAL AND COMPUTATIONAL ADVANCES

AXEL HENNINGSSON

Solid
Mechanics

Doctoral Thesis

Inferring Crystal Strain Distributions from X-ray Diffraction Data: Analytical and Computational Advances

Axel Henningsson

LUND UNIVERSITY

Akademisk avhandling som för avläggande av teknologie doktorsexamen vid tekniska fakulteten
vid Lunds universitet kommer att offentligen försvaras fredagen den 15 december 2023 klockan 09.00
i sal M:E, M-building, Ole Römers väg 1, Lund.

Fakultetsopponent: Philip J. Withers, The University of Manchester, Storbritannien.

Doctoral thesis which by due permission of the Faculty of Engineering at Lund University,
will be publicly defended on the 15th of December 2023 at 09.00
in room M:E of the M-building, Ole Römers väg 1, Lund, Sweden.

Faculty opponent: Philip J. Withers, The University of Manchester, United Kingdom.

Organization: LUND UNIVERSITY, Division of Solid Mechanics, Lund University,
P.O. Box 118, SE-221 00 LUND, Sweden

Document name: DOCTORAL DISSERTATION

Date of issue: December 2023

Author(s): Axel Henningsson

Sponsoring organization:

Title and subtitle: Inferring Crystal Strain Distributions from X-ray Diffraction Data:
Analytical and Computational Advances

Abstract:

By harnessing the powers of polycrystalline materials an unprecedented, technologically-driven age has taken form over the last 100 years. The polycrystal is today, arguably, the most central building block for electronics, renewable energy, transportation and medical equipment industries. This material class is the reason for the emergence of the powerful microprocessors, semiconductors, memory chips and integrated circuits driving the computing revolution, which seem to be ever accelerating. To advance our efforts in all of these areas a deep understanding of the mechanics that govern the polycrystal is crucial. Today, state-of-the-art far-field X-ray microscopy techniques can non-destructively record diffraction from the individual crystal grains in a polycrystalline aggregate. By analysing the recorded diffraction patterns, volume averaged orientations and strains of the individual crystal grains can be mapped. In this thesis we upgrade these microscopy techniques beyond the recording of grain averaged properties to also extract information on the strain tensor fields as they vary across the crystal domains. While we exclusively focus this thesis around the Three Dimensional X-ray Diffraction microscope (3DXRD) and its variants, other avenues of application are possible, including microscopes that use neutron and electron based techniques.

We show that data generated by well established scanning diffraction techniques can be used to reconstruct, in 3D, intragranular strain tensor maps. The inference of the strain tensor field is made possible by emphasising the tomographic aspects of the inverse problem. Multiple regression methods are derived, featuring both the popular least squares maximum likelihood estimator as well as Bayesian inference alternatives. The presented regression methods are enriched with constraints that can be used to stabilise the strain inversion when data are scarce, noisy and/or non-uniformly sampled. The developed algorithms are implemented and validated by use of synthetic, simulated, diffraction data. Additionally, applications to state of the art real world synchrotron diffraction data are presented.

As the number of data grow, the prospect of an increased spatial resolution in strain follows and the computational aspects of the inverse problem become a pressing concern. With the help of matrix algebra we bring the problem closer to an algebraic absorption tomography setting. Our result shortens the reconstruction compute time, simplifies the computer implementation and provides easier access to GPU acceleration.

For the popular case of full-field measurements, when the beam probe is intentionally taken wider than the crystal diameter, the spatial resolution in strain is lost. For these acquisition geometries we provide alternative methods that can recover the probability distribution of the intragranular strain tensor fields (strain PDF). That is; the probability of encountering any one particular strain tensor as a result of randomly (uniformly) traversing a point in the grain. In the case of Gaussian strain PDFs, analytical results from this research allow for a parametric description of the null-space of the inversion problem and a closed form solution is derived. In the general case, when the strain PDFs is non-Gaussian, we provide an iterative finite basis expansion scheme.

Beyond the development of methods for strain inversion we derive diffraction simulation models that pave the way for the next generation of diffraction strain estimation techniques. These models are infused by analytical solutions to a time-dependent version of the Laue equations that unlocks exploration of optimal data acquisition strategies.

In summary, this thesis introduces a collection of mathematical advancements that enhance the capabilities of well-established X-ray diffraction microscopy techniques. By employing the developed algorithms, polycrystalline deformation mechanisms can be studied simultaneously at the inter- and intragranular levels.

Key words: X-ray diffraction, polycrystals, inverse problems, strain

Classification system and/or index terms (if any)

Supplementary bibliographical information

Language: English

ISBN: 978-91-8039-835-0

Recipient’s notes

Number of pages: 166

Price

Security classification

Signature

Date 2023-10-25

Department of Construction Sciences
Solid Mechanics

ISRN LUTFD2/TFHF-23/1069-SE(1-166)
ISBN: 978-91-8039-835-0 (print)
ISBN: 978-91-8039-836-7 (pdf)

Inferring Crystal Strain Distributions from X-ray Diffraction Data: Analytical and Computational Advances

Doctoral Thesis by

Axel Henningsson

Printed by Media-Tryck AB, Lund, Sweden
For information, address:
Division of Solid Mechanics, Lund University, Box 118, SE-221 00 Lund, Sweden
Homepage: http://www.solid.lth.se

"Good science is 99% perspiration and 1% inspiration" - Thomas Edison
... but only if it is also 100% cheerfully shared with others.

Preface

Thomas Edison will have made the rather cheerless prediction that good science consists of 1% inspiration and 99% perspiration. However, sound science must also feature a strong element of critical evaluation, which I believe Edison would not oppose. As I look back on my last 1583 days of research it becomes evident that the narrative extends beyond a mere 16 days of respite within an otherwise arid landscape paved by backbreaking hard work. This fact worries me (in a good way), as it suggests that Edison's model fails to encapsulate the human experience of the scientific exercise. Fortunately, in my view, this model flaw has a a simple remedy. I believe Edison inadvertently overlooked the most vital element of all scientific work: the companionship of colleagues, friends, and mentors. In fact, without this crucial ingredient the research in this thesis would not have been possible. It is therefore my pleasure to here express my gratitude for the support extended to me by so many friendly hands over the years.

Thank you Stephen Hall, Johan Hektor, and Jonathan Wright, who trusted me as a Master's student and guided me through my early academic endeavours. Your watchful guidance during those initial steps meant a lot to me.

Stephen, your unwavering support and encouragement throughout my PhD studies have been instrumental in shaping me as a scientist. I am truly grateful for the freedom you provided me and for believing in my potential. It has been a pleasure working with you.

I would also like to express my heartfelt thanks to my dear friend Johannes Hendriks, whose insights helped me discover a deeper beauty in probabilistic estimation. I have learned a great deal from our interactions. Adrian Wills, your shared fascination with the profound aspects of reality, not only when it comes to mathematics, left me with a feeling similar to that of hope. The warm welcome my family and I received from all of you, including Johannes and Adrian's families, upon our arrival in Australia far exceeded our expectations. Special thanks to Vicki and Pete Hill for providing us with a home and lending a helping hand throughout our stay. An act of random kindness which meant a great deal to me. I know the same goes for Malin and the kids.

To Malin, my dear wife, whom have not ceased for a second to forcefully and fervently cheer on any and all of my scientific efforts I can say only this; I love you too.

To my fellow PhD students, thank you for the stimulating discussions, enjoyable moments, and unwavering support you have provided. You are all dear to me. A special shout-out to my office mates Stefanos, Vilmer, and Shubankar—our conversations have been enriching and enjoyable. Not least when it comes to life after math.

Henning Poulsen, your PhD thesis was the first scientific work I read when embarking on my research journey. Having the opportunity to work with and learn from you directly has been an invaluable experience. Thank you for believing in me as a researcher. I am now more than happy to be able to repay the favour with a PhD thesis of my own.

I am also grateful for the support I have received from other members of the Division of Solid Mechanics over the years. Thank you, Jonas Engqvist, for the assistance in the preparation of experiments. Your engineering skill is an inspiration to me. Thank you also, Matti Ristinmaa, I enjoyed equally the experience to teach with you as that of being taught by you (not least when it came to the extracurricular topics).

Although the list of acknowledgements could be much longer, the essence of good science is maintaining focus. Thus, with that in mind, I present the culmination of my work as a PhD student; a contribution to the field of strain tensor estimation in polycrystals. I thoroughly enjoyed the research behind this thesis, and it is my hope that you will equally enjoy reading it.

Hässleholm, July 2023
Axel Henningsson

Abstract

By harnessing the powers of polycrystalline materials an unprecedented, technologically-driven age has taken form over the last 100 years. The polycrystal is today, arguably, the most central building block for electronics, renewable energy, transportation and medical equipment industries. This material class is the reason for the emergence of the powerful microprocessors, semiconductors, memory chips and integrated circuits driving the computing revolution, which seem to be ever accelerating. To advance our efforts in all of these areas a deep understanding of the mechanics that govern the polycrystal is crucial. Today, state-of-the-art far-field X-ray microscopy techniques can non-destructively record diffraction from the individual crystal grains in a polycrystalline aggregate. By analysing the recorded diffraction patterns, volume averaged orientations and strains of the individual crystal grains can be mapped. In this thesis we upgrade these microscopy techniques beyond the recording of grain averaged properties to also extract information on the strain tensor fields as they vary across the crystal domains. While we exclusively focus this thesis around the Three Dimensional X-ray Diffraction microscope (3DXRD) and its variants, other avenues of application are possible, including microscopes that use neutron and electron based techniques.

We show that data generated by well established scanning diffraction techniques can be used to reconstruct, in 3D, intragranular strain tensor maps. The inference of the strain tensor field is made possible by emphasising the tomographic aspects of the inverse problem. Multiple regression methods are derived, featuring both the popular least squares maximum likelihood estimator as well as Bayesian inference alternatives. The presented regression methods are enriched with constraints that can be used to stabilise the strain inversion when data are scarce, noisy and/or non-uniformly sampled. The developed algorithms are implemented and validated by use of synthetic, simulated, diffraction data. Additionally, applications to state of the art real world synchrotron diffraction data are presented.

As the number of data grow, the prospect of an increased spatial resolution in strain follows and the computational aspects of the inverse problem become a pressing concern. With the help of matrix algebra we bring the problem closer to an algebraic absorption tomography setting. Our result shortens the reconstruction compute time, simplifies the computer implementation and provides easier access to GPU acceleration.

For the popular case of full-field measurements, when the beam probe is intentionally taken wider than the crystal diameter, the spatial resolution in strain is lost. For these acquisition geometries we provide alternative methods that can recover the probability distribution of the intragranular strain tensor fields (strain PDF). That is; the probability of encountering any one particular strain tensor as a result of randomly (uniformly) traversing a point in the grain. In the case of Gaussian strain PDFs, analytical results from this research allow for a parametric description of the null-space of the inversion problem and a closed form solution is derived. In the general case, when the strain PDFs is non-Gaussian, we provide an iterative finite basis expansion scheme.

Beyond the development of methods for strain inversion we derive diffraction simulation models that pave the way for the next generation of diffraction strain estimation techniques. These models are infused by analytical solutions to a time-dependent version of the Laue equations that unlocks exploration of optimal data acquisition strategies.

In summary, this thesis introduces a collection of mathematical advancements that enhance the capabilities of well-established X-ray diffraction microscopy techniques. By employing the developed algorithms, polycrystalline deformation mechanisms can be studied simultaneously at the inter- and intragranular levels.

Popular Science Summary

Polycrystals are found in abundance in nature. For example, metals, rocks and sand are all formed out of aggregates of single crystals. The properties of the individual crystals grains in these materials govern the mechanical attributes of the macroscopic solids. As science has progressed over the last century, we have learned how to control these properties and, subsequently, polycrystals have found numerous industrial applications. Today, polycrystals plays a central role in computer, transportation, medical, energy and semiconductor industries, to name a few.

In many applications it is important to understand how the individual crystal grains in the polycrystal deform under external stimuli. For instance, in the development of solar cells, crystal strain can cause so-called band-gap variations that are directly linked to the performance of the cell. Consequently, the scientific community has, over the last decades, developed a suite of microscopy methods to probe the inner workings of polycrystals. Among these methods are high-energy X-ray diffraction techniques that are specially designed to probe statistically representative volumes of polycrystals. Historically, these methods have been used to investigate grain-average properties in polycrystals. Within this class of microscopes, we focus primarily on a variant that is designed to scan a narrow X-ray beam across the sample. Measurements generated in this way have the potential to yield sub-grain resolution while, at the same time, being representative of hundreds of grains within the sample. We unlock this intragranular potential by deriving mathematical algorithms that uncover the crystal strains with a sub-grain resolution. Our results therefore pave the way for the study of polycrystal deformation mechanisms across the length-scales. This will enable scientist to study the coupling between inter- and intragranular effects in a new way and, thus, holds the potential of unlocking a new suite of secrets about the inner workings of the polycrystal.

Polulärvetenskaplig sammanfattning (SWE)

Polykristaller återfinns rikligen i vår naturliga omgivning. Metaller, mineraler, bergarter och sand är bara några exempel på fasta material vilka är uppbyggda av kristallkorn. De enskilda kristallkornens egenskaper dominerar de mekaniska attributen hos det makroskopiska aggregatet. I takt med vetenskapens framsteg har vår förståelse för polykristallen ökat och vi har lärt oss hur vi kan kontrollera dess egenskaper för industriella applikationer. Idag spelar polykristaller en central roll i dator-, transport-, medicin-, energi- och halvledarindustrier, för att nämna några.

I många applikationer är det viktigt att förstå hur de enskilda kornen deformeras vid externa stimuli. Exempelvis vid utvecklingen av solceller kan kristalltöjningar leda till så kallade bandgapsvariationer, vilka är direkt kopplade till solcellens verkningsgrad. Som en följd av detta har mikroskopimetoder väl lämpade för att studera de inre mekanismerna hos polykristaller utvecklats under de senaste årtiondena. Bland dessa återfinns diffraktionsmetoder som är speciellt utvecklade för att studera statistiskt representativa volymer av polykristaller med hjälp av högenergetiska röntgenstrålar. Historiskt sett har dessa metoder använts främst för att mäta genomsnittliga egenskaper hos enskilda kristaller i ett aggregat. Inom denna klass av mikroskopimetoder inriktar vi oss främst på en variant som är designad för att skanna en smal röntgenstråle över provet. Mätdata av denna typ har potential att generera information på en längdskala som är mindre än de enskilda kornen i polykristallen, samtidigt som uppmätt data kan vara representativ för hundratals korn i provet. Vi låser upp denna inneboende potential genom att matematiskt härleda algoritmer kapabla att beräkna töjningarna i de enskilda kristallerna med en upplösning på subkornsnivå. Våra resultat banar väg för ett simultant studium av polykristallina deformationsmekanismer över flera längdskalor. Kopplingen mellan inter- och intrakorneffekter kan nu studeras på ett nytt sätt, med potential att låsa upp en ny svit av hemligheter kring polykristallens inre mekanismer.

List of appended papers

This doctoral thesis is based on the following manuscripts:

Paper A
Axel Henningsson, Stephen A. Hall, Jonathan P. Wright, Johan Hektor
Reconstructing intragranular strain fields in polycrystalline materials from scanning 3DXRD data
Journal of Applied Crystallography 53, 314–325. (2020)

Paper B
Axel Henningsson and Johannes Hendriks
Intragranular strain estimation in far-field scanning X-ray diffraction using a Gaussian process
Journal of Applied Crystallography 54, 1057-1070. (2021)

Paper C
Axel Henningsson and Stephen A. Hall
xrd_simulator: 3D X-ray diffraction simulation software supporting 3D polycrystalline microstructure morphology descriptions
Journal of Applied Crystallography 56, 282–292. (2023)

Paper D
Axel Henningsson and Stephen A. Hall
An efficient system matrix factorisation for strain tensor tomography
Acta Crystallographica Section A: Foundations and Advances, A79 (2023)

Paper E
Axel Henningsson, Adrian Wills, Stephen A Hall, Johannes Hendriks,
Jonathan P. Wright, Thomas B. Schön, Henning F. Poulsen
Inferring the probability distribution over strain tensors in polycrystals from diffraction based measurements
Computer methods in Applied Mechanics and Engineering, Volume 417, Part A. (2023)

Contributions of the main author

The author of this thesis has prepared and written all of the appended papers. The vast majority of the numerical implementations and derivations presented in paper A,C,D and E is the work of the author of this thesis. The regression framework described in paper B was developed and implemented in close collaboration with Johannes Hendriks. All analytical derivations presented in the appended papers, as far as they can be considered novel to the field, is the contribution of the author of this thesis. Data used to validate the developed algorhtms in Paper A, B and C were collected by Johan Hektor, Stephen Hall and Jonathan Wright.

Papers not included in this thesis

Axel Henningsson and Stephen A. Hall
A Continuity Flow Based Tomographic Reconstruction Algorithm
for 4D Multi-Beam High Temporal—Low Angular Sampling
Journal of Imaging, 7, 246. (2021)

Mohmad M. Thakur, Axel Henningsson, Jonas Engqvist,
Pierre-Olivier Autran, Jonathan P. Wright, Ryan C. Hurley
On mesoscale modeling of concrete: Role of heterogeneities on local
stresses, strains, and representative volume element
Cement and Concrete Research, Volume 163. (2023)

Johan Hektor, Stephen A. Hall, Axel Henningsson, Jonas Engqvist,
Matti Ristinmaa, Filip Lenrick, Jonathan P. Wright
Scanning 3DXRD Measurement of Grain Growth, Stress, and Formation
of Cu_6Sn_5 around a Tin Whisker during Heat Treatment
Materials, 12, 446. (2019)

Contents

Appended papers

Chapter 1

Introduction

The rigorous mathematical treatment of the mechanics of macroscopic objects finds its origins with Isaac Newton. With the advent of the publication of *"The Prinicipia"* in 1687 the motion of the celestial bodies were predicted to astonishing precision. This work was made possible by the more profound, preceding discovery of the mathematics of continuous change of functions or *"the method of fluxions"*, as Newton put it. At the same time Gottfried Wilhelm Leibniz independently found his way to the same method of calculus. And so, upon the shoulders of these two giants, Augustin-Louis Cauchy (1789) laid out the framework of continuum mechanics as we perceive it today. Cauchy generalised Newton's laws of motion, originally applied to rigid body systems, to that of continua. Indeed Cauchy's fundamental lemma is in direct analogy with Newton's third law in its stating that the points of any one body is held together by a continuous distribution of tractions, $\boldsymbol{t}_n \in \mathbb{R}^3$, acting across the imaginary internal surfaces of the body. Cauchy proved that at any one point, $\boldsymbol{x} = \begin{bmatrix} x & y & z \end{bmatrix}^T \in \mathbb{R}^3$, in the body, the traction acting on a plane passing through $\boldsymbol{x}$ with unit normal, $\hat{\boldsymbol{n}}$, can be described by a second order tensor,

$$\boldsymbol{\sigma} = \begin{bmatrix} \sigma_{11} & \sigma_{12} & \sigma_{13} \\ \sigma_{21} & \sigma_{22} & \sigma_{23} \\ \sigma_{31} & \sigma_{32} & \sigma_{33} \end{bmatrix}. \tag{1.1}$$

Although one may very well construct an infinite number of unique planes passing through $\boldsymbol{x}$ each with some normal $\hat{\boldsymbol{n}}$, the traction on these planar surfaces is described consistently by the same stress tensor,

$$\boldsymbol{t}_n = \boldsymbol{\sigma}\hat{\boldsymbol{n}}. \tag{1.2}$$

The traction distribution at a fixed point, $\boldsymbol{x}$, as described by a stress tensor is illustrated in Figure 1.1 as a function of $\hat{\boldsymbol{n}}$. It is clear that the stress tensor is, thus, a vehicle that richly encodes the distribution of traction at each point in the body.

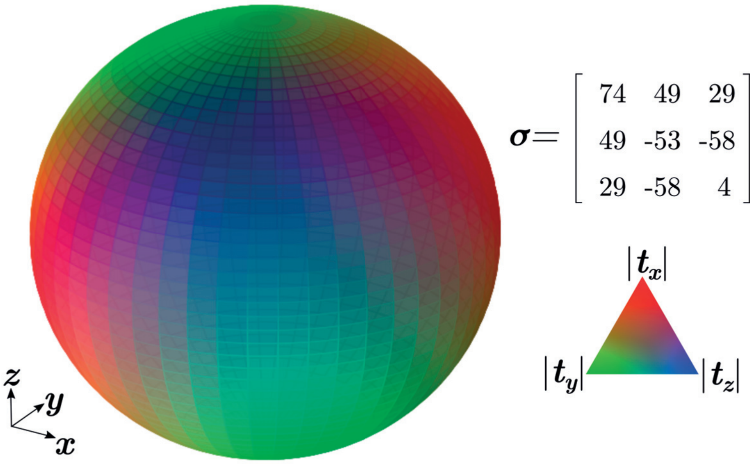

Figure 1.1: Conceptual illustration of a stress tensor, $\boldsymbol{\sigma}$. A traction, $\mathbf{t}_n = \boldsymbol{\sigma}\hat{\boldsymbol{n}}$, is associated to each direction on the unit sphere, $\hat{\boldsymbol{n}}$. Normalising the traction distribution, each traction is represented by an rgb colour value; $(|t_x|, |t_y|, |t_z|)$.

For static conditions, in the absence of moments per unit volume, the Cauchy stress, $\boldsymbol{\sigma}$, becomes symmetric and the traction distribution at $\boldsymbol{x}$ is fully described by 6 scalar values, $\sigma_{11}, \sigma_{22}, \sigma_{33}, \sigma_{12}, \sigma_{13}, \sigma_{23}$. These 6 scalar fields are commonly used in models that predict plasticity, failure, dislocation creep, damage etc. Accurate approximations to the stress distribution therefore, preoccupies the mind of the materials engineer. However, it is, unfortunately, not possible to directly measure the stress in a body. Indeed, such a project is as futile as that of directly measuring force, a quantity that is wholly a derivative of space, time and mass. Fortunately, the motion, or the deformation, of a system can be measured insofar as it can be put in relation to other spatial objects. The fundamental role of constitutive modelling is therefore to provide the map between deformation and stress. To discuss such constitutive mappings it is natural to start by considering a compact spatial domain, $\boldsymbol{x}_0 \in \Omega_0$, which we define as an undeformed reference configuration. Subject to loads, the body deforms and we find the new static equilibrium configuration, $\boldsymbol{x} \in \Omega$. The map, $\boldsymbol{x} = \boldsymbol{\varphi}(\boldsymbol{x}_0)$, has now rearranged the material points of the body. When the deformation map, $\boldsymbol{\varphi}$, is differentiable, we can provide a locally linear map between an infinitesimal line segment in the reference configuration, $\Delta\boldsymbol{x}_0$, and its deformed counterpart, $\Delta\boldsymbol{x}$, as

$$\Delta\boldsymbol{x} = \frac{\Delta\boldsymbol{x}}{\Delta\boldsymbol{x}_0}\Delta\boldsymbol{x}_0 = \nabla\boldsymbol{\varphi}\Delta\boldsymbol{x}_0 = \boldsymbol{F}\Delta\boldsymbol{x}_0, \tag{1.3}$$

where ∇ is the gradient operator and the second order tensor $\boldsymbol{F}$ is known as the deformation gradient tensor. Although it may be possible to write a constitutive relation as $\boldsymbol{\sigma} = \boldsymbol{f}(\boldsymbol{\varphi})$ or $\boldsymbol{\sigma} = \boldsymbol{g}(\boldsymbol{F})$ where $\boldsymbol{f}$ and $\boldsymbol{g}$ are stress maps, the typical postulate made in constitutive modelling is that rigid body motions do not give rise to stress. The measure of how much a local deformation differs from a pure rigid body motion can be captured by a strain tensor. For instance, letting $\boldsymbol{I}$ be the identity tensor, the Green-Lagrange strain tensor,

$$\boldsymbol{E} = \frac{1}{2}(\boldsymbol{F}^T\boldsymbol{F} - \boldsymbol{I}), \tag{1.4}$$

is realised to be independent of rigid body motion by considering the polar decomposition of the deformation gradient tensor, $\boldsymbol{F} = \boldsymbol{R}\boldsymbol{S}$, where $\boldsymbol{R}$ is a pure rotation and $\boldsymbol{S}$ is the right stretch tensor. For small deformations, the Taylor expansion of equation (1.4) with respect to $\boldsymbol{F} - \boldsymbol{I}$ yields the small strain tensor,

$$\boldsymbol{\epsilon} = \frac{1}{2}(\boldsymbol{F}^T + \boldsymbol{F}) - \boldsymbol{I}. \tag{1.5}$$

In analogy with Cauchy's stress tensor, $\boldsymbol{\sigma}$, the small strain tensor, $\boldsymbol{\epsilon}$, describes the distributed deformations across all possible surfaces passing through a point in the body. For instance, the elongation between two parallel planes with normal $\hat{\boldsymbol{n}}$, connected by a line segment of original length $||\Delta\boldsymbol{x}_0||_2$, is given by

$$\hat{\boldsymbol{n}}^T\boldsymbol{\epsilon}\hat{\boldsymbol{n}} = \frac{1}{2}(\hat{\boldsymbol{n}}^T\boldsymbol{F}^T\hat{\boldsymbol{n}} + \hat{\boldsymbol{n}}^T\boldsymbol{F}\hat{\boldsymbol{n}}) - \hat{\boldsymbol{n}}^T\hat{\boldsymbol{n}} = \hat{\boldsymbol{n}}^T\boldsymbol{n} - 1 \approx \frac{||\Delta\boldsymbol{x}||_2 - ||\Delta\boldsymbol{x}_0||_2}{||\Delta\boldsymbol{x}_0||_2}, \tag{1.6}$$

where $\boldsymbol{n} = \boldsymbol{F}\hat{\boldsymbol{n}} = \Delta\boldsymbol{x}/||\Delta\boldsymbol{x}_0||_2$.

The simplest possible constitutive model relating strain to stress is Hooke's law for linear elasticity,

$$\bar{\boldsymbol{\sigma}} = \boldsymbol{D}\bar{\boldsymbol{\epsilon}}, \tag{1.7}$$

where $\bar{\boldsymbol{\epsilon}} = \begin{bmatrix}\epsilon_{11}, \epsilon_{22}, \epsilon_{33}, \epsilon_{12}, \epsilon_{13}, \epsilon_{23}\end{bmatrix}^T \in \mathbb{R}^{6\times 1}$ and $\boldsymbol{D} \in \mathbb{R}^{6\times 6}$. As $\boldsymbol{\epsilon} = \boldsymbol{0}$ must correspond to $\boldsymbol{\sigma} = \boldsymbol{0}$ by definition, regardless of the constitutive properties of the material, it follows by Taylor expansion that Hooke's law is valid for all materials if the strain is sufficiently small. In general, when the strain is finite, the stress is a nonlinear function of strain, $\bar{\boldsymbol{\sigma}} = \bar{\boldsymbol{\sigma}}(\bar{\boldsymbol{\epsilon}})$. Since the publication of Robert Hooke (1676) stating, in original latin, that *ut tensio, sic vis* (meaning; as the extension, so the force) enormous effort has been put into developing constitutive laws reaching far beyond the linear approximations made by Hooke. To approximate the stress evolution in a body it is, therefore, often sufficient to devise an experiment in which the strain tensor evolution can be accurately determined. Once the strain is known, the stress can be approximated by constitutive considerations. The canonical experimental setup is the uniaxial test in which the specimen is subject to controlled boundary displacements that can, ideally, be compared to the undeformed length of the specimen to arrive at the axial-strain.

The stress associated to a uniaxial test is, in reality, an aggregated macroscopic quantity arising from a probably heterogeneous stress state in the body. When considering polycrystalline materials, such as metals and rocks, the individual grains in the aggregate will respond differently to the macroscopic boundary displacement. To predict the local, microscopic, response of such bodies the stress-strain curves classically derived from uniaxial testing carry little value. Indeed, to paraphrase Egon Orowan Nabarro and Argon (1995) and Tadmor and Miller (2011);

> *"..the ambition to deduce the inner workings of a polycrystalline material from a macroscopic uniaxial tensile test is as futile as that of trying to reverse engineer the mechanics of a pocket watch from its stress-strain curve."*
> *- pharaphrase Egon Orowan*

Nevertheless, a deep microscopic understanding of polycrystalline materials is core to many challenges pressing modern society. Polycrystals serve as a fundamental building block for computer electronics, semi-conductors and renewable energy technology as well as transportation and medical equipment industries. For instance, in the development of solar cells crystal strains can cause band-gap variations that are directly linked to the efficiency of the cells (Mar Lucas et al., 2021). Moreover, stress driven diffusion in tin (Sn) coated copper (Cu) electronics components has been hypothesised as responsible for tin whisker growth leading to component failure by short-circuit (Hektor et al., 2019). The deformation mechanisms of polycrystalline materials also play a key role in construction engineering including, for example, concrete casting (Thakur et al., 2023) and additive manufacturing (Carneiro et al., 2021).

In this thesis, we discuss how the elastic strains inside the individual crystals that are members of a polycrystalline aggregate can be measured. The experimental method suite under consideration is that of X-ray diffraction. As described in Chapter 2 the procedure is to illuminate the polycrystal by energetic photons while recording the diffracted signal using a digital area detector. In particular, this thesis presents a series of analytical, algorithmic and computational contributions to the inverse problems arising in these experimental applications. That is to say; we focus on the question of how to recover the strain tensor distributions in the individual crystals given a diffraction data series. This includes the study of data analysis and data reductions, forward model developments and, importantly, statistical inference analysis. By advancing the mathematical understanding and computational tractability of these topics we provide tools for the scientific and engineering community apt to deduce the inner workings of the "pocket watch" that is the polycrystal.

The measurement approach explicitly considered in this thesis is the Three Dimensional X-ray Diffraction microscope (3DXRD) (Poulsen, 2004a; Bernier et al., 2020) and the scanning variant (Hayashi et al., 2015; Wright et al., 2020). State-of-the-art 3DXRD experiments routinely recover grain maps with a per crystal volume averaged strain tensor and orientation. In this thesis we extend these capabilities by deriving methods that further exploit the diffraction data from the 3DXRD microscope to make predictions about the strain on an intragranular level. The results may find application in similar microscopes that, instead of X-rays, use neutron (Santisteban et al., 2002; Tremsin et al., 2012; Hendriks et al., 2019) or electron probes (Liu et al., 2011).

The bulk intellectual contribution of this thesis is found in the appended papers. The preceding chapters have been written with the intention of providing a conceptual introduction to the physical, experimental and mathematical constructions that the appended research papers lean on. As such the language and depth of the discussion has been tailored to a less formal and more inviting presentation. In this same spirit, the (central) mathematical derivations found in the research papers have been sifted to not unnecessarily obscure the painting of a bigger picture for the reader. The first part of the thesis starts in Chapter 2 by guiding the reader through the realm of crystal diffraction. Once the concept of diffraction is established, Chapter 3 surveys methods to deduce grain average and grain statistical strain quantities from diffraction data based on full grain illumination. Subsequently, the case of scanning-3DXRD is considered and, as such, Chapters 4 and 5 introduces some fundamentals of tomographic reconstruction and statistical estimation. These mathematical methods are then applied to diffraction data in Chapter 6 where the reconstruction of spatial strain maps in single crystals is discussed. Finally, in Chapter 7 we conclude our findings and give an outlook towards future research questions.

Chapter 2

Diffraction from Polycrystals

At the Bavarian Academy of Sciences on the 8th of June 1912, the theory of Max von Laue on the diffraction of X-rays from crystalline structures was made public (Ewald, 1960). With a strong background in optics, Laue was able to theorise that, at wavelengths shorter than the inter-atomic distances of a crystalline solid, diffraction like behaviour should be observable upon X-ray illumination. The recording of the first X-ray diffraction patterns from a copper sulphate crystal (Herausgeber, 1952; Authier, 2013) confirmed Laue's theory and opened up a new world of microscopy opportunities granting access to the inner workings of a wide range of solids at an astonishingly fine length-scale. The same confidence that Laue himself immediately put in his theory is now widely embraced:

> "*Once I had conceived the idea of X-ray diffraction in crystals this appeared so evident to me that I never understood the astonishment it produced among scientists, nor, indeed, the doubts expressed in the course of the first few years.*"
> - Max von Laue, (Ewald, 1960)

The enormous scientific value produced by the subsequent microscopy methods developed on the backbone of diffraction theory can hardly be stressed enough. As an example the Cambridge Structural Database contains, today, over 1 000 000 organic and metal-organic crystal structures all reconstructed using diffraction techniques The Cambridge Structural Database (2019). Before presenting the key Laue equations we shall first need to give a mathematical definition of the polycrystal.

2.1 Crystals

A single crystal can be defined as a periodic arrangement of atoms or molecules on a lattice (Tadmor and Miller, 2011; Als-Nielsen and McMorrow, 2011). The repeating unit or motif in the crystal is found at locations

$$\boldsymbol{r} = n_1\boldsymbol{a}_1 + n_2\boldsymbol{a}_2 + n_3\boldsymbol{a}_3, \tag{2.1}$$

where $n_1, n_2, n_3 \in \mathbb{Z}$ are integers and $\boldsymbol{a}_1, \boldsymbol{a}_2, \boldsymbol{a}_3 \in \mathbb{R}^3$ are real-space vectors. A crystal structure is conventionally described by a minimal parallel-piped that shares the symmetry of the lattice. The vectors connecting the corners of this parallel-piped are denoted $\boldsymbol{a}, \boldsymbol{b}, \boldsymbol{c} \in \mathbb{R}^3$, as depicted in Figure 2.1, and are referred to as the crystal axes. The angles formed between the crystal axes, as well as the length of these axes, form a set of 6 scalar parameters that are sufficient to describe the unit cell,

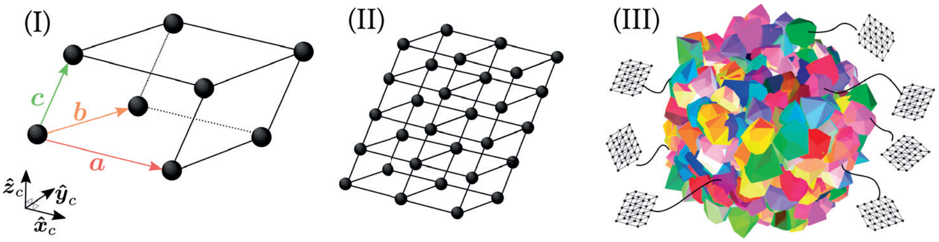

Figure 2.1: A crystal is described by a unit cell (I) defined by its crystal axes $\boldsymbol{a}, \boldsymbol{b}, \boldsymbol{c}$*. Note that the crystal axes form a right handed set:* $\boldsymbol{a}^T(\boldsymbol{b}\times\boldsymbol{c}) > 0$, $\boldsymbol{b}^T(\boldsymbol{c}\times\boldsymbol{a}) > 0$, $\boldsymbol{c}^T(\boldsymbol{a}\times\boldsymbol{b}) > 0$*. A crystal is formed by repeating the cell in a space filling manner (II). An aggregate composed of many single crystals with distinct orientations defines a polycrystal (III).*

$$\begin{aligned} \alpha &= \arccos\left(\frac{\boldsymbol{b}^T\boldsymbol{c}}{bc}\right), \qquad & a &= \sqrt{\boldsymbol{a}^T\boldsymbol{a}}, \\ \beta &= \arccos\left(\frac{\boldsymbol{a}^T\boldsymbol{c}}{ac}\right), \qquad & b &= \sqrt{\boldsymbol{b}^T\boldsymbol{b}}, \\ \gamma &= \arccos\left(\frac{\boldsymbol{a}^T\boldsymbol{b}}{ab}\right), \qquad & c &= \sqrt{\boldsymbol{c}^T\boldsymbol{c}}. \end{aligned} \tag{2.2}$$

In relation to some fixed Cartesian reference coordinate system, a crystal is said to possess an orientation described by a rotation matrix $\boldsymbol{U} \in \mathbb{R}^{3\times3}$. This rotation refers to the mapping necessary to bring an internal Cartesian crystal coordinate system, subscripted c, into alignment with the external reference coordinates. Here we define the Cartesian crystal system to have an axis, $\hat{\boldsymbol{z}}_c$, along the crystal $\boldsymbol{c}$ axis, an axis $\hat{\boldsymbol{y}}_c$ parallel to the projection of the $\boldsymbol{b}$ axis onto the plane with normal $\hat{\boldsymbol{z}}_c$, and a final axis $\hat{\boldsymbol{x}}_c = \hat{\boldsymbol{y}}_c \times \hat{\boldsymbol{z}}_c$, where × denotes cross product of vectors (Note that $\boldsymbol{a}_1, \boldsymbol{a}_2, \boldsymbol{a}_3$ are defined in this crystal coordinate frame). A polycrystalline material can then be defined as a set of crystals, each featuring a distinct orientation matrix, $\boldsymbol{U}$ (the term distinct can be somewhat vague in this context, but typically refers to a local change in orientation larger than about 0.5^o).

2.2 X-ray Diffraction

The motif in the crystal lattice is populated by a group of atoms bound together by an electron density. The simplest model of X-ray diffraction from a crystal is built on the realisation that the electrons present in each motif in the lattice will re-irradiate photons when subject to an incident electromagnetic wave. The amplitude of the scattered radiation from the crystal, as perceived from a distant point $\boldsymbol{x}$, is proportional to a sum over N spherical waves, where N is the number of unit cells in the lattice. Denoting the propagation direction of the incident planar waves by $\hat{\boldsymbol{k}}_c$ and the direction of scattering by $\hat{\boldsymbol{k}}'_c$ we find the phase difference, $\Delta\phi$, between the scattered waves emitted from $\boldsymbol{r}_0 = \boldsymbol{0}$ and $\boldsymbol{r}_j$ as

$$\Delta\phi = \frac{2\pi}{\lambda}(\hat{\boldsymbol{k}}_c - \hat{\boldsymbol{k}}'_c)^T \boldsymbol{r}_j, \tag{2.3}$$

where λ is the wavelength of the X-rays (it is assumed that the scattering is elastic, i.e the X-ray energy is preserved throughout scattering). The geometrical situation is illustrated in 2D in Figure 2.2. The scattered intensity perceived at our distant location $\boldsymbol{x}$ is clearly maximised when the phase differences of scattering contributions from $\boldsymbol{r}_0$ and $\boldsymbol{r}_j$ are multiples of 2π, i.e., when the scattered waves are in phase at $\boldsymbol{x}$. Introducing the diffraction vector, $\boldsymbol{G}_c = 2\pi(\hat{\boldsymbol{k}}'_c - \hat{\boldsymbol{k}}_c)/\lambda$, the diffraction condition can be formulated as

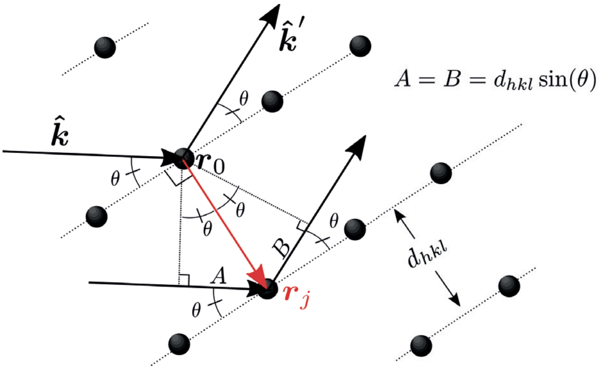

Figure 2.2: The phase shift of light irradiated from two lattice sites, $\boldsymbol{r}_0$ *and* $\boldsymbol{r}_j$ *is found as* $\Delta\phi = (2\pi/\lambda)(\hat{\boldsymbol{k}}'_c - \hat{\boldsymbol{k}}'_c)^T\boldsymbol{r}_j$ *where* $\hat{\boldsymbol{k}}_c$ *and* $\hat{\boldsymbol{k}}'_c$ *denote the propagation direction of incident and scattered waves respectively.*

$$\boldsymbol{G}_c^T \boldsymbol{r}_j = 2\pi m, \tag{2.4}$$

where m is an integer. The Laue equations, which are elaborated upon in the following section, are the solutions to the diffraction condition given in (2.4). The final equations modulating the number of photons scattered per unit time to some solid angle is affected by a long array of considerations such as structure factors, polarisation factors, Lorentz factors and atomic form factors, to name a few. Nevertheless, the diffraction condition given in equation (2.4) can be considered to be the most central component in predicting diffraction from a crystal in an experimental setting. The reader is referred to Als-Nielsen and McMorrow (2011) for a more in depth introduction to X-ray scattering.

2.3 The Laue Equations

To solve equation (2.4) we recall the definition of the crystal lattice vector, $\boldsymbol{r}_j$, from equation (2.1) and find that

$$n_1\boldsymbol{G}_c^T\boldsymbol{a}_1 + n_2\boldsymbol{G}_c^T\boldsymbol{a}_2 + n_3\boldsymbol{G}_c^T\boldsymbol{a}_3 = 2\pi m. \tag{2.5}$$

Since equation (2.5) is to hold for all integers, n_1, n_2, n_3, m, it follows that

$$\boldsymbol{G}_c^T\boldsymbol{a}_i = 2\pi m_i, \quad \forall i, \tag{2.6}$$

where m_i is an integer. Transposing and stacking these equations, targeting $\boldsymbol{G}_c$ as the unknown, we find that,

$$\begin{bmatrix} \boldsymbol{a}_1^T \\ \boldsymbol{a}_2^T \\ \boldsymbol{a}_3^T \end{bmatrix} \boldsymbol{G}_c = 2\pi\boldsymbol{G}_{hkl}, \tag{2.7}$$

where $\boldsymbol{G}_{hkl} = \begin{bmatrix} h & k & l \end{bmatrix}^T$ and $h = m_1, k = m_2, l = m_3$ are integers . Denoting the system matrix containing the lattice vectors as $\boldsymbol{A}^T$ we find that

$$\boldsymbol{G}_c = 2\pi\boldsymbol{A}^{-T}\boldsymbol{G}_{hkl}. \tag{2.8}$$

Throughout this work we shall assume that the selected unit cell has crystal axes identical to those of the lattice basis, i.e $\boldsymbol{a}_1 = \boldsymbol{a}$, $\boldsymbol{a}_2 = \boldsymbol{b}$ and $\boldsymbol{a}_3 = \boldsymbol{c}$, i.e.,

$$\boldsymbol{A} = \begin{bmatrix} \boldsymbol{a} & \boldsymbol{b} & \boldsymbol{c} \end{bmatrix}. \tag{2.9}$$

Introducing the matrix $\boldsymbol{B} = 2\pi\boldsymbol{A}^{-T}$ we conclude that the diffraction vector, $\boldsymbol{G}_c$, as described in the crystal coordinate frame must fulfil the Laue equations,

$$\boldsymbol{G}_c = \boldsymbol{B}\boldsymbol{G}_{hkl}, \tag{2.10}$$

for diffraction to be observed. Alternatively, when deploying an external reference frame, independent of grain orientation, we write,

$$\boldsymbol{G} = \boldsymbol{U}\boldsymbol{B}\boldsymbol{G}_{hkl}, \tag{2.11}$$

where $\boldsymbol{U}$ is the crystal grain orientation.

Soon after the discovery of crystal X-ray diffraction by Max von Laue, William Henry Bragg, and his son, Lawrence Bragg, published, together (Bragg and Bragg, 1913; Bragg et al., 1962; Phillips, 1979), a special scalar reduction of equation (2.11) known as Bragg's law,

$$2d_{hkl}\sin(\theta) = m\lambda, \tag{2.12}$$

where d_{hkl} is the spacing between planes in the crystal with normal along $\boldsymbol{G}$, θ is the Bragg angle, formed between $\hat{\boldsymbol{k}}$ and the scattering planes and m is again an integer. To see that Bragg's law follows from the Laue equations we introduce the projection matrix,

$$\boldsymbol{P}_G = \frac{\boldsymbol{G}\boldsymbol{G}^T}{\boldsymbol{G}^T\boldsymbol{G}} - \boldsymbol{I}, \tag{2.13}$$

which maps any vector onto a plane with unit normal along $\boldsymbol{G}$. Multiplying the Laue equations (2.11) from the left with $\boldsymbol{P}_G$ we find

$$\boldsymbol{P}_G\boldsymbol{G} = \boldsymbol{P}_G\boldsymbol{U}\boldsymbol{B}\boldsymbol{G}_{hkl} = \boldsymbol{0}. \tag{2.14}$$

Inserting the definition of the diffraction vector, $\boldsymbol{G} = 2\pi(\hat{\boldsymbol{k}}' - \boldsymbol{k})/\lambda$, we find that

$$\frac{2\pi}{\lambda}\boldsymbol{P}_G(\hat{\boldsymbol{k}}' - \boldsymbol{k}) = \boldsymbol{0}. \tag{2.15}$$

It follows that,

$$\boldsymbol{P}_G\hat{\boldsymbol{k}}' = \boldsymbol{P}_G\boldsymbol{k}, \tag{2.16}$$

which implies that the angle of reflection and incidence between the X-ray propagation direction and the considered lattice planes (defined by h, k, l) is one and the same, θ, during diffraction. With this relation known it is easy to derive Bragg's law from geometrical considerations of triangles in a 2D plane, as illustrated in Figure 2.2.

2.4 Measuring Diffraction

With the Laue equations derived, we are ready to ask the question of how to set up an X-ray diffraction experiment such that the crystal orientation matrix $\boldsymbol{U}$ and the crystal cell parameters $a, b, c, \alpha, \beta, \gamma$ can be estimated. In this thesis we have worked almost exclusively with the synchrotron based Three Dimensional Diffraction Microscope (3DXRD) as pioneered by Poulsen (2004b) and co-workers (also known as High Energy Diffraction Microscopy (HEDM), Bernier et al. (2020)). In this setting the polycrystal is placed on a turntable featuring a single fixed axis of rotation while illuminated by a high energy (∼10-100keV) monochromatic X-ray beam. A 2D flat area detector is placed far behind (∼ 100-200 mm) the sample to record the scattered X-rays originating from the individual crystals in the aggregate. To ensure that the diffraction conditions (2.11) are met, each recorded diffraction pattern is collected continuously as the sample rotates over a fixed angular interval $\omega \ \pm \Delta\omega/2$. The result of this procedure is a series of spotty diffraction patterns where each scattering event (diffraction peak) is associated to an unknown crystal in the sample. In Figure 2.3 we provide an illustrative simulation showing how the diffraction pattern is affected by the number of illuminated grains in the sample. Further details on how monochromatic X-ray scattering can modelled in this type of experimental setting can be found in Paper C (Henningsson and Hall, 2023) where we presented an open source computer code for this purpose. The number of grains that can be analysed with the 3DXRD microscope is ultimately limited by diffraction spot overlap with polycrystalline aggregates featuring a few thousand grains representing the typical limit (Lauridsen et al., 2001; Sørensen et al., 2012; Sharma et al., 2012; Wozniak et al., 2014).

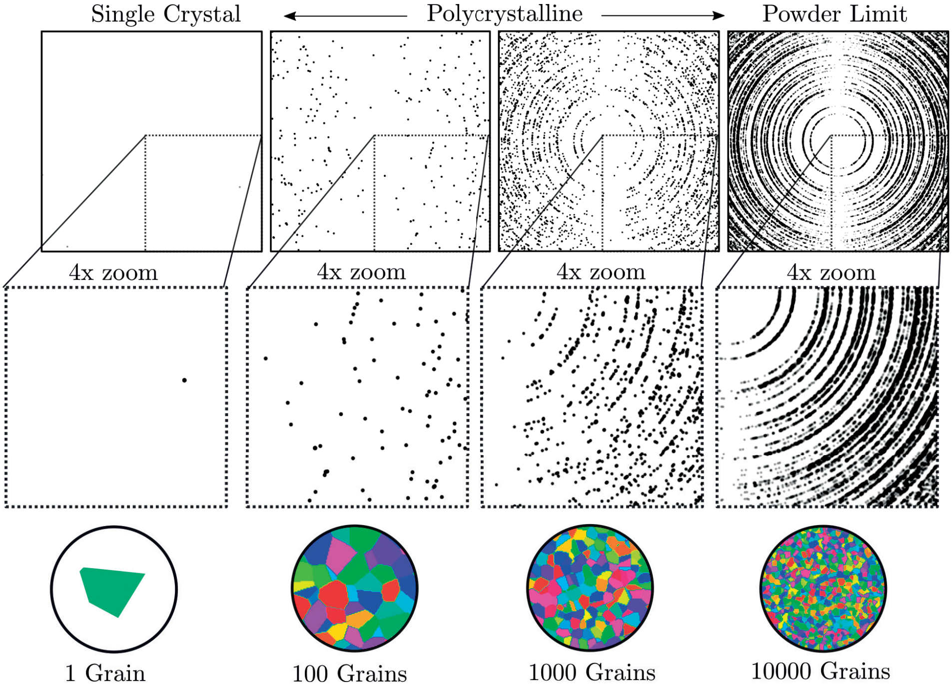

Figure 2.3: Simulated diffraction patterns from a SiO_2 *polycrystal integrated over a* $\Delta\omega = 1^o$ *rocking interval. The number of illuminated grains increased from left to right. In the limit when the diffraction spots are merging into "powder rings" per-grain analysis is not possible. The geometry used in the simulation is similar to the 3DXRD setup in Figure 2.4, but with a wide beam illuminating the entire polycrystal at all times.*

The size of the incident X-ray beam is variable in 3DXRD microscopy which allows the user to limit the number of illuminated grains at a single rotation setting. This not only helps to alleviate diffraction spot overlap but also provides a means to increase the spatial resolution of the data analysis owing to the fact that a known sub-volume of the sample is associated to each diffraction pattern. In Figure 2.4 the scanning-3DXRD scenario is depicted which is often defined by selecting a beam size cross section smaller than that of the average grain cross section Hayashi et al. (2015) Hayashi et al. (2017) Hayashi et al. (2019).

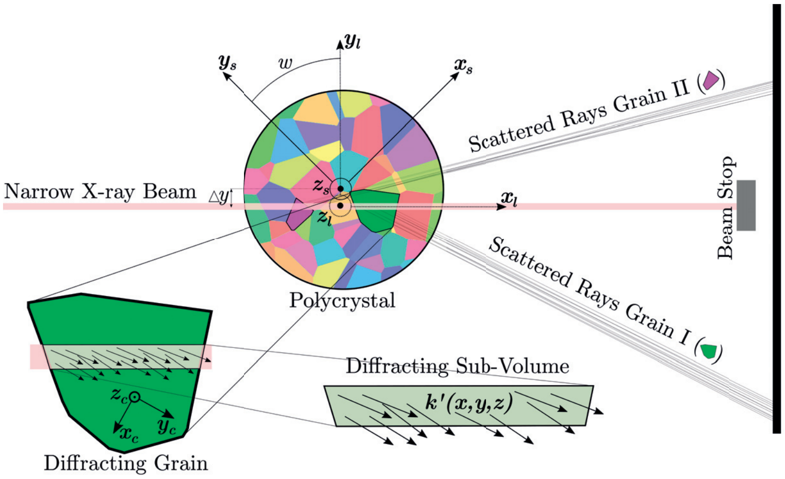

Figure 2.4: The 3DXRD geometry presented in a top down view (x-y-plane) for the special case of scanning-3DXRD. At each sample translation (Δy) a rotation is performed around the $\hat{\boldsymbol{z}}_s$-axis and the resulting diffraction from the polycrystalline sample is collected on a 2D area detector. The position of a recorded diffraction peak is a function of the $\boldsymbol{k}' = \boldsymbol{k}'(\boldsymbol{x})$ field existing on a diffracting sub-volume associated to a single crystal in the sample.

The procedure of processing a series of diffraction pattern images into a list of grain orientations, $\boldsymbol{U}$, is often referred to as indexing and many algorithms exists for doing so given that an initial, approximate, estimate of $\boldsymbol{B}$ exists (Schmidt, 2014). We will not survey these methods in this thesis, but simply conclude that, once the grain orientations are known, further analysis on a per-grain basis can be achieved by segmenting out the subset of diffraction data associate to each grain. In the following chapter we will discuss how these data can be used to provide an estimate of the crystal strain tensor.

Chapter 3

Aggregated Measures of Strain

The placement of the detector at a significant distance behind the sample is a key feature of the 3DXRD microscope. This arrangement yields a highly sensitive diffraction peak position in the detector plane, making it responsive to even minor perturbations in the crystal unit cell parameters including a high sensitivity to crystal strain. We shall now illustrate this fact by considering a set of diffracting Miller planes with indices h, k, l, lattice plane separation d^0_{hkl}, and unit normal $\hat{\boldsymbol{\kappa}}$. Let us now perturb the inter-planar distance, d^0_{hkl}, with a small, strain, s_{hkl}, as

$$d_{hkl} = d^0_{hkl}(1 + \hat{\boldsymbol{\kappa}}^T \boldsymbol{\epsilon} \hat{\boldsymbol{\kappa}}) = d^0_{hkl}(1 + s_{hkl}). \tag{3.1}$$

The Bragg equation 2.12 for $m = 1$ now provide a model Bragg angle, θ_0, corresponding to a strain free lattice state, and a model Bragg angle, θ, corresponding to a deformed state:

$$\begin{aligned} \sin(\theta_0) &= \frac{\lambda}{2d^0_{hkl}}; \quad \text{strain free lattice state,} \\ \sin(\theta) &= \frac{\lambda}{2d_{hkl}}; \quad \text{deformed lattice state.} \end{aligned} \tag{3.2}$$

For a detector perfectly aligned perpendicular to the beam and situated at distance, D, behind the diffracting crystal, the radial coordinate, r, at which the diffracted rays will intersect the detector, can be computed as

$$\begin{aligned} r_0 &= D \tan\big(2\theta_0\big); \quad \text{strain free lattice state,} \\ r &= D \tan\big(2\theta\big); \quad \text{deformed lattice state.} \end{aligned} \tag{3.3}$$

Combining equations (3.1),(3.2) and (3.3) the radial shift in diffraction peak position, $\Delta r = r_0 - r$, is seen to depend linearly on the detector distance, D, and non-linearly on the remaining parameters

$$\Delta r = D \left[\tan\left(2 \arcsin\left(\frac{\lambda}{2d^0_{hkl}} \right) \right) - \tan\left(2 \arcsin\left(\frac{\lambda}{2d^0_{hkl}(1 + s_{hkl})} \right) \right) \right]. \tag{3.4}$$

From this analysis it is clear that for a fixed strain, s_{hkl}, the peak shift, Δr, is maximised by moving the detector far away, $D \rightarrow \infty$. In practice the detector has a finite size, so, by placing the detector very far from the sample, high angle peaks are lost beyond the detector bounds. This is problematic in two ways; firstly, because we want to measure as many diffraction peaks as possible, to maintain a well posed inversion problem, and, secondly, because high angle diffraction peaks give more accurate strain measures than low angle diffraction peaks. The later of these issues is realised by considering the derivative of Δr with respect to Bragg angle as

$$\frac{\partial \Delta r}{\partial \theta_0} = \frac{D}{\cos^2(2\theta_0)}, \tag{3.5}$$

which clearly is maximised for large Bragg angles, θ_0. The selection of detector distance, D, is therefore a trade-off between resolving many high-angle diffraction peaks and maximising the overall resolution in strain. It is worth mentioning that, although the prediction is that the resolution in strain is ever increasing with D (assuming some peaks hit the detector), in practice, the X-rays are not perfectly monochromatic and so the energy bandwidth will limit the resolution achievable, which is typically 10^{-4} in state of the art 3DXRD experiments (Borbély et al., 2014). Another important conclusion from the above discussion is that, in 3DXRD, we want the detector to be large, allowing us to increase D without loosing diffraction peaks to the detector bounds. Today, this is practically achieved using panel detectors featuring multiple sub-detector panels tightly arranged to form a large single large area detector which may feature a total size in the range of tens of cm (Lienert et al., 2013). In Figure 3.1 we summarise our discussion on strain sensitivity by illustrating how the shift in diffraction peak position, Δr, varies with detector distance D, lattice plane separation, d^0_{hkl}, and X-ray energy for a fixed strain of $s_{hkl} = 10^{-4}$.

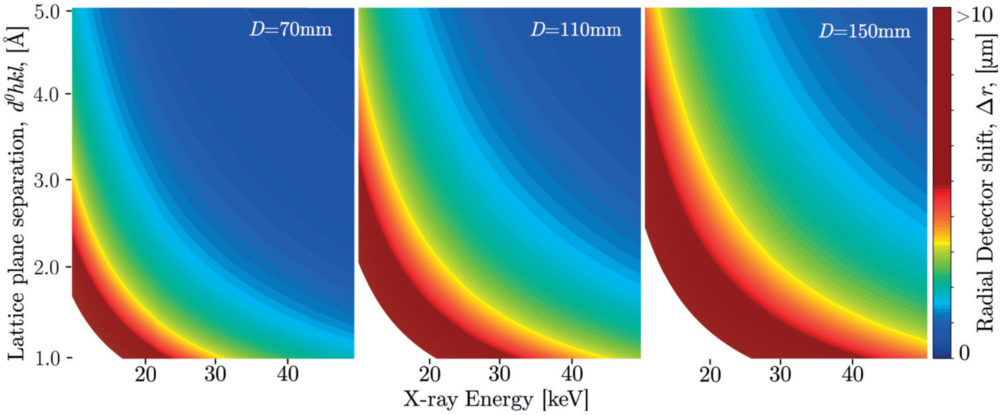

Figure 3.1: The diffraction peak position, Δr, is seen to vary with with detector distance D, lattice plane separation, d^0_{hkl}, and X-ray energy for a fixed strain of $s_{hkl} = 10^{-4}$.

3.1 Deformation and Diffraction Vectors

We shall now show how the directional strain measure, s_{hkl}, discussed in the previous section can be connected to the Laue equations (2.11) and the matrices $\boldsymbol{U}$ and $\boldsymbol{B}$. This connection is a necessary prerequisite to later formulate strain inversion models that estimate the crystal strain tensor from a set of diffraction peaks. Let us therefore return to the concept of a deformation gradient tensor, $\boldsymbol{F}$, that describes the local deformation map from reference to deformed configuration, as described in Chapter 1 equation (1.3). The exposition takes place in the sample coordinate system where an incremental material line, $\boldsymbol{\Delta x_0}$, existing in a reference configuration (subscript 0), is mapped by $\boldsymbol{F}$ to a deformed material line, $\Delta \boldsymbol{x}_{curr}$, existing in the current, deformed, configuration,

$$\Delta \boldsymbol{x}_{curr} = \boldsymbol{F} \Delta \boldsymbol{x}_0. \tag{3.6}$$

Defining a set of reference crystal axes,

$$\boldsymbol{A}_0 = \begin{bmatrix} \boldsymbol{a}_0 & \boldsymbol{b}_0 & \boldsymbol{c}_0 \end{bmatrix}, \tag{3.7}$$

we find the corresponding deformed unit cell as,

$$\boldsymbol{A}_{curr} = \boldsymbol{F} \boldsymbol{A}_0. \tag{3.8}$$

The set of experimentally observed diffraction vectors, $\{\boldsymbol{G}^1, \boldsymbol{G}^2, ..., \boldsymbol{G}^m\}$, is a function, $\mathcal{G}[\cdot]$, of the deformed unit cell, as

$$\mathcal{G}[\boldsymbol{A}_{cur}] = \{\boldsymbol{G}^1, \boldsymbol{G}^2, ..., \boldsymbol{G}^m\}. \tag{3.9}$$

Importantly, from an experimental observer point of view, there exist modes of deformation to which the diffraction signal is immutable. Consider, for example, dislocation glide that results in constant-volume plastic deformation such that the crystal structure appears unchanged. Historically, in the context of 3DXRD, the deformation, $\boldsymbol{F}$, has been implicitly assumed to only contain contributions that are observable in diffraction (this convention is followed in Paper E). In Paper C we suggest an extended formalism that deals explicitly with the diffraction observable and diffraction un-observable deformation contributions. This framework is reiterated in the following and starts with a multiplicative split of the deformation gradient tensor into an elastic, $\boldsymbol{F}_e$, and plastic, $\boldsymbol{F}_p$, part as

$$\boldsymbol{F} = \boldsymbol{F}_e \boldsymbol{F}_p. \tag{3.10}$$

While this split is similar to that used in crystal plasticity (Kröner, 1959; Lee and Liu, 1967; Clifton, 1972; Clayton and McDowell, 2003; Jiao and Fish, 2018), here we define $\boldsymbol{F}_e$ as a deformation that perturbs the measured diffraction vectors,

$$\mathcal{G}[\boldsymbol{F}_e \boldsymbol{A}_0] \neq \mathcal{G}[\boldsymbol{A}_0], \tag{3.11}$$

while, in contrast, $\boldsymbol{F}_p$ is defined as a deformation that leaves the measured diffraction vectors unchanged,

$$\mathcal{G}[\boldsymbol{F}_p\boldsymbol{A}_0] = \mathcal{G}[\boldsymbol{A}_0]. \tag{3.12}$$

Using the factorisation in equation (3.10), we may now define a fictive configuration, $\boldsymbol{A}$, as

$$\boldsymbol{A} = \boldsymbol{F}_e\boldsymbol{A}_0, \tag{3.13}$$

with the special property that

$$\mathcal{G}[\boldsymbol{A}] = \mathcal{G}[\boldsymbol{A}_{curr}], \tag{3.14}$$

i.e., $\boldsymbol{A}$ is diffraction equivalent to $\boldsymbol{A}_{curr}$. From equation (3.13) it follows that,

$$\boldsymbol{F}_e = \boldsymbol{A}\boldsymbol{A}_0^{-1}. \tag{3.15}$$

Combining equation (3.15) with the Laue equations,

$$\boldsymbol{G} = 2\pi\boldsymbol{A}^{-T}\boldsymbol{G}_{hkl}, \tag{3.16}$$

we arrive at a relation between deformation gradients and diffraction vectors as

$$\boldsymbol{F}_e^T\boldsymbol{G} = \boldsymbol{G}_0, \tag{3.17}$$

where

$$\boldsymbol{G}_0 = 2\pi\boldsymbol{A}_0^{-T}\boldsymbol{G}_{hkl}. \tag{3.18}$$

3.1.1 Strain and Diffraction Vectors

We now seek the final link between equation (3.17) and a strain tensor. Following equation (1.4) the Green-Lagrange strain can be split into an elastic, $\boldsymbol{E}_e$, and plastic, $\boldsymbol{E}_p$, part (Clayton and McDowell, 2003),

$$\boldsymbol{E} = \frac{1}{2}\boldsymbol{F}_p^{-T}(\boldsymbol{F}^T\boldsymbol{F} - \boldsymbol{I})\boldsymbol{F}_p^{-1} = \underbrace{\frac{1}{2}(\boldsymbol{F}_e^T\boldsymbol{F}_e - \boldsymbol{I})}_{\boldsymbol{E}_e} + \underbrace{\frac{1}{2}(\boldsymbol{I} - \boldsymbol{F}_p^{-T}\boldsymbol{F}_p^{-1})}_{\boldsymbol{E}_p}, \tag{3.19}$$

where $\boldsymbol{E}_e$ is seen to be defined in an intermediate, plastically deformed, configuration (see Paper E, appendix A, for a summary of configurations). Taylor expanding equation (3.19) we find the small strain tensor as

$$\boldsymbol{\epsilon} = \frac{1}{2}(\boldsymbol{F}_e^T + \boldsymbol{F}_e) - \boldsymbol{I}. \tag{3.20}$$

Multiplying equation (3.20) by $\boldsymbol{G}^T$ from the left and $\boldsymbol{G}$ from the right and using our result from equation (3.17), we find

$$\boldsymbol{G}^T\boldsymbol{\epsilon}\boldsymbol{G} = \frac{1}{2}(\boldsymbol{G}^T\boldsymbol{G}_0 + \boldsymbol{G}_0^T\boldsymbol{G}) - \boldsymbol{G}^T\boldsymbol{G} = \boldsymbol{G}^T\boldsymbol{G}_0 - \boldsymbol{G}^T\boldsymbol{G}. \tag{3.21}$$

Normalising equation (3.21) by $\boldsymbol{G}^T\boldsymbol{G}$ we arrive at relation between the scalar directional strain, s_{hkl}, and the strain tensor as

$$s_{hkl} = \hat{\boldsymbol{\kappa}}_{hkl}^T \boldsymbol{\epsilon} \hat{\boldsymbol{\kappa}}_{hkl} = \frac{\boldsymbol{G}^T\boldsymbol{G}_0}{\boldsymbol{G}^T\boldsymbol{G}} - 1, \tag{3.22}$$

where the diffracting lattice plane normal, $\hat{\boldsymbol{\kappa}}_{hkl}$, is defined as

$$\hat{\boldsymbol{\kappa}}_{hkl} = \frac{\boldsymbol{G}}{||\boldsymbol{G}||_2}. \tag{3.23}$$

Equation 3.22 connects the Laue equations via the measured diffraction vectors, $\boldsymbol{G}$, to the directional strain, s_{hkl}, in the crystal. This relation is one of the cornerstones for the type of strain estimation pursued in this thesis. Importantly, the involved quantity $\boldsymbol{G}^T\boldsymbol{G}$ is independent of lattice rotations, while the quantity $\boldsymbol{G}^T\boldsymbol{G}_0$ is weakly orientation dependent as we work under the assumption that $\boldsymbol{U}^T\boldsymbol{U}_0 \approx \boldsymbol{I}$. This motivates the decoupling of strain and crystal rotations.

3.1.2 Generalisations to Large Strains

For large deformations the approximation used in equation (3.22) breaks down. To quantify the error associated to this approximation, we consider the more general case of large elastic strain $\boldsymbol{E}_e$. From the definition of $\boldsymbol{E}_e$ in equation (3.19), it follows that,

$$\boldsymbol{G}^T\boldsymbol{E}_e\boldsymbol{G} = \frac{1}{2}(\boldsymbol{G}^T\boldsymbol{F}_e^T\boldsymbol{F}_e\boldsymbol{G} - \boldsymbol{G}^T\boldsymbol{G}). \tag{3.24}$$

In contrast to the case of small strains the format of equation (3.24) does not admit direct use of equation (3.17). To advance from equation (3.24) we use a polar decomposition (Truesdell et al., 1965) of $\boldsymbol{F}_e$ as

$$\boldsymbol{F}_e = \boldsymbol{R}\boldsymbol{S}, \tag{3.25}$$

where $\boldsymbol{R} \in \mathbb{R}^{3\times 3}$ is a rotation matrix and $\boldsymbol{S}$ is the symmetric right stretch tensor. Multiplying $\boldsymbol{E}_e$ in equation (3.19) by $\boldsymbol{R}^T\boldsymbol{G}$ from left and right and using the polar decomposition, we find

$$\boldsymbol{G}^T\boldsymbol{R}\boldsymbol{E}_e\boldsymbol{R}^T\boldsymbol{G} = \frac{1}{2}(\boldsymbol{G}^T\boldsymbol{R}\boldsymbol{S}^T\boldsymbol{S}\boldsymbol{R}^T\boldsymbol{G} - \boldsymbol{G}^T\boldsymbol{G}), \tag{3.26}$$

where it was used that $\boldsymbol{R}^T\boldsymbol{R} = \boldsymbol{R}\boldsymbol{R}^T = \boldsymbol{I}$. Considering equation (3.17) and using the polar decomposition, we find that

$$\boldsymbol{F}_e^T\boldsymbol{G} = \boldsymbol{S}^T\boldsymbol{R}^T\boldsymbol{G} = \boldsymbol{S}\boldsymbol{R}^T\boldsymbol{G} = \boldsymbol{G}_0, \tag{3.27}$$

where it was used that $\boldsymbol{S} = \boldsymbol{S}^T$. Insertion of (3.27) in equation (3.26) yields

$$\boldsymbol{G}^T\boldsymbol{R}\boldsymbol{E}_e\boldsymbol{R}^T\boldsymbol{G} = \frac{1}{2}(\boldsymbol{G}_0^T\boldsymbol{G}_0 - \boldsymbol{G}^T\boldsymbol{G}), \tag{3.28}$$

where we note that the right hand side contains only terms related to the known vectors $\boldsymbol{G}$ and $\boldsymbol{G}_0$. Normalisation by $\boldsymbol{G}$ yields an alternative format of equation (3.26) as

$$\hat{\boldsymbol{\kappa}}_{hkl}^T \boldsymbol{R}\boldsymbol{E}_e\boldsymbol{R}^T\hat{\boldsymbol{\kappa}}_{hkl} = \frac{\boldsymbol{G}_0^T\boldsymbol{G}_0 - \boldsymbol{G}^T\boldsymbol{G}}{2\boldsymbol{G}^T\boldsymbol{G}}. \tag{3.29}$$

The left hand side in equation (3.29) describes a scalar strain existing in an unknown direction, $\boldsymbol{R}^T\hat{\boldsymbol{\kappa}}_{hkl}$, introducing an error in the directional strain as,

$$\Delta s_{hkl} = \hat{\boldsymbol{\kappa}}_{hkl}^T \boldsymbol{R}\boldsymbol{E}_e\boldsymbol{R}^T\hat{\boldsymbol{\kappa}}_{hkl} - \hat{\boldsymbol{\kappa}}_{hkl}^T\boldsymbol{E}_e\hat{\boldsymbol{\kappa}}_{hkl}. \tag{3.30}$$

Alternatively, we find that

$$\Delta s_{hkl} = \hat{\boldsymbol{\kappa}}_{hkl}^T(\boldsymbol{R}\boldsymbol{E}_e\boldsymbol{R}^T - \boldsymbol{E}_e)\hat{\boldsymbol{\kappa}}_{hkl}. \tag{3.31}$$

revealing that the error, Δs_{hkl}, arises from a mismatch between the rotated tensor $\boldsymbol{R}\boldsymbol{E}_e\boldsymbol{S}^T\boldsymbol{R}^T$ and the un-rotated tensor $\boldsymbol{E}_e$. To illustrate how the error, Δs_{hkl}, in equation (3.31) varies with the rotation ($\boldsymbol{R}$) and strain ($\boldsymbol{E}_e$) amplitudes we present a numerical simulation in Figure 3.2 where we have computed the standard deviation, σ_e, of Δs_{hkl} from sets of random deformation states. For each strain-orientation magnitude in Figure 3.2, 1000 random draws of $\boldsymbol{R}$, $\boldsymbol{E}_e$ and $\boldsymbol{\kappa}_{hkl}$ where performed, and each draw was used to produce a scalar error in strain, Δs_{hkl}, by multiplying through according to equation (3.31). The strain magnitude in Figure 3.2 corresponds to the largest component of strain present within the randomly uniformly generated tensor. Likewise each rotation magnitude corresponds to the number of degrees of rotation the randomly uniformly generated $\boldsymbol{R}$ represents. We conclude from equation (3.31) and Figure 3.2 that the error, Δs_{hkl}, can, in general, be small in the presence of large stretches, $\boldsymbol{S}$, given that the rotation, $\boldsymbol{R}$, is moderate.

We close this section by noting that, in the Papers appended to this thesis, we have used the small strain approximation made in equation (3.20). As will become apparent in Chapter 6, this distinction has no practical relevance in scanning-3DXRD, where s_{hkl} must anyways be Taylor expanded to deal with the fact that the measured strain signal is integrated over sub-volumes within the crystal. In these applications joint reconstruction of the coupled strain-orientation field seems to be the most promising route forward (see Paper D, appendix). For other applications, the generalisation to large strains by following the approach outlined above is the subject of ongoing research.

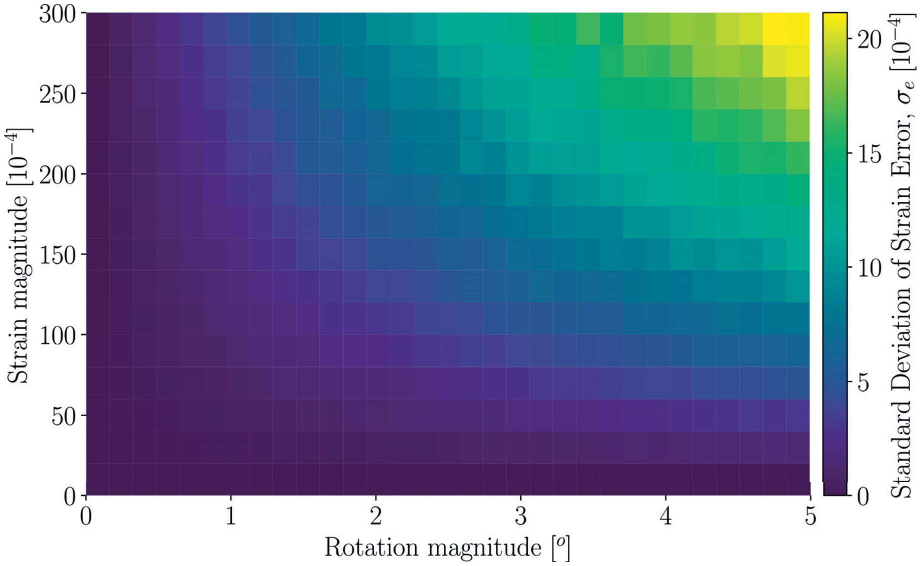

Figure 3.2: The standard deviation, σ_e, of the error in strain, Δs_{hkl}, is seen to increase with the strain and rotation magnitude.

3.2 Grain Average Strain Estimation

As pointed out by Margulies et al. (2002), given a set of directions, $\hat{\boldsymbol{\kappa}}_{hkl}$, each associated to a strain, s_{hkl}, it is possible to reconstruct a grain average strain tensor, $\boldsymbol{\epsilon}$ (Margulies et al., 2002; Poulsen et al., 2001; Oddershede et al., 2010; Bernier et al., 2011). Such a reconstruction can be achieved by solving a set of linear equations where each diffraction peak adds a single row in the system matrix. To outline this procedure we start by denoting

$$\hat{\boldsymbol{\kappa}}_{hkl} = \begin{bmatrix} \kappa_x \\ \kappa_y \\ \kappa_z \end{bmatrix}, \tag{3.32}$$

and note that the measurement of a single diffraction peak gives us the scalar equation

$$\begin{aligned} &\hat{\boldsymbol{\kappa}}_{hkl}^T \boldsymbol{\epsilon} \hat{\boldsymbol{\kappa}}_{hkl} = (\epsilon_{11}\kappa_x + \epsilon_{12}\kappa_y + \epsilon_{13}\kappa_z)\kappa_x + \\ &(\epsilon_{12}\kappa_x + \epsilon_{22}\kappa_y + \epsilon_{23}\kappa_z)\kappa_y + (\epsilon_{13}\kappa_x + \epsilon_{23}\kappa_y + \epsilon_{33}\kappa_z)\kappa_z = \\ &\kappa_x^2\epsilon_{11} + \kappa_y^2\epsilon_{22} + \kappa_z^2\epsilon_{33} + 2\kappa_x\kappa_y\epsilon_{12} + 2\kappa_x\kappa_z\epsilon_{13} + 2\kappa_y\kappa_z\epsilon_{23} = \bar{\boldsymbol{\kappa}}^T\bar{\boldsymbol{\epsilon}}, \end{aligned} \tag{3.33}$$

where

$$\begin{aligned} \bar{\boldsymbol{\kappa}} &= \begin{bmatrix} \kappa_x^2 & \kappa_y^2 & \kappa_z^2 & 2\kappa_x\kappa_y & 2\kappa_x\kappa_z & 2\kappa_y\kappa_z \end{bmatrix}^T, \\ \bar{\boldsymbol{\epsilon}} &= \begin{bmatrix} \epsilon_{11} & \epsilon_{22} & \epsilon_{33} & \epsilon_{12} & \epsilon_{13} & \epsilon_{23} \end{bmatrix}^T. \end{aligned} \tag{3.34}$$

Considering a set of m diffraction peaks, each originating from the same crystal grain, we find a system of equations as

$$\underbrace{\begin{bmatrix} \bar{\boldsymbol{\kappa}}_1^T \\ \bar{\boldsymbol{\kappa}}_2^T \\ \vdots \\ \bar{\boldsymbol{\kappa}}_m^T \end{bmatrix}}_{\boldsymbol{K}} \bar{\boldsymbol{\epsilon}} = \underbrace{\begin{bmatrix} s_{hkl}^{(1)} \\ s_{hkl}^{(2)} \\ \vdots \\ s_{hkl}^{(m)} \end{bmatrix}}_{\boldsymbol{s}}. \tag{3.35}$$

In 3DXRD, owing to the high X-ray energy and the large detector, $\boldsymbol{K}$ can be of full column rank using only 6 distinct diffraction peaks. However, in practice, more peaks are desirable to mitigate noise. In Paper E, we provide a deeper and more technically involved discussion on how and why this inverse problem is well posed in 3DXRD. Importantly, though, the strain tensor fitted by such a procedure is a volume average property of the grain and the local, intragranular strain, may very well deviate from this value. In this thesis we extend these concepts by focusing on the estimation of higher order statistics of the intragranular strain distribution, going beyond the mean. In analogue with Egon Orowan's pocket watch illustration discussed in Chapter 1, the grain average strains can be put in relation to the intragranular strain response of the individual crystals in the same way as the macroscopic stress strain curve can be put in relation to grain average strains. Indeed, the intragranular strain distribution promises to reveal a whole new set of mechanical properties of the polycrystal. Motivated by this, we proceed in the following section to give a brief outline of the methods developed in Paper E, which give a mathematical framework for estimating the per-grain strain tensor probability distribution.

For the interested reader we find it worth mentioning that while we used directional strains of the form $s_{hkl} = \hat{\boldsymbol{\kappa}}^T \boldsymbol{\epsilon} \hat{\boldsymbol{\kappa}}$ in the above, one may also pursue equations that encode shear strains in the grain as $\gamma_{hkl,hkl'} = \hat{\boldsymbol{\kappa}}_{hkl}^T \boldsymbol{\epsilon} \hat{\boldsymbol{\kappa}}_{hkl'}$ where $\hat{\boldsymbol{\kappa}}_{hkl} \neq \hat{\boldsymbol{\kappa}}_{hkl'}$. The diffraction vectors involved in equation (3.21) would then originate from two distinct set of Miller planes. While this is beneficial to consider when estimating grain average strains it is less use-full when the pairs of diffraction vectors (hkl, hkl') are associated with non-overlapping sub-volumes of the grain, which is typically the case for the intragranular methods discussed in this thesis.

3.3 Statistical Strain Distributions

For a mosaic crystal, as shown by Barton and Bernier (2012) and Behnken (2000), it is possible to consider a strain orientation density function which describes the mean strain, not of the entire crystal grain, but of each individual orientation present within the crystal. In this model $\boldsymbol{U} = \boldsymbol{U}(\boldsymbol{x})$ varies on the crystal domain and $\boldsymbol{U}_0 \neq \boldsymbol{U}$. The reconstruction of the strain orientation density function has been shown to be feasible in 3DXRD/HEDM type experiments, c.f, Bernier and Miller (2006). In the work we present in Paper E, we expand upon this theory by considering a density distribution over strain tensors fully decoupled from orientations. In cases when the crystal mosaicity is moderate, but the strain considerable, the strain tensor distribution is distinct from the strain orientation density function in the sense that it still captures the variety of strain states present within the crystal while the strain orientation density function will, in this case, be limited to capturing the grain average strain.

Central to the methods developed in Paper E is the concept of histograms over directional strain. These are derivatives of intensity variations within the individual diffraction peaks collected in 3DXRD. The idea is that, while the centre of gravity of the diffraction peak provides information on the crystal average strain, the radial peak profile is encoding a distribution over strain states. The directional strain, s, is now considered to be a spatial function on the crystal domain, as

$$s(\boldsymbol{x}) = \hat{\boldsymbol{\kappa}}^T \boldsymbol{\epsilon}(\boldsymbol{x}) \hat{\boldsymbol{\kappa}}. \tag{3.36}$$

As a result, we find, using Bragg's law, that the scattering angle, $\theta = \theta(\boldsymbol{x})$, varies over the crystal domain as

$$\theta(\boldsymbol{x}) = \arcsin\left(\frac{\lambda}{2d(1 + s(\boldsymbol{x}))}\right). \tag{3.37}$$

By the same argument, placing the detector at distance D from the grain, we expect a radial spread of scattered rays at the detector surface, as

$$r(\boldsymbol{x}) = D\tan(2\theta(\boldsymbol{x})). \tag{3.38}$$

The intensity of a diffraction peak, I, at any one radial detector coordinate, $I = I(r)$, is therefore proportional to the scattering sub-volume of the grain, $I(r) \propto V_f(r)$. The functional form of $V_f(r)$ is, in general, non-linear, and owes its shape to the interplay between the crystal strain tensor field and the lattice plane normal direction associated to the diffraction peak. To exemplify how each set of Miller indices can generate drastically different volume fraction distributions, $V_f(r)$, we consider a spherical crystal grain of alpha-quartz subject to an elastic strain tensor field (similar to that presented in Paper E) and present, in Figure 3.3, the normalised radial peak profiles for some selected Miller indices.

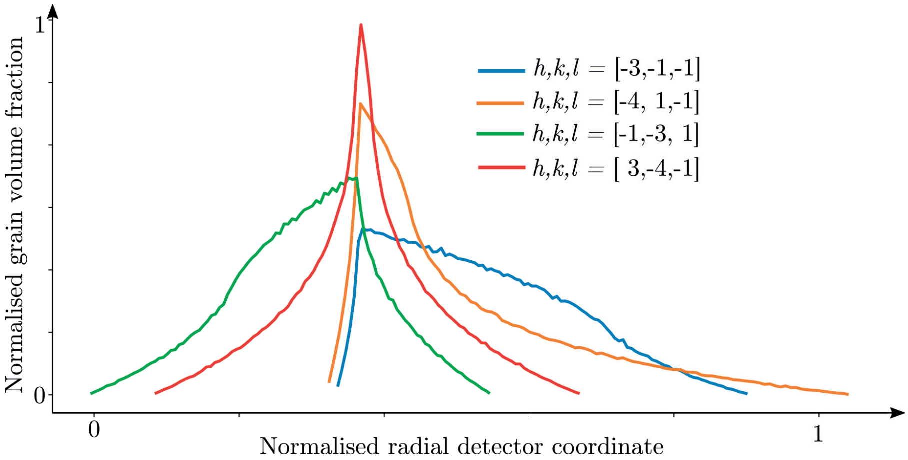

Figure 3.3: Simulated histograms over directional strain originating from a spherical silica grain subject to an elastic strain field.

As the detector in 3DXRD is discretised, $V_f(r)$ is, in practice, available in histogram form with a bin-width that is limited by the detector resolution. As the shift in radial coordinate, r, is directly linked to a directional strain in the grain, histograms over $V_f(r)$ encode an underlying distribution over strain tensors. In Paper E we derive an inversion scheme that yields an estimate of the strain tensor probability density function given a set of histograms over directional strains, i.e., we show how to compute the probability of encountering any one particular strain tensor as a result of randomly (uniformly) visiting a point in the grain. This type of statistical strain analysis generates aggregate measures of strain in the sense that the spatial distribution of the strain is unknown. To recover the spatial strain field, scanning-3DXRD type methods coupled with tomographic inversion techniques can be used. This is the topic of Paper A, Paper B and Chapter 6 in this thesis. A key element to recover the spatial distribution of strain is the concept of tomography. We, therefore, devote the following chapter to a brief introduction of this concept. With the addition of some fundamental concepts from Estimation Theory in Chapter 5 we shall be able to outline Paper A and B as we arrive at Chapter 6.

Chapter 4

Integral Measurements & Tomography

One of the fundamental advantages of utilising X-ray and Neutron techniques in materials research lies in their ability to penetrate dense objects, making them invaluable non-destructive bulk probes for scientists. However, due to this attribute, these microscopes can not offer direct, point-wise measurements of the spatial distribution within a sample. Instead, the collected signals are associated to sub-domains in the sample volume and the measurement model is an integral one.

In Chapter 3, we introduced a strain analysis where the diffracting sub-volume was considered to be a point-like crystal and effects due to the finite size of the grain were disregarded. While this approximation can be appropriate for many diffraction applications, the case of scanning-3DXRD will not admit such simplifications. The diffracting volume must now be modelled as an intersection between the narrow beam and the grain (recall Figure 2.4, Chapter 2). The situation is similar to one of the most canonical X-ray microscopy methods; absorption tomography. In X-ray absorption tomography a 2D array of detector pixels measures a transmitted X-ray intensity, I_t, which is regulated in magnitude by the optical path length of the X-rays traversed through the sample. The X-ray transmittance of the sample, T, is typically modelled using the Beer-Lambert law,

$$T = \frac{I_0}{I_t} = \exp\big(- \sum_i^n \sigma_i \int_{\mathcal{R}} n_i(\boldsymbol{x}) d\boldsymbol{x} \big), \tag{4.1}$$

where I_0 is the incident X-ray intensity, σ_i is the attenuation cross section of the i:th material species in the sample, n_i is the corresponding number density and the integral domain, $\mathcal{R}$, is defined by the X-ray sample intersection path. By log-transforming equation (4.1) and defining the attenuation coefficient field as $\mu(\boldsymbol{x}) = \sum_i^n \sigma_i n_i(\boldsymbol{x})$ we may write

$$y(\boldsymbol{s}) = -\log\left(\frac{I_0(\boldsymbol{s})}{I_t(\boldsymbol{s})}\right) = \int_{\mathcal{R}} \mu(\boldsymbol{x}) d\boldsymbol{x}, \tag{4.2}$$

where the detector surface is parameterised by $\boldsymbol{s}$. Making use of the Fourier Slice Theorem discovered by Bracewell (1956), it is possible to construct analytical solutions to (4.2). One of the most popular algorithms taking this analytical path is Filtered Back Projection (FBP) (Withers et al., 2021). In FBP the collected projection data, $y(\boldsymbol{s})$, are Fourier transformed, filtered and then back-projected (Kak and Slaney, 2001; Natterer, 2001). The result is a spatial field, $\mu(\boldsymbol{x})$, computed as a sequence of independent 2D slices, $\mu(x, y, z = z_{fixed})$. Owing to the use of fast Fourier transforms, FBP enjoys benefits in terms of low RAM usage and low computational complexity. In the early history of tomography, the Fourier Slice Theorem was put into great practical use as Godfrey Hounsfield developed the first medical CT-scanners, an achievement that earned him the Nobel prize in 1979 (Bhattacharyya, 2016).

Instead of resorting to analytical solutions it is possible to recover μ by solving a large sparse systems of linear equations, an approach sometimes referred to as algebraic reconstruction. Over the last decade, the trend in computing has steered away from CPU usage towards GPU usage (Willemink and Noël, 2019). As a result of this performance boost, the more computationally involved algebraic methods have become popular. These methods consider each ray integral in equation (4.2) as a linear equation,

$$\begin{aligned} y_1 &= \int_{\mathcal{R}_1} \mu(\boldsymbol{x}) d\boldsymbol{x}, \\ &\vdots \\ y_i &= \int_{\mathcal{R}_i} \mu(\boldsymbol{x}) d\boldsymbol{x}, \\ &\vdots \\ y_m &= \int_{\mathcal{R}_m} \mu(\boldsymbol{x}) d\boldsymbol{x}. \end{aligned} \tag{4.3}$$

Alternatively, in matrix format, we find

$$\boldsymbol{y} = \boldsymbol{P}\boldsymbol{\mu}, \tag{4.4}$$

where $\boldsymbol{P}$ is the projection matrix that approximates the line integral over $\mathcal{R}$ for a given discretisation of μ (typically representing μ as a piece-wise constant pixel image). When a single Cartesian slice of the sample is considered, $\mu(x, y, z = z_{fixed})$, the corresponding projection operator, $\boldsymbol{P}$, is often said to produce the sinogram of μ, as named by Johan Radon (Radon, 1986) who famously gave the first description of the transform. In Figure 4.1 the situation is illustrated for a single slice, $z = z_{fixed}$, of an object. Each projection of the object forms a 1D scalar function that is a column in the sinogram image. The task discussed above can then be thought of as that of inverting the sinogram into a real space image of $\mu(x, y, z = z_{fixed})$.

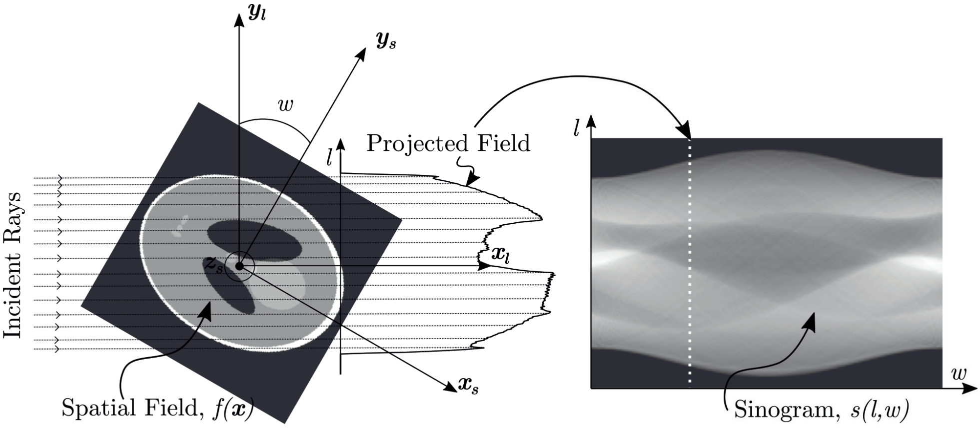

Figure 4.1: A scalar spatial field, $f(\boldsymbol{x})$, is projected along linear paths collapsing the image into a 1D scalar function (left). By stacking all projections, from $\omega = 0^o$ to $\omega = 180^o$, we find the sinogram of $f(\boldsymbol{x})$ (right).

The measurements produced in scanning-3DXRD can be put in analogy with the absorption tomography setting. Each measured diffraction peak is the result of the scattering taking place on a single ray path, $\mathcal{R}$. Converting the peak centre of gravity (with respect to intensity) into directional strains, we arrive at a ray transform of the form

$$y_i = \frac{1}{L_i}\int_{\mathcal{R}_i} \hat{\boldsymbol{\kappa}}_i^T \boldsymbol{\epsilon}(\boldsymbol{x})\hat{\boldsymbol{\kappa}}_i \boldsymbol{dx}, \quad L_i = \int_{\mathcal{R}_i} \boldsymbol{dx}, \tag{4.5}$$

where the path lengths of the rays through the grain volume, L_i, can be computed once the grain boundary is known. The recovery of a grain shape is a necessary prerequisite for strain regression by equation (4.5) to be possible. To achieve a grain shape reconstruction in scanning-3DXRD the individual line-scans can be assembled into a sinogram of accumulated diffracted intensities. Every h, k, l reflection then constitutes a single projection that is proportional to the scattering volume. The situation is illustrated in Figure 4.2 where the formed sinogram is converted into a grain density field using FBP. It is worth noting that in the work presented in this thesis we have used the segmented grain density field in conjunction with equation (4.5).

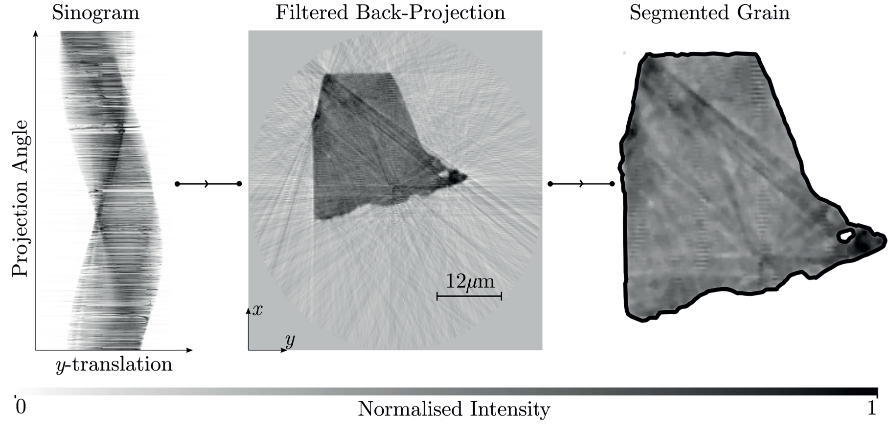

Figure 4.2: Illustration of grain shape reconstruction by applying Filtered Back Projection to the diffracted intensities of a single grain of zirconium (Zr). The raw diffraction data were collected at the ESRF ID11 beamline and made available by courtesy of Hamidreza Abdolvand and Alireza Tondro, The University of Western Ontario, Canada.

While the grain shape can be reconstructed using established tomographic methods (Poulsen and Schmidt, 2003; Poulsen and Fu, 2003; Markussen et al., 2004; Fu et al., 2006; Batenburg et al., 2010), equation (4.5) does not admit standard tomographic analysis for recovery of the strain tensor field, $\boldsymbol{\epsilon}(\boldsymbol{x})$. This is due to the fact that the strain sampling direction, $\hat{\boldsymbol{\kappa}}_i$, is variable between measurements and, thus, the individual equations do not refer to the same scalar field. In Paper A, these difficulties are overcome by modifying the projection matrix, $\boldsymbol{P}$, to include the strain sampling direction information. Moreover, in Paper D, we discuss how to best factorise the modified projection matrix to leverage state-of-the-art ray-tracing libraries used in absorption tomography. We shall return to these topics in more detail in Chapter 6. Before discussing the spatial reconstruction of $\boldsymbol{\epsilon}(\boldsymbol{x})$ it shall be useful to briefly introduce the reader to the two main estimation techniques used in this thesis; Constrained Weighted Least Squares regression and Gaussian Process regression. These are classical mathematical methods for regularised inversion, handling the case of too few data and the presence of noise in the data.

For the dedicated reader we would like to close this chapter with a remark on the relation between the tomography equations and the reconstruction method derived in Paper E. Just as the Radon transform treats the formation of a sinogram as integrals across hyper planes of dimension one less than the image space (i.e line integrals for 2D images) the transform described in Paper E brings the 6D image space into a sinogram like object by integrating across hyper-planes of dimension 5D. In the approach taken in Paper E the reconstructed field is the scalar strain tensor probability distribution and, as a consequence, each integral measurement actually refers to the same quantity (in contrast to equation (4.5)). While these two facts suggest that analytical reconstruction approaches may be feasible, the available projection data come in a non-standard angular distribution.

Nevertheless, by producing a modified projection matrix, $\boldsymbol{P}$, suitable for the task and applying standard regression techniques, reconstruction can be achieved. This illustrates the utility of adopting an algebraic reconstruction technique over a Fourier based one. At the expense of more computations, algebraic techniques can be modified to suit a wide range of applications.

Chapter 5

Estimation Techniques

Regression analysis comprises a set of statistical techniques commonly used for modelling the relationship between a set of dependent variables and a set of independent variables. Regression tools are statistical frameworks that form one of the most fundamental building blocks for the scientist, enabling them to make informed predictions, uncover patterns in data and to estimate unknown parameters from noisy observations. As a result, regression analysis is finds application across virtually all scientific fields. The conjecture is that the dependent variables, y_i, can be expressed in terms of the independent variables, x_i, by a model function, f,

$$y_i = f(x_1, x_2, \ldots, x_{m-1}, x_m). \tag{5.1}$$

Faced with a set of observed data, y_i, regression analysis then provides a framework for making predictions about the independent variables, x_i, by uncovering the patterns in the data. The relationship between the dependent and independent variables is typically referred to as a regression or measurement model. The task in regression analysis is to estimate the unknown parameters, or coefficients, x_i, in the regression model given a set of observed data, y_i. The, perhaps, most extensively used class of regression analysis is linear regression, where the relationship between the dependent and independent variables is assumed to be linear,

$$y_i = \boldsymbol{a}_i^T \boldsymbol{x} + \boldsymbol{b}_i, \quad \boldsymbol{x}, \boldsymbol{a}_i, \boldsymbol{b}_i \in \mathbb{R}^n. \tag{5.2}$$

This assumption often leads to great simplifications and can in many cases facilitate a unique recovery of the dependent variables, depending on the available data. On the other hand, the restriction to linear models is not always sufficient to capture the underlying patterns in the data, in which case the wider class of non-linear models can be resorted to. When the measured data are sparse, compared to the number of dependent variables, or corrupted with high levels of noise, the regression model is often adapted to gain a well posed inversion problem, a procedure known as regularisation.

In this chapter, we shall discuss the regression tools that have been used in the papers connected to this thesis. As regression analysis is deployed across many scientific fields, with varying degree of model and inference complexity, some of the concepts presented in this chapter may seem trivial to the reader, while others may pose a more serious challenge, depending on background. We have therefore deliberately extended the current chapter to ensure that fundamental concepts are covered. To make the exposition as clear as possible, and to not simply repeat the content already presented within Papers A-E, it will be useful to explain different types of regression through a single recurring example throughout the chapter. To put focus on the regression analysis, we select an example featuring scalar 1D ($x_i, y_i = f(x_i)$) data pairs. The example considered is a data series published in Rubino et al. (2019) containing historical measurements of carbon dioxide (CO_2) levels in the earths atmosphere collected through ice core analysis. To make our example more illustrative, we have removed every 20th data point from the original data series and corrupted the remaining data with zero mean Gaussian noise. The standard deviation of the noise was taken as a linear function in the year AD making the oldest observations the most uncertain, with a standard deviation of 10ppm, and the most recent observation the least uncertain, with a standard deviation of 1ppm. The original data, as well as the example data used throughout this chapter, can be viewed in Figure 5.1.

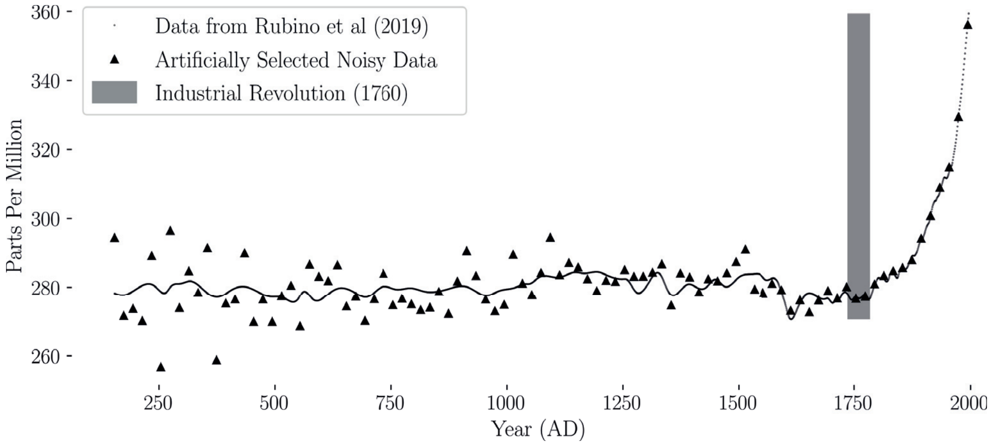

Figure 5.1: Earth atmosphere carbon dioxide (CO_2) concentration (parts per million) as a function of year AD, as published by Rubino et al. (2019).

In our example the independent variable, x, is the year AD and the dependent variable is the corresponding ppm of CO_2 in the earths atmosphere, $y_i = f(x_i)$. From now on we shall consider the original data series of Rubino et al. (2019) as our ground truth function that we are aiming to reconstruct. At our disposal we have our sparser, artificially created, noisy data series that we consider to be our measurements, y_i. In our example, which features point-wise measurements, the general format of the regression model is deliberately simple,

$$y_i = f(x_i) + e_i, \quad e_i \sim \mathcal{N}(0, \sigma_i^2), \tag{5.3}$$

where the additive independent Gaussian noise, e_i, features a standard deviation of $\sigma(x) = 10 - 9x/1994$. It is now the task to find a functional format of f such that the observations, y_i, become probable given the noise model, $e_i \sim \mathcal{N}(0, \sigma_i^2)$.

5.1 Weighted Least Squares Regression

The essential idea in Weighted Least Squares regression (WLSQ) (a.k.a weighted linear regression) is to find a predictor function, $f^*(x_i) \approx f(x_i)$, such that the observations, y_i, are probably explained given a noise model. This means that measurements with higher variance should be less adhered to compared to low variance measurements. In WLSQ the functional form of the predictor is freely chosen within the class of functions that are linear in the set of free parameters, $\hat{\boldsymbol{\beta}}$,

$$f^*(x_i, \hat{\boldsymbol{\beta}}) = \boldsymbol{a}_i^T \hat{\boldsymbol{\beta}}, \tag{5.4}$$

where the vector $\boldsymbol{a}_i^T = \boldsymbol{a}^T(x_i)$ can be (and often is) a non-linear function in x_i. When there exist no covariances between measurements, $\mathbb{V}[y_i, y_j] = 0$, the following cost function is to be minimised with respect to $\hat{\boldsymbol{\beta}}$,

$$C(\hat{\boldsymbol{\beta}}) = \sum_i \frac{1}{\sigma_i^2}(y_i - f^*(x_i, \hat{\boldsymbol{\beta}}))^2, \quad \forall i. \tag{5.5}$$

When the data noise is Gaussian, WLSQ regression provides the maximum likelihood estimator. That is to say; the joint probability, $p(y_i|x_i, \boldsymbol{a}, \sigma_i)$, of observing the measurements given the model parameters is maximised. The computed predictor function, f^*, then represents the most likely function (within the allowed function class, $f^* = \boldsymbol{a}_i^T \hat{\boldsymbol{\beta}}$) for explaining the data. To see this we adapt a more general matrix notation as

$$C(\hat{\boldsymbol{\beta}}) = (\boldsymbol{y} - \boldsymbol{A}\hat{\boldsymbol{\beta}})^T \boldsymbol{C}_{noise}^{-1} (\boldsymbol{y} - \boldsymbol{A}\hat{\boldsymbol{\beta}}), \tag{5.6}$$

where the rows of the matrix $\boldsymbol{A}$ are $\boldsymbol{a}_i^T$ and $\boldsymbol{C}_{noise}$ is the covariance matrix of the noise (which is diagonal in our example). Using our matrix notation, the measurement model in equation (5.3) reads as

$$\boldsymbol{y} = \boldsymbol{A}\hat{\boldsymbol{\beta}} + \boldsymbol{e}, \quad \boldsymbol{e} \sim \mathcal{N}(\boldsymbol{0}, \boldsymbol{C}_{noise}), \tag{5.7}$$

and we find that the measurements, $\boldsymbol{y}$, are jointly Gaussian. The probability of observing a particular $\boldsymbol{y}$ is, therefore, proportional to

$$\exp(-(\boldsymbol{y} - \boldsymbol{A}\hat{\boldsymbol{\beta}})^T \boldsymbol{C}_{noise}^{-1} (\boldsymbol{y} - \boldsymbol{A}\hat{\boldsymbol{\beta}})) \propto p(\boldsymbol{y}|\boldsymbol{C}_{noise}). \tag{5.8}$$

By log-transforming equation (5.8), we conclude that the task is to maximise the expression for $C(\hat{\boldsymbol{\beta}})$ in equation (5.6), and it follows that WLSQ is the maximum likelihood estimator of $\hat{\boldsymbol{\beta}}$ (as long as the additive noise is Gaussian). The closed form solution to this maximisation problem is found from the gradient equation as

$$\hat{\boldsymbol{\beta}} = (\boldsymbol{A}^T \boldsymbol{C}_{noise}^{-1} \boldsymbol{A})^{-1} (\boldsymbol{A}^T \boldsymbol{C}_{noise}^{-1}) \boldsymbol{y}. \tag{5.9}$$

To illustrate the above discussed equations we now return to our example CO_2 data (from Figure 5.1) and show in Example 5.1.1 how the ppm level in the earths atmosphere can be estimated by a smooth function using WLSQ.

Example 5.1.1

Let us return to the CO_2 data we selected in Figure 5.1 and make use of the WLSQ estimator. Here, we choose to model the predictor, f^*, with a set of 46 equally spaced radial basis functions, positioned at $x_k = 0, 44.44, .., 2000$, as

$$\boldsymbol{a}^T(x) = \left[\exp\left(-\frac{1}{2}\frac{(x-x_1)^2}{90^2}\right) \quad \dots \quad \exp\left(-\frac{1}{2}\frac{(x-x_m)^2}{90^2}\right)\right]. \tag{5.10}$$

The result of constructing the matrix $\boldsymbol{A}$ and applying the estimator in equation (5.9) can be viewed in Figure 5.2.

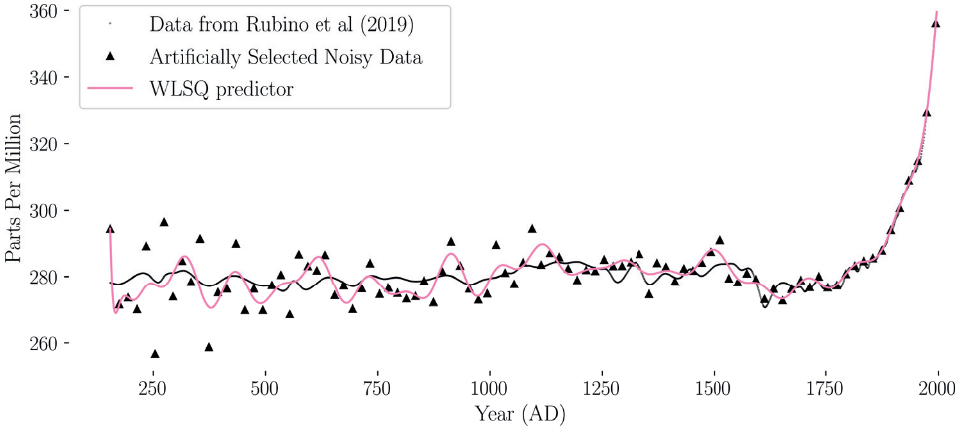

Figure 5.2: WLSQ fit of Earth atmosphere carbon dioxide (CO_2) concentration (parts per million) as a function of year AD.

The selection of the columns of $\boldsymbol{A}$ (i.e the functions $\boldsymbol{a}^T(x_i)$) are often referred to as basis functions. These play a crucial role in the WLSQ regression and must be carefully selected depending on the application. The fact that WLSQ regression is the maximum likelihood estimator of $\hat{\boldsymbol{\beta}}$ does not mean that the resulting estimation itself is reliable. We must also require that the basis selection is a good approximation to the underlying laws that govern the structure of the data. For instance, it is easy to see that fitting a line, $\boldsymbol{a}^T(x_i) = \begin{bmatrix} x_i & 1 \end{bmatrix}$, to the data in our Example 5.1.1 would not perform well by any reasonable metric of fit. Such a model would fail completely to capture the post industrial acceleration of CO_2 levels in the atmosphere observed from the late modern period.

5.2 Gaussian Process Regression

Gaussian Process Regression, or Kriging as it is often called, was originally developed to estimate the spatial distribution of gold ore at the Witwatersrand reef complex in South

Africa given samples from a small number of boreholes (Krige, 1951). In contrast to WLSQ, the goal of Gaussian Process regression is no longer to compute a single maximum likelihood predictor function, f^*, but rather to arrive at a distribution over possible function predictors, $f(x_i) \sim \mathcal{N}(\mu(x_i), \mathbb{V}[f(x_i), f(x_j)])$, such that every possible predictor function is associated to a likelihood, $p(f|\boldsymbol{y})$. In a Gaussian Process the vector,

$$\boldsymbol{y} = \begin{bmatrix} f(x_1) + e_1 & f(x_2) + e_2 & ... & f(x_m) + e_m \end{bmatrix}^T, \tag{5.11}$$

that is formed from the input sequence of m inquiry points, $x_1, x_2, ..., x_m$, is assumed to follow a multivariate Gaussian distribution. The idea is that the formation of the measurements, $\boldsymbol{y}$, originates from a series of transformations of the underlying independent variables, $\boldsymbol{x}$, that all preserve Gaussian properties, hence the name; Gaussian Process. Whenever this approximation can be tolerated, the Gaussian Process regression framework can be exploited to recover $p(f|\boldsymbol{y})$.

Gaussian Process regression belongs to a class of Bayesian estimation techniques in which the concept of a probability distribution over predictors is central. Although the true function, f, may be completely deterministic, as it represents, perhaps, some laws of nature, from the scientist perspective, working with limited information, many different (not equally probable) explanations to the observed data may exist. To express this, Bayesian estimation starts by explicitly stating what prior beliefs on the form of function, f, exist. When there is no prior information about f, prior to the observations $\boldsymbol{y}$, it is common to let the prior distribution be uniform. Only after the prior beliefs have been expressed mathematically can the data, $\boldsymbol{y}$, be considered. Bayesian estimation is then concerned with computing an updated, posterior distribution, $p(f|\boldsymbol{y})$, that is conditioned on the measurements, $\boldsymbol{y}$, in accordance with Baye's rule,

$$p(f|\boldsymbol{y}) = \frac{p(\boldsymbol{y}|f)p(f)}{p(\boldsymbol{y})}, \tag{5.12}$$

where $p(f)$ is the prior distribution. In this context, the Gaussian Process becomes a special case of Bayesian estimation in which the prior distribution, $p(f)$, is believed to be Gaussian. Consider for instance the prediction vector formed over a finite number of inquiry locations as

$$\boldsymbol{f} = \begin{bmatrix} f(x_1) & f(x_2) & ... & f(x_m) \end{bmatrix}^T, \tag{5.13}$$

with the noisy observations, $\boldsymbol{y}$, modelled as

$$\boldsymbol{y} = \boldsymbol{L}\boldsymbol{f}(\boldsymbol{x}) + \boldsymbol{e}, \quad \boldsymbol{e} \sim \mathcal{N}(\boldsymbol{0}, \boldsymbol{I}\sigma_e^2), \quad \boldsymbol{f} \sim \mathcal{N}(\boldsymbol{\mu}, \boldsymbol{C}), \tag{5.14}$$

where the matrix $\boldsymbol{L}$ represent a linear transform. In this situation the variable, $\boldsymbol{y}$, follows a normal distribution as it represents a linear combination of normally distributed stochastic variables. The joint distribution of $\boldsymbol{f}$ and $\boldsymbol{y}$ become

$$\begin{bmatrix} \boldsymbol{f} \\ \boldsymbol{y} \end{bmatrix} \sim \mathcal{N}\left(\begin{bmatrix} \mathbb{E}[\boldsymbol{f}] \\ \boldsymbol{L}\mathbb{E}[\boldsymbol{f}] \end{bmatrix}, \begin{bmatrix} \boldsymbol{C} & \boldsymbol{C}\boldsymbol{L}^T \\ \boldsymbol{L}\boldsymbol{C} & \boldsymbol{L}\boldsymbol{C}\boldsymbol{L}^T + \boldsymbol{I}\sigma_e^{-2} \end{bmatrix} \right). \tag{5.15}$$

From equation (5.15) we see that the sought, conditional, distribution $p(\boldsymbol{f}|\boldsymbol{y})$ must also follow a Gaussian distribution. The mean and covariance can be found by explicitly writing out the exponent of the joint Gaussian distribution in equation (5.15), complete the square and collect the terms. The result is that

$$\begin{aligned} \mathbb{E}[\boldsymbol{f}|\boldsymbol{y}] &= \mathbb{E}[\boldsymbol{f}] + \boldsymbol{C}\boldsymbol{L}^T(\boldsymbol{L}\boldsymbol{C}\boldsymbol{L}^T + \boldsymbol{I}\sigma_e^2)^{-1}(\boldsymbol{y} - \mathbb{E}[\boldsymbol{y}]), \\ \mathbb{V}[\boldsymbol{f},\boldsymbol{f}|\boldsymbol{y}] &= \boldsymbol{C} - \boldsymbol{C}\boldsymbol{L}^T(\boldsymbol{L}\boldsymbol{C}\boldsymbol{L}^T + \boldsymbol{I}\sigma_e^2)^{-1}\boldsymbol{L}\boldsymbol{C}, \end{aligned} \tag{5.16}$$

where $\mathbb{E}$ and $\mathbb{V}$ are the expectation and variance operators respectively. The result presented in equation (5.16) is known as the *posterior distribution* of $\boldsymbol{f}$ while the initially postulated distribution of $\boldsymbol{f} \sim \mathcal{N}(\boldsymbol{\mu}, \boldsymbol{C})$, before conditioning on the measurements, $\boldsymbol{y}$, is known as the *prior distribution.* For the physicist the introduction of a prior distribution over functions may (or may not) seem unmotivated. However, the reader should bare in mind that it is not the physical process itself that we are describing with the prior distribution. Rather it is our *beliefs* or *restrictions* on the function, $f(x)$, that we are describing via the postulated prior distribution. For instance, in our CO_2 example, negative values of $f(x)$ are very unlikely (probability zero) and likewise $f > 10^6$ is nonsensical. The weakest possible prior distribution we can select would, thus, be the uniform distribution on this feasible CO_2 ppm interval. Such a distribution can be approximated by a Gaussian with large variance. Illustrating, instead, a somewhat stronger prior, we may incorporate knowledge about the human anatomy and survival conditions from which it can be concluded that CO_2 levels above 40000 ppm are improbable. Strong priors exist in many situations. This is the case for elastic strain estimation, in which we know that the laws of Newton must not be violated by the estimated strain field. In Paper B we show how the Gaussian Process regression framework can be exploited to reconstruct strain fields adhering to the equilibrium equations, as long as the crystal orientation and stiffness are approximately known. As expected, it was shown in Paper B that once the strong prior of equilibrium was adopted the number of data needed to infer the strain field was drastically reduced.

In general, the selection of the prior covariance, $\boldsymbol{C}$, need not be diagonal. In fact in many regression problems the target function, $f(x)$, is spatially correlated, and this is one of the reason why a Gaussian Proccess approach is often adopted. The presence of spatial correlation,

$$\mathbb{V}[f(x), f(x')] \neq 0, \tag{5.17}$$

is clearly the case for our CO_2 data in Figure 5.1, where the ppm levels of one year is strongly correlated to the ppm levels of the following (and previous) year(s). Typically, the covariance of the prior distribution is described by a continuous function, $k(x, x')$, called a *kernel.* The kernel can be evaluated at probe locations to construct the instances of a covariance matrix, i.e.,

$$\mathbb{V}[f(x), f(x')] = k(x, x'). \tag{5.18}$$

By tuning a set of free parameters, included in the kernel functional form, different correlation length-scales and and variance magnitudes can be encoded in the prior distribution. For instance, the kernel functional format may be selected manually from a wide class of functions after which the numerical values of the parameters of the kernel can be optimised by maximising the out-of-sample likelihood, a procedure known as *hyper-parameter optimisation*.

There exists much more to be said about Gaussian Process regression, not least with respect to the many methods developed to ease the computational burden of the method, which is $\mathcal{O}(m^3)$ due to the formation and inversion of the $m \times m$ matrix, $(\boldsymbol{LCL}^T + \boldsymbol{I}\sigma_e^2)^{-1}$, found in equations (5.16). The interested reader may resort to Rasmussen (2003) for a deeper walk-trough of the Gaussian Process. Here we shall now instead turn to our example CO_2 data and put the GP-regression framework to use in Example 5.2.1.

Example 5.2.1

Let us now again return to the CO_2 data we selected in Figure 5.1 and make use of the GP-regression framework. For simplicity we shall set the prior distribution mean to zero (Note that this does not mean that the posterior distribution will have zero mean). To encode the prior belief that the data are temporally correlated, we shall use a so called squared exponential kernel to describe the prior covariance matrix,

$$\mathbb{V}[f(x), f(x')] = k(x, x') = \sigma_{prior}^2 \exp\left(-\frac{(x - x')^2}{2\ell^2}\right). \tag{5.19}$$

The squared exponential kernel suggest that correlation is increasing with decreasing distance between x and x' reflecting our prior beliefs. Without any further information we shall set the covariance magnitude large, $\sigma_{prior} = 1000$ ppm, to make sure that we cover a wide range of possible outcomes. The correlation length-scale was selected to be in the range of a human generation, $\ell = 90$ years. This means that we enter the regression with the prior belief that the ppm level at the year of birth of a human is correlated to the ppm level at the year of passing of that same human being. Using equation (5.16), forming the involved matrices and solving the equation systems yields the results illustrated in Figure 5.3.

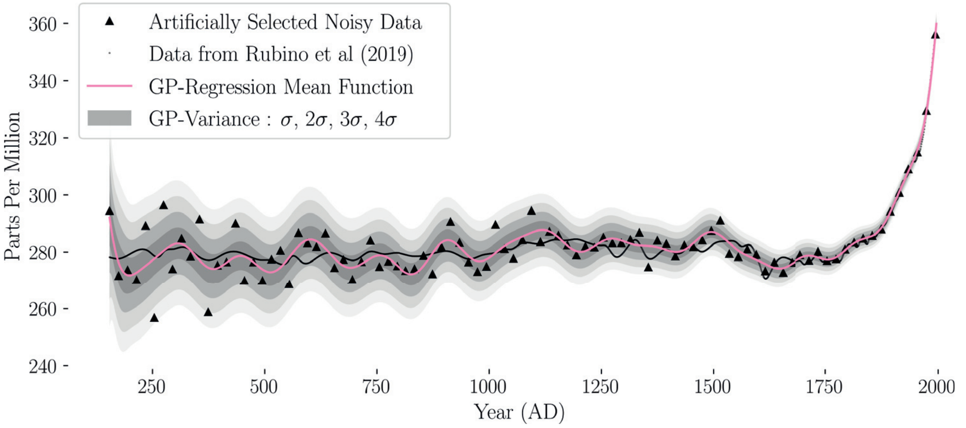

Figure 5.3: Gaussian Process Regression used to estimate the Earth's atmosphere carbon dioxide (CO_2) concentration as a function of year AD. The result of the GP-regression is a distribution over functions. The mean of this distribution as well as its variance are illustrated as a solid line and shaded percentiles respectively.

From Example 5.2.1, it is clear from the shaded regions of Figure 5.3 that the estimation of the ppm levels is more uncertain in the distant past compared to the modern age. This is a result of the artificial Gaussian noise model used to create our virtual sparse data series (of course we are not claiming that this is the actual case for the data published in

Rubino et al. (2019)). Similar variation in uncertainty can be seen for data sequences that are non-uniformly distributed as illustrated in Example 5.2.2.

Example 5.2.2

Let us imagine that all the CO_2 data between the years 1450-1550 AD has been lost and that we desire to perform our regression on the remaining, non-uniformly distributed, data. With exactly the same model parameters as those used in Example 5.2.1 we find the result of GP regression illustrated in Figure 5.4. It is clear to see that the uncertainty in the fit (gray regions) is now much elevated around the period 1450-1550 AD, which contains no data points. As the squared exponential kernel included in the prior is correlating neighbouring points, the uncertainty just after 1450 AD and just before 1550 AD is seen to be smaller than at 1500 AD.

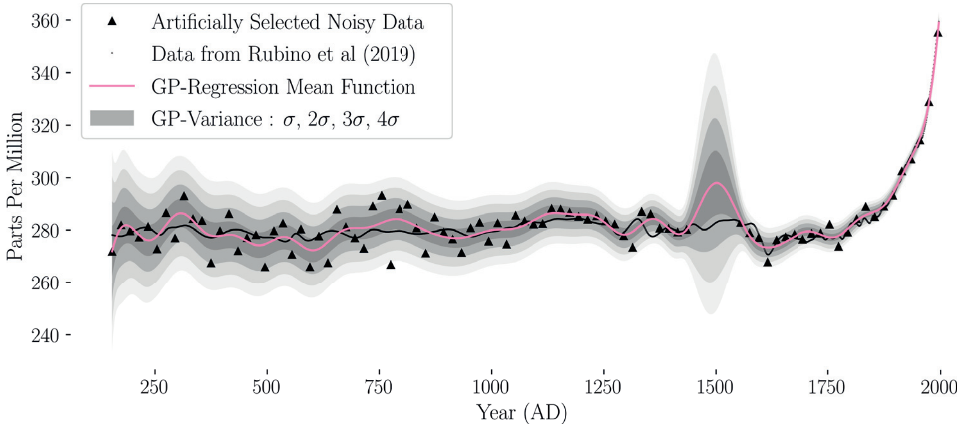

Figure 5.4: Gaussian Process Regression used to estimate the Earth atmosphere carbon dioxide (CO_2) concentration as a function of year AD. The uncertainty of the GP is regulated by the prior variance, the noise variance and the local data density, as can be seen from the 1450-1550 AD interval.

5.3 Constraints & Regularisation

The prior distribution selected for $f(x)$ in the GP-framework serves as a regularisation of the inversion problem. In the presence of very noisy data, or even missing data, the prior will dominate the reconstructed posterior distribution. We mentioned previously that we used an equilibrium prior in Paper B when reconstructing the elastic strain tensor field spatially in single crystals. Considering the CO_2 data in Example 5.2.1 we saw that the reconstructed mean function was smooth even in regions with high noise. This is a result of our prior selection with a kernel that was a squared exponential. Since the kernel is correlating data over a fixed length scale, ℓ, the reconstruction will be smooth with respect to this length scale.

In the WLSQ approach it is possible to likewise enforce smoothness, or some other constraint, by adding a penalty term, P, to the cost function as

$$C(\hat{\boldsymbol{\beta}}) = (\boldsymbol{y} - \boldsymbol{A}\hat{\boldsymbol{\beta}})^T \boldsymbol{C}^{-1} (\boldsymbol{y} - \boldsymbol{A}\hat{\boldsymbol{\beta}}) + P(\hat{\boldsymbol{\beta}}), \tag{5.20}$$

where P is large when the desired constraint is violated. This approach is similar to that we have adopted in Paper A, where the local strain gradients were constrained to be bounded in magnitude. Considering the CO_2 data in Example 5.1.1, we saw that the WLSQ reconstruction was smooth even without the addition of any such penalty term. This is a result of our basis function selection in which we implicitly constrained $f(x)$ by describing it as a sum of smooth Gaussian functions. The fact that WLSQ regression is implicitly constrained by the basis function selection, described by the columns of $\boldsymbol{A}$, emphasises the fact that regression from a finite set of measurements with the aim of retrieving a continuous spatial or temporal distribution always requires prior information to make sense. Should the prior in the GP regression be selected with diagonal covariance, then we would find a reconstructed mean function featuring a series of delta spikes reaching out to each measured data point. Likewise the WLSQ regression would do no better should the basis set be selected as a set of Dirac delta functions centred at the measurement locations. In this sense, it is fair to say that all regression methods must impose constraints on the reconstructed field and the question is never *if* constraints are needed, but rather *how many*, or *how strong*, constraints are needed. In the WLSQ regression, the prior assumptions are encoded through the the basis selection while in the Gaussian Process regression framework constraints are explicitly stated in the language of probabilities by providing a prior distribution, $p(f)$. Luckily, many real-world estimation problems are bestowed with rich spatial and temporal correlation patterns, which is why, in general, it is possible to give useful estimates of an underlying continuous function, f, from a finite data series, $\boldsymbol{y}$. This is a manifestation of the more fundamental principles of causality that govern our world and allow us to make predictions about unknown events through the use of mathematical models.

Chapter 6

Spatially Resolved Strain Tensor Tomography

In Chapters 2 and 3 we described the scanning-3DXRD experimental setup, discussed the concept of diffraction and how a diffraction signal can be processed into a measure of strain. Then, in Chapters 4 and 5 we introduced the concepts of tomography and estimation. In this chapter we shall bring together all of these topics and introduce the reader to spatial strain tensor estimation in single crystals, going beyond the aggregated strain measures, such as grain mean strains and grain strain tensor probability distributions, discussed in Chapter 3.2 and 3.3. Here we focus on the spatial variation of strain with the goal of arriving at a strain tensor function, $\boldsymbol{\epsilon}(\boldsymbol{x})$, dependent of spatial coordinate in the grain, $\boldsymbol{x}$. In Paper A, we derive a method to recover $\boldsymbol{\epsilon}(\boldsymbol{x})$, one z-slice at the time, much like what is done in the majority of absorption tomography algorithms. In paper B we derive a method to recover $\boldsymbol{\epsilon}(\boldsymbol{x})$ as a 3D field. In this Chapter, we provide an introductory exploration of both of these concepts in a 2D setting. The Chapter is divided into two parts; first we give a theoretical outline of how $\boldsymbol{\epsilon}(\boldsymbol{x})$ can be recovered in scanning-3DXRD. After this introduction we provide examples of the utility of these methods by highlighting some recent results from synchrotron experiments.

6.1 The Regression Model

As previously mentioned in Chapter 4, and stated in equation (4.5), our (noise free) measurement model is

$$y_i = \frac{1}{L_i}\int_{\mathcal{R}_i} \hat{\boldsymbol{\kappa}}_i^T \boldsymbol{\epsilon}(\boldsymbol{x}) \hat{\boldsymbol{\kappa}}_i \boldsymbol{dx}, \quad L_i = \int_{\mathcal{R}_i} \boldsymbol{dx}. \tag{6.1}$$

This model offers a streamlined perspective on diffraction, embracing the implicit assumptions that:

(I) the entire grain-beam intersection region, $\mathcal{R}_i$, scatters simultaneously at a fixed turn-table rotation angle, w;

(II) that $\hat{\boldsymbol{\kappa}}_i = \hat{\boldsymbol{\kappa}}_i(\boldsymbol{x})$ is a known function on the domain of $\mathcal{R}_i$;

(III) that the integral strain measures, y_i, can be extracted from the diffraction data.

When the first of these approximations is violated the strain signal, y_i, will be associated to an erroneous region of the grain. For moderate intragranular misorientations on $\mathcal{R}_i$ ($< 1^o$) the induced error is limited. Likewise, the error associated to wrongly setting $\hat{\boldsymbol{\kappa}}_i$ as a constant on $\mathcal{R}_i$ is negligible for small deformations. With regards to the third assumption we stress that it is the the mean diffraction vector on $\mathcal{R}_i$,

$$\langle \boldsymbol{G}_i \rangle = \frac{1}{L_i} \int_{\mathcal{R}_i} \boldsymbol{G}_i(\boldsymbol{x}) d\boldsymbol{x}, \tag{6.2}$$

that is that is available from the measured diffraction data (the spatially varying function, $\boldsymbol{G}_i = \boldsymbol{G}_i(\boldsymbol{x})$, is unknown). The strain measure derived in Chapter 3, equation 3.22, can, therefore, not be directly utilised, as

$$y_i = \frac{1}{L_i} \int_{\mathcal{R}_i} s_{hkl} \boldsymbol{dx} = \frac{1}{L_i} \int_{\mathcal{R}_i} \frac{\boldsymbol{G}_i^T \boldsymbol{G}_0}{\boldsymbol{G}_i^T \boldsymbol{G}_i} \boldsymbol{dx} - 1. \tag{6.3}$$

To resolve this, we introduce a Taylor expansion of equation (6.3) around the reference state, $\boldsymbol{G}_0$, and find that

$$y_i \approx 1 - \frac{1}{L_i} \int_{\mathcal{R}_i} \frac{\boldsymbol{G}_i^T \boldsymbol{G}_0}{\boldsymbol{G}_0^T \boldsymbol{G}_0} \boldsymbol{dx} = 1 - \frac{\boldsymbol{G}_0^T \langle \boldsymbol{G} \rangle_i}{\boldsymbol{G}_0^T \boldsymbol{G}_0}, \tag{6.4}$$

such that $y_i = y_i(\langle \boldsymbol{G} \rangle_i)$ becomes a function of the known quantity $\langle \boldsymbol{G} \rangle_i$. This approach makes it possible to approximately fulfil assumption (III). As a side note, we refer back to the discussion on large strains in Chapter 3, section 3.1.2, where we mentioned that in scanning-3DXRD it does not matter if the directional strain measure, s_{hkl}, is derived from a large or a small strain tensor. Indeed, Taylor expanding equation (3.29) around $\boldsymbol{G}_0$ and integrating we find that

$$y_i = \frac{1}{L_i} \int_{\mathcal{R}_i} \frac{\boldsymbol{G}_0^T \boldsymbol{G}_0 - \boldsymbol{G}_i^T \boldsymbol{G}_i}{2 \boldsymbol{G}_i^T \boldsymbol{G}_i} \boldsymbol{dx} \approx 1 - \frac{1}{L_i} \int_{\mathcal{R}_i} \frac{\boldsymbol{G}_i^T \boldsymbol{G}_0}{\boldsymbol{G}_0^T \boldsymbol{G}_0} \boldsymbol{dx} = 1 - \frac{\boldsymbol{G}_0^T \langle \boldsymbol{G} \rangle_i}{\boldsymbol{G}_0^T \boldsymbol{G}_0}, \tag{6.5}$$

which is equivalent to (6.4).

The errors associated to all of the above assumptions are discussed in Paper A and Paper B. Especially, an extensive numerical study quantifying the error associated to the Taylor expansion made in equation (6.4) is presented in the Appendix of Paper B. In Paper B, the strain field was reconstructed in a 100μm simulated SiO_2 crystal featuring intragranular misorientations ($\sim 1.0^o$ over $\mathcal{R}_i$) and strain variations ($\sim 50 \times 10^{-4}$ over $\mathcal{R}_i$). It was found that the root mean squared errors of the residual strain field, comparing reconstructed to ground truth strains, was in the range $\sim \pm 2 \times 10^{-4}$, depending on the used regression method and considered strain component. In conclusion, for moderately mosaic crystals, in the limit of small strains, the model established in equation (6.1) can be used to reconstruct the strain field to a good approximation.

Using the notation developed in Chapter 3 (equation 3.33), we may formulate our measurement model as

$$y_i = \frac{1}{L_i} \int_{\mathcal{R}_i} \bar{\boldsymbol{\kappa}}_i^T \bar{\boldsymbol{\epsilon}}(\boldsymbol{x}) \boldsymbol{dx} = \mathcal{M}_i \bar{\boldsymbol{\epsilon}}(\boldsymbol{x}), \tag{6.6}$$

where the integral operator $\mathcal{M}_i$ was introduced. In practice the strain signal, y_i, is noisy and features a resolution that varies with Bragg angle θ such that high angle peaks are more accurate measures of directional strain compared to low angle peaks. To account for this fact, and to allow for a robust treatment of outliers, we introduce an additive independent Gaussian noise, $e_i \sim \mathcal{N}(0, \sigma_{ei}^2)$, into our model equation (6.6) and arrive at

$$y_i = \mathcal{M}_i \bar{\boldsymbol{\epsilon}}(\boldsymbol{x}) + e_i, \tag{6.7}$$

where the task is to find $\bar{\boldsymbol{\epsilon}}(\boldsymbol{x})$ such that the measurements, y_i, are likely to be observed. Alternatively, we may collect a set of m available measurements into a vector, $\boldsymbol{y}$, and form a vectorised set of equations

$$\underbrace{\begin{bmatrix} y_1 \\ y_2 \\ \vdots \\ y_m \end{bmatrix}}_{\boldsymbol{y}} = \underbrace{\begin{bmatrix} \mathcal{M}_1 \\ \mathcal{M}_2 \\ \vdots \\ \mathcal{M}_m \end{bmatrix}}_{\boldsymbol{\mathcal{M}}} \bar{\boldsymbol{\epsilon}}(\boldsymbol{x}) + \underbrace{\begin{bmatrix} e_1 \\ e_2 \\ \vdots \\ e_m \end{bmatrix}}_{\boldsymbol{e}}, \tag{6.8}$$

where, in the following, we select $\boldsymbol{y}$ to hold the measurements of a single z-slice of a grain. This selection is computationally superior to that of including all measurements, from all z-scan positions, into $\boldsymbol{y}$, and can be leveraged as long as the data from a single grain slice is sufficient to close the equation system (6.8). When the data are sparse and/or there is significant noise, it can, instead, be beneficial to treat the grain in a global setting, including all measurements collected into $\boldsymbol{y}$ (assuming, of course, that a space filling scan across the $y - z$ plane is available). In the global setting, the correlation of the strain field in the z-direction can be used as an additional constraint resulting in a more well-posed version of (6.8). In either scenario, it is possible to estimate $\boldsymbol{\epsilon}$ by means of WLSQ or GP regression. The following sections are dedicated to deriving the problem specific ingredients for these regressors such that they can be effectively deployed to solve our target equation system (6.8).

6.2 Regression by WLSQ

As discussed in Chapter 5, to make use of the WLSQ regressor we must define $\bar{\boldsymbol{\epsilon}}$ on a finite basis expansion,

$$\bar{\boldsymbol{\epsilon}}(\boldsymbol{x}) = \sum_{i=1}^{i=B} \boldsymbol{c}_j \varphi_j(\boldsymbol{x}), \quad \varphi_j \in \mathbb{R}, \quad \boldsymbol{c}_j \in \mathbb{R}^{6\times1}. \tag{6.9}$$

One approach to solving equation (6.8) is to use the same pixel decomposition of $\bar{\boldsymbol{\epsilon}}$ as is used in algebraic tomography methods (i.e., a grid of regular rectangular pixels is used to represent the strain field). The strain tensor field is assumed to be piece-wise constant across each pixel in a z-layer and the integral operator $\boldsymbol{\mathcal{M}}$ becomes a sparse matrix, $\boldsymbol{A}$, that can be viewed as a projection matrix. Letting the constant strain in pixel number j be denoted $\bar{\boldsymbol{\epsilon}}_j$ and stacking all pixel strain tensors into a global column vector, $\boldsymbol{s} \in \mathbb{R}^{6K \times 1}$, we find that equation (6.8) reduces to a set of linear equations as

$$\boldsymbol{y} = \boldsymbol{A}\boldsymbol{s} + \boldsymbol{e}, \quad \boldsymbol{s} = \begin{bmatrix} \bar{\boldsymbol{\epsilon}}_1 \\ \bar{\boldsymbol{\epsilon}}_2 \\ \vdots \\ \bar{\boldsymbol{\epsilon}}_K \end{bmatrix}, \tag{6.10}$$

where K is the total number of pixels present in the discretisation. The formation of $\boldsymbol{A}$ involves ray-tracing through the pixel grid in combination with the incorporation of the inner product operator $\bar{\boldsymbol{\kappa}}$. The assembly of a single row of $\boldsymbol{A}$ is schematically illustrated in Figure 6.1.

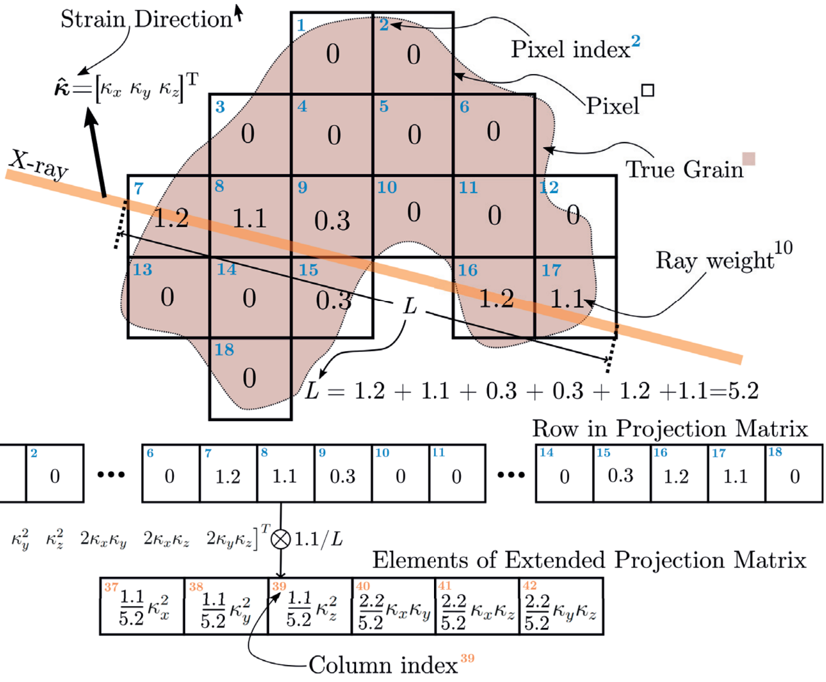

Figure 6.1: The formation of an extended projection matrix is schematically illustrated. The ray-pixel intersection lengths (ray weights) are multiplied with the outer product operator $\bar{\boldsymbol{\kappa}}$ to form an expanded projection matrix.

To solve equation (6.10) for $\boldsymbol{s}$, we let $\boldsymbol{C}_{noise}$ denote the noise covariance matrix and find from equation 5.9 that

$$\boldsymbol{s} = (\boldsymbol{A}^T\boldsymbol{C}_{noise}^{-1}\boldsymbol{A})^{-1}\boldsymbol{A}^T\boldsymbol{C}_{noise}^{-1}\boldsymbol{y}. \tag{6.11}$$

As an example, in Paper A, the noise covariance was selected as a diagonal matrix with the weights

$$(\boldsymbol{C}_{noise})_{ii} = \left|\frac{y_i(\theta_i) - y_i(\theta_i + \Delta\theta_i)}{\Delta\theta}\right|, \tag{6.12}$$

where diffraction peak number i provides a measure of a directional strain y_i at Bragg angle θ_i, and $\Delta\theta_i$ is the angle covered by a single detector pixel at the current diffraction peak position. We mention here that a future perspective for this research is the possibility to build a more complex error model with the prospect of further improving the accuracy in strain reconstruction. One possible avenue would be to use `xrd_simulator` (Paper C) to propagate uncertainty in experimental parameters as well as uncertainty in grain shape and mean orientation into a numerical estimate of the peak centre of gravity error.

To encode prior information on the solution vector $\boldsymbol{s}$, one alternative is to modify the basis set, φ_j, in equation (6.9). This can be performed directly by implementing the integral operator $\boldsymbol{\mathcal{M}}$ for the selected functional form of φ_j or, as a practical alternative, one may choose to implement an interpolation matrix, $\boldsymbol{K}$, that renders the analytical format of, φ_j, onto the previously discussed pixel basis of $\boldsymbol{\mathcal{M}}$. For instance, as an example, if we let φ_j be a radial basis function with length-scale $l \in \mathbb{R}$ centred at $\boldsymbol{\mu}_j \in \mathbb{R}^{3\times 1}$,

$$\varphi_j = \exp\left(\frac{(\boldsymbol{x} - \boldsymbol{\mu}_j)^T(\boldsymbol{x} - \boldsymbol{\mu}_j)}{2l^2}\right), \tag{6.13}$$

we find that the column number j of the interpolation matrix, $\boldsymbol{K}$, holds the rendering of φ_j on the pixel grid coordinates and the closed form WLSQ solution now become

$$\boldsymbol{s} = (\boldsymbol{K}^T\boldsymbol{A}^T\boldsymbol{C}_{noise}^{-1}\boldsymbol{A}\boldsymbol{K})^{-1}\boldsymbol{K}^T\boldsymbol{A}^T\boldsymbol{C}_{noise}^{-1}\boldsymbol{y}. \tag{6.14}$$

This rendering approach can be especially beneficial in combination with the ideas discussed in Paper D where we present a matrix decomposition of $\boldsymbol{A}$ such that standard tomographic ray tracing libraries can be used (the astra-toolbox, for example; van Aarle et al. (2015), van Aarle et al. (2016)). To maintain the computational benefits of this formulation while at the same time maintaining the freedom of selecting φ_j arbitrarily, it is essential that the interpolation matrix, $\boldsymbol{K}$, is formed such that the ray-tracing of the forward and backward pass are still cast as a pixel projection problems. When φ_j is taken with limited local support, $\boldsymbol{K}$ become sparse, which ensures computational efficiency. Alternatively, when, φ_j has global support and $\boldsymbol{K}$ is dense, computational efficiency can still be maintained as long as a highly limited number of basis functions are used.

When constraints are to be enforced on the solution vector, $\boldsymbol{s}$, and these are not easily expressed in terms of modifying the basis of $\boldsymbol{s}$, it is useful to work with a global cost function as

$$C(\boldsymbol{s}) = (\boldsymbol{A}\boldsymbol{s} - \boldsymbol{y})^T\boldsymbol{C}_{noise}^{-1}(\boldsymbol{A}\boldsymbol{s} - \boldsymbol{y}). \tag{6.15}$$

In Paper A, equation (6.15) was combined with the absolute smoothing constraint

$$|\boldsymbol{c}_j - \boldsymbol{c}_{j^n}| < \mathbf{1}\xi, \tag{6.16}$$

where $|\cdot|$ represents component-wise absolute value, $\boldsymbol{c}_{j^n}$ is the strain tensor in pixel j^n that is in the 8-neighbourhood to pixel number j and the scalar $\xi > 0$ regulates the smoothness of the solution $\boldsymbol{s}$. Equation (6.16) can be expressed as a set of linear constraints as

$$\boldsymbol{C}\boldsymbol{s} > -\mathbf{1}\xi, \quad \boldsymbol{C}\boldsymbol{s} < \mathbf{1}\xi, \tag{6.17}$$

where $\boldsymbol{C}$ is a sparse matrix that forms the neighbourhood differences between the individual pixel strain tensors in accordance with equation (6.16). The modified WLSQ problem to solve is then

$$\begin{aligned} &Argmin \quad C = (\boldsymbol{A}\boldsymbol{s} - \boldsymbol{y})^T \boldsymbol{C}_{noise}^{-1} (\boldsymbol{A}\boldsymbol{s} - \boldsymbol{y}), \\ &s.t \quad \boldsymbol{C}\boldsymbol{s} > -\mathbf{1}\xi, \\ &and \quad \boldsymbol{C}\boldsymbol{s} < \mathbf{1}\xi, \end{aligned} \tag{6.18}$$

which represents a quadratic, convex, programming problem and can be solved using any of a number of well researched numerical gradient based optimisation techniques.

Having covered some of the possible reconstruction settings that can be used in conjunction with WLSQ, we are now ready to illustrate the discussed concepts with an example. In Example 6.2.1 we consider a simulated strain field from a single spherical grain of alpha-quartz SiO_2 in the following. Later in this chapter we will return to this example strain tensor field as we give a similar discussion on the GP regression framework. While the exact details of the simulation example is less relevant for the exposition, we give a brief summary for the interested reader in the following. First a strain tensor field was generated by pseudo randomly drawing from a Gaussian Process that was modified to encode self-equilibrium in accordance with the Maxwell's stress functions. Data, y_i, were then formed by assigning a spatially constant random orientation to the grain and making a random uniform selection of 50 allowable h, k, l Miller indices of the P3221 space group featuring diffraction angles, $\theta = [4^o, 13^o]$, for a wavelength of $\lambda = 0.284\,57\,\text{Å}$. Directional strains, $s_{hkl} = \hat{\boldsymbol{\kappa}}_{hkl}^T \boldsymbol{\epsilon}(\boldsymbol{x}) \hat{\boldsymbol{\kappa}}_{hkl}$, were then formed by computing $\boldsymbol{G}$-vectors, normalising into $\hat{\boldsymbol{\kappa}}_{hkl}$ directions and projecting the resulting scalar fields at the turntable angles, ω, at which diffraction was predicted to be observed according to the Laue equations. The resulting data vector, $\boldsymbol{y}$, was corrupted with independent additive Gaussian noise with standard deviation $\sigma_n = \theta^{-1} \times 10^{-4}$ (with θ in units of degrees). To simulate outliers, 7 out of the 50 diffraction events were selected for elevated noising, as $\sigma_n = 7 \times \theta^{-1} \times 10^{-4}$.

Example 6.2.1

WLSQ Strain Regression
Constructing the matrix $\boldsymbol{A}$ as illustrated in Figure 6.1 and using both the pixel basis ($\boldsymbol{K} = \boldsymbol{I}$) as well as the radial basis in equation (6.13) we illustrate the reconstructed $\epsilon_{xx}(\boldsymbol{x})$ field corresponding to our previously described simulation in Figure 6.2. The main point is here to show the impact of parameter and model selection to the reconstructed field. To this end we have reconstructed the strain field both with noise weights (WW) as well as without (NW). The latter of these cases (NW) corresponds to setting the noise covariance to identity, $\boldsymbol{C}_{noise} = \boldsymbol{I}$, while the former (WW) deploys the true noise covariance.

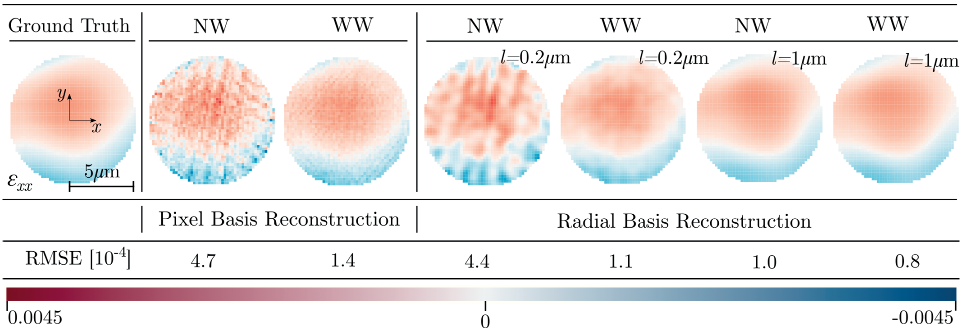

Figure 6.2: WLSQ strain reconstruction for different parameter choices. The strain field originates from the single crystal quartz example described in section 6.2.

Increasing the length-scale of the radial basis expansion as seen to the right in Figure 6.1 causes the set of possible solutions to shrink until the problem becomes well defined, even in the presence of a poor noise model ($\boldsymbol{C}_{noise} = \boldsymbol{I}$). Reversely, when the strain reconstruction is allowed to oscillate over a small length-scale it becomes important to properly model the noise.

6.3 Regression by a Gaussian Process

As previously discussed in Chapter 5, an alternative approach to WLSQ regression is Gaussian Process regression. Combing the linear measurement model defined in equation (6.10) with the expression for the posterior distribution defined in equation (5.16), we find that GP regression yields the posterior distribution over strains as

$$\begin{aligned} \mathbb{E}[\boldsymbol{\epsilon}|\boldsymbol{y}] &= \mathbb{E}[\boldsymbol{\epsilon}] + \boldsymbol{C}\boldsymbol{A}^T(\boldsymbol{A}\boldsymbol{C}\boldsymbol{A}^T + \boldsymbol{C}_{noise})^{-1}(\boldsymbol{y} - \mathbb{E}[\boldsymbol{y}]), \\ \mathbb{V}[\boldsymbol{\epsilon}, \boldsymbol{\epsilon}|\boldsymbol{y}] &= \boldsymbol{C} - \boldsymbol{C}\boldsymbol{A}^T(\boldsymbol{A}\boldsymbol{C}\boldsymbol{A}^T + \boldsymbol{C}_{noise})^{-1}\boldsymbol{A}\boldsymbol{C}, \end{aligned} \tag{6.19}$$

where $\boldsymbol{C}$ is the prior spatial covariance of strain (defined on the pixel basis grid) and $\mathbb{E}[\boldsymbol{\epsilon}] = \boldsymbol{0}$ in the following. Note that here we have implicitly decomposed the kernel function, $\boldsymbol{k}(\boldsymbol{x}, \boldsymbol{x}')$, on the pixel basis, which is why we are able to use the same matrix operator $\boldsymbol{A}$ in equation (6.19) as was previously used in the WLSQ regression. In Paper B, where we incorporated an equilibrium constraint in the prior distribution, we instead chose a spectral method were the kernel was decomposed on a finite series of Fourier waves. In fact, any decomposition of the kernel such that the integral model in equation (6.6) can be solved (or accurately approximated) is possible, and different selections of kernel decomposition will lead to different computational complexity and memory requirements on the forward pass operator $\boldsymbol{A}$ (and will be more or less difficult to implement on a computer). Ideally, the GP regression is basis free in the sense that the analytical solution of the posterior can be written as

$$\mathbb{E}[\boldsymbol{\epsilon}|\boldsymbol{y}] = \mathbb{E}[\boldsymbol{\epsilon}] + \boldsymbol{k}\boldsymbol{\mathcal{M}}^T(\boldsymbol{\mathcal{M}}\boldsymbol{k}\boldsymbol{\mathcal{M}}^T + \boldsymbol{C}_{noise})^{-1}(\boldsymbol{y} - \mathbb{E}[\boldsymbol{y}]), \tag{6.20}$$

where the prior covariance of strain, $\boldsymbol{k} \in \mathbb{R}^{6\times6}$, has been chosen as a diagonal matrix in our work,

$$\boldsymbol{k}(\boldsymbol{x}, \boldsymbol{x}') = \begin{bmatrix} k_{11}(\boldsymbol{x}, \boldsymbol{x}') & 0 & 0 & 0 & 0 & 0 \\ 0 & k_{22}(\boldsymbol{x}, \boldsymbol{x}') & 0 & 0 & 0 & 0 \\ 0 & 0 & k_{33}(\boldsymbol{x}, \boldsymbol{x}') & 0 & 0 & 0 \\ 0 & 0 & 0 & k_{12}(\boldsymbol{x}, \boldsymbol{x}') & 0 & 0 \\ 0 & 0 & 0 & 0 & k_{13}(\boldsymbol{x}, \boldsymbol{x}') & 0 \\ 0 & 0 & 0 & 0 & 0 & k_{23}(\boldsymbol{x}, \boldsymbol{x}') \end{bmatrix}. \tag{6.21}$$

Unfortunately, we do not know of any suitable kernel function that has a closed form solution to the double integral $\boldsymbol{\mathcal{M}}\boldsymbol{k}\boldsymbol{\mathcal{M}}^T$ in equation (6.20); this motivates the use of kernel decomposition techniques. Note that it is the kernel that is represented on a finite basis in the GP regression framework and not the strain field, as is the case in WLSQ regression. In this sense, GP regression can be said to be basis free, even in the case when the kernel is approximated by a finite series of basis functions.

The kernel functions, $k_{ij}(\boldsymbol{x}, \boldsymbol{x}')$, which define the GP prior covariance, can be selected among the class of positive definite functions (i.e., when evaluated over a finite set of coordinates, $x_1, x_2, ..., x_N$, the resulting covariance matrix, $\boldsymbol{C}$, must be positive definite). In this chapter we shall use a version of the squared exponential kernel,

$$k_{ii}(\boldsymbol{x}, \boldsymbol{x}') = \sigma^2 \exp\left(\frac{(\boldsymbol{x} - \boldsymbol{x}')^T(\boldsymbol{x} - \boldsymbol{x}')}{4l^2}\right), \tag{6.22}$$

where σ regulates the prior uncertainty and l the correlation length-scale. Many other selections are possible, and to give one more example, we introduce the rational quadratic kernel as

$$k_{ii}(\boldsymbol{x}, \boldsymbol{x}') = \sigma^2\left(1 + \frac{(\boldsymbol{x} - \boldsymbol{x}')^T(\boldsymbol{x} - \boldsymbol{x}')}{4\alpha l^2}\right)^{-\alpha}. \tag{6.23}$$

Both equations (6.22) and (6.23) represent functions that are well known to be positive definite and can, thus, constitute feasible kernel choices. Each kernel encodes a different correlation structure in the underlying target field that is to be reconstructed from data. When the correlation structure of the target field is unknown, it is common to try different kernels and evaluate the probability of observing the measured data, $\boldsymbol{y}$, for each selection. In Example 6.3.1 and Figure 6.3 we illustrate the functional form and type of fields that are represented by the squared exponential and rational quadratic kernel. The key takeaway here is that the kernel functional form, together with the kernel parameters, encode a prior belief on what type of correlation structure is believed to dominate the reconstructed field.

Example 6.3.1

GP sampling with different kernels

Consider a GP over a scalar field on $\mathbb{R}^2$ with kernel $k(\boldsymbol{x}, \boldsymbol{x}')$ and mean, $\boldsymbol{\mu}$. By taking a singular value decomposition of the resulting covariance matrix such that $\boldsymbol{C} = \boldsymbol{U}\boldsymbol{S}\boldsymbol{U}^T$ with $\boldsymbol{C}, \boldsymbol{U}, \boldsymbol{S} \in \mathbb{R}^{n \times n}$ and $\boldsymbol{S}$ is a diagonal matrix holding the singular values of $\boldsymbol{C}$, it is possible to draw a random sample, $\boldsymbol{f}$, from the GP as

$$\boldsymbol{f} = \boldsymbol{\mu} + U\sqrt{\boldsymbol{S}}\boldsymbol{w} \tag{6.24}$$

where $\boldsymbol{w} \sim \mathcal{N}(0, 1)$ is white noise. This fact can be realised by considering that the stochastic variable $\boldsymbol{Z} = \boldsymbol{\mu} + \boldsymbol{U}\sqrt{\boldsymbol{S}}\boldsymbol{w}$ has covariance $\Sigma_{\boldsymbol{Z}} = \boldsymbol{U}\boldsymbol{S}\boldsymbol{U}^T = \boldsymbol{C}$ and thus a sample of $\boldsymbol{Z}$ is a sample from our GP. In Figure 6.3, samples generated in accordance with equation (6.24) are illustrated for the case of a squared exponential (left) and rational quadratic (right) kernel respectively. We note that the kernel choice controls the class of functions that the GP considers likely.

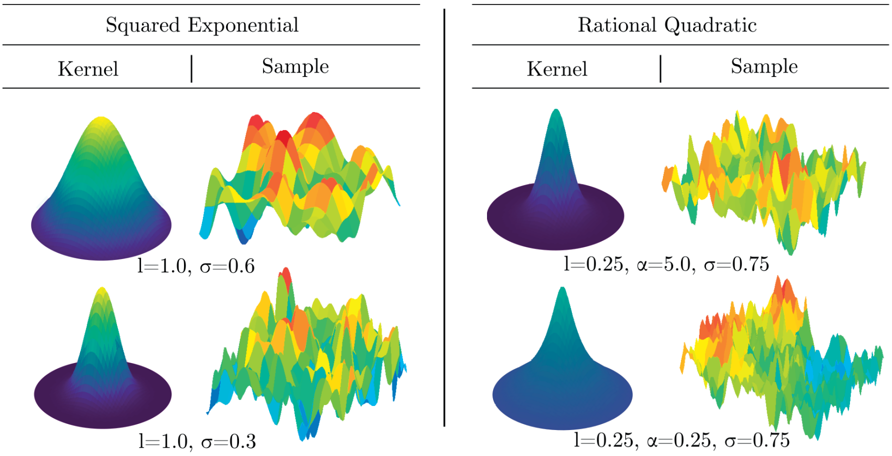

Figure 6.3: The Squared Exponential (equation (6.22)*) and Rational Quadratic (equation* (6.23)*) Kernels are illustrated for different parameter choices. Corresponding randomly sampled fields, generated from a scalar GP on* $\mathbb{R}^2$*, are shown next to each kernel selection.*

In Paper B we extend these concepts further by defining the kernel not as the correlation of strain, but rather as the correlation of an underlying stress function, which is then mapped through a partial differential operator (i.e., a linear map) to create an ”effective strain kernel”, which encodes mechanical self equilibrium. In general it is possible to enforce linear constraints into a GP (Jidling et al., 2017). The reasoning is as follows:

consider $\boldsymbol{\mathcal{L}}$ to be a linear transform and let $\boldsymbol{f}$ be a vector valued GP on $\boldsymbol{x}$. We require

$$\mathcal{L}\boldsymbol{f}(\boldsymbol{x}) = \mathbf{0} \tag{6.25}$$

and find that if $\mathcal{L}^\dagger$ can be established such that

$$\mathcal{L}\mathcal{L}^\dagger\boldsymbol{g}(\boldsymbol{x}) = \mathbf{0}, \tag{6.26}$$

for all selections of the auxiliary GP, $\boldsymbol{g}(\boldsymbol{x}) \sim (\boldsymbol{\mu}, \boldsymbol{\Sigma})$, then the sought GP is

$$\boldsymbol{f} \sim \left(\mathcal{L}^\dagger\boldsymbol{\mu}, \mathcal{L}^\dagger\boldsymbol{\Sigma}(\mathcal{L}^\dagger)^*\right), \tag{6.27}$$

where $(\mathcal{L}^\dagger)^*$ is the adjoint of $\mathcal{L}^\dagger$. The argument uses the fact that a linear transform acting on a multivariate Gaussian distributed random variable results in a new random variable that also follows a multivariate Gaussian distribution.

Returning to our simulated strain field in Example 6.2.1, it is now natural to ask how the selection of kernel parameters will impact the quality of the strain reconstruction. In example 6.3.2 we show GP regression for the squared exponential kernel using different length-scales, l.

Example 6.3.2

GP Strain Regression

Considering again a GP over a scalar field on $\mathbb{R}^2$ with prior kernel

$$k(\boldsymbol{x}, \boldsymbol{x}') = \sigma^2 \exp\left(\frac{(\boldsymbol{x} - \boldsymbol{x}')^T(\boldsymbol{x} - \boldsymbol{x}')}{4l^2}\right), \tag{6.28}$$

Adopting a zero mean for our prior we may compute the expected value of the posterior distribution, conditioned on our strain measurements $\boldsymbol{y}$, in accordance with equation (6.19). The results of this procedure, for different selections of l with $\sigma = 0.01$ constant, are shown in Figure 6.4.

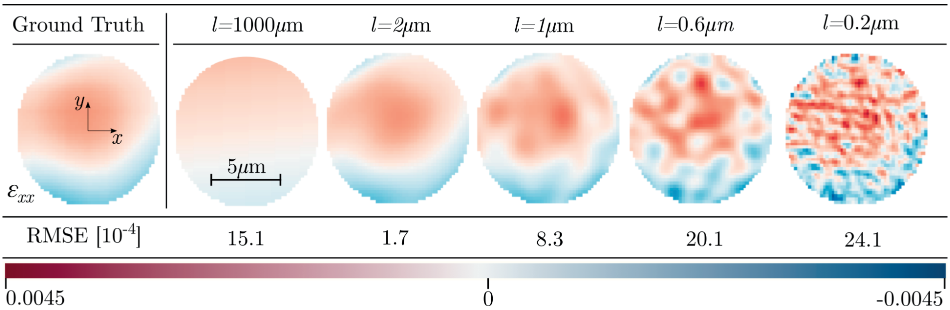

Figure 6.4: Impact of the correlation length-scale parameter, l, in Gaussian Process regression of the strain field in the single crystal quartz example described in section 6.2. As the correlation length becomes small, the field is allowed to oscillate (right), very large correlation lengths produces little freedom for the reconstructed field to vary (left).

Small length-scales, l, (Figure 6.4 right) in the prior will result in a posterior with high total variation while, in contrast, a very large l (Figure 6.4 left) encodes the prior belief that the strain field is constant.

To make an informed selection of hyper parameters, $\sigma, l, \alpha, ...$, of the prior distribution use can be made of optimisation methods (Rasmussen, 2003). For instance, we may minimise the negative logarithm of the out-of-sample-likelihood with respect to the hyper parameters (Gregg et al., 2020),

$$Argmin_{\sigma,l,\alpha,...} - \log\left(p(\boldsymbol{y}_{test}|\boldsymbol{y}_{train}, \boldsymbol{k}(\boldsymbol{x}, \boldsymbol{x}', \sigma, l, \alpha, ...))\right), \tag{6.29}$$

where a random subset of the measurements, $\boldsymbol{y}_{train}$, is used to construct the posterior of the GP and the remaining, unused, data, $\boldsymbol{y}_{test}$, are used for validation. Solving equation (6.29) corresponds to finding the hyper parameters that maximise the probability of observing $\boldsymbol{y}_{train}$. For instance, let 80 % of the line integral strain measurements be contained in

$\boldsymbol{y}_{train}$. For a fixed set of hyper parameters we can construct the posterior of the GP, conditioning only on $\boldsymbol{y}_{train}$. We then evaluate the probability of observing $\boldsymbol{y}_{test}$ given the current posterior. To maximise this probability it is possible to compute gradients with respect to hyper parameters and use numerical descent schemes to find a probable set of hyper parameters. This, so-called, hyper parameter optimisation procedure is a great benefit of the GP framework, as it enables the data to steer the parameter selection.

6.4 The Optimal Estimator?

The reader may now be inclined to ask which of the two discussed regression methods, GP or WLSQ, is superior for estimating strain tensor fields in practice. This question does however not admit a simple answer in our view. The reality is, instead, that each of the two options features a range of different benefits and drawbacks. For instance, using the analytical results in Paper D, WLSQ regression is computationally fast and memory efficient while GP regression is infamous for its high memory usage and poor computational complexity. On the other hand well developed methods for hyper parameter optimisation exist in the GP framework, which, arguably, makes parameter selection less arbitrary. The statistician then only need to select a functional form of the kernel before regression can take place while the versions of WLSQ discussed here require the basis functions to be manually selected. That being said, in many cases the two methods can be reconciled to yield similar results by adapting the formulations and the input parameters. The argument then tends more towards the kind of debates sometimes seen between Bayesian and frequentist followers on the interpretations of probabilities (Hackenberger, 2019). Although the author would prefer to side with the Bayesians in these discussion (in the good company of Gauss and Laplace) the discussion has become less practical at this point. To illustrate that both GP and WLSQ can be successfully (and un-successfully) used to the same end, we show, in Figure 6.5, a range of strain estimations considering the example strain field used previously in this chapter. The maximum likelihood estimation from the WLSQ regression and the expected value of a GP posterior have been plotted in Figure 6.5 such that each row facilitates comparisons for a single strain tensor component. As can be seen in the rightmost column (RQ) a bad kernel (rational quadratic with poor parameters) will result in errors in the reconstructed, strain while an optimised selection gives a close-to-correct estimation using a GP. Likewise in columns 2 and 3 (PB vs PBW where PB is shorthand for pixel basis) we see that when the WLSQ basis is uncorrelated the need for a good noise model (PBW) can be crucial. When instead a radial basis is used, and adapted to feature the same correlation length-scale as in the GP kernel, the results (RBF and RBFW) are similar to what can be achieved with a GP featuring a squared exponential kernel (SQE).

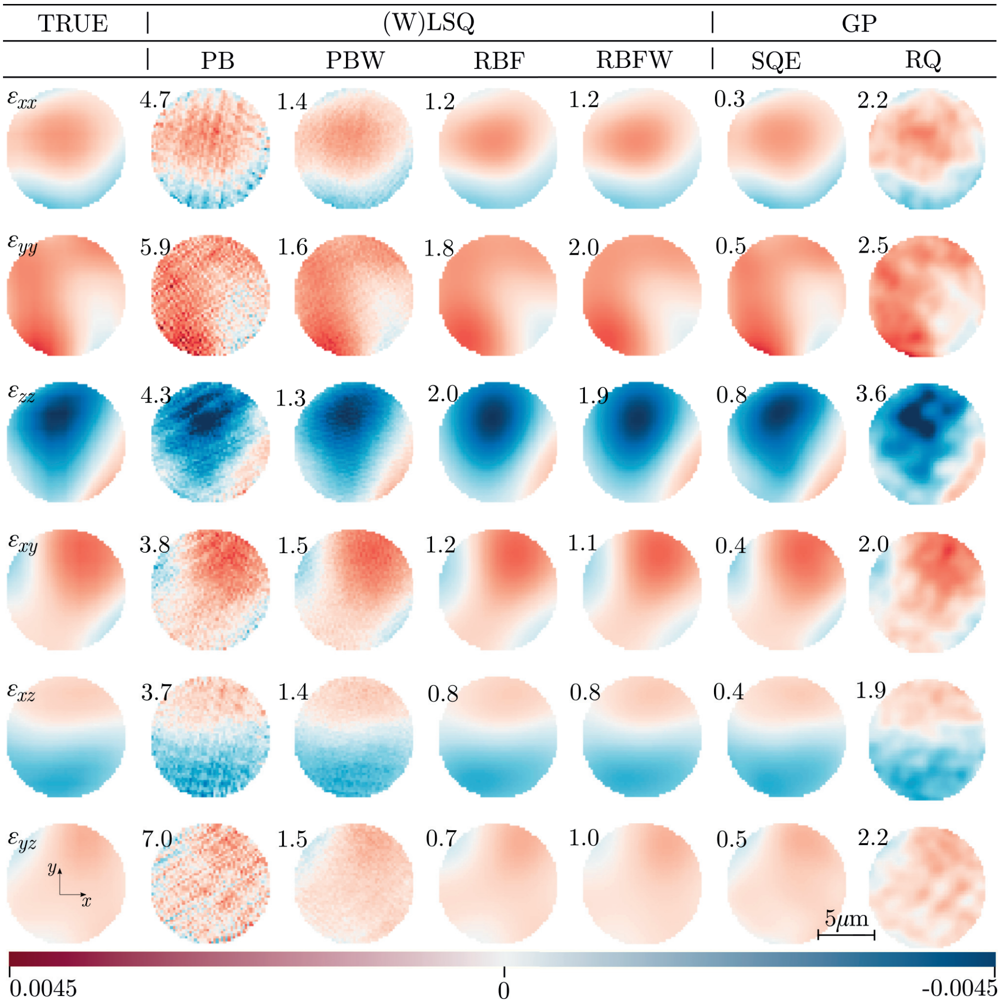

Figure 6.5: Reconstruction of a synthetic strain tensor field using 50 projections of average strain with $\hat{\boldsymbol{\kappa}}$ directions generated from alpha-quartz crystal (space group P3221) with random orientation. A suit of reconstruction options are presented from left to right as; Least Squares Pixel Basis (PB), Least Squares Pixel Basis with noise Weights (PBW), Least Squares with Radial Basis Functions ($l = 2\mu m$) (RBF), Least Squares with Radial Basis Functions ($l = 2\mu m$) and noise Weights (RBFW), GP with Squared Exponential kernel (SQE) ($l = 2\mu m$, $\sigma = 0.01$), GP with Rational Quadratic kernel (RQ) ($l = 2\mu m$, $\sigma = 0.01$, $\alpha = 0.1$)). The RMSE of the residual fields (subtracting ground truth from reconstruction) is shown to the top left of each reconstruction in units of $\times 10^{-4}$.

6.5 Applications & Examples

To show how the methods discussed in this thesis are being put to use to address materials research questions, we highlight three examples of 3D strain (and stress) tensor field reconstructions from scanning-3DXRD diffraction data. These scanning-3DXRD experiments where conducted at the ESRF ID11 beamline by the author and colleagues from Lund University, The University of Western Ontario, Canada and Mines de Saint-Étienne, France, respectively. Apart from these three examples, the methods developed in Paper A and Paper B were previously demonstrated (as seen in the published manuscripts) on a single grain of tin (Sn) within a polycrystalline sample originating from the data collected by Hektor et al. (2019). Other, previous efforts, include measurements on photonic crystals conducted in collaboration with Hergen Stieglitz and Johan Hektor at the DESY nanofocus station (beamline P03). Measurements of residual stress in natural silica sand grains embedded within a concrete matrix were recently conducted in collaboration with Ryan Hurley, Johns Hopkins Whiting School of Enginering, USA, and the resulting strain fields are currently being analysed in relation to Eshelby elliptical inclusion theory. Moreover, a recent experiment conducted by the main author of this thesis, in collaboration with colleagues from Lund University and Malmö University, is being analysed at the time of writing. This study concerns the fracture mechanisms of single crystal alpha-quartz (SiO_2) investigated by means of in-situ loading with the aim of reconstructing the intragranular deformation field before (and during) failure. In conclusion, the demand for spatially resolved strain tensor maps on an intragranular scale is currently on the rise providing a strong motivation for the mathematical work and algorithmic developments presented in this thesis.

In situ Loaded Spherical Silica Ensemble

Silicate minerals make up 90% of the Earth crust with silicon dioxide (Quartz) being the second most abundant mineral in Earth's continental crust. In granular form, silica sand is used in glass, foundries, construction, ceramics and the chemical industry. When subject to loading, the grain ensemble rearranges and forms inter- and intragranular force paths distributing the load through the grain network. In Figure 6.6 the stress distribution of a small ensemble of quasi-spherical milled silica grains (12 crystals) under 60N of uniaxial load is shown. The sample was scanned at the ESRF ID11 beamline and the strain tensor field was reconstructed using a WLSQ approach with a voxel basis selected to match the beam width of 25μm. A local smoothing constraint was incorporated into the reconstruction through the use of a trust-constraint solver. The estimated strain field was converted to stresses using an anisotropic elastic model. The resulting principal stress maps (Figure 6.6 B) show stress concentrations at the external cylinder wall and piston contacts as well as around the inter-granular contacts. At the subsequent load step of 90N several grains shattered and in Figure 6.6 B the first principal stress field (present at 60N) at an interface of fracture has been rendered on top of the grain shards. These results provide a unique opportunity to study the coupling between inter- and intragranular failure mechanics of sand. The Figure was modified from Vestin (2022) with permission.

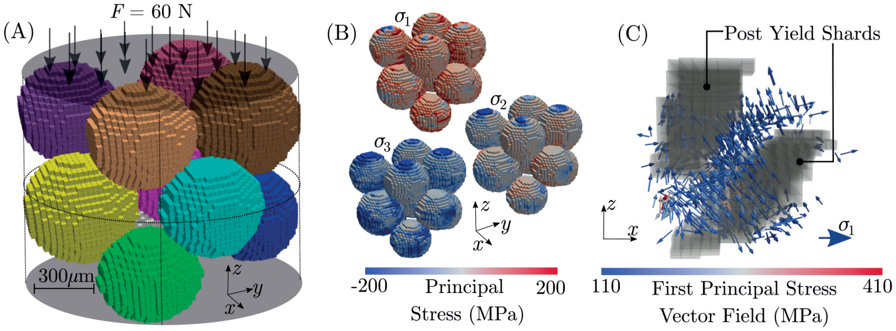

Figure 6.6: An Alpha-quartz ensemble (SiO_2) under 60N of axial load (A). The intragranular strain tensor field has been reconstructed using WLSQ with a pixel basis and converted into stress providing 3D volume renderings of the principal stresses, σ_1, σ_3, σ_3 (B). The central grain (purple in A) fractured at the subsequent load step of 90N. The broken shards are rendered together with the intragranular principal stress field formed in the grain before the yield point (60N) in (C). The figure material is the courtesy of Philip Vestin, Lund University, and represents a modification from results presented in Vestin (2022). The original data were collected at the ESRF ID11 beamline.

Hydrogen Embrittlement in a Zirconium Alloy

Zirconium alloys are used extensively in almost all water-cooled nuclear reactors. Their high corrosion resistance, resistance to radiation damage and transparency to thermal neutrons makes them an ideal choice for pressure tubes and fuel rod cladding (Yau and Annamalai, 2016). The cladding alloy separates the outer layer of the fuel rods from the reactor coolant and prevents radioactive fission products from contaminating the reactor coolant (Allen et al., 2012). As the zirconium is exposed to high levels of hydrogen, contained in the hot water, a new phase called zirconium hydride might form within the metal. This process is a safety concern as it causes hydrogen embrittlement, deteriorating the mechanical properties the zirconium alloy (Tondro, 2023; Abdolvand et al., 2018; Alawadi and Abdolvand, 2020). Figure 6.7 shows a preliminary stress map in a 30 μm zirconium sample scanned at the ESRF ID11 beamline by Hamidreza Abdolvand and Alireza Tondro from The University of Western Ontario, Canada. The strain tensor field was reconstructed using a WLSQ approach with a piece-wise cubic basis and accelerated by the use of the matrix factorisation derived in Paper D. The intermediate phase (ZrH) has been marked in gray for a selected slice in z while the stress maps have been rendered as colormaps over the four distinct zirconium grains.

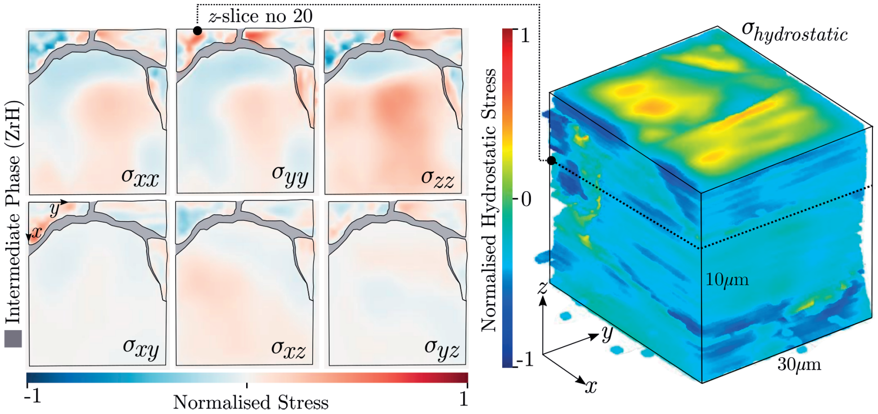

Figure 6.7: The reconstructed strain maps in a zirconium (Zr) sample has been stacked in z and converted to stresses providing a 3D stress volume rendering. Grain shape reconstruction and strain reconstruction, using WLSQ with a piece-wise cubic spline basis, was performed in collaboration with colleagues from The University of Western Ontario, Canada. The stress magnitudes have been normalised as the results are currently in preparation for publication. The data were collected at the ESRF ID11 beamline and made available by Hamidreza Abdolvand and Alireza Tondro.

Residual Surface Stress in laser treated iron (Fe)

With the development of highly focused femtosecond laser pulses, three-dimensional writing in solid materials has become possible over the last decades (Malinauskas et al., 2016). These laser techniques can be considered a promising tool for a broad range of engineering applications as they enable fabrication of sub-micron 3D objects. When used with metals the laser treatment leads to shock peening that induces surface residual stress (Majumdar et al., 2016). In Figure 6.8, we show preliminary results of the strain tensor distribution in an iron (Fe) sample scanned at the ESRF ID11 beamline using a 0.5μm beam. Prior to the X-ray measurements the sample was irradiated by a femtosecond laser. The magnitude and distribution of the corresponding residual stress field are of importance with respect to component corrosion crack and fatigue resistance, among other things. To respect the fact that the results are currently being prepared for publication we here only present the strain tensor field and use a normalised colorbar. The strain field was reconstructed using a WLSQ approach with noise covariance derived from Bragg angles, θ, as described in Paper A. A radial basis expansion was used in conjunction with the matrix factorisation described in Paper D which enabled the use of GPUs. The 2D slice shown in Figure 6.8 was reconstructed in approximately one hour using a NVIDIA A40 GPU card.

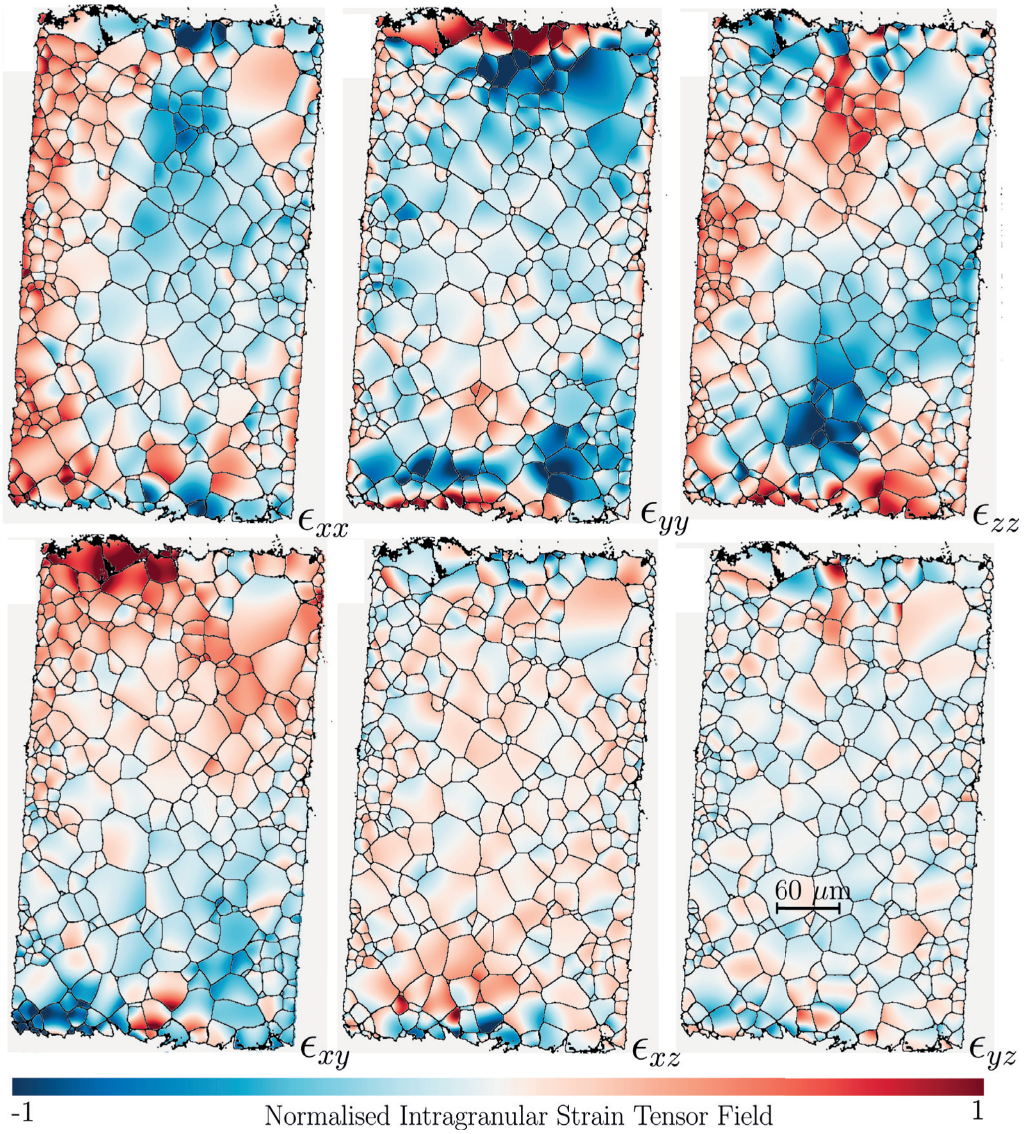

Figure 6.8: Residual strain tensor distribution in an iron (Fe) sample after laser surface treatment. The scanning X-ray diffraction data were collected at ESRF beamline ID11 under the lead of professor András Borbély, Mines St-Etienne, France. Data analysis was conducted in collaboration with Jonathan Wright and András Borbély.

Chapter 7

Conclusions & Future Perspectives

In this thesis we have treated the estimation of intragranular, small-strain, elastic, tensor fields from X-ray diffraction data. In Paper E, we provided a mathematical foundation for reconstruction of the per-crystal strain tensor probability distributions given full-field 3DXRD data. For scanning-3DXRD, Paper A and Paper B show how the spatial map of strain can be recovered on the domain of the crystal, with the option to include prior constraints in the regression tailored to the application. The methods, which were already demonstrated in Paper A and B to be computationally feasible for real world synchrotron data, can be combined with the analytical results in Paper D to further the computationally scalability. These results enable the study of deformation mechanics on finer length-scales than previously possible in scanning-3DXRD, with state of the art experiments featuring spatial resolutions in the range of a few hundreds of nano-meters.

As the derived methods are rapidly being adopted by the materials research community, a range of new, open, research questions are starting to form. Firstly, whenever mathematical advances provide upgrades to an already existing experimental method, it is important to let the new algorithmic capabilities feedback into the experimental design. For instance, in 3DXRD, the sample is rotated around a single fixed axis throughout the measurement sequence (z-axis). This choice will impact how the error in strain measurements is distributed among the strain tensor components and it is natural to ask if a tilted axis of rotation would be better? Questions like this must be resolved in an integrated way, searching for experimental designs that are practically feasible while, at the same time, maximising the utility of the output data of the microscope in connection to the algorithmic development. The reduction of scan-times in 3DXRD is, for instance, in competition with the acquisition of the ”perfect” data set, which would entail a series of scans with different rotation axes. Similarly, if the mathematical complexity of the reconstruction algorithms can be reduced, a larger scientific audience may be reached. With the help of the computer tools developed in Paper C we are prepared to launch a new series of investigations addressing these types of questions. The freedom to simulate a wide range of non-standard 3DXRD situations will not only allow us, and others, to continue optimising the the microscope, but also enables us to address yet another, perhaps more pressing, question; the generalisation to large deformations.

In paper A, we focused the discussion on the reconstruction of small strains in scanning-3DXRD. Nevertheless, as we evaluated different regression alternatives, we touched upon the possibility to use more complete diffraction models, including large intragranular misorientations. Recent work by Li et al. (2023) show results that seem to have combined such a model with stochastic gradient descent methods to arrive at the full deformation field, as far as it is observable in 3DXRD (there is a discussion to be had on different modes of plastic deformations). Although their method has not yet been published, these advances appear to be promising. Similarly, the author is currently working on several alternative formulations with the aim of incorporating large deformations. The challenge, here, is to maintain the good numerical properties of the inverse problem, in terms of convexity, conditioning and incorporation of constraints. Forward models that stay true to the Laue equations in the setting of large deformations must admit that the scattering from a ray domain, $\mathcal{R}_i$, can not be associated to a single angular position of the sample, ω. In fact, for large deformations, the volume fraction of $\mathcal{R}_i$ that scatters at a given ω setting is a function of the crystal deformation state which makes the diffraction model discontinuous as well as non-linear. Another route is to consider high-angle diffraction peaks as suggested by (Wright et al., 2020), effectively reducing the problem to that of direct back-projection with a standard tomography model. Recent experiments suggest that this is a possibility for at least some samples and setups. The reconstruction problem would then be reduced to 9 independent standard tomographic problems by first solving a sequence of estimation problems, one for each ray domain, $\mathcal{R}_i$. In this approach, all data collected over a finite angular increment, $\Delta\omega$, are approximated to originate from a single ray domain positioned at the centre of the angular range. When enough diffraction peaks are present over $\Delta\omega$ the analysis then admits an average unit cell to be established on $\mathcal{R}_i$ and the tomographic reconstruction becomes standard.

In conclusion, this thesis introduces a collection of mathematical advancements that improve the capabilities of well-established X-ray diffraction microscopy techniques. By employing the developed algorithms, polycrystalline deformation mechanisms can be studied across the inter- and intragranular levels simultaneously.

Summary of appended papers

Paper A: The strain tensor estimation problem is presented in a WLSQ setting with focus on the tomographic aspects of the problem. Several alternative formulations are discussed and compared to a point-by-point fitting method previously suggested in the literature. It is found that the tomographic properties of the problem are key for correctly estimating the strain tensor field in single crystals. The methods derived are demonstrated on real synchrotron data as well as on simulated validation examples.

Paper B: The concepts developed in Paper A are extended and incorporated into a Gaussian Process regression framework. The prior distribution is taken from a class of continuous and differentiable linear elastic strain functions that satisfy the point-wise equilibrium equations. Existing methods for relaxing the computational efforts of the GP regression, as well as optimising the hyper parameters of the model, are modified for the target application. The GP framework is demonstrated on synchrotron data as well as on simulated validation examples. Compared to the WLSQ framework in Paper A, it was found that the number of data needed to correctly estimate the strain tensor field was greatly reduced as a result of the constrained Bayesian formulation.

Paper C: A diffraction simulation framework for 3DXRD-like experiments is developed and validated. The mathematical formulation encompasses arbitrary rigid body motions of the sample while at the same time allowing for general sample and beam morphology descriptions. This is made possible by deriving and solving a time-dependent version of the Laue diffraction equations. The developed equations are implemented in python, packaged for distribution and released as an open source library named `xrd_simulator`.

Paper D: A multiplicative split of the system matrix in strain tensor tomography is derived and presented. The factorisation reveals two parts; one that is related to the directional weighting of strain and one that is related to a pure (classical) tomographic projection. The results allow standard ray-tracing models to be used in the implementation of the forward operator and its adjoint. Resulting iterative solvers can be made to approach computational speeds and RAM efficiency corresponding to the modern GPU implementations found in several algebraic reconstruction algorithms for absorption tomography.

Paper E: The strain estimation problem is discussed in the setting of small crystal grains and a large X-ray beam, such that the intragranular spatial resolution is lost. It is found that, while the strain tensor field is unrecoverable, the strain tensor probability distribution (strain PDF) can be estimated from diffraction peak strain broadening. A method for recovering the strain PDF using a radial basis expansion on strain space ($\mathbb{R}^6$) is derived and demonstrated. For the special case of multivariate Gaussian strain PDFs, the null-space of the problem is parameterised analytically and the set of all maximum likelihood estimates satisfying data are given in a closed form.

References

Abdolvand, H., Wright, J., and Wilkinson, A. J. (2018). Strong grain neighbour effects in polycrystals. *Nat Commun*, 9:171.

Alawadi, A. and Abdolvand, H. (2020). Measurement and modeling of micro residual stresses in zirconium crystals in three dimension. *Journal of the Mechanics and Physics of Solids*, 135:103799.

Allen, T., Konings, R., and Motta, A. (2012). 5.03 - corrosion of zirconium alloys. In Konings, R. J., editor, *Comprehensive Nuclear Materials*, pages 49–68. Elsevier, Oxford.

Als-Nielsen, J. and McMorrow, D. (2011). *Elements of Modern X-ray Physics*. John Wiley & Sons, Ltd.

Authier, A. (2013). *Early Days of X-ray Crystallography*. Oxford University Press.

Barton, N. R. and Bernier, J. V. (2012). A method for intragranular orientation and lattice strain distribution determination. *Journal of Applied Crystallography*, 45(6):1145–1155.

Batenburg, K. J., Sijbers, J., Poulsen, H. F., and Knudsen, E. (2010). DART: a robust algorithm for fast reconstruction of three-dimensional grain maps. *Journal of Applied Crystallography*, 43(6):1464–1473.

Behnken, H. (2000). Strain-function method for the direct evaluation of intergranular strains and stresses. *physica status solidi (a)*, 177(2):401–418.

Bernier, J. V., Barton, N. R., Lienert, U., and Miller, M. P. (2011). Far-field high-energy diffraction microscopy: a tool for intergranular orientation and strain analysis. *The Journal of Strain Analysis for Engineering Design*, 46(7):527–547.

Bernier, J. V. and Miller, M. P. (2006). A direct method for the determination of the mean orientation-dependent elastic strains and stresses in polycrystalline materials from strain pole figures. *Journal of Applied Crystallography*, 39(3):358–368.

Bernier, J. V., Suter, R. M., Rollett, A. D., and Almer, J. D. (2020). High-energy x-ray diffraction microscopy in materials science. *Annual Review of Materials Research*, 50(1):395–436.

Bhattacharyya, K. B. (2016). Godfrey newbold hounsfield (1919-2004): The man who revolutionized neuroimaging. *Annals of Indian Academy of Neurology*, 19(4):448–450.

Borbély, A., Renversade, L., Kenesei, P., and Wright, J. (2014). On the calibration of high-energy X-ray diffraction setups. I. Assessing tilt and spatial distortion of the area detector. *Journal of Applied Crystallography*, 47(3):1042–1053.

Bracewell, R. N. (1956). Strip integration in radio astronomy. *Australian Journal of Physics*, 9(2):198–217.

Bragg, W. H. and Bragg, W. L. (1913). The reflection of x-rays by crystals. *Proceedings of the Royal Society of London. Series A, Containing Papers of a Mathematical and Physical Character*, 88(605):428–438.

Bragg, W. L., Caroe, G. M., and Hartley, H. B. (1962). Sir william bragg, f. r. s. (1862-1942). *Notes and Records of the Royal Society of London*, 17(2):169–182.

Carneiro, V. H., Rawson, S. D., Puga, H., and Withers, P. J. (2021). Macro-, meso- and microstructural characterization of metallic lattice structures manufactured by additive manufacturing assisted investment casting. *Scientific Reports*, 11(1):4974.

Clayton, J. and McDowell, D. (2003). A multiscale multiplicative decomposition for elasto-plasticity of polycrystals. *International Journal of Plasticity*, 19(9):1401–1444.

Clifton, R. J. (1972). On the Equivalence of FeFp and FpFe. *Journal of Applied Mechanics*, 39(1):287–289.

Ewald, P. P. (1960). Max von laue, 1879-1960. *Biographical Memoirs of Fellows of the Royal Society*, 6:134–156.

Fu, X., Knudsen, E., Poulsen, H. F., Herman, G. T., Carvalho, B. M., and Liao, H. Y. (2006). Optimized algebraic reconstruction technique for generation of grain maps based on three-dimensional x-ray diffraction (3DXRD). *Optical Engineering*, 45(11):116501.

Gregg, A., Hendriks, J., Wensrich, C., and O'Dell, N. (2020). Radial basis functions and improved hyperparameter optimisation for gaussian process strain estimation. *Nuclear Instruments and Methods in Physics Research Section B: Beam Interactions with Materials and Atoms*, 480:67–77.

Hackenberger, B. K. (2019). Bayes or not bayes, is this the question? *Croatian medical journal*, 60(1):50–52.

Hayashi, Y., Hirose, Y., and Seno, Y. (2015). Polycrystal orientation mapping using scanning three-dimensional X-ray diffraction microscopy. *Journal of Applied Crystallography*, 48(4):1094–1101.

Hayashi, Y., Setoyama, D., Hirose, Y., Yoshida, T., and Kimura, H. (2019). Intragranular three-dimensional stress tensor fields in plastically deformed polycrystals. *Science*, 366(6472):1492–1496.

Hayashi, Y., Setoyama, D., and Seno, Y. (2017). Scanning three-dimensional x-ray diffraction microscopy with a high-energy microbeam at spring-8. *Materials Science Forum*, 905:157–164.

Hektor, J., Hall, S. A., Henningsson, N. A., Engqvist, J., Ristinmaa, M., Lenrick, F., and Wright, J. P. (2019). Scanning 3DXRD measurement of grain growth, stress, and formation of cu6sn5 around a tin whisker during heat treatment. *Materials*, 12(3).

Hendriks, J. N., Gregg, A. W. T., Jackson, R. R., Wensrich, C. M., Wills, A., Tremsin, A. S., Shinohara, T., Luzin, V., and Kirstein, O. (2019). Tomographic reconstruction of triaxial strain fields from bragg-edge neutron imaging. *Phys. Rev. Mater.*, 3:113803.

Henningsson, A. and Hall, S. A. (2023). *xrd_simulator*: 3D X-ray diffraction simulation software supporting 3D polycrystalline microstructure morphology descriptions. *Journal of Applied Crystallography*, 56(1):282–292.

Herausgeber (1952). Vor 40 jahren. *Naturwissenschaften*, 39(16):361–361.

Jiao, Y. and Fish, J. (2018). On the equivalence between the multiplicative hyper-elasto-plasticity and the additive hypo-elasto-plasticity based on the modified kinetic logarithmic stress rate. *Computer Methods in Applied Mechanics and Engineering*, 340:824–863.

Jidling, C., Wahlström, N., Wills, A., and Schön, T. B. (2017). Linearly constrained gaussian processes.

Kak, A. and Slaney, M. (2001). *Principles of Computerized Tomographic Imaging*. Classics in Applied Mathematics. Society for Industrial and Applied Mathematics.

Krige, D. (1951). A statistical approach to some basic mine valuation problems on the witwatersrand. *Journal of the Southern African Institute of Mining and Metallurgy*, 52(6):119–139.

Kröner, E. (1959). Allgemeine kontinuumstheorie der versetzungen und eigenspannungen. *Archive for Rational Mechanics and Analysis*, 4:273–334.

Lauridsen, E. M., Schmidt, S., Suter, R. M., and Poulsen, H. F. (2001). Tracking: a method for structural characterization of grains in powders or polycrystals. *Journal of Applied Crystallography*, 34(6):744–750.

Lee, E. H. and Liu, D. T. (1967). Finite-Strain Elastic—Plastic Theory with Application to Plane-Wave Analysis. *Journal of Applied Physics*, 38(1):19–27.

Li, W., Sharma, H., Peter, K., Ravi, S., Sehitoglu, H., and Bucsek, A. (2023). Resolving intragranular stress fields in plastically deformed titanium using point-focused high-energy diffraction microscopy. *Journal of Materials Research*, 38(1):165–178.

Lienert, U., Gutschmidt, S., v. Zimmermann, M., Nowak, R., and Drube, W. (2013). Beamline p21, technical design report. Technical report, PETRA III.

Liu, H. H., Schmidt, S., Poulsen, H. F., Godfrey, A., Liu, Z. Q., Sharon, J. A., and Huang, X. (2011). Three-dimensional orientation mapping in the transmission electron microscope. *Science*, 332(6031):833–834.

Majumdar, J. D., Gurevich, E. L., Kumari, R., and Ostendorf, A. (2016). Investigation on femto-second laser irradiation assisted shock peening of medium carbon (0.4 *Applied Surface Science*, 364:133–140.

Malinauskas, M., Žukauskas, A., Hasegawa, S., Hayasaki, Y., Mizeikis, V., Buividas, R., and Juodkazis, S. (2016). Ultrafast laser processing of materials: from science to industry. *Light: Science & Applications*, 5(8):e16133–e16133.

Mar Lucas, M., Ramos, T., Jørgensen, P. S., Canulescu, S., Kenesei, P., Wright, J., Poulsen, H. F., and Andreasen, J. W. (2021). Non-destructive determination of phase, size, and strain of individual grains in polycrystalline photovoltaic materials. *Journal of Alloys and Compounds*, 887:161364.

Margulies, L., Lorentzen, T., Poulsen, H., and Leffers, T. (2002). Strain tensor development in a single grain in the bulk of a polycrystal under loading. *Acta Materialia*, 50(7):1771 – 1779.

Markussen, T., Fu, X., Margulies, L., Lauridsen, E. M., Nielsen, S. F., Schmidt, S., and Poulsen, H. F. (2004). An algebraic algorithm for generation of three-dimensional grain maps based on diffraction with a wide beam of hard X-rays. *Journal of Applied Crystallography*, 37(1):96–102.

Nabarro, F. R. N. and Argon, A. S. (1995). Egon Orowan. 2 August 1902-3 August 1989. *Biographical Memoirs of Fellows of the Royal Society*, 41:317–340.

Natterer, F. (2001). *The Mathematics of Computerized Tomography.* Classics in Applied Mathematics. Society for Industrial and Applied Mathematics.

Oddershede, J., Schmidt, S., Poulsen, H. F., Sørensen, H. O., Wright, J., and Reimers, W. (2010). Determining grain resolved stresses in polycrystalline materials using three-dimensional X-ray diffraction. *Journal of Applied Crystallography*, 43(3):539–549.

Phillips, D. C. (1979). William lawrence bragg, 31 march 1890 - 1 july 1971. *Biographical Memoirs of Fellows of the Royal Society*, 25:74–143.

Poulsen, H. (2004a). *3DXRD – a new probe for materials science.* PhD thesis, DTU.

Poulsen, H. (2004b). *3DXRD – a new probe for materials science.* PhD thesis, Risø National Laboratory.

Poulsen, H. F. and Fu, X. (2003). Generation of grain maps by an algebraic reconstruction technique. *Journal of Applied Crystallography*, 36(4):1062–1068.

Poulsen, H. F., Nielsen, S. F., Lauridsen, E. M., Schmidt, S., Suter, R. M., Lienert, U., Margulies, L., Lorentzen, T., and Juul Jensen, D. (2001). Three-dimensional maps of grain boundaries and the stress state of individual grains in polycrystals and powders. *Journal of Applied Crystallography*, 34(6):751–756.

Poulsen, H. F. and Schmidt, S. (2003). Reconstruction of grain boundaries in polycrystals by filtered back-projection of diffraction spots. *Journal of Applied Crystallography*, 36(2):319–325.

Radon, J. (1986). On the determination of functions from their integral values along certain manifolds. *IEEE Transactions on Medical Imaging*, 5(4):170–176.

Rasmussen, C. E. (2003). Gaussian processes in machine learning. In *Summer School on Machine Learning*, pages 63–71. Springer.

Rubino, M., Etheridge, D., Thornton, D., Howden, R., Allison, C., Francey, R., Langenfelds, R., Steele, P., Trudinger, C., Spencer, D., Curran, M., van Ommen, T., and Smith, A. (2019). Revised records of atmospheric trace gases co2, ch4, n2o and δ^{13}c-co2 over the last 2000 years from law dome, antarctica. *Earth System Science Data*, 11:473–492.

Santisteban, J., Edwards, L., Fitzpatrick, M., Steuwer, A., Withers, P., Daymond, M., Johnson, M., Rhodes, N., and Schooneveld, E. (2002). Strain imaging by bragg edge neutron transmission. *Nuclear Instruments and Methods in Physics Research Section A: Accelerators, Spectrometers, Detectors and Associated Equipment*, 481(1):765–768.

Schmidt, S. (2014). *GrainSpotter*: a fast and robust polycrystalline indexing algorithm. *Journal of Applied Crystallography*, 47(1):276–284.

Sharma, H., Huizenga, R. M., and Offerman, S. E. (2012). A fast methodology to determine the characteristics of thousands of grains using three-dimensional X-ray diffraction. I. Overlapping diffraction peaks and parameters of the experimental setup. *Journal of Applied Crystallography*, 45(4):693–704.

Sørensen, H., Schmidt, S., Wright, J., Vaughan, G., Techert, S., Garman, E., Oddershede, J., Davaasambuu, J., Paithankar, K., Gundlach, C., and Poulsen, H. (2012). Multigrain crystallography. *Zeitschrift f"ur Kristallographie–Crystalline Materials*, 227(1):63–78.

Tadmor, E. B. and Miller, R. E. (2011). *Introduction*, page 1–18. Cambridge University Press.

Thakur, M. M., Henningsson, N. A., Engqvist, J., Autran, P.-O., Wright, J. P., and Hurley, R. C. (2023). On mesoscale modeling of concrete: Role of heterogeneities on local stresses, strains, and representative volume element. *Cement and Concrete Research*, 163:107031.

The Cambridge Structural Database (2019). Retrieved May 16, 2019.

Tondro, A. (2023). *Microstructure-informed modeling of hydrogen diffusion in zirconium polycrystals*. PhD thesis, Electronic Thesis and Dissertation Repository.

Tremsin, A. S., McPhate, J. B., Steuwer, A., Kockelmann, W., M Paradowska, A., Kelleher, J. F., Vallerga, J. V., Siegmund, O. H. W., and Feller, W. B. (2012). High-resolution strain mapping through time-of-flight neutron transmission diffraction with a microchannel plate neutron counting detector. *Strain*, 48(4):296–305.

Truesdell, C., Noll, W., Truesdell, C., and Noll, W. (1965). *The non-linear field theories of mechanics*. Springer.

van Aarle, W., Palenstijn, W. J., Cant, J., Janssens, E., Bleichrodt, F., Dabravolski, A., Beenhouwer, J. D., Batenburg, K. J., and Sijbers, J. (2016). Fast and flexible x-ray tomography using the astra toolbox. *Opt. Express*, 24(22):25129–25147.

van Aarle, W., Palenstijn, W. J., De Beenhouwer, J., Altantzis, T., Bals, S., Batenburg, K. J., and Sijbers, J. (2015). The astra toolbox: A platform for advanced algorithm development in electron tomography. *Ultramicroscopy*, 157:35–47.

Vestin, P. (2022). Estimation and interpretation of the intra-granular stress and strain evolution in a uniaxially loaded silica sample using scanning x-ray diffraction. Student Paper.

Willemink, M. J. and Noël, P. B. (2019). The evolution of image reconstruction for ct–from filtered back projection to artificial intelligence. *European Radiology*, 29(5):2185–2195.

Withers, P. J., Bouman, C., Carmignato, S., Cnudde, V., Grimaldi, D., Hagen, C. K., Maire, E., Manley, M., Du Plessis, A., and Stock, S. R. (2021). X-ray computed tomography. *Nature Reviews Methods Primers*, 1(1):18.

Wozniak, J. M., Sharma, H., Armstrong, T. G., Wilde, M., Almer, J. D., and Foster, I. (2014). Big data staging with mpi-io for interactive x-ray science. In *2014 IEEE/ACM International Symposium on Big Data Computing*, pages 26–34.

Wright, J., Giacobbe, C., and Majkut, M. (2020). New opportunities at the materials science beamline at esrf to exploit high energy nano-focus x-ray beams. *Current Opinion in Solid State and Materials Science*, 24(2):100818.

Yau, T.-L. and Annamalai, V. (2016). Corrosion of zirconium and its alloys. In *Reference Module in Materials Science and Materials Engineering*. Elsevier.

Paper A

Axel Henningsson, Stephen A. Hall, Jonathan P. Wright, Johan Hektor

Reconstructing intragranular strain fields in polycrystalline materials from scanning 3DXRD data

In: Journal of Applied Crystallography 53, 314–325. (2020)

JOURNAL OF APPLIED CRYSTALLOGRAPHY

ISSN 1600-5767

Reconstructing intragranular strain fields in polycrystalline materials from scanning 3DXRD data

N. Axel Henningsson,[a]* Stephen A. Hall,[a] Jonathan P. Wright[b] and Johan Hektor[c,d]

[a]Division of Solid Mechanics, Lund University, Box 118, 221 00 Lund, Sweden, [b]European Synchrotron Radiation Facility (ESRF), 71 Avenue des Martyrs, 38000 Grenoble, France, [c]Deutsches Elektronen-Synchrotron (DESY), Notkestrasse 85, 22607 Hamburg, Germany, and [d]Helmholtz-Zentrum Geesthacht, Notkestrasse 85, 22607 Hamburg, Germany. *Correspondence e-mail: axel.henningsson@solid.lth.se

Received 27 August 2019
Accepted 25 January 2020

Edited by A. Borbély, Ecole National Supérieure des Mines, Saint-Etienne, France

Keywords: intragranular strain; X-ray diffraction; 3DXRD; tomography.

Two methods for reconstructing intragranular strain fields are developed for scanning three-dimensional X-ray diffraction (3DXRD). The methods are compared with a third approach where voxels are reconstructed independently of their neighbours [Hayashi, Setoyama & Seno (2017). *Mater. Sci. Forum*, **905**, 157–164]. The 3D strain field of a tin grain, located within a sample of approximately 70 grains, is analysed and compared across reconstruction methods. Implicit assumptions of sub-problem independence, made in the independent voxel reconstruction method, are demonstrated to introduce bias and reduce reconstruction accuracy. It is verified that the two proposed methods remedy these problems by taking the spatial properties of the inverse problem into account. Improvements in reconstruction quality achieved by the two proposed methods are further supported by reconstructions using synthetic diffraction data.

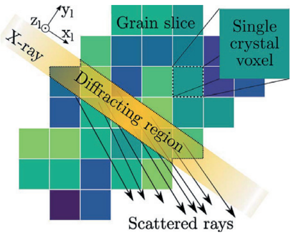

1. Introduction

Modern synchrotrons provide X-ray beams of sufficiently high brilliance to enable the study of granular and inter-granular phenomena in dense polycrystalline materials. Relying on the use of parallel and monochromatic X-rays, Poulsen (2004) and co-workers developed three-dimensional X-ray diffraction (3DXRD). The 3DXRD technique provides a nondestructive way of studying polycrystalline materials on a grain-by-grain basis. Since then, the method has been refined and adopted in several synchrotron facilities across the globe.

In 3DXRD, to avoid diffraction spot overlap, the beam cross section can be reduced, thus limiting the number of simultaneously illuminated grains. The sample must then be rotated and translated to multiple positions to cover a full volume, a procedure which is sometimes known under the name of scanning 3DXRD (Hayashi *et al.*, 2015). If the beam cross section is small enough, diffraction originating from sub-parts of grains is measured. This opens up the possibility to reconstruct intragranular variations in the crystal structure.

For near-field 3DXRD measurements, using a line beam, suggestions on intragranular orientation reconstructions were first put forth by Rodek *et al.* (2007), as an extension to previous work on discrete grain mapping (Alpers *et al.*, 2006). The method was refined by Kulshreshth *et al.* (2009) to provide access to the intragranular orientation map on a per-voxel basis. None of this work, however, considers intragranular strain, and although it is well known that grain average strain can be determined from far-field 3DXRD measurements, only recently has scanning 3DXRD been used to retrieve intragranular strain variations (Hayashi *et al.*, 2017; Hektor *et al.*, 2019). The work of Hayashi *et al.* (2017) is the first suggestion on how to perform the reconstruction of intragranular strain variations from far-field measurements. The method refines the crystal structure at every point by fitting the orientation and lattice parameters of a single crystal to the subset of reflections that illuminate the point. However, several problems exist with this approach; we have found it may produce artefacts related to both strain state and grain orientation (Henningsson, 2019).

It has also been suggested, in the case of powder diffraction, that the full strain tensor can be retrieved using filtered back projection with a sufficient number of measurement directions (Lionheart & Withers, 2015). Similar ideas could, perhaps, be applied to scanning 3DXRD, which measures discrete diffraction events rather than powder rings. If the full strain tensor is to be retrieved via back projection, it would seem that rotations about several different axes are necessary. The time constraints, which are already severe for 3D scanning methods, make such a technique unfeasible. Instead, this paper explores reconstruction techniques that utilize information gathered from rotations about a single axis. As pointed out by Hendriks *et al.* (2019), the information gathered from rotations about a single axis might be enough to accurately reconstruct the strain distribution. We will present two methods that are capable of reconstructing an intragranular strain tensor field from scanning 3DXRD data. We compare our results with an implementation of the approach suggested by Hayashi *et al.* (2017) and show how our developments improve the quality of the reconstruction.

Sections 2 and 3 describe the experimental setup and data preprocessing. The frameworks for all three reconstruction approaches are then presented in sections 4, 5 and 6. Reconstructions of the 3D strain field present in a columnar Sn grain embedded in a polycrystalline sample [data originating from the study of Hektor *et al.* (2019)], together with reconstructions from synthetic diffraction data and error analysis, are presented in Section 7. Finally, the results and their implications are discussed in Section 8.

2. Experimental setup

For scanning 3DXRD, a sample is mounted on an ω turntable that carries a rigidly attached sample coordinate system, subscripted ω (Fig. 1).

The sample coordinate system is associated with a laboratory coordinate system, subscripted l, which serves as a fixed reference point in all measurements. Both of these coordinate systems are Cartesian, and the $x_{\rm l}$ axis is taken as parallel with the incident X-ray beam. During acquisition, the turntable holding the sample is free to rotate around the z_ω axis and to translate along the fixed transverse beam directions $y_{\rm l}$ and $z_{\rm l}$. For alignment, the turntable has the freedom to translate in three dimensions, $(x_{\rm l}, y_{\rm l}, z_{\rm l})$, as well as to rotate around each of the three axes $(x_\omega, y_\omega, z_\omega)$. Initially, when no motors of the turntable have been used, the laboratory and sample coordinate systems are by definition aligned. As the detector, situated a distance D from the sample, will in general not be mounted perfectly perpendicular to the incoming X-ray beam, an initial calibration of detector tilt and distance is needed. The detector tilt in relation to $y_{\rm l}$ and z_ω, as well as the wedge angle between $z_{\rm l}$ and w_ω, was calibrated following the procedure described in the documentation of the software package *ImageD11* (Wright, 2005). For further discussion see *e.g.* Oddershede *et al.* (2010) and Borbely *et al.* (2014). The intersection between beam centre and detector forms the origin of the 2D Cartesian coordinate system $y_{\rm d}$–$z_{\rm d}$. The relation between a vector, $\mathbf{v}$, in the laboratory coordinate system and in the sample system now becomes

$$\mathbf{v}_{\rm l} = \boldsymbol{\Omega}\mathbf{v}_\omega = \begin{bmatrix} \cos(\omega) & -\sin(\omega) & 0 \\ \sin(\omega) & \cos(\omega) & 0 \\ 0 & 0 & 1 \end{bmatrix} \mathbf{v}_\omega. \qquad (1)$$

Defining η as the azimuthal angle measured from $z_{\rm d}$ to a considered diffraction peak, the geometry of Fig. 1 gives the scattering vector, $\mathbf{G}_{\rm l}$, in the laboratory frame as

$$\mathbf{G}_{\rm l} = \frac{2\pi}{\lambda} \begin{bmatrix} \cos(2\theta) - 1 \\ -\sin(2\theta)\sin(\eta) \\ \sin(2\theta)\cos(\eta) \end{bmatrix}, \qquad (2)$$

where λ is the X-ray wavelength and θ the Bragg scattering angle. On the basis of the conventions of Busing & Levy (1967) together with the modified definitions given by Lauridsen *et al.* (2001), the transformation of a scattering vector from reciprocal space, subscripted *hkl*, to the laboratory frame is

$$\mathbf{G}_{\rm l} = \boldsymbol{\Omega}\,\mathbf{UB}\,\mathbf{G}_{hkl}, \qquad (3)$$

where the columns of the **UB** matrix are the reciprocal space lattice vectors. Note that in equation (3), in contrast to Lauridsen *et al.* (2001), we refer here to a point within a grain rather than the grain average properties, similarly to the work of Alpers *et al.* (2006). Furthermore, to avoid confusion, it should be noted that, in the work of Lauridsen *et al.* (2001), an additional coordinate system is used, allowing the sample coordinate system to not be aligned with the ω coordinate system. In our formulation, however, we have taken these coordinate systems to be aligned, and thus the ω system and sample system are one and the same thing. Naturally, the

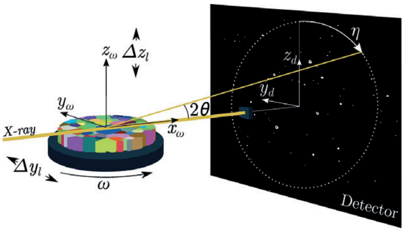

Figure 1
Experimental setup of scanning 3DXRD. The ω turntable holding the sample is rotated around z_ω and translated in the fixed $y_{\rm l}z_{\rm l}$ plane during acquisition.

choice of coordinate systems is arbitrary, as long as the transformation operation into the laboratory system is known.

To acquire information on an intragranular length scale the X-ray beam must not illuminate the entire grain during diffraction. The spatial resolution will be limited by the X-ray beam size and the number of different angular projections that can be recorded. To collect data from the entire volume of interest, the turntable, which holds the sample, is translated across the X-ray beam. This means that the rotation axis, z_ω, is given a new position in relation to the laboratory coordinate system. At each position the sample is rotated continuously about the z_ω axis and images are integrated and read out every $\mathrm{d}\omega$ degrees. The recorded 2D diffraction pattern at each y_l, z_l, ω setting is the integrated intensity measured over the step length, $\mathrm{d}\omega$. In the following we refer to the collection of frames taken over a range of ω but at a single y_l, z_l setting as a 'frame-stack'. A point in the frame-stack is defined either by the three diffraction angles (η, θ, ω) of Fig. 1 or by use of the detector plane coordinates (y_d, z_d, ω). The dimensionality of the complete data set is 5D (sample stage position y_l, z_l, ω and diffraction angles η, θ).

3. Data preprocessing

Before strain reconstruction can take place, the 2D diffraction patterns need to be processed to determine the average properties of the grains. The following four steps of analysis summarize the preprocessing:

(1) Image processing: spatial corrections, background subtraction, thresholding and peak centre-of-mass extraction.

(2) Calibration of experimental geometry and determination of scattering vectors **G**.

(3) Peak/grain indexing.

(4) Grain shape reconstruction.

Because the experimental data originated from a FReLoN4M detector, spatial corrections are necessary. These were performed using a dedicated lookup table provided by the ESRF ID11 beamline [see Borbely *et al.* (2014) for further discussion]. Background correction was then performed, for each frame-stack, on a per-pixel basis, such that for each individual pixel the minimum intensity recorded by the pixel, throughout the frame-stack, was subtracted.

To calculate peak centre-of-mass coordinates, the frame-stack was thresholded and analysed as a volume. Each diffraction peak was extended to a 3D object and assigned the y_d, z_d, ω coordinates of the centre of mass of the 3D intensity distribution. Scattering vectors and Bragg angles can be deduced from the peak centre of mass, after calibration of the experimental setup.

Peak/grain indexing is the procedure to find a set of crystallographic orientations, strains and grain centroid positions that together can correctly account for the observed diffraction data. Grains were indexed using the indexing algorithm in *ImageD11*. To fit an average set of unit-cell parameters to individual grains, methods analogous to those of Oddershede *et al.* (2010) and Edmiston *et al.* (2011) were used.

There are several ways to reconstruct the grain shapes from the diffraction data. In this paper we have used filtered back projection, as described by Poulsen & Schmidt (2003). The sample volume is reconstructed by computing one slice in z_l at a time and forming, for each grain, a sinogram of diffracted intensities. The inverse Radon transform of the sinogram provides an approximation of the grain shapes and location in the slice. To define grain boundaries, each grain shape was thresholded using a threshold proportional to the most intense voxel within the grain. Overlap between grains was resolved by selecting the grain with the highest intensity at each conflict voxel as the occupant of that voxel. Note that discrete reconstruction methods could provide higher-quality grain maps (*cf*. Alpers *et al.*, 2006; Rodek *et al.*, 2007; Kulshreshth *et al.*, 2009). In this paper, however, we had access to a high number of reflections per grain (>100), and thus the filtered back projection approach performed satisfactorily.

In summary, after preprocessing the diffraction data, we are left with

(1) a list of peak positions (y_d, z_d, ω) with corresponding sample stage (y_l, z_l) settings;

(2) a list of grain average orientations and strains;

(3) a mapping of diffraction peaks to grains;

(4) a voxelated volume describing the grain shapes.

Assuming that the above quantities are available, we proceed, in sections 4–6, to describe three methods for intragranular strain reconstruction. Each of these methods relies on the minimization of a cost function. The starting guess in the minimization procedure is taken as the grain average properties emerging from the preprocessing steps described above.

4. Single-crystal refinement (SCR)

It has previously been suggested by Hayashi *et al.* (2017) that the lattice state at a point $\mathbf{P} = (x_\omega, y_\omega, z_\omega)$ within a grain can be approximated by refining the lattice parameters with respect to the subset of diffraction peaks which intersect **P**. The sample stage translation, Δy_l, that will ensure that **P** is illuminated at a given ω is found via rotation around the z_ω axis:

$$\Delta y_\mathrm{l}(\omega) = x_\omega \sin(\omega) + y_\omega \cos(\omega). \qquad (4)$$

By use of equation (4) the subset of measured diffraction peaks that include scattering from **P** can be extracted. Forward-modelled peak positions, produced using a single-crystal scattering model, are then fitted to the measured peak centre-of-mass coordinates. The resulting lattice orientation and strain tensor are assigned to point **P**.

For a given lattice orientation (**U**), unit cell (**B**) and Miller plane ($\mathbf{G}_{hkl}$), the resulting forward-modelled peak position, expressed in terms of the angles η, θ, ω, is found by combining equations (2) and (3).

In this paper we implement the above concepts, introducing weights to the errors formed between observed and modelled peak positions. The weighted errors ($\Delta\eta$, $\Delta\theta$, $\Delta\omega$) are taken as

$$\Delta\omega = W_\omega(\omega_\mathrm{o} - \omega_\mathrm{m}) \quad \text{where} \quad W_\omega = 2/\mathrm{d}\omega, \tag{5}$$

$$\Delta\theta = W_{2\theta}(2\theta_\mathrm{o} - 2\theta_\mathrm{m}) \quad \text{where} \quad W_{2\theta} = D/s_\mathrm{pix}, \tag{6}$$

$$\Delta\eta = W_\eta(\eta_\mathrm{o} - \eta_\mathrm{m}) \quad \text{where} \quad W_\eta = W_{2\theta}\tan 2\theta. \tag{7}$$

The subscripts o and m stand for observed and modelled, respectively, D is the detector-to-sample distance, and s_pix is the detector pixel size. Note that weighting is essential to account for the experimental resolution being variable with the Bragg angle, θ, and dependent on the selected step size $\mathrm{d}\omega$.

We assign to **P** the **UB** matrix [equation (3)] that minimizes the cost function

$$\mathcal{S} = \sum_{i=1}^{K}(\Delta\omega_i^2 + \Delta\theta_i^2 + \Delta\eta_i^2). \tag{8}$$

The sum is here taken over all reflections, K, that were assigned to **P** via equation (4). From the resulting optimal **UB** matrix, strain can be computed, given some reference lattice parameters that define a relaxed unit cell.

The minimization of (8) was performed using a least-squares algorithm provided in the Python library SciPy (Jones *et al.*, 2001). The implementation was based on the *ImageD11* software and can be found at (https://github.com/FABLE-3DXRD/S3DXRD).

The full strain tensor field is retrieved by repeating the single-crystal refinement procedure for all points on a uniform grid with spacing equal to the beam width. As pointed out by Hayashi *et al.* (2015), the best possible spatial resolution of this approach is limited by double the beam width. This is apparent by considering that equation (4) is fulfilled as long as any part of the beam intersects **P**.

4.1. Inaccuracy and bias

The key assumption in SCR is that measurements of single points within the volume of a grain can be made. An observed diffraction peak is, however, the result of a volume integral taken over the region of the grain intersected by the beam. The properties of a diffraction peak (η, θ, ω) are therefore average properties, measured over a sub-volume of the grain. In fact, the reconstruction of strain and lattice orientation is a tomography problem, and in general the solution to a ray transform cannot be replaced by a point-by-point fit. By neglecting this fact, SCR will introduce a bias in the reconstructed lattice. Letting the operator $\mathcal{L}$ map from the combined strain-orientation field, $\mathbf{f}(\mathbf{x})$, to measurements, and letting V denote the volume of an integration region $\mathcal{R}$, we illustrate the problem in Fig. 2.

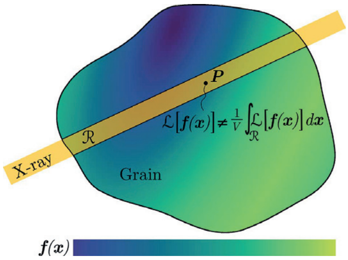

Figure 2
X-ray measurement from a region $\mathcal{R}$ in a grain experiencing a non-uniform vector field, $\mathbf{f}(\mathbf{x})$, of strain and lattice orientation (illustrated by colour variation). The measured signal from $\mathcal{R}$ is related to the integral over the intersected region $\mathcal{R}$, which in general is different from the state at point **P**.

When integration is performed over an illuminated region, the difference between a point measurement, $\mathcal{L}[\mathbf{f}(\mathbf{P})]$, and the integrated value, $(1/V)\int_{\mathcal{R}}\mathcal{L}[\mathbf{f}(\mathbf{P})]\,\mathrm{d}\mathbf{x}$, will naturally depend on the distribution of the integrated field. In the case where the integrated field is uniform over the illuminated region, the difference will be zero. If, however, the field varies over the illuminated region, the difference will in general not be zero. If $\mathbf{f}(\mathbf{x})$ displays sharp features, these will be especially difficult to capture. Likewise, if gradients are present, their magnitudes will in general be reduced, and this damping will be some complicated function of $\mathbf{f}(\mathbf{x})$ and the distribution of measurements. As we will demonstrate through simulations later (Section 7), the magnitude of these errors can be severe, which motivates the development of new reconstruction methods that respect the tomographic nature of the problem in hand.

5. Polycrystal refinement (PCR)

To remedy the bias of SCR, we seek to formulate a reconstruction method that takes the spatial variation across the grain into account. We propose to discard equation (4) and instead consider all points of the grain simultaneously. This is made possible by modelling diffraction not from one single crystal but from a set of single crystals, similarly to the approach developed by Rodek *et al.* (2007). Each crystal is made to occupy a discrete voxel within the grain, as illustrated in Fig. 3.

For a given y_l, z_l, ω setting, all voxels within the grain slice intersected by the beam take part in diffraction. Scattering vectors are assigned using equation (3) and propagated to the detector plane, resulting in clusters of predicted single-crystal diffraction peaks. To form a peak centre-of-mass coordinate

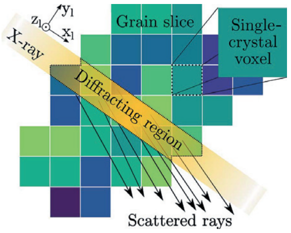

Figure 3
Diffraction is modelled as a set of cubic single crystals. Each crystal carries an independent lattice orientation and strain tensor (illustrated as colour variation).

from the clustered, simulated, diffraction peaks, the scattered intensities must be taken into account. The intensity scattered from a single crystal is, in general, a function of several variables. However, as the peak centre of mass is sought, only the intensity variation within the peak need be captured. The volume formed by the intersection of beam and voxel is proportional to the number of illuminated unit cells of the single crystal, which in turn is believed to be what dominates intensity variation within a single peak. Using the volume fractions as intensity weights, each peak cluster can be converted to a peak position, ($y_{\rm d}$, $z_{\rm d}$, ω). More details on the forward model are provided by Henningsson (2019).

Similarly to SCR, the cost function must be a measure of the mismatch between the observed and modelled diffraction data. Using the Euclidean norm of the peak centre-of-mass coordinates we take the cost as

$$\mathcal{P} = \tfrac{1}{2}\sum_{j=1}^{M}(\Delta y_{{\rm d}j}^2 + \Delta z_{{\rm d}j}^2 + \Delta\omega_j^2), \tag{9}$$

where $\Delta y_{\rm d}$, $\Delta z_{\rm d}$ and $\Delta\omega$ are the differences between observed and modelled peak positions expressed in units of pixels and rotation step lengths, dω, respectively. The sum in equation (9) ranges over M, defined as the total number of observed diffraction peaks of the grain. Notice that no weights with respect to detector position are necessary in (9), as the involved quantities are expressed in units of pixels and rotation step lengths. Instead, in this formulation the modelled and measured diffraction patterns are compared directly using the in-plane detector variables $y_{\rm d}$ and $z_{\rm d}$ together with the normalized rotation angle $\omega/{\rm d}\omega$. Therefore, no discrimination should be made, but all modelled peaks should be considered to fit equally well to the data, as the weighting is already built in to the forward model. Naturally, other factors might also be considered to be included in the weighting, such as photon counts and peak shapes (*cf.* Edmiston *et al.*, 2011). However, in this work, weighting has been limited to detector positions of the diffraction peaks.

The orientation and strain tensor of each single-crystal voxel composing the reconstructed grain slice is found by minimizing the cost function $\mathcal{P}$. The minimization could be done with respect to Euler angles and lattice parameters, the nine components of the **UB** matrix, or Euler angles and the six strain tensor components. In this paper we used the Euler angles and the six strain tensor components. We emphasize that in PCR, like in SCR, the Jacobian of the cost function is determined numerically and the inverse problem is solved by iterative forward modelling. The computational effort of finding the Jacobian can be greatly reduced by using a kinematic approximation such that each voxel scatters independently of its neighbours. This means that the derivative of $\mathcal{P}$ with respect to a single variable, x, can be deduced from the current model by replacing only the scattered rays of the voxel affected by the perturbation in x. Here the cost (9) was minimized using a standard steepest-descent method (Barzilai & Borwein, 1988) together with a three-point finite difference scheme.

6. Algebraic strain refinement (ASR)

Polycrystal refinement succeeds in accounting for the spatial dependency of the inverse problem. However, the computational efficiency and complexity of implementation can be improved. Especially desirable would be an easy and efficient implementation of constraints to suppress high-frequency variations in the strain tensor field, emerging from the minimization of equation (9). Such a regularization incorporates the assumption that the strain at a point in the grain is highly correlated to the strain at neighbouring points. To formulate such a method, we drop the concept of a forward model, and instead we seek to find a linear system of equations that will fit a discretized strain-orientation field to diffraction data directly.

In the pursuit of grain average properties, Poulsen *et al.* (2001) suggested that equation (3) could be used to simultaneously fit strain and orientation for a single grain. In scanning 3DXRD, each measurement provides information on the average scattering vector, $\bar{\mathbf{G}}_\omega$, in the region of the grain illuminated by the beam. To accommodate a matrix formulation, linear in the components of the **UB** matrix, we recast equation (3) as

$$\mathbf{G}_\omega = \mathbf{UB}\,\mathbf{G}_{hkl} = \mathbf{ho}, \tag{10}$$

where **h** is a 3 × 9 matrix containing the Miller indices (h, k, l) and **o** is a 9 × 1 vector that holds the components of the **UB** matrix, UB_{ij}, *i.e.*

$$\mathbf{h} = \begin{pmatrix} h & 0 & 0 \\ k & 0 & 0 \\ l & 0 & 0 \\ 0 & h & 0 \\ 0 & k & 0 \\ 0 & l & 0 \\ 0 & 0 & h \\ 0 & 0 & k \\ 0 & 0 & l \end{pmatrix}^{\rm T}, \quad \mathbf{o} = \begin{pmatrix} UB_{11} \\ UB_{12} \\ UB_{13} \\ UB_{21} \\ UB_{22} \\ UB_{23} \\ UB_{31} \\ UB_{32} \\ UB_{33} \end{pmatrix}^{\rm T}. \tag{11}$$

Let us now consider an illuminated region, $\mathcal{R}$, formed by the intersection between beam and grain. Assuming that all points in $\mathcal{R}$ scatter in the rotation interval dω, the average scattering vector becomes

$$\bar{\mathbf{G}}_\omega = (1/V_{\rm tot})\int_{\mathcal{R}} \mathbf{ho}(x_\omega, y_\omega, z_\omega)\,{\rm d}x_\omega\,{\rm d}y_\omega\,{\rm d}z_\omega, \tag{12}$$

where

$$V_{\rm tot} = \int_{\mathcal{R}} {\rm d}x_\omega\,{\rm d}y_\omega\,{\rm d}z_\omega \tag{13}$$

and **o** is allowed to vary in $\mathcal{R}$. Discretizing the grain into voxels and approximating **o** as constant over each voxel, equation (12) gives

$$\bar{\mathbf{G}}_\omega \simeq (1/V_{\rm tot})\sum_{i=1}^{N} V_i\mathbf{ho}_i, \tag{14}$$

where N is the number of voxels and V_i the volume of intersection between $\mathcal{R}$ and voxel number i. If all observed scattering vectors of a grain are considered simultaneously, a matrix formulation is achieved:

$$\underbrace{\mathbf{H}}_{3M\times 9N}\underbrace{\mathbf{u}}_{9N\times 1}=\underbrace{\mathbf{g}}_{3M\times 1}, \tag{15}$$

where

$$\mathbf{H}=\begin{bmatrix}(V_1/V^1_{\rm tot})\mathbf{h}^1 & \cdots & (V_N/V^1_{\rm tot})\mathbf{h}^1\\ \vdots & \ddots & \vdots\\ (V_1/V^M_{\rm tot})\mathbf{h}^M & \cdots & (V_N/V^M_{\rm tot})\mathbf{h}^M\end{bmatrix},$$
$$\mathbf{u}=\begin{pmatrix}\mathbf{o}_1\\ \vdots\\ \mathbf{o}_N\end{pmatrix},\quad \mathbf{g}=\begin{pmatrix}\bar{\mathbf{G}}^1_\omega\\ \vdots\\ \bar{\mathbf{G}}^M_\omega\end{pmatrix}, \tag{16}$$

and the total number of measured scattering vectors is M. By solving equation (15) in a least-squares sense, the orientation and strain state of the grain can be retrieved. Before doing so, however, the incorporation of weights to account for variable experimental resolution is needed. Additionally, some constraint of smoothness to the strain is required. These seem possible to derive and impose, but not trivial to implement. If the constraints are to be formulated in terms of absolute smoothness of strain, the conversion into $\mathbf{o}$ makes them nonlinear. Although methods for solving such problems exist, they seem to scale poorly with the number of unknowns unless the derivatives of the constraints can be provided analytically. Therefore we choose a simpler formulation, where the matrix equation is linear in the strain tensor components directly. This is possible by converting the peak centre-of-mass coordinates into average strain measurements.

6.1. Peak position to average strain

As pointed out by Poulsen *et al.* (2001) and Margulies *et al.* (2002), for hard X-rays and small Bragg angles the strain associated with a reflection is well approximated by

$$\bar{\varepsilon}_{\rm m}=\frac{\sin(\theta_{\rm r})-\sin(\theta_{\rm m})}{\sin(\theta_{\rm m})}, \tag{17}$$

where $\theta_{\rm m}$ is the measured angle of diffraction and $\theta_{\rm r}$ is the corresponding angle of diffraction expected for a relaxed reference state. The scalar measured strain, $\bar{\varepsilon}_{\rm m}$, is an average property of the region $\mathcal{R}$, and as explained by Lionheart & Withers (2015), it exists in the direction perpendicular to the diffracting Miller planes.

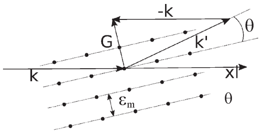

Figure 4
Bragg scattering from a 2D lattice. The direction in which the average strain $\bar{\varepsilon}_{\rm m}$ exists is parallel to $\mathbf{G}_{\rm l}$.

Considering the definition of the scattering vector, $\mathbf{G}_l=\mathbf{s}-\mathbf{s}_0$, illustrated in Fig. 4, a unit vector, $\bar{\mathbf{n}}_\omega$, in the strain direction is given as

$$\bar{\mathbf{n}}_\omega=\mathbf{\Omega}^{\rm T}\mathbf{G}_{\rm l}/\|\mathbf{G}_{\rm l}\|. \tag{18}$$

Using equations (17) and (18), each measured peak position can be converted to a corresponding average strain, $\bar{\varepsilon}_{\rm m}$, and average strain direction, $\bar{\mathbf{n}}_\omega$. Considering multiple measurements from a single grain, the strain tensor can be deduced from the two quantities $(\bar{\varepsilon}_m, \bar{\mathbf{n}}_\omega)$, as laid out by Poulsen *et al.* (2001) and Margulies *et al.* (2002). In their original work, part of the strain tensor was retrieved as a grain average property. Here, we seek to extend these concepts to the scanning 3DXRD case and compute the full strain tensor field, as it varies spatially within a grain.

6.2. Matrix formulation

In analogy with equation (12), we have

$$\bar{\varepsilon}_{\rm m}=(1/V_{\rm tot})\int\limits_{\mathcal{R}}\bar{\mathbf{n}}^{\rm T}_\omega\mathbf{E}_\omega\bar{\mathbf{n}}_\omega\,{\rm d}x_\omega\,{\rm d}y_\omega\,{\rm d}z_\omega, \tag{19}$$

where $\mathbf{E}_\omega$ is the strain tensor at point $(x_\omega, y_\omega, z_\omega)$ given in the ω coordinate system. The discrete form becomes

$$\bar{\varepsilon}_{\rm m}\simeq(1/V_{\rm tot})\sum_{i=1}^{N}V_i\bar{\mathbf{n}}^{\rm T}_\omega\mathbf{E}_i\bar{\mathbf{n}}_\omega. \tag{20}$$

Considering all measured scattering vectors of a grain we can introduce a projection matrix, $\mathbf{A}$, that projects a given strain tensor field, specified by the vector $\mathbf{s}$, into average strain measurements, $\bar{\varepsilon}_{\rm m}$. If the measured average strains are stored in the vector $\mathbf{m}$, we seek the solution, $\mathbf{s}$, to the linear equation system

$$\underbrace{\mathbf{A}}_{M\times 6N}\underbrace{\mathbf{s}}_{6N\times 1}=\underbrace{\mathbf{m}}_{M\times 1}. \tag{21}$$

Explicitly, the matrices $\mathbf{A}$, $\mathbf{s}$ and $\mathbf{m}$ take the form

$$\mathbf{A}=\begin{bmatrix}(V^1_1/V^1_{\rm tot})\mathbf{a}^1 & \cdots & (V^1_N/V^1_{\rm tot})\mathbf{a}^1\\ \vdots & \ddots & \vdots\\ (V^M_1/V^M_{\rm tot})\mathbf{a}^M & \cdots & (V^M_N/V^M_{\rm tot})\mathbf{a}^M\end{bmatrix},$$
$$\mathbf{s}=\begin{pmatrix}\boldsymbol{\epsilon}_1\\ \vdots\\ \boldsymbol{\epsilon}_N\end{pmatrix},\quad \mathbf{m}=\begin{pmatrix}\bar{\varepsilon}_1\\ \vdots\\ \bar{\varepsilon}_M\end{pmatrix}, \tag{22}$$

where $\mathbf{a}$ contains the components of the strain direction $\bar{\mathbf{n}}_\omega$ as

$$\mathbf{a}=\begin{pmatrix}n_1^2 & n_2^2 & n_3^2 & 2n_2n_3 & 2n_1n_3 & 2n_1n_2\end{pmatrix} \tag{23}$$

and $\boldsymbol{\epsilon}$ contains the six independent strain components of a voxel in Voigt notation:

$$\boldsymbol{\epsilon}=\begin{pmatrix}E_{11} & E_{22} & E_{33} & E_{23} & E_{13} & E_{12}\end{pmatrix}^{\rm T}. \tag{24}$$

6.3. Weighting

Since equation (21) is formulated in terms of average strain, which is a function of diffraction angle θ, the weights should be related to the measurement uncertainty in θ. For a given measurement we choose here the weight, w, as

$$w = \left(\Delta r \frac{\partial \bar{\varepsilon}_{\rm m}}{\partial r}\right)^{-1}, \tag{25}$$

where Δr is the measurement uncertainty in the radial direction of the detector, r, and $\partial \bar{\varepsilon}_{\rm m}/\partial r$ can be found numerically from equation (17). The value of Δr can be extracted from peak-by-peak fits (Edmiston *et al.*, 2011). In the specific cases presented in this paper, we make a simplification and assume a constant value $\Delta r = 0.1$ pixels (Borbely *et al.*, 2014). This is motivated by a low-angle approximation for high-energy diffraction. In the work presented here, the maximum angle of diffraction was $2\theta = 16^\circ$. The constant value selected for Δr will have no impact on the weighted solution to the problem. However, if one seeks to evaluate the fit quality of computed strains, $\mathbf{s}$, to data, $\mathbf{m}$, a selection of Δr is necessary to indicate the error margin of the measurements.

In matrix format we now have

$$\mathbf{wAs} = \mathbf{wm}, \tag{26}$$

where $\mathbf{w}$ is a diagonal matrix holding the weights.

6.4. Constraints

If the least-squares solution to (26) is sought, the corresponding cost function could be formulated as

$$\mathcal{A} = \tfrac{1}{2}||\mathbf{wAs} - \mathbf{wm}||_2^2, \tag{27}$$

where $||\cdot||_2$ is the Euclidean norm. We formulate the desired smoothness constraint for each component of strain, E_{ij}, as

$$b_1 \leq \Delta E_{ij}(x_\omega, y_\omega, z_\omega) \leq b_2, \tag{28}$$

where $\Delta E_{ij}(x_\omega, y_\omega, z_\omega)$ is the difference in strain between two neighbouring voxels. The fixed bounds b_1 and b_2 provide a lower and upper bound, respectively, and therefore regulate the maximum change in strain between two voxels. Neighbours are here defined as two voxels in a grain slice that share at least one corner point. The minimization of (27) under the constraint of (28) can be performed in several ways. Here, we have used a trust-region algorithm described by Byrd *et al.* (1999) and implemented in the Python library SciPy. Whatever iterative scheme is deployed, it is emphasized that both the Jacobian and the Hessian of the problem are known analytically, something which simplifies the minimization of equation (27).

7. Results

The strain state of a columnar tin (Sn) grain was reconstructed with the presented methods: SCR, PCR and ASR. The diffraction data originated from the experiment described by Hektor *et al.* (2019) and were collected at the nanostation of the ESRF ID11 synchrotron beamline. The grain selected for reconstruction (Fig. 5) was chosen because it exhibited a strain gradient, found in previous work using the SCR method. In principle, there is no hindrance to performing reconstructions for full sample volumes, featuring many grains. However, the focus of this article is to validate the theory and approximations underlying the presented reconstruction methods. For further practical applications the implementations should be optimized, and we note that when reconstructing many grains simultaneously all three methods are easily run in parallel.

Table 1
Experimental parameters.

Wavelength	0.22 Å
Sample-to-detector distance	163 mm
Dectector pixel size	50 × 50 µm
Detector dimensions	2048 × 2048 pixels
Beam size	0.25 × 0.25 µm
ω rotation interval	[0°, 180°]
ω step length	1°

Relevant experimental parameters can be found in Table 1.

Preprocessing of the diffraction data was performed primarily using the *FABLE* software suite (Sørensen *et al.*, 2012). The grain shapes were deduced using filtered back projection as discussed in Section 3. Implementation of the back projection is available at https://github.com/FABLE-3DXRD/S3DXRD, together with implementations of the three reconstruction algorithms.

Owing to time constraints, the experiment was performed with a step size of 0.5 µm in z, which is to be compared with the beam size of 0.25 µm. Linear interpolation between reconstructed slices has thus been performed in the presentation of 3D strain fields. Further specifics regarding the sample preparation, background of the experiment and diffraction data preprocessing are given by Hektor *et al.* (2019).

As strain is a measure of relative displacement, a reference configuration must be selected. Here we have used the lattice parameters of Table 2 to define a relaxed Sn unit cell. These

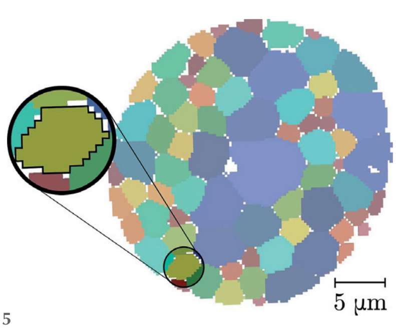

Figure 5
Sample cross section at $z = 0$ of the sample scanned by Hektor *et al.* (2019), produced via filtered back projection. The grains are randomly coloured by index, with the grain selected for strain reconstruction highlighted. The voxel dimension is 0.25 × 0.25 × 0.25 µm.

Table 2
Relaxed reference lattice parameters.

a	b	c	α	β	γ
5.81127 Å	5.81127 Å	3.17320 Å	90.0°	90.0°	90.0°

parameters represent the sample average lattice parameters, calibrated during grain indexing using the *ImageD11* software.

All strain fields presented in this paper are given in the ω coordinate system. In ASR, the constraint imposed on the strain difference, ΔE_{ij}, between two neighbouring voxels was taken as

$$|\Delta E_{ij}| < 5 \times 10^{-4}. \qquad (29)$$

The resulting reconstructions of the selected grain are presented in Fig. 6.

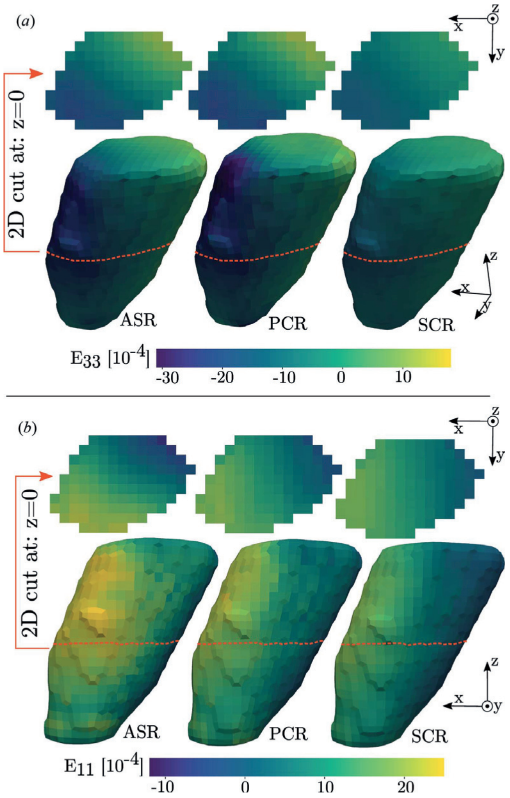

Figure 6
Reconstruction of axial strain tensor components, E_{33} in (*a*) and E_{11} in (*b*), for a tin grain. The result is seen to vary with reconstruction method from left to right. A smoothing filter has been applied to the topology of the 3D grain surface for visualization purposes. Two-dimensional cross sections, at z = 0, are illustrated, with the method varying from left to right.

The agreement between the reconstructions provides important information on the accuracy of the methods. A set of residual fields are introduced to illustrate this. These are defined as the difference in reconstructed strain fields between the three methods. Three such fields can be formed, subtracting the results of SCR from the results of ASR and PCR, and the results of PCR from those of ASR. The Euclidean norms of these residual fields are presented in Fig. 7 and provide an overview measure of agreement between the three methods.

Regarding ASR, the fit of the solution, **s**, to measurements, **m**, can be evaluated by analysing individual diffraction peaks.

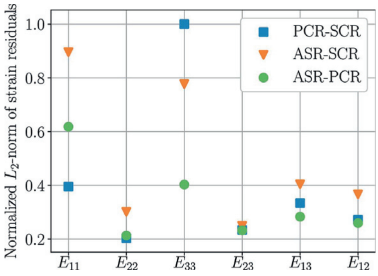

Figure 7
Normalized Euclidean norms of the difference in reconstructed strain compared between SCR, PCR and ASR. PCR-SCR corresponds to taking the solution of SCR at every point and subtracting it from the solution of PCR *etc*. The data correspond to the grain in Fig. 6.

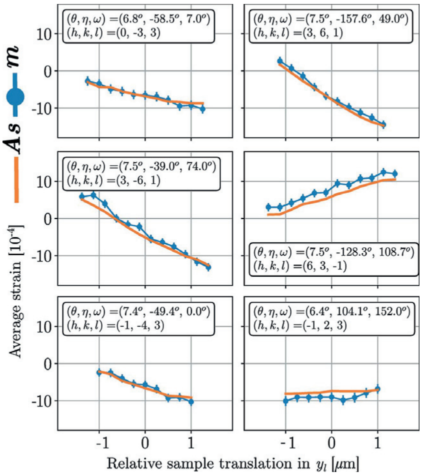

Figure 8
Subsets of computed average strains (**As**) compared with subsets of measured average strains (**m**) for ASR. Each subplot corresponds to the strain profile of a single selected diffraction peak. This means that different subsets of the scalar instances of the vectors **As** and **m** are displayed in the six subplots. The data originate from the grain in Fig. 6, where a total number of 321 diffraction peaks were used for fitting. The error bars were computed as the reciprocal of the weights in equation (25), with Δr = 0.1.

Such analysis can also serve as verification that any reconstructed strain gradients are indeed present in the underlying data. In Fig. 8 the product **As** is plotted against the measured average strains, **m**, for six selected diffraction peaks out of 321 used peaks, at grain slice $z_l = 0$. The peaks were selected to give a good spread in η, ω and to have a relatively high diffraction angle, θ, since such peaks have a higher influence (weight) on the solution of the least-squares problem. Each presented diffraction peak is associated with a set of Miller indices (h, k, l) and an angular setting (θ, η, ω), as indicated in the subplots of Fig. 8. As the grain is translated across the X-ray beam the Miller planes experiencing a favourable Bragg condition will diffract, creating a profile of average strain along the beam. Multiplying the constant uncertainty in peak position, Δr, by the strain sensitivity, $\partial\bar{\varepsilon}_{\rm m}/\partial r$, provides an estimate of the local strain uncertainty of each measurement [*i.e.* the inverse of the weights in equation (25)]. To illustrate this, error bars have been put on the measurement points in Fig. 8. The expected uncertainty was taken as $\Delta r = 0.1$ pixels, in accordance with the work of Borbely *et al.* (2014).

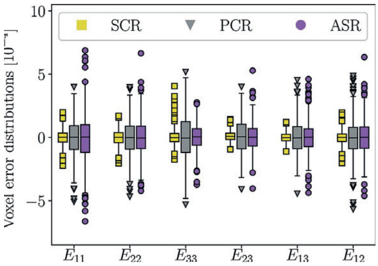

Figure 9
Error in strain fields due to normally distributed noise in peak positions. Outliers are defined by deviations from the mean value by more than ±1.5 times the interquartile range. The data correspond to the grain in Fig. 6.

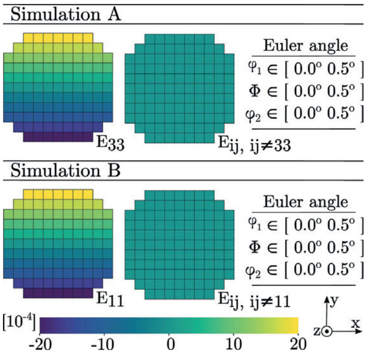

Figure 10
Input topology, strain state and mosaicity of a simulated tin grain slice comprising a total of 109 voxels. In both A and B all three Euler angles (φ_1, Φ, φ_2) vary linearly with x, from 0° (left) to 0.5° (right).

To evaluate the impact of noise on the reconstructed strain fields, the peak positions were perturbed and a secondary reconstruction performed. Noise was drawn from a normal distribution with expectation value 0 and standard deviation σ:

$$\sigma_\omega = 0.5^\circ, \quad \sigma_{y_{\rm d}} = 0.5\ \text{pixels}, \quad \sigma_{z_{\rm d}} = 0.5\ \text{pixels}. \qquad (30)$$

It is important to appreciate that noise is introduced into the peak centre-of-mass coordinates rather than the raw detector images. The peak positions are normally computed by combining several pixel intensities, and thus a given perturbation of the peak position will, in general, correspond to a greater measurement noise in the raw data. However, to investigate the worst-case scenario, when a diffraction peak is composed of a single pixel, we select the noise as stated in equation (30). Residual fields were defined as the difference between reconstructed strain fields using the perturbed and original peak centre-of-mass positions, respectively. An estimate of the propagated error is retrieved by down-sampling the residual fields into 2 × 2 voxel sub-regions. If instead the field is not down-sampled the propagated error will appear

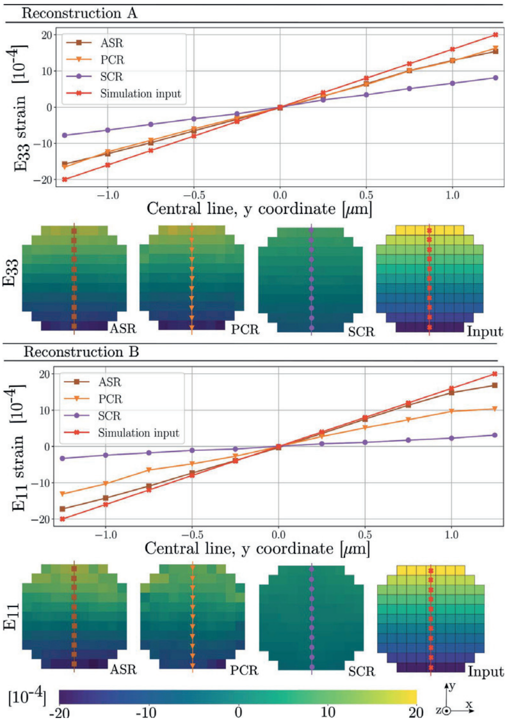

Figure 11
Reconstruction of axial strain tensor components corresponding to the two simulations presented in Fig. 10. The result is seen to vary with reconstruction method from left to right. The strain along the central vertical line of the grain is illustrated as line plots for each of the simulations.

greater. However, the resolution of the SCR method is two times the beam width as discussed previously. Furthermore, it is reasonable to define error in terms of low-frequency variations in the strain field. The down-sampled residual fields are presented as a box plot in Fig. 9, including all three methods and six strain components.

Finally, we present reconstructions of synthetic diffraction data produced using the forward model coupled to PCR. Before peak centre-of-mass coordinates were computed, the modelled data were binned by $d\omega$ and detector pixel size. The parameters of the simulations were taken to equal those of Tables 1 and 2 and equation (29). Diffraction from an Sn slice was simulated two separate times, featuring a linear strain gradient in either E_{33} or E_{11}. The input to these two simulations is presented in Fig. 10.

To mimic a mosaic spread, a gradient in each of the three Euler angles (φ_1, Φ, φ_2) was introduced. Starting from a crystal orientation aligned with the ω coordinate system, $\varphi_1 = \Phi = \varphi_2 = 0$, the gradient was made to increase in the positive x_ω direction by uniformly increasing all of the Euler angles to a maximum of $\varphi_1 = \Phi = \varphi_2 = 0.5^\circ$. The results of the two simulations are presented in Fig. 11.

To investigate the reconstruction of more complex strain states, a third simulation has been performed (Appendix *A*). This simulation features strain in all six components of the strain tensor and can thus provide insight into the reconstruction of shear strains, which have not been covered much in the above.

8. Discussion

Fig. 7 indicates that the greatest discrepancy in reconstructed strain between the three methods is found in the E_{11} and E_{33} strain components. Turning first to the E_{33} strain, we find that ASR and PCR are in agreement while the reconstruction of SCR deviates. Indeed, the 3D reconstructions in Fig. 6(*a*) reveal reduced amplitudes for SCR. As discussed in Section 4, this is explained by the invalid assumption of sub-problem independence made in SCR. Reflections probing the E_{33} strain are available from all ω angles, and thus the single-crystal fit to a point will be influenced by points across the entire grain. Simulation A, presented in Fig. 11, further implies that ASR and PCR here provide more accurate descriptions of the strain state than SCR.

Regarding the E_{11} strain, Fig. 7 shows a higher level of agreement between PCR and SCR than between ASR and PCR. This is an example of when the assumption of sub-problem independence happens to work. Examining Fig. 6(*b*) we see a strain gradient with a significant component along the x axis. This strain will be probed mostly at $\omega \simeq 90^\circ$, *i.e.* perpendicular to the gradient direction. This means that the single-crystal fit to any point will be influenced mostly by points featuring the same E_{11} strain. If instead the E_{11} strain state had featured a gradient with a significant component in the y direction, SCR would again break down. This is verified by simulation B, also presented in Fig. 11, where the E_{11} strain gradient has been selected to align with the y direction instead of the x direction.

Apart from the confirmation of bias in SCR, which is related to the direction of the gradient, we also note that simulations A and B imply that the E_{33} strain component is more retrievable than the E_{11} component for ASR and PCR. To understand this we emphasize that, in general, measurements of a specific strain component are not uniformly sampled. In this case, although the strain in the direction of the rotation axis, E_{33}, has an equal chance of being sampled at any given ω setting, the strain along the beam direction, E_{11}, will mostly be probed close to $\omega = 90^\circ$. Therefore, the reconstruction of the E_{11} strain will be a less well posed tomography problem than the reconstruction of E_{33}. This was also noted by Margulies *et al.* (2002).

The diffraction peak analysis presented in Fig. 8 verifies that the reconstructed strain gradients are indeed present in the underlying data. In regards to the fit quality of ASR, we draw attention to the use of absolute strains in the reconstruction procedure. If the average position of each diffraction peak had been subtracted before reconstruction, it is possible that some systematic errors could be avoided. However, such a method would unfortunately not be able to give approximations to the absolute values of strain but would be limited to reconstructing relative strain variations within the grains.

The interquartile range of the propagated errors in Fig. 9 is approximately 2×10^{-4} or lower for all three methods. The elevated sensitivity of ASR and PCR compared with SCR is believed to be related to the incorporation of volume weights. In ASR and PCR, few reflections can carry a high weight in relation to a strain component for a voxel. This leads to a diminished probability for noise to cancel out between reflections. In SCR, all reflections related to a voxel are equally weighted in terms of illuminated voxel volume, and thus the perturbations in peak position are more likely to cancel out. This is a necessary deficit of PCR and ASR, as any method taking the spatial dependence of the problem into account must also incorporate some sort of weighting based on illuminated fractions. Therefore, it would seem that the precision of SCR, seen as compact distributions in Fig. 9, is a symptom of the damping of the strain field.

It should be recognized that the inverse problem being undertaken features coupling between strain and orientation. This means that a strain state can give diffraction peak position shifts not only in 2θ but also in ω and η. PCR aims to recover both orientation and strain, while ASR assumes a uniform orientation within the grain. However, Figs. 11, 14 and 15 (see Appendix *A*) indicate that the input orientation gradient has a small impact on the strain reconstruction of both ASR and PCR. In fact, the strain reconstruction of ASR is more accurate than that of PCR. This is promising as ASR is both computationally faster and easier to implement than PCR.

For further work it could be interesting to incorporate a compatibility or equilibrium constraint into the strain reconstruction, similar to what is suggested by Jidling *et al.* (2018) and for equilibrium constraints demonstrated through simulations of bulk materials by Hendriks *et al.* (2019). Such constraints enjoy a simple physical interpretation and would in this sense be a superior choice over the smoothness constraint adopted in ASR. Furthermore, in the case of considerable plastic deformation, when the crystals display abrupt lattice discontinuities, the validity of the smoothness constraint could be questioned.

Additionally, the PCR method suggests that more detailed information in the raw data could be taken into account since the driving model produces synthetic diffraction patterns. For instance, the match between peak shapes could be used instead of peak centre-of-mass coordinates to enhance accuracy. This could be performed by modifying the cost function (9) to incorporate the activated pixel pattern, similarly to Suter *et al.* (2006) and Li & Suter (2013).

9. Conclusions

Work towards reconstructing the strain tensor variation on an intragranular level for scanning 3DXRD experiments is presented. It is established that reconstruction methods should take the spatial (tomographic) properties of the inverse problem into account. Through simulations, the PCR and ASR methods developed in this paper have been shown to provide more consistent approximations to the input strain tensor fields than the previously suggested method, SCR. The ASR method operates on the assumption of a smooth strain field and should be used with caution in the presence of lattice discontinuities. The methods have been shown to be computationally viable in the context of synchrotron diffraction data by reconstructions of a tin grain embedded within a polycrystalline sample. By analysing individual diffraction peaks, it was verified that the reconstructed strain gradient was a real feature of the underlying data.

APPENDIX *A*
Further reconstructions from synthetic diffraction data

To further investigate the reconstruction quality of the full strain tensor, E_{ij}, an additional simulation and reconstruction set is presented. The simulation was defined similarly to that of Fig. 10 with two exceptions. (i) Strain gradients were introduced in all six strain tensor components simultaneously. (ii) The linear strain gradients were taken to vary in the x direction. The simulation input is illustrated in Fig. 12. Note that in the corresponding reconstructions of SCR, PCR and ASR (Figs. 13–15) the colour bar is rescaled to facilitate strain

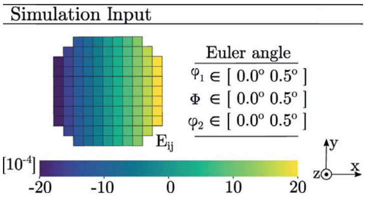

Figure 12
Input topology, strain state and mosaicity of a simulated tin grain slice comprising a total of 109 voxels. All three Euler angles (φ_1, Φ, φ_2) vary linearly with x, from 0° (left) to 0.5° (right). Likewise all six strain components vary linearly with x, from -20×10^{-4} (left) to $+20 \times 10^{-4}$ (right).

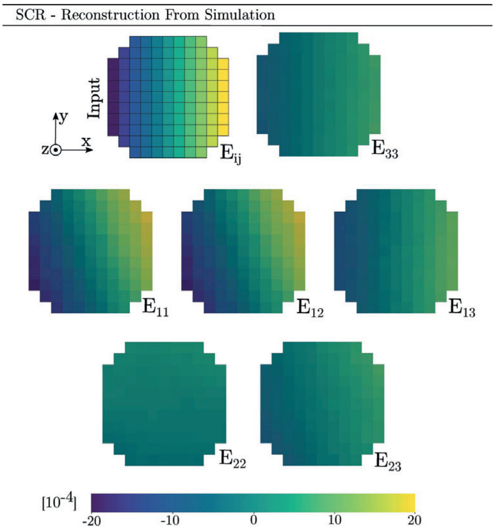

Figure 13
Reconstruction by SCR of full strain tensor corresponding to the simulation presented in Fig. 12. The top-left sub-figure represents the simulation input strain field, rescaled to the current colour range.

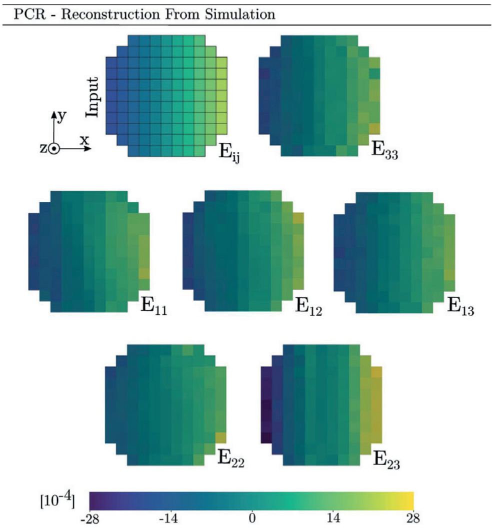

Figure 14
Reconstruction by PCR of full strain tensor corresponding to the simulation presented in Fig. 12. The top-left sub-figure represents the simulation input strain field, rescaled to the current colour range.

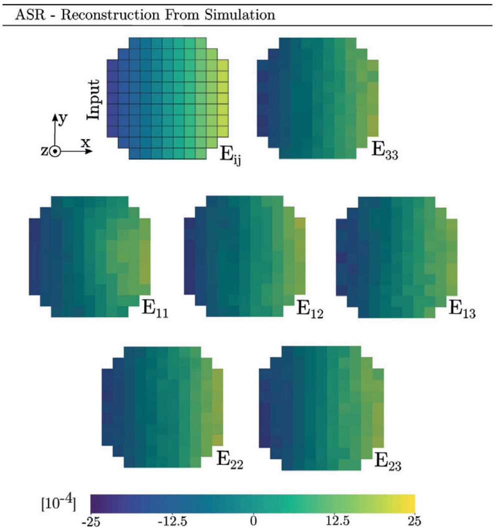

Figure 15
Reconstruction by ASR of full strain tensor corresponding to the simulation presented in Fig. 12. The top-left sub-figure represents the simulation input strain field, rescaled to the current colour range.

values that exceed the simulation input range. Each figure therefore includes a reference input grain slice to enable comparisons.

Acknowledgements

The authors are grateful for the beamtime provided by the ESRF, beamline ID11, where the diffraction data were collected (Hektor *et al.*, 2019). Furthermore, the authors extend their gratitude to the reviewers for several valuable improvements to the paper.

References

Alpers, A., Poulsen, H. F., Knudsen, E. & Herman, G. T. (2006). *J. Appl. Cryst.* **39**, 582–588.
Barzilai, J. & Borwein, J. J. (1988). *IMA J. Numer. Anal.* **8**, 141–148.
Borbely, A., Renversade, L., Kenesei, P. & Wright, J. (2014). *J. Appl. Cryst.* **47**, 1042–1053.
Busing, W. R. & Levy, H. A. (1967). *Acta Cryst.* **22**, 457–464.
Byrd, R. H., Hribar, M. E. & Nocedal, J. (1999). *SIAM J. Optimization*, **9**, 877–900.
Edmiston, J. K., Barton, N. R., Bernier, J. V., Johnson, G. C. & Steigmann, D. J. (2011). *J. Appl. Cryst.* **44**, 299–312.
Hayashi, Y., Hirose, Y. & Seno, Y. (2015). *J. Appl. Cryst.* **48**, 1094–1101.
Hayashi, Y., Setoyama, D. & Seno, Y. (2017). *Mater. Sci. Forum*, **905**, 157–164.
Hektor, J., Hall, S. A., Henningsson, N. A., Engqvist, J., Ristinmaa, M., Lenrick, F. & Wright, J. P. (2019). *Materials*, **12**, 446.
Hendriks, J. N., Wensrich, C. M. & Wills, A. (2019). *arXiv*: 1903.02158.
Henningsson, A. (2019). Student paper, Lund University, Sweden. http://lup.lub.lu.se/student-papers/record/8972668.
Jidling, C., Hendriks, J., Wahlström, N., Gregg, A., Schön, T. B., Wensrich, C. & Wills, A. (2018). *Nucl. Instrum. Methods Phys. Res. B*, **436**, 141–155.
Jones, E., Oliphant, T., Peterson, P. *et al.* (2001). *SciPy*, http://www.scipy.org/.
Kulshreshth, A. K., Alpers, A., Herman, G. T., Knudsen, E., Rodek, L. & Poulsen, H. F. (2009). *Inverse Probl.* **3**, 69–85.
Lauridsen, E. M., Schmidt, S., Suter, R. M. & Poulsen, H. F. (2001). *J. Appl. Cryst.* **34**, 744–750.
Li, S. F. & Suter, R. M. (2013). *J. Appl. Cryst.* **46**, 512–524.
Lionheart, W. R. B. & Withers, P. J. (2015). *Inverse Probl.* **31**, 045005.
Margulies, L., Lorentzen, T., Poulsen, H. & Leffers, T. (2002). *Acta Mater.* **50**, 1771–1779.
Oddershede, J., Schmidt, S., Poulsen, H. F., Sørensen, H. O., Wright, J. & Reimers, W. (2010). *J. Appl. Cryst.* **43**, 539–549.
Poulsen, H. (2004). PhD thesis, Risø National Laboratory, Roskilde, Denmark.
Poulsen, H. F., Nielsen, S. F., Lauridsen, E. M., Schmidt, S., Suter, R. M., Lienert, U., Margulies, L., Lorentzen, T. & Juul Jensen, D. (2001). *J. Appl. Cryst.* **34**, 751–756.
Poulsen, H. F. & Schmidt, S. (2003). *J. Appl. Cryst.* **36**, 319–325.
Rodek, L., Poulsen, H. F., Knudsen, E. & Herman, G. T. (2007). *J. Appl. Cryst.* **40**, 313–321.
Sørensen, H. O., Schmidt, S., Wright, J., Vaughan, G. B. M., Techert, S., Garman, E., Oddershede, J., Davaasambuu, J. S., Paithankar, K., Gundlach, C. & Poulsen, H. F. (2012). *Z. Kristallogr.* **227**, 63–78.
Suter, R., Hennessy, D., Xiao, C. & Lienert, U. (2006). *Rev. Sci. Instrum.* **77**, 123905.
Wright, J. (2005). *ImageD11*, https://github.com/FABLE-3DXRD/ImageD11/.

Paper B

Axel Henningsson and Johannes Hendriks

Intragranular strain estimation in far-field scanning X-ray diffraction using a Gaussian process

In: Journal of Applied Crystallography 54, 1057-1070. (2021)

JOURNAL OF
APPLIED
CRYSTALLOGRAPHY

ISSN 1600-5767

Intragranular strain estimation in far-field scanning X-ray diffraction using a Gaussian process

Axel Henningsson[a]* and Johannes Hendriks[b]

[a]Division of Solid Mechanics, Lund University, Lund, Sweden, and [b]School of Engineering, The University of Newcastle, Callaghan, NSW 2308, Australia. *Correspondence e-mail: axel.henningsson@solid.lth.se

Received 16 February 2021
Accepted 13 May 2021

Edited by A. Borbély, Ecole National Supérieure des Mines, Saint-Etienne, France

Keywords: three-dimensional X-ray diffraction (3DXRD); intragranular strain; Gaussian processes; scanning X-ray diffraction.

A new method for estimation of intragranular strain fields in polycrystalline materials based on scanning three-dimensional X-ray diffraction (scanning 3DXRD) data is presented and evaluated. Given an *a priori* known anisotropic compliance, the regression method enforces the balance of linear and angular momentum in the linear elastic strain field reconstruction. By using a Gaussian process (GP), the presented method can yield a spatial estimate of the uncertainty of the reconstructed strain field. Furthermore, constraints on spatial smoothness can be optimized with respect to measurements through hyperparameter estimation. These three features address weaknesses discussed for previously existing scanning 3DXRD reconstruction methods and, thus, offer a more robust strain field estimation. The method is twofold validated: firstly by reconstruction from synthetic diffraction data, and secondly by reconstruction of a previously studied tin (Sn) grain embedded in a polycrystalline specimen. Comparison against reconstructions achieved by a recently proposed algebraic inversion technique is also presented. It is found that the GP regression consistently produces reconstructions with lower root-mean-square errors, mean absolute errors and maximum absolute errors across all six components of strain.

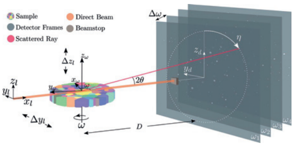

1. Introduction

Three-dimensional X-ray diffraction (3DXRD), as pioneered by Poulsen (2004) and co-workers, is a nondestructive materials probe for the study of bulk polycrystalline materials. The experimental technique is typically implemented at synchrotron facilities where access to hard X-rays ($\geq$10 keV) facilitates the study of dense materials with sample dimensions in the millimetre range. In contrast to powder diffraction, 3DXRD enables studies on a per-grain basis, which requires that the Debye–Scherrer rings consist of a set of well defined, separable single-crystal peaks. To achieve this, the beam and sample dimensions must be selected accordingly, limiting the number of grains illuminated per detector readout. By various computer-aided algorithms (*cf.* Lauridsen *et al.*, 2001), the single-crystal diffraction peaks can be segmented and categorized on a per-grain basis, enabling the study of individual crystals within a sample. Typical quantities retrieved from such analyses are the grain average strain and average orientation (Poulsen *et al.*, 2001; Oddershede *et al.*, 2010). From further analysis it also possible to retrieve an approximate grain topology map (Poulsen & Schmidt, 2003; Poulsen & Fu, 2003; Markussen *et al.*, 2004; Alpers *et al.*, 2006).

Reducing the X-ray beam cross section to sub-grain dimensions not only allows for the study of samples with large numbers of grains but also enables the investigation of intragranular variations. This special case of 3DXRD is commonly referred to as scanning 3DXRD since, to acquire a full data

https://doi.org/10.1107/S1600576721005112

set, the narrow beam must be scanned across the sample. In this setting, it is possible to measure the diffraction signal from approximate line segments across the grains, collecting information on the intragranular structure. Any inversion procedure, in pursuit of such intragranular quantities, then poses a rich tomography problem where the ray transform typically involves higher-order tensorial fields.

Recent advances in diffraction contrast tomography (Reischig & Ludwig, 2020) show promising results for inversion for both orientation and strain fields in three dimensions with intragranular resolution. In scanning 3DXRD where higher angular resolution on scattering vectors is achieved at the cost of diffraction peak resolution (Nervo *et al.*, 2014), multiple proposals for inversion operating solely from scattering vectors have been made. Initially, Hayashi *et al.* (2015, 2017) proposed a method for a per-voxel strain refinement to approximate intragranular strains using scanning 3DXRD data. Unfortunately, this procedure was shown to introduce bias in the reconstruction related to strain state (Hayashi *et al.*, 2019; Hektor *et al.*, 2019). These obstacles were later overcome by Henningsson *et al.* (2020), who proposed an inversion method that takes the tomographic nature of the problem into account. As has been pointed out by several other authors (*cf.* Margulies *et al.*, 2002; Lionheart & Withers, 2015), the sampling of strain is not uniform in 3DXRD and, as a result, some additional constraints on the reconstructed field are often desirable. Henningsson *et al.* (2020) proposed a simple smoothing constraint to each of the strain components with success. However, the parameter selection and the physical interpretation of these constraints are not well defined.

For powder-diffraction-type data, excellent progress to overcome the weaknesses highlighted above has been made using a Gaussian process (Hendriks *et al.*, 2020). In this current work, we adapt the Gaussian process (GP) framework to scanning 3DXRD and extend it to a wider class of anisotropic materials. This framework allows for the introduction of a static equilibrium constraint, which ensures that the retrieved strain reconstruction will satisfy the balance of both angular and linear momentum. The GP naturally incorporates spatial correlation in the predicted fields via a covariance function, which, together with the equilibrium prior, replaces the need for previously used smoothing constraints. Moreover, the GP produces an estimate of the uncertainty in the reconstructed strain field, as a by-product of regression. Overall, the presented regression procedure addresses several weaknesses of previous work and provides a tool for uncertainty estimation in the reconstructed strain fields.

2. Diffraction measurements

2.1. Experimental acquisition

In scanning 3DXRD, a polycrystalline specimen is placed on a sample stage associated with an attached coordinate system ($\hat{\mathbf{x}}_\omega$, $\hat{\mathbf{y}}_\omega$, $\hat{\mathbf{z}}_\omega$). The sample stage commonly has several degrees of freedom, some of which are used for initial alignment and calibration and others for data collection. Since the calibration procedure is the same for all 3DXRD-type experiments, here we only describe the degrees of freedom related to data acquisition; for details on calibration see Oddershede *et al.* (2010), Edmiston *et al.* (2011), Borbely *et al.* (2014) and Sharma *et al.* (2012). A fixed laboratory coordinate system ($\hat{\mathbf{x}}_\mathrm{l}$, $\hat{\mathbf{y}}_\mathrm{l}$, $\hat{\mathbf{z}}_\mathrm{l}$) is introduced, which is related to the sample coordinate system through a positive rotation about $\hat{\mathbf{z}}_\mathrm{l}$ and a translation in the $y_\mathrm{l}z_\mathrm{l}$ plane (Fig. 1). For a given sample position (y_l, z_l), rotation in ω is performed in discrete steps of $\Delta\omega$. The scattered intensity in each $\Delta\omega$ rotation interval is generally integrated during the acquisition, resulting in a series of frames for each (y_l, z_l) position. After any necessary spatial distortion corrections have been made, the raw pixelated image stacks (y_d, z_d, ω) can be segmented into separate connected regions of diffracted intensity for which centroids and average intensities can be calculated. The resulting data set is six dimensional, with each diffraction peak average intensity and detector centroid (θ, η) mapping to a sample stage setting (y_l, z_l, ω).

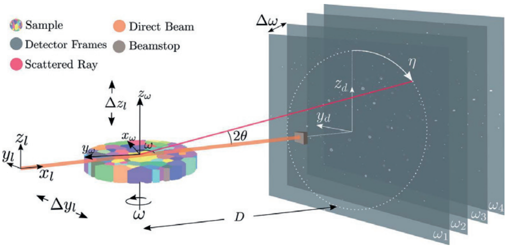

Figure 1
Scanning 3DXRD experimental setup. The sample coordinate system (subscript ω) is attached to the sample turntable while the laboratory (subscript l) coordinate system is fixed in relation to the sample. The sample is rotated and translated in the $y_\mathrm{l}z_\mathrm{l}$ plane across the beam to record diffraction from the full volume [modified from Henningsson *et al.* (2020)].

2.2. Laue equations and scattering notation

From the diffraction peak centroids (θ, η) it is possible to compute scattering vectors, $\mathbf{G}$, defined in the laboratory frame as

$$\mathbf{G}_\mathrm{l} = \frac{2\pi}{\lambda}\begin{bmatrix} \cos(2\theta) - 1 \\ -\sin(2\theta)\sin(\eta) \\ \sin(2\theta)\cos(\eta) \end{bmatrix}. \tag{1}$$

Using the notation of Poulsen (2004) and considering that the Laue equations are fulfilled during diffraction, we can also express the scattering vectors as

$$\mathbf{G}_\mathrm{l} = \boldsymbol{\Omega}\mathbf{U}\mathbf{B}\mathbf{G}_{hkl}, \tag{2}$$

where $\boldsymbol{\Omega}$ and $\mathbf{U}$ are unitary square 3 × 3 rotation matrices describing, respectively, the turntable rotation around $\hat{\mathbf{z}}_\omega$ and the crystal unit-cell orientation with respect to the ω-coordinate system. The matrices $\mathbf{U}$ and $\mathbf{B}$ can now be uniquely defined as the polar decomposition of their inverse product, $(\mathbf{UB})^{-1}$, in which the rows contain the real-space unit-cell lattice vectors **a**, **b** and **c** described in the sample ω-coordinate system:

$$(\mathbf{UB})^{-1} = \begin{bmatrix} \mathbf{a}^{\mathrm{T}} \\ \mathbf{b}^{\mathrm{T}} \\ \mathbf{c}^{\mathrm{T}} \end{bmatrix} = \begin{bmatrix} a_1 & a_2 & a_3 \\ b_1 & b_2 & b_3 \\ c_1 & c_2 & c_3 \end{bmatrix}. \tag{3}$$

The integer vector $\mathbf{G}_{hkl} = [h \;\; k \;\; l]^{\mathrm{T}}$ holds the Miller indices.

2.3. Grain mapping

Given a measured set of scattering vectors, the procedure known as grain mapping is concerned with finding a set of uniform crystals that explain the data. In this setting, grains are represented by their average $(\mathbf{UB})^{-1}$ matrices together with their real-space centroid coordinates. To contextualize the grain-mapping procedure, a simplified schematic of the scanning 3DXRD analysis steps is presented in Fig. 2.

In essence, the grain-mapping procedure results in a map between diffraction peaks and individual average grain $(\mathbf{UB})^{-1}$ matrices and centroids. The diffraction peaks associated with a single grain can be extracted from such peak–grain maps and grain shape reconstruction can be performed by tomographic methods (*cf.* Poulsen & Schmidt, 2003; Alpers *et al.*, 2006), utilizing the scattered intensity associated with each diffraction peak. The peak–grain maps also enable studies on a per-grain basis, something which simplifies analysis both conceptually and computationally. Software for performing grain mapping is freely available in the *ImageD11* package (Wright, 2005), and further details on various algorithm options can be found in the literature (Moscicki *et al.*, 2009; Oddershede *et al.*, 2010; Edmiston *et al.*, 2011; Sharma *et al.*, 2012; Schmidt, 2014). In this paper we are concerned with reconstruction of intragranular strain, and thus we focus on the final step of analysis and proceed with the assumption that all preceding quantities have been computed.

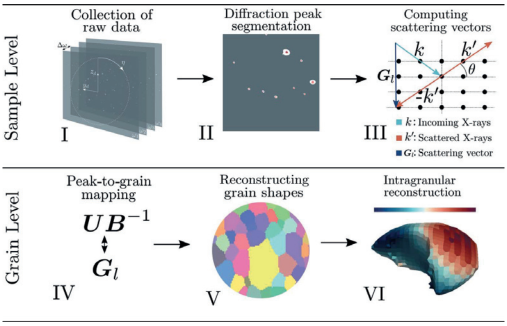

Figure 2
Simplified schematic of analysis steps commonly performed on scanning 3DXRD data. From raw detector data (I), the per-peak centroids (η, θ) and average intensities are retrieved (II). The scattering vectors can then be computed (III) and input into a peak-grain mapping algorithm (IV). From the produced maps, per-grain shape reconstruction can take place (V). Finally, intragranular quantities can be sought (VI).

3. Measurement model

3.1. Strain revealing transformations

Henningsson *et al.* (2020) described the procedure to calculate strains in individual lattice planes from scanning 3DXRD measurements via the Bragg equations as first laid out by Poulsen *et al.* (2001) and Margulies *et al.* (2002). To enrich the framework, allow for consistent use of the Laue equations and clarify how the integration of strain can take place, here we adopt a different route, rewriting the Laue equations and performing a first-order Taylor series expansion. We start by recollecting that the 3 × 3 continuum deformation gradient tensor, **F**, should have the property that

$$\mathbf{v} = \mathbf{F}\mathbf{v}_0, \tag{4}$$

where $\mathbf{v}_0$ is a vector in the reference configuration and **v** is the corresponding deformed vector. Applying this to a crystal reference unit cell $(\mathbf{a}_0, \mathbf{b}_0, \mathbf{c}_0)$ given in the sample ω-coordinate system and collecting the equation in matrix format, we find that

$$\begin{bmatrix} \mathbf{a} & \mathbf{b} & \mathbf{c} \end{bmatrix} = \mathbf{F}\begin{bmatrix} \mathbf{a}_0 & \mathbf{b}_0 & \mathbf{c}_0 \end{bmatrix}. \tag{5}$$

With (3) this allows us to identify that

$$\begin{aligned} &(\mathbf{UB})^{-\mathrm{T}} = \mathbf{F}(\mathbf{U}_0\mathbf{B}_0)^{-\mathrm{T}} \Leftrightarrow \\ &\mathbf{F}(\mathbf{U}_0\mathbf{B}_0)^{-\mathrm{T}}(\mathbf{U}_0\mathbf{B}_0)^{\mathrm{T}} = (\mathbf{UB})^{-\mathrm{T}}(\mathbf{U}_0\mathbf{B}_0)^{\mathrm{T}} \Leftrightarrow \\ &\mathbf{F} = (\mathbf{UB})^{-\mathrm{T}}(\mathbf{U}_0\mathbf{B}_0)^{\mathrm{T}}, \end{aligned} \tag{6}$$

where $\mathbf{U}_0$ and $\mathbf{B}_0$ define an undeformed crystal lattice. We can now relate the quantities involved in the Laue equations (1) to the strain tensor by considering that the infinitesimal strain tensor in the sample ω-coordinate system is defined as

$$\boldsymbol{\epsilon}_\omega = \tfrac{1}{2}(\mathbf{F}^{\mathrm{T}} + \mathbf{F}) - \mathbf{I}, \tag{7}$$

where **I** is the identity tensor. An introduction to elasticity theory is provided by Ottosen & Ristinmaa (2005). Insertion of (6) into (7) gives

$$\boldsymbol{\epsilon}_\omega = \tfrac{1}{2}\left[(\mathbf{U}_0\mathbf{B}_0)(\mathbf{UB})^{-1} + (\mathbf{UB})^{-\mathrm{T}}(\mathbf{U}_0\mathbf{B}_0)^{\mathrm{T}}\right] - \mathbf{I}. \tag{8}$$

The observable quantity in 3DXRD is the scattering vectors and a useful formulation must therefore relate $\boldsymbol{\epsilon}_\omega$ to $\mathbf{G}_\omega$, together with the known quantities $\mathbf{U}_0$ and $\mathbf{B}_0$. To achieve this we consider the strain in a single direction, introducing the unit vector $\hat{\boldsymbol{\kappa}}$ into (8) as

$$\hat{\boldsymbol{\kappa}}^{\mathrm{T}}\boldsymbol{\epsilon}_\omega\hat{\boldsymbol{\kappa}} = \tfrac{1}{2}\hat{\boldsymbol{\kappa}}^{\mathrm{T}}\left[(\mathbf{U}_0\mathbf{B}_0)(\mathbf{UB})^{-1} + (\mathbf{UB})^{-\mathrm{T}}(\mathbf{U}_0\mathbf{B}_0)^{\mathrm{T}}\right]\hat{\boldsymbol{\kappa}} - 1. \tag{9}$$

The problem is now to select $\hat{\boldsymbol{\kappa}}$ such that the right-hand side reduces to an observable quantity. From (2) we may define

$$\mathbf{G}_\omega = \boldsymbol{\Omega}^{-1}\mathbf{G}_l = \mathbf{UB}\mathbf{G}_{hkl}, \tag{10}$$

and sample the strain parallel to this scattering vector as

$$\hat{\boldsymbol{\kappa}} = \frac{\mathbf{G}_\omega}{||\mathbf{G}_\omega||} = \frac{\mathbf{UB}\mathbf{G}_{hkl}}{||\mathbf{G}_\omega||}. \tag{11}$$

Insertion into (9) now reduces (9) to

$$
\begin{aligned}
&\hat{\boldsymbol{\kappa}}^{\mathrm{T}}\boldsymbol{\epsilon}_{\omega}\hat{\boldsymbol{\kappa}}\\
&=\tfrac{1}{2}\frac{\mathbf{G}_{hkl}^{\mathrm{T}}(\mathbf{UB})^{\mathrm{T}}}{||\mathbf{G}_{\omega}||}\left[(\mathbf{U}_0\mathbf{B}_0)(\mathbf{UB})^{-1}+(\mathbf{UB})^{-\mathrm{T}}(\mathbf{U}_0\mathbf{B}_0)^{\mathrm{T}}\right]\frac{(\mathbf{UB})\mathbf{G}_{hkl}}{||\mathbf{G}_{\omega}||}-1\\
&=\frac{1}{2\mathbf{G}_{\omega}^{\mathrm{T}}\mathbf{G}_{\omega}}\left[\mathbf{G}_{hkl}^{\mathrm{T}}(\mathbf{UB})^{\mathrm{T}}(\mathbf{U}_0\mathbf{B}_0)\mathbf{G}_{hkl}+\mathbf{G}_{hkl}^{\mathrm{T}}(\mathbf{U}_0\mathbf{B}_0)^{\mathrm{T}}(\mathbf{UB})\mathbf{G}_{hkl}\right]-1\\
&=\frac{1}{2\mathbf{G}_{\omega}^{\mathrm{T}}\mathbf{G}_{\omega}}\left[\mathbf{G}_{\omega}^{\mathrm{T}}\mathbf{G}_{\omega}^{(0)}+(\mathbf{G}_{\omega}^{(0)})^{\mathrm{T}}\mathbf{G}_{\omega}\right]-1=\frac{\mathbf{G}_{\omega}^{\mathrm{T}}\mathbf{G}_{\omega}^{(0)}}{\mathbf{G}_{\omega}^{\mathrm{T}}\mathbf{G}_{\omega}}-1, \qquad (12)
\end{aligned}
$$

where

$$\mathbf{G}_{\omega}^{(0)}=\boldsymbol{\Omega}^{-1}\mathbf{G}_{\mathrm{l}}^{(0)}=\mathbf{U}_0\mathbf{B}_0\mathbf{G}_{hkl}. \qquad (13)$$

This selection of unit vector $\hat{\boldsymbol{\kappa}}$ not only guarantees that $\boldsymbol{\epsilon}_{\omega}$ is the only unknown in (12) but further spreads the sampling of strain to all directions defined by the measured set of scattering vectors $\mathbf{G}_{\omega}$. For high X-ray energies, although not uniform, this spread is typically good (Lauridsen *et al.*, 2001), explaining why, in general, strain reconstruction is possible in 3DXRD.

3.2. Tensorial ray transform

So far we have worked with equations (2)–(12) as if scattering occurred from a single point. This is typically the approximation made in 3DXRD when only grain average properties are required. For scanning 3DXRD, when pursuing intragranular quantities, we must consider that scattering takes place from grain sub-regions, illuminated by the narrow X-ray beam. In fact, if the scattered intensity is the same from all points within the grain, the scattering vectors known to us from the experiment are average quantities over regions, $\mathcal{R}$, within the grain such that

$$\langle\mathbf{G}_{\omega}\rangle=\frac{1}{V}\int\limits_{\mathcal{R}}\mathbf{G}_{\omega}\,\mathrm{d}v=\frac{1}{V}\int\limits_{\mathcal{R}}\mathbf{UBG}_{hkl}\,\mathrm{d}v, \qquad (14)$$

where V is the total volume of $\mathcal{R}$, $\mathrm{d}v$ is the differential on $\mathcal{R}$ and $\langle\cdot\rangle$ indicates volume average. We run now the risk of invalidating our previous result (12) since the local scattering vectors $\mathbf{G}_{\omega}=\mathbf{G}_{\omega}(x_{\omega}, y_{\omega}, z_{\omega})$ are unknown in scanning 3DXRD. To maintain a useful expression we must further transform (12) into an equation in $\langle\mathbf{G}_{\omega}\rangle$ rather than $\mathbf{G}_{\omega}$. However, since the strain is nonlinear in $\mathbf{G}_{\omega}$, direct volume integration of (12) is not possible. Fortunately though, we may obtain an approximation by Taylor expansion of (12) at $\mathbf{G}_{\omega}=\mathbf{G}_{\omega}^{(0)}$ to first order:

$$\hat{\boldsymbol{\kappa}}^{\mathrm{T}}\boldsymbol{\epsilon}_{\omega}\hat{\boldsymbol{\kappa}}\simeq 1-\frac{\mathbf{G}_{\omega}^{\mathrm{T}}\mathbf{G}_{\omega}^{(0)}}{(\mathbf{G}_{\omega}^{(0)})^{\mathrm{T}}\mathbf{G}_{\omega}^{(0)}}. \qquad (15)$$

By selecting a uniform reference configuration in space, integration of (15) now gives, with (14), that

$$y=\frac{1}{V}\int\limits_{\mathcal{R}}\hat{\boldsymbol{\kappa}}^{\mathrm{T}}\boldsymbol{\epsilon}_{\omega}\hat{\boldsymbol{\kappa}}\,\mathrm{d}v\simeq 1-\frac{\langle\mathbf{G}_{\omega}\rangle^{\mathrm{T}}\mathbf{G}_{\omega}^{(0)}}{(\mathbf{G}_{\omega}^{(0)})^{\mathrm{T}}\mathbf{G}_{\omega}^{(0)}}, \qquad (16)$$

where we introduce the scalar average strain measure $y=y(\hat{\boldsymbol{\kappa}})$.

Finally, in any inversion scheme where $\boldsymbol{\epsilon}_{\omega}$ constitute the free variables, we must be able to execute the forward model that is the integral of (16). For this purpose the direction of strain, $\hat{\boldsymbol{\kappa}}$, must be approximated. Using the already introduced assumption that $\mathbf{G}_{\omega}$ varies weakly over $\mathcal{R}$ we can write

$$\hat{\boldsymbol{\kappa}}\simeq\frac{\langle\mathbf{G}_{\omega}\rangle}{||\langle\mathbf{G}_{\omega}\rangle||}. \qquad (17)$$

We note that, equally, the approximation $\hat{\boldsymbol{\kappa}}\simeq\mathbf{G}_{\omega}^{(0)}/||\mathbf{G}_{\omega}^{(0)}||$ could have been made.

In conclusion, (16) and (17) relate the measured average scattering vectors, $\langle\mathbf{G}_{\omega}\rangle$, to the underlying strain field, $\boldsymbol{\epsilon}_{\omega}(x_{\omega}, y_{\omega}, z_{\omega})$, with the strain tensor being the only involved unknown quantity.

The approximations made in (16) and (17) will give rise to an error in the integrated strain value y. The magnitude of this error will strongly depend on the spatial distribution of intragranular strain and orientation. To demonstrate that the approximations made in (16) and (17) are accurate for small strains and moderate mosaic spreads, we provide an extended analysis of this error in Appendix *A*. This discussion also highlights why, and when, it is possible to reconstruct intragranular strain independently of intragranular orientation in scanning 3DXRD.

3.3. Estimated uncertainty

To finalize the measurement model we introduce an additive Gaussian error e into (16), representing measurement uncertainty. Furthermore, to simplify both computation and further analytical derivations we approximate the volume integral over $\mathcal{R}$ by a corresponding line integral going through the geometrical centre of this region. Finally, we have the measurement model

$$y=\frac{1}{L}\int\limits_{\mathcal{L}}\hat{\boldsymbol{\kappa}}^{\mathrm{T}}\boldsymbol{\epsilon}_{\omega}\hat{\boldsymbol{\kappa}}\,\mathrm{d}l+e, \qquad (18)$$

where L is the length of the line segment $\mathcal{L}$, $\mathrm{d}l$ is the differential on $\mathcal{L}$ and e is the additive normally distributed noise:

$$e\sim\mathcal{N}(\mathbb{E}[e], \mathbb{C}[e, e]), \qquad (19)$$

with expectation value $\mathbb{E}[e]$ and covariance $\mathbb{C}[e, e]$.

The measurement noise is assumed to be zero mean ($\mathbb{E}[e_i]=0$) and independent ($\mathbb{C}[e_i, e_j]=0$) with the variance selected in accordance with previous work (Borbely *et al.*, 2014; Henningsson *et al.*, 2020),

$$\mathbb{C}[e_i, e_i]=\left(\frac{\partial y}{\partial r}\right)^{-2}, \qquad (20)$$

where $r=r(\theta)$ is the radial detector coordinate and the indices i and j indicate unique measurements. Other estimations of $\mathbb{C}[e_i, e_i]$ are possible. Importantly, though, the variance should depend on the scattering angle 2θ, as, for a 2D detector with uniform pixel size, the measurement uncertainty increases with decreasing scattering angle.

4. Regression procedure

Equation (18) is a ray transform that contains information on the average directional strain for a region within the grain. The problem to reconstruct the full strain tensor field from a series of such measurements is therefore tomographic in nature, and the measurements y are highly spatially entangled as the regions $\mathcal{L}$ will intersect in general. A collection of N measurements,

$$\mathbf{y} = \begin{bmatrix} y_1 & y_2 & \dots & y_j & \dots & y_N \end{bmatrix}^{\rm T}, \qquad (21)$$

could represent the second member of a linear equation system where (18) is used to form a system matrix and a vector of unknown strains defined on some finite basis. This has been described by Henningsson *et al.* (2020) for a voxel basis, using a weighted least-squares (WLSQ) approach to retrieve the strain field. As we will discuss in Section 4.1, in this work we adapt these ideas to a Gaussian process framework, not solving for a deterministic strain field but instead calculating the probability distribution of strain at each spatial coordinate, revealing a distribution over strain tensor functions.

Before proceeding any further, it is useful to introduce a vector notation along with some geometrical quantities related to the integration path $\mathcal{L}$ (Fig. 3).

Since $\boldsymbol{\epsilon}^{\rm T} = \boldsymbol{\epsilon}$ we can uniquely represent the strain tensor field in sparser format by introducing the column vector

$$\bar{\boldsymbol{\epsilon}}(\mathbf{x}) = \begin{bmatrix} \epsilon_{xx}(\mathbf{x}) & \epsilon_{yy}(\mathbf{x}) & \epsilon_{zz}(\mathbf{x}) & \epsilon_{xy}(\mathbf{x}) & \epsilon_{xz}(\mathbf{x}) & \epsilon_{yz}(\mathbf{x}) \end{bmatrix}^{\rm T}. \qquad (22)$$

To represent the tensor product $\hat{\boldsymbol{\kappa}}^{\rm T}\boldsymbol{\epsilon}_{\omega}\hat{\boldsymbol{\kappa}}$ involved in (18) using $\bar{\boldsymbol{\epsilon}}$ we seek the corresponding vector $\bar{\boldsymbol{\kappa}}$ such that the equality $\bar{\boldsymbol{\kappa}}^{\rm T}\bar{\boldsymbol{\epsilon}} = \hat{\boldsymbol{\kappa}}^{\rm T}\boldsymbol{\epsilon}_{\omega}\hat{\boldsymbol{\kappa}}$ holds true. We find by expansion that

$$\bar{\boldsymbol{\kappa}} = \begin{bmatrix} \kappa_x^2 & \kappa_y^2 & \kappa_z^2 & 2\kappa_x\kappa_y & 2\kappa_x\kappa_z & 2\kappa_y\kappa_z \end{bmatrix}^{\rm T}. \qquad (23)$$

Next, denoting the intersection points between the X-ray beam and the grain boundary by $\mathbf{p}_0, \mathbf{p}_1, \dots, \mathbf{p}_M$ and letting the Euclidean length of these illuminated regions be labelled $L_i = ||\mathbf{p}_i - \mathbf{p}_{i+1}||_2$, we find, for measurement number j, that

$$y_j = e_j + \sum_{i=0}^{i=M-1} \frac{1}{L_i} \int\limits_0^{L_i} \bar{\boldsymbol{\kappa}}^{\rm T}\bar{\boldsymbol{\epsilon}}(\mathbf{p}_i + \hat{\mathbf{n}}s)\,{\rm d}s = e_j + \mathcal{M}_j\bar{\boldsymbol{\epsilon}}, \qquad (24)$$

where the symbol $\mathcal{M}_j$ is shorthand for the integral operator corresponding to measurement number j, s is a scalar, $\hat{\mathbf{n}}$ is a unit vector along the X-ray beam and $\bar{\boldsymbol{\epsilon}} = \bar{\boldsymbol{\epsilon}}(\mathbf{p}_i + \hat{\mathbf{n}}s)$ is a function over a compact support in the grain volume. Considering the full measurement set $\mathbf{y}$ defined in (21), we introduce a compact notation,

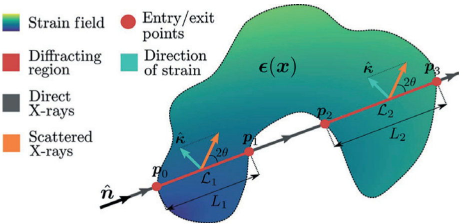

Figure 3
A single crystal under elastic deformation illuminated by an X-ray beam. Scattering takes place along the illuminated region $\mathcal{L} = \mathcal{L}_1 + \mathcal{L}_2$.

$$\mathbf{y} = \mathcal{M}\bar{\boldsymbol{\epsilon}} + \mathbf{e}, \qquad (25)$$

where $\mathcal{M}$ and $\mathbf{e}$ are column vectors formed in analogy with (21).

4.1. Gaussian process regression

A Gaussian process is any stochastic process in which all subsets of a generated stochastic sequence of measurements form multivariate normal distributions (Rasmussen, 2003). The regression procedure associated with a Gaussian process, known as Gaussian process regression, can be described in terms of basic statistical theorems and quantities. The central idea is to exploit the fact that linear operators acting on normally distributed variables form again normal distributions. The goal is to arrive at the distribution of the Gaussian process that, for some spatial function $f(\mathbf{x})$, describes the probability of finding a value f at coordinate $\mathbf{x}$ together with the covariance of $f(\mathbf{x})$ with other spatial locations $f(\mathbf{x}')$.

In the scanning 3DXRD case, we consider the measurement series, $\mathbf{y}$, generated by some underlying strain tensor field, $\bar{\boldsymbol{\epsilon}}(\mathbf{x})$, and seek to calculate at each spatial coordinate, $\mathbf{x}$, the probability distribution $p[\bar{\boldsymbol{\epsilon}}(\mathbf{x})|\mathbf{y}]$, *i.e.* the probability of finding a specified strain tensor $\bar{\boldsymbol{\epsilon}}$ at $\mathbf{x}$ given the measurements $\mathbf{y}$. As we will show, if we assume a Gaussian process prior and Gaussian noise, this probability distribution is multivariate normal, and the covariance of strain at any two points, $\mathbb{C}[\bar{\boldsymbol{\epsilon}} = \bar{\boldsymbol{\epsilon}}(\mathbf{x}), \bar{\boldsymbol{\epsilon}}' = \bar{\boldsymbol{\epsilon}}(\mathbf{x}')]$, together with the strain expectation value, $\mathbb{E}[\bar{\boldsymbol{\epsilon}}(\mathbf{x})]$, will be revealed by the regression.

If it is assumed that $\bar{\boldsymbol{\epsilon}}(\mathbf{x})$ is normally distributed,

$$\bar{\boldsymbol{\epsilon}}(\mathbf{x}) \sim \mathcal{N}(\mathbb{E}[\bar{\boldsymbol{\epsilon}}], \mathbb{C}[\bar{\boldsymbol{\epsilon}}, \bar{\boldsymbol{\epsilon}}']), \qquad (26)$$

it follows directly that $\mathbf{y}$ is multivariate normal,

$$\mathbf{y} \sim \mathcal{N}(\mathbb{E}[\mathbf{y}], \mathbb{C}[\mathbf{y}, \mathbf{y}]), \qquad (27)$$

since it is a linear combination of the independent normal distributions $\bar{\boldsymbol{\epsilon}}(\mathbf{x})$ and $\mathbf{e}$. Considering then the joint distribution of $\bar{\boldsymbol{\epsilon}}(\mathbf{x})$ and $\mathbf{y}$ we can calculate

$$\begin{bmatrix} \bar{\boldsymbol{\epsilon}} \\ \mathbf{y} \end{bmatrix} \sim \mathcal{N}\left(\begin{bmatrix} \mathbf{I} \\ \mathcal{M} \end{bmatrix} \mathbb{E}[\bar{\boldsymbol{\epsilon}}], \begin{bmatrix} \mathbb{C}[\bar{\boldsymbol{\epsilon}}, \bar{\boldsymbol{\epsilon}}'] & \mathbb{C}[\bar{\boldsymbol{\epsilon}}, \bar{\boldsymbol{\epsilon}}']\mathcal{M}^{\rm T} \\ \mathcal{M}\mathbb{C}[\bar{\boldsymbol{\epsilon}}, \bar{\boldsymbol{\epsilon}}'] & \mathcal{M}\mathbb{C}[\bar{\boldsymbol{\epsilon}}, \bar{\boldsymbol{\epsilon}}']\mathcal{M}^{\rm T} + \mathbb{C}[\mathbf{e}, \mathbf{e}] \end{bmatrix} \right), \qquad (28)$$

where $\mathbf{I}$ is an identity operator and we use the fact that $\mathbf{y}$ is a linear transformation of two normally distributed variables $\bar{\boldsymbol{\epsilon}}(\mathbf{x})$ and $\mathbf{e}$. The joint probability of (28) now gives us the sought distribution, $p[\bar{\boldsymbol{\epsilon}}(\mathbf{x})|\mathbf{y}]$, which is again normal. Its variance and expectation value can be found by writing out (28) in analytical exponent form, with fixed $\mathbf{y}$, and completing the exponent square. The closed-form solution can be obtained as

$$\begin{aligned}\mathbb{E}[\bar{\boldsymbol{\epsilon}}|\mathbf{y}] &= \mathbb{E}[\bar{\boldsymbol{\epsilon}}] + \mathbb{C}[\bar{\boldsymbol{\epsilon}}, \bar{\boldsymbol{\epsilon}}']\mathcal{M}^{\mathrm{T}}\big(\mathcal{M}\mathbb{C}[\bar{\boldsymbol{\epsilon}}, \bar{\boldsymbol{\epsilon}}']\mathcal{M}^{\mathrm{T}} \\ &\quad + \mathbb{C}[\mathbf{e}, \mathbf{e}]\big)^{-1}(\mathbf{y} - \mathbb{E}[\mathbf{y}]), \\ \mathbb{C}[\bar{\boldsymbol{\epsilon}}, \bar{\boldsymbol{\epsilon}}'|\mathbf{y}] &= \mathbb{C}[\bar{\boldsymbol{\epsilon}}, \bar{\boldsymbol{\epsilon}}'] - \mathbb{C}[\bar{\boldsymbol{\epsilon}}, \bar{\boldsymbol{\epsilon}}']\mathcal{M}^{\mathrm{T}}\big(\mathcal{M}\mathbb{C}[\bar{\boldsymbol{\epsilon}}, \bar{\boldsymbol{\epsilon}}']\mathcal{M}^{\mathrm{T}} \\ &\quad + \mathbb{C}[\mathbf{e}, \mathbf{e}]\big)^{-1}\mathcal{M}\mathbb{C}[\bar{\boldsymbol{\epsilon}}, \bar{\boldsymbol{\epsilon}}'].\end{aligned} \tag{29}$$

Before any approximate or analytical solutions to the involved transformations of $\mathbb{C}[\bar{\boldsymbol{\epsilon}}, \bar{\boldsymbol{\epsilon}}']$ by $\mathcal{M}$ can be given, it remains first to specify the prior distribution of $\bar{\boldsymbol{\epsilon}}(\mathbf{x})$.

4.2. Equilibrium prior

Since the closed-form solution of (29) requires only that $\bar{\boldsymbol{\epsilon}}(\mathbf{x})$ is normal, we are free to incorporate prior knowledge on $\bar{\boldsymbol{\epsilon}}(\mathbf{x})$ by making a parametrization of $\bar{\boldsymbol{\epsilon}}(\mathbf{x})$ as linear transformations of some other underlying normal distributions. Since $\bar{\boldsymbol{\epsilon}}(\mathbf{x})$ represents a linear elastic strain field and the scanning 3DXRD experiment is assumed to take place on a sample at rest, we expect that the accompanying stress field $\bar{\boldsymbol{\sigma}}$ will be in static equilibrium. This can be expressed as a linear map

$$\bar{\boldsymbol{\epsilon}}(\mathbf{x}) = \mathbf{H}\bar{\boldsymbol{\sigma}}(\mathbf{x}), \tag{30}$$

where $\mathbf{H}$ is an anisotropic compliance matrix that is orientation dependent, $\mathbf{H} = \mathbf{H}(\mathbf{U}) \simeq \mathbf{H}(\mathbf{U}_0)$. The set of analytical functions $\bar{\boldsymbol{\sigma}}(\mathbf{x})$ that satisfy balance of angular and linear momentum are known as the Beltrami stress functions. These may be described as a linear map

$$\bar{\boldsymbol{\sigma}}(\mathbf{x}) = \mathcal{B}\bar{\boldsymbol{\Phi}}(\mathbf{x}), \tag{31}$$

where $\bar{\boldsymbol{\Phi}}(\mathbf{x})$ is a column vector holding six Beltrami stress functions, which are required to be twice differentiable, and

$$\mathcal{B} = \begin{bmatrix} 0 & \frac{\partial^2}{\partial z^2} & \frac{\partial^2}{\partial y^2} & 0 & 0 & -2\frac{\partial^2}{\partial y \partial z} \\ \frac{\partial^2}{\partial z^2} & 0 & \frac{\partial^2}{\partial x^2} & 0 & -2\frac{\partial^2}{\partial x \partial y} & 0 \\ \frac{\partial^2}{\partial y^2} & \frac{\partial^2}{\partial x^2} & 0 & -2\frac{\partial^2}{\partial x \partial y} & 0 & 0 \\ 0 & 0 & -\frac{\partial^2}{\partial x \partial y} & -\frac{\partial^2}{\partial z^2} & \frac{\partial^2}{\partial y \partial z} & \frac{\partial^2}{\partial x \partial z} \\ -\frac{\partial^2}{\partial y \partial z} & 0 & 0 & \frac{\partial^2}{\partial x \partial z} & \frac{\partial^2}{\partial x \partial y} & -\frac{\partial^2}{\partial x^2} \\ 0 & -\frac{\partial^2}{\partial x \partial z} & 0 & \frac{\partial^2}{\partial y \partial z} & -\frac{\partial^2}{\partial y^2} & \frac{\partial^2}{\partial x \partial y} \end{bmatrix}. \tag{32}$$

We have then

$$\bar{\boldsymbol{\epsilon}}(\mathbf{x}) = \mathbf{H}\mathcal{B}\bar{\boldsymbol{\Phi}}(\mathbf{x}), \tag{33}$$

and must now make an assumption on the distribution of $\bar{\boldsymbol{\Phi}}(\mathbf{x})$. Without any further prior knowledge we select a zero-mean normal distribution with

$$\mathbb{E}[\bar{\boldsymbol{\Phi}}] = \begin{bmatrix} 0 \\ 0 \\ 0 \\ 0 \\ 0 \\ 0 \end{bmatrix}, \quad \mathbb{C}[\bar{\boldsymbol{\Phi}}, \bar{\boldsymbol{\Phi}}'] = \begin{bmatrix} k_1 & 0 & 0 & 0 & 0 & 0 \\ 0 & k_2 & 0 & 0 & 0 & 0 \\ 0 & 0 & k_3 & 0 & 0 & 0 \\ 0 & 0 & 0 & k_4 & 0 & 0 \\ 0 & 0 & 0 & 0 & k_5 & 0 \\ 0 & 0 & 0 & 0 & 0 & k_6 \end{bmatrix}, \tag{34}$$

where the covariance functions $k_i = k_i(\mathbf{x}, \mathbf{x}')$ describe the spatial correlation of the field. In this work, we have used the stationary squared-exponential covariance function,

$$k_i(\mathbf{x}, \mathbf{x}') = \sigma_i^2 \exp\left(\frac{-\mathbf{r}^{\mathrm{T}}\mathbf{r}}{2\mathbf{l}_i^{\mathrm{T}}\mathbf{l}_i}\right), \quad \mathbf{r} = \mathbf{x} - \mathbf{x}', \quad \mathbf{l}_i = \begin{bmatrix} l_{ix} & l_{iy} & l_{iz} \end{bmatrix}^{\mathrm{T}}, \tag{35}$$

introducing a smoothness assumption into the strain field reconstruction. The unknown hyperparameters defined by $\mathbf{l}_i$ and σ_i are thus in total $6 \times 4 = 24$ in our case. These variables will be estimated through an initial optimization process known as hyperparameter optimization; we will return to how this is done later. First we highlight that the zero-mean prior assumption on the Beltrami stress functions, $\bar{\boldsymbol{\Phi}}(\mathbf{x})$, does not imply that the posterior distribution of strain, $\bar{\boldsymbol{\epsilon}}(\mathbf{x})$, will be zero mean. This is realized upon examination of equation (29), which shows that a prior mean of $\mathbb{E}[\bar{\boldsymbol{\epsilon}}] = 0$ does not imply that the conditional posterior $\mathbb{E}[\bar{\boldsymbol{\epsilon}}|\mathbf{y}]$ will be zero. Other selections for the prior mean are possible; however, when such additional prior information is unknown, a zero-mean selection is preferable for simplicity.

In total, these selections impose that (i) the strain field is in a point-wise static equilibrium and (ii) the strain field has a local spatial correlation to neighbouring points. The resulting prior distribution of strain is

$$\bar{\boldsymbol{\epsilon}} \sim \mathcal{N}(\mathbf{0}, \mathbf{H}\mathcal{B}\mathbb{C}[\bar{\boldsymbol{\Phi}}, \bar{\boldsymbol{\Phi}}']\mathcal{B}^{\mathrm{T}}\mathbf{H}^{\mathrm{T}}). \tag{36}$$

4.3. Equilibrium posterior distribution

With the prior information of equilibrium and spatial correlation now encoded into the strain field we can insert

$$\mathbb{C}[\bar{\boldsymbol{\epsilon}}, \bar{\boldsymbol{\epsilon}}'] = \mathbf{H}\mathcal{B}\mathbb{C}[\bar{\boldsymbol{\Phi}}, \bar{\boldsymbol{\Phi}}']\mathcal{B}^{\mathrm{T}}\mathbf{H}^{\mathrm{T}} \tag{37}$$

into equation (29) to arrive at a final expression in which only the hyperparameters remain to be estimated. The covariance between measurements takes on the form

$$\mathbb{C}[\mathbf{y}, \mathbf{y}] = \mathcal{M}\mathbf{H}\mathcal{B}\mathbb{C}[\bar{\boldsymbol{\Phi}}, \bar{\boldsymbol{\Phi}}']\mathcal{B}^{\mathrm{T}}\mathbf{H}^{\mathrm{T}}\mathcal{M}^{\mathrm{T}}, \tag{38}$$

which involves, through the mappings $\mathcal{M}$, a double integral over the two times partially differentiated squared exponential in (35). The solution to this double line integral is intractable, although some work has been done to show that for $l_x = l_y = l_z$ it can be analytically reduced to a single integral (Hendriks, Gregg *et al.*, 2019). However, the numerical integration remains too computationally costly for practical use. This motivates the use of an approximation scheme on a reduced basis for which closed-form solutions to all involved quantities of (29) are again recovered (Jidling *et al.*, 2018).

4.4. Finite basis approximations

Decomposing (35) onto a Fourier basis,

$$\varphi_{ik}(\mathbf{x}) = \frac{1}{L_x L_y L_z}\sin[\lambda_{xik}(x+L_x)]\sin[\lambda_{yik}(y+L_y)] \times \sin[\lambda_{zik}(z+L_z)], \tag{39}$$

where the scalars λ and L are the frequencies and phases, respectively, we find that

$$k_i(\mathbf{x},\mathbf{x}') \simeq \sum_{k=1}^{k=m}\varphi_{ik}(\mathbf{x})s_{ik}\varphi_{ik}(\mathbf{x}') = \boldsymbol{\varphi}_i^{\rm T}\mathbf{s}_i\boldsymbol{\varphi}_i'. \tag{40}$$

$\mathbf{s}_i$ is a diagonal matrix of basis coefficients, s_{ik}, which are the spectral densities of (35). Specifically it is possible to show (Solin & Särkkä, 2020) that the kth spectral density is

$$s_{ik} = \sigma_i^2(2\pi)^{2/3}l_{ix}l_{iy}l_{iz}\exp\left[-\tfrac{1}{2}(l_{ix}^2\lambda_{xik}^2 + l_{iy}^2\lambda_{yik}^2 + l_{iz}^2\lambda_{zik}^2)\right]. \tag{41}$$

With the vector notation

$$\boldsymbol{\phi} = \begin{bmatrix}\varphi_1\\ \varphi_2\\ \varphi_3\\ \varphi_4\\ \varphi_5\\ \varphi_6\end{bmatrix}, \quad \mathbf{S} = \begin{bmatrix}\mathbf{s}_1 & \mathbf{0} & \mathbf{0} & \mathbf{0} & \mathbf{0} & \mathbf{0}\\ \mathbf{0} & \mathbf{s}_2 & \mathbf{0} & \mathbf{0} & \mathbf{0} & \mathbf{0}\\ \mathbf{0} & \mathbf{0} & \mathbf{s}_3 & \mathbf{0} & \mathbf{0} & \mathbf{0}\\ \mathbf{0} & \mathbf{0} & \mathbf{0} & \mathbf{s}_4 & \mathbf{0} & \mathbf{0}\\ \mathbf{0} & \mathbf{0} & \mathbf{0} & \mathbf{0} & \mathbf{s}_5 & \mathbf{0}\\ \mathbf{0} & \mathbf{0} & \mathbf{0} & \mathbf{0} & \mathbf{0} & \mathbf{s}_6\end{bmatrix}, \tag{42}$$

where $\mathbf{0}$ is a matrix of zeros, we find the approximate covariance

$$\mathbb{C}[\bar{\boldsymbol{\Phi}},\bar{\boldsymbol{\Phi}}'] = \boldsymbol{\phi}^{\rm T}\mathbf{S}\boldsymbol{\phi}'. \tag{43}$$

Insertion of (43) into (37) now yields

$$\mathbb{C}[\bar{\boldsymbol{\epsilon}},\bar{\boldsymbol{\epsilon}}'] = \mathbf{H}\mathcal{B}\boldsymbol{\phi}^{\rm T}\mathbf{S}\boldsymbol{\phi}'\mathcal{B}^{\rm T}\mathbf{H}^{\rm T}. \tag{44}$$

Introducing the quantities

$$\boldsymbol{\phi}_\epsilon = \mathbf{H}\mathcal{B}\boldsymbol{\phi}^{\rm T}, \quad \boldsymbol{\phi}_y = \mathcal{M}\boldsymbol{\phi}_\epsilon, \tag{45}$$

we finally arrive at the approximate posterior mean and covariance of strain using (29):

$$\begin{aligned}\mathbb{E}[\bar{\boldsymbol{\epsilon}}|\mathbf{y}] &= \mathbb{E}[\bar{\boldsymbol{\epsilon}}] + \boldsymbol{\phi}_\epsilon\mathbf{S}\boldsymbol{\phi}_y^{\rm T}\left(\boldsymbol{\phi}_y\mathbf{S}\boldsymbol{\phi}_y^{\rm T} + \mathbb{C}[\mathbf{e},\mathbf{e}]\right)^{-1}(\mathbf{y}-\mathbb{E}[\mathbf{y}]),\\ \mathbb{C}[\bar{\boldsymbol{\epsilon}},\bar{\boldsymbol{\epsilon}}|\mathbf{y}] &= \boldsymbol{\phi}_\epsilon\mathbf{S}\boldsymbol{\phi}_\epsilon^{\rm T} - \boldsymbol{\phi}_\epsilon\mathbf{S}\boldsymbol{\phi}_y^{\rm T}\left(\boldsymbol{\phi}_y\mathbf{S}\boldsymbol{\phi}_y^{\rm T} + \mathbb{C}[\mathbf{e},\mathbf{e}]\right)^{-1}\boldsymbol{\phi}_y\mathbf{S}\boldsymbol{\phi}_\epsilon^{\rm T}.\end{aligned} \tag{46}$$

The computational complexity can be further reduced by algebraically rearranging this equation to avoid forming the covariance matrices (Rasmussen, 2003), resulting in

$$\begin{aligned}\mathbb{E}[\bar{\boldsymbol{\epsilon}}|\mathbf{y}] &= \mathbb{E}[\bar{\boldsymbol{\epsilon}}] + \boldsymbol{\phi}_\epsilon\big(\boldsymbol{\phi}_y^{\rm T}\mathbb{C}[\mathbf{e},\mathbf{e}]^{-1}\boldsymbol{\phi}_y\\ &\qquad + \mathbf{S}^{-1}\big)^{-1}\boldsymbol{\phi}_y^{\rm T}\mathbb{C}[\mathbf{e},\mathbf{e}]^{-1}(\mathbf{y}-\mathbb{E}[\mathbf{y}]),\\ \mathbb{C}[\bar{\boldsymbol{\epsilon}},\bar{\boldsymbol{\epsilon}}|\mathbf{y}] &= \boldsymbol{\phi}_\epsilon\left(\boldsymbol{\phi}_y^{\rm T}\mathbb{C}[\mathbf{e},\mathbf{e}]^{-1}\boldsymbol{\phi}_y + \mathbf{S}^{-1}\right)^{-1}\boldsymbol{\phi}_\epsilon^{\rm T}.\end{aligned} \tag{47}$$

Here, the inverses $\mathbf{S}^{-1}$ and $\mathbb{C}[\mathbf{e},\mathbf{e}]^{-1}$ can be trivially computed, as the matrices are diagonal. For $m < N$, this reduces the computational complexity to $\mathcal{O}(Nm^2)$ from $\mathcal{O}(N^3)$ required for the inverse in (29) and (46). A numerically stable and efficient algorithm for solving these equations using the QR decomposition is given by Hendriks, Wensrich *et al.* (2019), together with analytical expressions for the various integral mappings $\mathcal{M}$. We note here that, although the introduced Fourier basis in (39) is defined over all space, the support of the reconstructed field in (47) is for all practical purposes that of the grain volume. This follows from the fact that the mappings executed through $\mathcal{M}$ are only performed over the grain, as indicated in (24), and requires that the period of the lowest frequency basis included is larger than the grain volume.

As $m \to \infty$ the approximate solution (47) approaches the exact solution (29) (Solin & Särkkä, 2020). In practice, however, we must select a finite m, leading to (35) being used in approximate form. To direct the selection of frequencies λ_{xik}, λ_{yik} and λ_{zik} in (40) use can be made of (41). In this work, we have selected the basis frequencies on an equidistant grid in $(\lambda_{xik}, \lambda_{yik}, \lambda_{zik})$ space such that the spectral densities were above a minimum threshold, *i.e.* we aim to achieve a desired coverage of the spectral density function. Specifically, we select

$$\begin{aligned}&\lambda_{xik} = \Delta\lambda_{xki}g_{xki}, \quad L_x = \frac{\pi}{2\Delta\lambda_{xki}}, \quad \Delta\lambda_{xki} = \frac{\nu}{l_{ix}R},\\ &\lambda_{yik} = \Delta\lambda_{yki}g_{yki}, \quad L_y = \frac{\pi}{2\Delta\lambda_{yki}}, \quad \Delta\lambda_{yki} = \frac{\nu}{l_{iy}R},\\ &\lambda_{zik} = \Delta\lambda_{zki}g_{zki}, \quad L_x = \frac{\pi}{2\Delta\lambda_{zki}}, \quad \Delta\lambda_{zki} = \frac{\nu}{l_{iz}R},\\ &g_{xki}^2 + g_{yki}^2 + g_{zki}^2 \le R^2,\end{aligned} \tag{48}$$

where $(g_{xki}, g_{yki}, g_{zki})$ are positive integers such that $(\Delta\lambda_{xki}g_{xki}, \Delta\lambda_{yki}g_{yki}, \Delta\lambda_{zki}g_{zki})$ defines equidistant grid points excluding the origin, and ν controls the desired coverage of the spectral density.

To see how ν controls this coverage, we use equation (48) to write the spectral density in (41) as a function of ν, giving

$$\begin{aligned}s_{ik} &= \sigma_i^2(2\pi)^{2/3}l_{ix}l_{iy}l_{iz}\exp\left[-\frac{\nu^2}{2R^2}(g_{xki}^2 + g_{yki}^2 + g_{zki}^2)\right]\\ &\ge \sigma_i^2(2\pi)^{2/3}l_{ix}l_{iy}l_{iz}\exp\left(-\nu^2/2\right),\end{aligned} \tag{49}$$

where the inequality holds because the maximum value of $(g_{xki}, g_{yki}, g_{zki})$ is R^2. Hence, we can see that ν controls the minimum spectral density, or alternatively we could view it as controlling the proportion of the volume under the spectral density function we wish the basis functions to cover. Taking this view, $\nu = 1$ gives ∼68%, $\nu = 2$ gives ∼95% and $\nu = 3$ gives ∼99.7% volume coverage. In this work, we use $\nu = 3.5$, corresponding to approximately 0.9996% coverage of the volume under the spectral density function.

Continuing with this reasoning, we can view R as governing the resolution with which the basis functions cover the spectral density. Whilst larger R will result in a better approximation to the covariance function it also increases the computational cost and, in general, will have diminishing returns in terms of error reduction. A suggestion is to increase R, subject to computational limits, whilst observing a substantial reduction in residuals or improvement in the out-of-sample log likelihood – described in detail in the next section. For both the simulation and real data experiments in this work we have used $R = 5$, which results in a total of $m = 38$ used basis functions for each of the six covariance functions, $k_i(\mathbf{x},\mathbf{x}')$,

$i = 1, 2, \ldots, 6$. Increasing R beyond this was found to give minimal improvement.

To complete the regression scheme, we now discuss the selection of the hyperparameters l_{ix}, l_{iy}, l_{iz} and σ_i, which at this stage are the only unknowns in the formulation.

4.5. Hyperparameter selection

The hyperparameters, l_{ix}, l_{iy}, l_{iz} and σ_i, for the posterior conditional distribution can be determined through optimization (Rasmussen, 2003). Typically, this is done by either maximizing the log marginal likelihood or using a cross-validation approach and maximizing the 'out-of-sample' log likelihood, *i.e.* the likelihood of observing a set of measurements not used in the regression, $\tilde{\mathbf{y}}$. Following the work by Gregg *et al.* (2020), which demonstrates that maximizing the out-of-sample log likelihood yields better results for line integral measurements, we determine the hyperparameters by solving

$$\begin{aligned}\Theta_* = \arg\max_{\Theta} \log p_\Theta(\tilde{\mathbf{y}}|\mathbf{y}) &= \arg\max_{\Theta} -0.5 \log\det \mathbb{C}[\tilde{\mathbf{y}}, \tilde{\mathbf{y}}|\mathbf{y}] \\ &- 0.5(\tilde{\mathbf{y}} - \mathbb{E}[\tilde{\mathbf{y}}|\mathbf{y}])^{\mathrm{T}} \mathbb{C}[\tilde{\mathbf{y}}, \tilde{\mathbf{y}}|\mathbf{y}]^{-1} (\tilde{\mathbf{y}} - \mathbb{E}[\tilde{\mathbf{y}}|\mathbf{y}]). \qquad (50)\end{aligned}$$

where Θ is a vector holding the hyperparameters introduced in (35) and $\log p_\Theta(\tilde{\mathbf{y}}|\mathbf{y})$ is the out-of-sample log likelihood. By extension of (47), we have that

$$\begin{aligned}\mathbb{E}[\bar{\tilde{\mathbf{y}}}|\mathbf{y}] &= \mathbb{E}[\tilde{\mathbf{y}}] + \boldsymbol{\phi}_{\tilde{y}} \big(\boldsymbol{\phi}_y^{\mathrm{T}} \mathbb{C}[\mathbf{e}, \mathbf{e}]^{-1} \boldsymbol{\phi}_y \\ &\quad + \mathbf{S}^{-1}\big)^{-1} \boldsymbol{\phi}_y^{\mathrm{T}} \mathbb{C}[\mathbf{e}, \mathbf{e}]^{-1} (\mathbf{y} - \mathbb{E}[\mathbf{y}]), \qquad (51) \\ \mathbb{C}[\tilde{\mathbf{y}}, \tilde{\mathbf{y}}|\mathbf{y}] &= \boldsymbol{\phi}_{\tilde{y}} \big(\boldsymbol{\phi}_y^{\mathrm{T}} \mathbb{C}[\mathbf{e}, \mathbf{e}]^{-1} \boldsymbol{\phi}_y + \mathbf{S}^{-1}\big)^{-1} \boldsymbol{\phi}_{\tilde{y}}^{\mathrm{T}} + \mathbb{C}[\mathbf{e}, \mathbf{e}].\end{aligned}$$

Note that it is not essential that a global optimum is found in this procedure; in fact, in many cases, setting the hyperparameters to some reasonable fixed values will produce excellent reconstructions. In the case of scanning 3DXRD we have found that setting the hyperparameters uniformly to the grain diameter gives reasonable results and can serve as a good initial guess for optimization.

5. Validation

To validate the presented regression method we have generated simulated scanning 3DXRD data using a previously developed algorithm (Henningsson, 2019). This tool has been used with success in the past (*cf.* Hektor *et al.*, 2019; Henningsson *et al.*, 2020) and can provide an understanding of the limitations and benefits of scanning 3DXRD reconstruction methods. Briefly, the simulation input is specified as a set of cubic single-crystal voxels featuring individual strains and orientations together with an experimental setup. We refer the reader to Henningsson (2019) for additional details on the simulation algorithm, with an undocumented implementation available via https://github.com/FABLE-3DXRD/S3DXRD/. Strain reconstructions from generated diffraction data were compared with ground-truth input strain as well as an additional reconstruction method described by Henningsson *et al.* (2020). This reconstruction method, previously referred to as 'algebraic strain refinement' (ASR), uses a voxel basis for strain reconstruction and can, in short, be described as solving a global WLSQ problem. This least-squares approach operates from the same average directional strain data as the presented GP method.

5.1. Single-crystal simulation test case

Diffraction from a tin (Sn) grain subject to a nonuniform strain tensor field has been simulated for the nonconvex grain topology depicted in Fig. 4.

The grain was assigned an orientation field by introducing linear gradients in the three Euler (Bunge notation) angles, φ_1, Φ, φ_2, as

$$\varphi_1 = \Phi = \varphi_2 = \frac{\pi}{180}\left(45 + \frac{x}{130v} + \frac{z}{24v}\right), \qquad (52)$$

where v = 5 µm was the used voxel size and the grain origin was set at the grain centroid in the xy plane and at the bottom edge of the grain in z (Fig. 4). The maximum grain size in each dimension x, y and z was 26, 26 and 13 voxels, respectively.

The strain field was defined by a set of Maxwell stress functions, which are a subset of the more general class of Beltrami stress functions,

$$\bar{\boldsymbol{\Phi}} = \begin{bmatrix} A(x, y, z) & B(x, y, z) & C(x, y, z) & 0 & 0 & 0 \end{bmatrix}^{\mathrm{T}}. \qquad (53)$$

To achieve a relatively simple, but not trivial, strain field the functions A, B and C were selected as a cubic polynomial:

$$\begin{aligned}A = B = C = \rho_1(x - t_x)^3 + \rho_2(y - t_y)^3 + \rho_3(z - t_z)^3 \\ + \rho_4(x - t_x)(y - t_y)(z - t_z). \qquad (54)\end{aligned}$$

The stress was converted to strain by the elastic compliance matrix $\mathbf{C}$, as

$$\begin{bmatrix} \epsilon_{xx} \\ \epsilon_{yy} \\ \epsilon_{zz} \\ \epsilon_{xy} \\ \epsilon_{xz} \\ \epsilon_{yz} \end{bmatrix} = \mathbf{C}^{-1} \mathcal{B} \bar{\boldsymbol{\Phi}} = \mathbf{C}^{-1} \begin{bmatrix} 6\rho_3(z - t_z) + 6\rho_2(y - t_y) \\ 6\rho_1(x - t_x) + 6\rho_3(z - t_z) \\ 6\rho_2(y - t_y) + 6\rho_1(x - t_x) \\ \rho_4(t_z - z) \\ \rho_4(t_y - y) \\ \rho_4(t_x - x) \end{bmatrix}. \qquad (55)$$

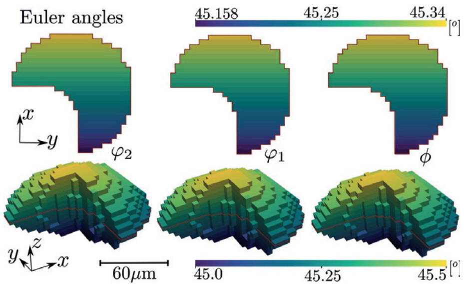

Figure 4
Grain topology input for diffraction simulation coloured by corresponding input Euler angle field in units of degrees. The top row represents central cuts through the 3D renderings below, as indicated by the red lines.

Table 1
Strain field parameters for diffraction simulation in units of µm.

ρ_1	ρ_2	ρ_3	ρ_4	t_x	t_y	t_z
100	100	100	1000	10	10	0

Table 2
Elasticity constants for single-crystal tin in units of GPa converted from Voigt notation as given by Darbandi *et al.* (2013).

C_{11}	C_{22}	C_{33}	C_{44}	C_{55}	C_{66}	C_{12}	C_{13}	C_{23}
72.3	72.3	88.4	48.0	44.0	44.0	59.4	35.8	35.8

Numerical values of the constants ρ_1, ρ_2, ρ_3, ρ_4, t_x, t_y and t_z are presented in Table 1.

The elasticity matrix for single-crystal tin was taken from Darbandi *et al.* (2013) (Table 2) and converted from Voigt notation to the used strain vector notation.

Parameters presented in Table 3 were used to define the experimental setup of the simulation.

The unit cell in Table 4 was used to define a strain-free lattice state.

Table 3
Experimental parameters used in single-grain simulation, corresponding to the results presented in Fig. 5.

Wavelength	0.22 Å
Sample-to-detector distance	163 mm
Detector pixel size	50 × 50 µm
Detector dimensions	2048 × 2048 pixels
Beam size	5 × 5 µm
ω rotation interval	[0, 180°]
$\Delta\omega$ step length	1°
Maximum grain size in x	130 µm
Maximum grain size in y	130 µm
Maximum grain size in z	65 µm

Table 4
Relaxed reference lattice parameters.

a	b	c	α	β	γ
5.81127 Å	5.81127 Å	3.17320 Å	90.0°	90.0°	90.0°

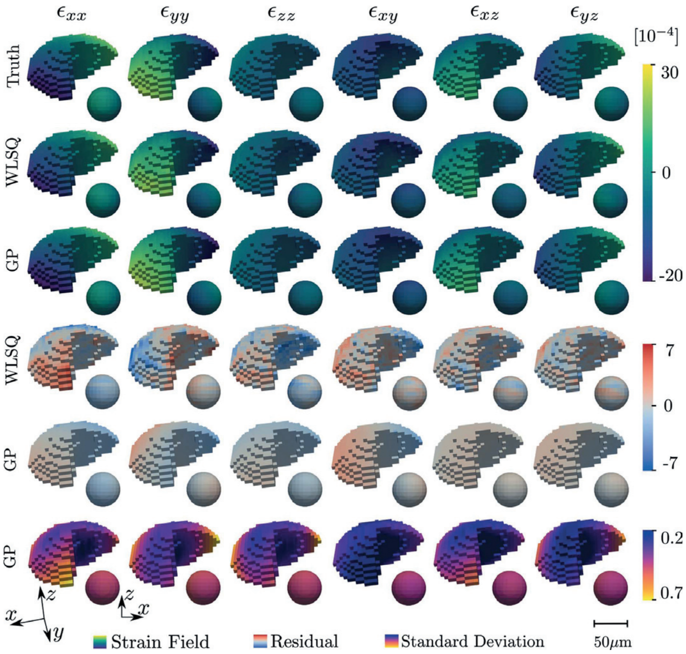

Figure 5
3D rendering of strain reconstructions for WLSQ and GP regression approaches. The top row defines the simulation ground truth as described in equation (55), with each column featuring a different strain component. The surface of the voxelated grain is presented, together with a pulled-out interior spherical cut centred at the grain centroid with a diameter of 50 µm. The corresponding coordinate systems are depicted in the bottom left of the figure. Three separate colormaps have been assigned to enhance contrast for the various fields. However, units of strain remain the same across plots ($\times 10^{-4}$). The residual field is defined as the difference between the ground truth and the reconstructed strain field.

The generated diffraction patterns were analysed on a per-z-slice basis using *ImageD11* (Wright, 2005) to compute scattering vectors and average crystal orientations for each z slice. The grain shape was then reconstructed on the basis of the normalized diffraction peak intensities using filtered backprojection (Poulsen & Schmidt, 2003). Next, the diffraction data were converted to average directional strains, as described in Section 3, and input into the WLSQ and GP reconstruction methods. The final reconstructed strain tensor fields are illustrated together with simulation ground-truth and residual fields in Fig. 5. The corresponding root-mean-square errors (RMSEs), mean absolute errors (MAEs) and maximum absolute errors for the residual fields are given in Table 5.

Hyperparameters were optimized using the L-BFGS-B algorithm, as implemented in *SciPy* (Jones *et al.*, 2001), with a maximum of ten line-search steps per iteration. Gradients were computed using automatic differentiation as implemented in *PyTorch* (Paszke *et al.*, 2019). In the first optimization iteration all hyperparameters were uniformly set to the grain radius. The convergence of the optimization is displayed in Fig. 6. The smoothness constraints for the WLSQ in the xy plane were set to 2.5×10^{-4}, limiting the maximum absolute difference in each strain tensor component between two neighbouring voxels [further details are provided by Henningsson *et al.* (2020)].

To assess how well the two methods (WSLQ and GP) utilize data, the MAE and RMSE of the reconstructed strain fields, as a function of the number of input measurement integrals, has been investigated. By measurements we here refer to the integral values, y_j, as defined in (24), together with their associated vectors ($\mathbf{p}_0$, $\hat{\boldsymbol{\kappa}}$, $\hat{\mathbf{n}}$). Measurements were permuted randomly and input into the WLSQ and GP reconstruction in initial sample sizes of 1, 2, 3, 4 and 5%, after which the sample size was increased in steps of 5% as indicated by the markers in Fig. 7. Since the GP hyperparameter optimization is a non-convex problem, the quality of any found local minima may vary between runs, and a better local minimum is not guaranteed with a larger measurement set owing to the different topology of the cost function. Thus, in order not to obscure the convergence rate of the GP method, we have selected to present results using fixed optimized hyperparameters found using 10% of the measurements as well as for non-optimized hyperparameters, set uniformly to the grain diameter. The resulting MAE and RMSE for the reconstructed residual fields were computed and averages over the six strain components were formed. The performance as a function of input measurements can be assessed by visual inspection of Fig. 7.

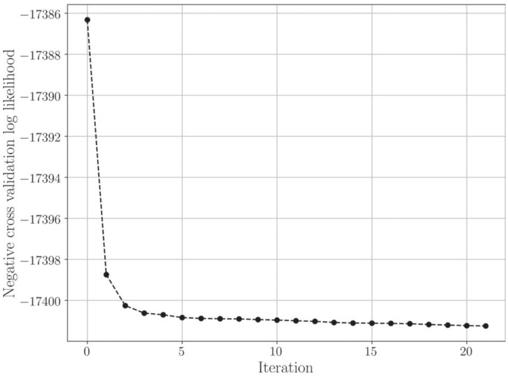

Figure 6
Negative cross-validation log likelihood reduction during hyperparameter optimization for the simulated grain presented in Figs. 4 and 5. Optimization was conducted using the L-BFGS-B algorithm as implemented in *SciPy* with a maximum of ten line-search steps per iteration. Gradients were computed using automatic differentiation as implemented in *PyTorch*.

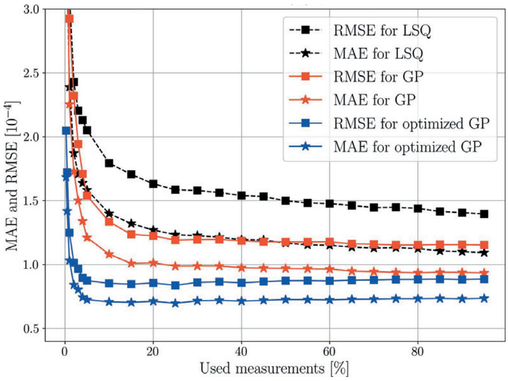

Figure 7
Average root-mean-square error (squares) and mean absolute error (stars) for the simulated grain presented in Figs. 4 and 5 as a function of used percentage of measurements. The performance of the Gaussian process regression (red and blue filled lines) is compared with that of the weighted least squares (black dashed lines). The RMSE and MAE were computed from the residual fields and averaged over the six reconstructed strain components to produce a scalar measure per reconstruction. Each point in the plot corresponds to a full 3D strain reconstruction using a random subset of the measured data.

Table 5
Root-mean-square errors, mean absolute errors and maximum absolute errors for the residual fields presented in Fig. 5.

The result of the Gaussian process regression is compared with the weighted least-squares fit (WLSQ). Values are unitless (strain) and on the same scale (10^{-4}) as in Fig. 5.

	RMSE		MAE		Maximum absolute error	
Strain	GP	WLSQ	GP	WLSQ	GP	WLSQ
ϵ_{xx}	1.322	2.076	1.101	1.737	2.791	7.42
ϵ_{yy}	1.042	1.371	0.846	0.999	3.856	6.094
ϵ_{zz}	0.887	1.489	0.769	1.157	1.914	6.736
ϵ_{xy}	1.122	1.511	0.955	1.172	2.778	6.306
ϵ_{xz}	0.24	1.04	0.198	0.798	1.506	4.85
ϵ_{yz}	0.48	0.958	0.399	0.742	1.34	4.652

5.2. Embedded tin grain

To further compare the GP and WLSQ reconstruction methods, analysis of a previously studied columnar tin grain has been included. This additional analysis further serves to show that the presented method is computationally feasible for state-of-the-art scanning 3DXRD data sets. Including hyperparameter optimization, the GP reconstruction was performed on a single CPU (Intel i7-8700K CPU @ 3.70 GHz) in 18 min and 9 s. As mentioned in Section 4.4, the computational complexity scales as $\mathcal{O}(Nm^2)$, where m is the number of basis functions and N the number of measurements. The corresponding runtime using fixed precomputed hyperparameters was 3.5 s. The data for this example from Hektor *et al.* (2019) and the input experimental parameters are identical to those presented in Table 3 except for the beam size, which was 0.25 µm. Similarly, the relaxed lattice state was as defined in Table 4. In the original experiment, the X-ray beam was scanned across the xy plane, producing a space-filling map of measurements. However, owing to time constraints, the data were collected for every second z layer, as seen in the rightmost column of Fig. 8. The reader is referred to the original publication (Hektor *et al.*, 2019) for further information on the experimental setup, sample and preliminary data analysis.

As the GP method uses a nonlocal basis representation of the strain field, as defined in equation (39), interpolation between measured slices is an automatic feature of the method. For the WLSQ method, although some interpolation scheme could be selected, we have chosen to present the raw reconstructions. This also highlights the added benefit of the

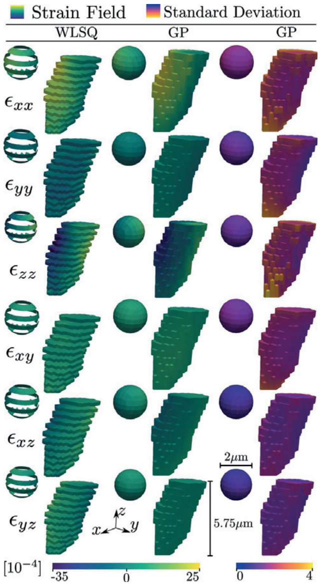

Figure 8
Reconstructed strain field using WLSQ (left column) and the GP method (middle column) of a columnar tin grain embedded within a polycrystalline sample. The rightmost column depicts the estimated uncertainty of the GP reconstruction. The 3D surface of the voxelated grain is presented together with a pull-out enlarged interior spherical cut with its centre at the grain centroid and a radius of 1 µm. Two separate colormaps have been assigned to enhance contrast for the various fields. However, the units of strain remain the same across plots ($\times 10^{-4}$).

selected basis for the GP method. Hyperparameter optimization and smoothness constraints for the WLSQ method were applied and selected as in Section 5.1.

6. Discussion

Comparison of the true and predicted fields in Fig. 5 for the two methods indicates that the reconstructions captured well the simulated input strain state. For all strain components in Table 5, both the RMSE and MAE are of the order of the expected experimentally limited strain resolution (10^{-4}). We note, however, that the GP has consistently lower RMSE, MAE and maximum absolute errors in comparison with the WLSQ. The enhanced performance is attributed to the joint effect of the equilibrium prior, optimized correlation kernel and nonlocal basis selection.

The results of Table 5 indicate that, in general, the strain tensor *z* components enjoy more accurate reconstructions than the *xy* components. This observation is in line with previous work (Margulies *et al.*, 2002; Lionheart & Withers, 2015; Henningsson *et al.*, 2020) and is explained by the nonuniform sampling of strain taking place in scanning 3DXRD. The GP regression quantifies this phenomenon via the reconstructed standard deviation fields (Fig. 5, bottom row). Indeed the uncertainty in the predicted mean is elevated for the *xx* and *yy* components, which show similar patterns to the residual fields.

On the performance of the two methods, Fig. 7 indicates that fewer measurements are needed for the GP compared with the WLSQ approach whilst achieving a more accurate result. Little reduction in the RMSE and MAE is seen for the GP after about 50% of the measurements have been introduced (about 20% for the optimized GP version). This could imply that it is possible to retrieve approximations to the full strain tensor field from reduced scanning 3DXRD data sets. This could be attractive as scanning 3DXRD typically has time-consuming measurement sequences. From Fig. 7 it is also clear that the final errors in reconstruction will be nonzero. This is so because the error in reconstruction is made up of both bias and variance. While the variance can be reduced by adding more measurements, the bias is due to systematic errors arising from incorrect model assumptions such as the line integral approximation, the truncated covariance basis series expansion, the Taylor series expansion related to the strain measure, the directional approximation of $\hat{\boldsymbol{\kappa}}$ and possibly further unknown sources. Since the bias cannot be removed by adding more measurements, the reconstruction error will face a lower nonzero bound.

It is evident that the reconstructed fields have maximum uncertainties at the boundary of the grain, as can be seen from the cutout spheres of Figs. 5 and 8. The elevated standard deviation at the grain surface is explained by the tomographic measurement procedure, which has an increasing measurement density towards the grain centroid. Furthermore, as measurements do not exist outside of the grain, points lying on the grain surface will, in some sense, have a reduced number of points that they are correlated with. In addition to these effects, the selected line beam approximation may have an impact on the grain boundary errors. If the full 3D profile of the beam had been used instead, a higher number of scans that partially graze the grain boundary could have been included in the analysis, thus increasing the measurement density at the boundary. In the current model, if a scan has a geometric centre that does not intersect the grain, it has no impact on the reconstruction, even though the full 3D beam may have some overlap with the grain. The main challenge with using a full 3D beam profile, rather than the line approximation, is to maintain analytical expressions during integration of the partial derivatives of the basis functions over the illuminated domain.

The predicted strain field of the columnar tin grain of Fig. 8 shows similar patterns for the two regression methods. The uncertainty is again seen to be reduced on the interior of the grain, and the posterior standard deviation is of the order of the experimental strain resolution of 10^{-4}. This validates the applicability of GP regression on real state-of-the-art scanning 3DXRD synchrotron data.

6.1. Outlook

Two future potential improvements to strain predictions should be mentioned. Firstly, the selection of covariance function, although restricted to give a positive definite covariance matrix, is not unique; other selections may outperform the squared-exponential kernel used here. Secondly, for polycrystalline samples, additional prior knowledge of grain boundary strain could be extracted by considering the total sample grain map and that tractions must cancel on the interfaces [*i.e.* incorporating and extending the work of Hendriks, Gregg *et al.* (2019)]. Two challenges with this exist: (i) the uncertainty in reconstructed grain shapes leading to uncertainty in the interface normal and (ii) uncertainty in the per-point grain orientation leading to uncertainty in the grain compliance. The first of these challenges may be addressed by using near-field techniques (Viganò *et al.*, 2016) in conjunction with scanning 3DXRD to achieve higher-resolution grain maps.

7. Conclusions

Intragranular strain estimation from scanning 3DXRD data using a Gaussian process is shown to provide a new and effective strain reconstruction method. By selecting a continuous differentiable Fourier basis for the Beltrami stress functions, a static equilibrium prior can be incorporated into the reconstruction, guaranteeing that the predicted strain field will satisfy the balance of both angular and linear momentum. The regression procedure results in a per-point estimated mean strain and per-point standard deviations, providing new means of estimating the per-point uncertainty of the reconstruction. Furthermore, the proposed method incorporates the spatial structure of the strain field by making use of a generic covariance function, optimized by maximizing the out-of-sample log likelihood. With the introduction of these three features, the equilibrium prior, the per-point uncertainty quantification and the optimized spatial smoothness constraints, the proposed regression method addresses weaknesses discussed in previously proposed reconstruction methods. Specifically, in comparison with a previously proposed weighted least-squares approach, it is found, from numerical simulations, that the Gaussian process regression consistently produces reconstructions with lower root-mean-square errors, mean absolute errors and maximum absolute errors across strain components. Moreover, it is shown that the reconstruction error as a function of the number of available measurements is reduced for the Gaussian process.

APPENDIX *A*
Error related to measurement approximations

To demonstrate the accuray of the approximations made in (15), we investigate the error associated with the fact that both strain and crystal orientation may vary along the ray path. To do this we must consider that the strain computed from (15) is further assigned to planes with approximate normals given by (17). Thus, there is a twofold error source to capture in the following analysis, arising partly from the integrated Taylor series expansion,

$$y = \frac{1}{V}\int_{\mathcal{L}} \hat{\boldsymbol{\kappa}}^{\mathrm{T}} \boldsymbol{\epsilon}_{\omega} \hat{\boldsymbol{\kappa}} \, \mathrm{d}v \simeq 1 - \frac{\langle \mathbf{G}_{\omega} \rangle^{\mathrm{T}} \mathbf{G}_{\omega}^{(0)}}{(\mathbf{G}_{\omega}^{(0)})^{\mathrm{T}} \mathbf{G}_{\omega}^{(0)}}, \tag{56}$$

and partly from assigning the average strain value, y, to an incorrect plane normal,

$$\hat{\boldsymbol{\kappa}} \simeq \langle \mathbf{G}_{\omega} \rangle / || \langle \mathbf{G}_{\omega} \rangle ||, \tag{57}$$

which in reality is not fixed but warps across the crystal $[\hat{\boldsymbol{\kappa}} = \hat{\boldsymbol{\kappa}}(\mathbf{x})]$.

To compute the error in strain we consider first the true average strain for a single line-integral measurement, y_{true}, existing in a fixed direction, $\hat{\boldsymbol{\kappa}}$:

$$y_{\mathrm{true}} = \frac{1}{L}\int_{\mathcal{L}} \hat{\boldsymbol{\kappa}}^{\mathrm{T}} \boldsymbol{\epsilon}_{\omega} \hat{\boldsymbol{\kappa}} \, \mathrm{d}s = \frac{1}{L} \hat{\boldsymbol{\kappa}}^{\mathrm{T}} \left(\int_{\mathcal{L}} \boldsymbol{\epsilon}_{\omega} \, \mathrm{d}s \right) \hat{\boldsymbol{\kappa}} = \hat{\boldsymbol{\kappa}}^{\mathrm{T}} \langle \boldsymbol{\epsilon}_{\omega} \rangle \hat{\boldsymbol{\kappa}}, \tag{58}$$

where the average strain tensor $\langle \boldsymbol{\epsilon}_{\omega} \rangle$ is unknown from the experiment. We stress that we are interested in the true strain for a fixed $\hat{\boldsymbol{\kappa}}$ since this is the normal that the approximation of (56) will eventually be assigned to. The sought absolute error now becomes

$$e_y = y - y_{\mathrm{true}} = 1 - \frac{\langle \mathbf{G}_{\omega} \rangle^{\mathrm{T}} \mathbf{G}_{\omega}^{(0)}}{(\mathbf{G}_{\omega}^{(0)})^{\mathrm{T}} \mathbf{G}_{\omega}^{(0)}} - \hat{\boldsymbol{\kappa}}^{\mathrm{T}} \langle \boldsymbol{\epsilon}_{\omega} \rangle \hat{\boldsymbol{\kappa}}. \tag{59}$$

For a given set of Miller planes, strain field, Euler angle field, reference unit cell and integration domain $\mathcal{L}$, equation (59) can be evaluated. To do so, two integrations must be performed, yielding individually $\langle \mathbf{G}_{\omega} \rangle$ and $\langle \boldsymbol{\epsilon}_{\omega} \rangle$. In the following we attempt to characterize (59) for a fixed reference unit cell (Table 4) while letting the remaining parameters vary according to a stochastic model described below. The goal is to study the distribution of the absolute errors as a function of increasing levels of intragranular strain and mosaicity to understand the limitations of the proposed measurement approximations.

We consider a spherical grain of fixed radius R_0 = 1.0 centred at the origin and define a random integration domain, $\mathcal{L}$, as

$$\begin{aligned}
&\mathbf{x} = \mathbf{p}_0 + s\hat{\mathbf{n}}, \quad s \in [0, L], \\
&\mathbf{p}_0 = R_0 \begin{bmatrix} \cos(a_1)\sin(a_2) \\ \sin(a_1)\sin(a_2) \\ \cos(a_2) \end{bmatrix}, \quad a_1 \sim \mathcal{U}(0, 2\pi), \quad a_2 \sim \mathcal{U}(0, \pi), \\
&\hat{\mathbf{n}} = \begin{bmatrix} \cos(b_1)\sin(b_2) \\ \sin(b_1)\sin(b_2) \\ \cos(b_2) \end{bmatrix}, \quad b_1 \sim \mathcal{U}(0, 2\pi), \quad b_2 \sim \mathcal{U}(0, \pi),
\end{aligned} \tag{60}$$

where L is determined by the sphere line intersection, $\mathbf{p}_0$ is a random uniform point on the sphere surface and $\hat{\mathbf{n}}$ is a unit vector also drawn from a random uniform distribution denoted $\mathcal{U}(\cdot, \cdot)$. We further define $\mathbf{G}_{hkl}$ as

$$\mathbf{G}_{hkl} = [h, k, l]^{\mathrm{T}}, \quad h, k, l \sim \mathcal{U}(-7, 7), \tag{61}$$

where the distribution has been limited to the interval $[-7, 7]$ to represent typical scanning 3DXRD data sets. Pseudo-random strain and orientation fields are introduced by constructing random samples of superimposed Fourier waves:

$$\epsilon_{xx}(\mathbf{x}) = \frac{A_\mathrm{s}}{f_0^{\max}} f_0(\mathbf{x}), \quad \epsilon_{yy}(\mathbf{x}) = \frac{A_\mathrm{s}}{f_1^{\max}} f_1(\mathbf{x}), \quad \epsilon_{zz}(\mathbf{x}) = \frac{A_\mathrm{s}}{f_2^{\max}} f_2(\mathbf{x}),$$
$$\epsilon_{xy}(\mathbf{x}) = \frac{A_\mathrm{s}}{f_3^{\max}} f_3(\mathbf{x}), \quad \epsilon_{xz}(\mathbf{x}) = \frac{A_\mathrm{s}}{f_4^{\max}} f_4(\mathbf{x}), \quad \epsilon_{yz}(\mathbf{x}) = \frac{A_\mathrm{s}}{f_5^{\max}} f_5(\mathbf{x}),$$
$$\varphi_1(\mathbf{x}) = \frac{A_\mathrm{e}}{f_6^{\max}} f_6(\mathbf{x}), \quad \Phi(\mathbf{x}) = \frac{A_\mathrm{e}}{f_7^{\max}} f_7(\mathbf{x}), \quad \varphi_2(\mathbf{x}) = \frac{A_\mathrm{e}}{f_8^{\max}} f_8(\mathbf{x}),$$
$$f_k(\mathbf{x}) = \sum_{i=1}^{n=25} c_i \sin\left[f_{ix}(x + p_{ix})\right] \sin\left[f_{iy}(y + p_{iy})\right] \sin\left[f_i z(z + p_{iz})\right],$$
$$c_i \sim \mathcal{U}(-1, 1), \quad f_{ix}, f_{iy}, f_{iz} \sim \mathcal{U}\left(\frac{10}{R_0}, \frac{1}{2R_0}\right),$$
$$p_{ix}, p_{iy}, p_{iz} \sim \mathcal{U}(-R_0, R_0), \;\; f_k^{\max} = \arg\max_{\mathbf{x}} |f_k(\mathbf{x})|, \;\; \mathbf{x}^\mathrm{T}\mathbf{x} < R_0^2, \tag{62}$$

where the two scale parameters A_s and A_e regulate the maximum difference between any two points within the field and allow for the strain field (scaled by A_s) and orientation field (scaled by A_e) to vary on different scales simultaneously. The necessary normalizing factors $f_k^{\max}$ were computed by sampling the fields on equidistant grids of $\sim$1000 points and selecting the maximum absolute value. Typical fields generated by the model can be seen in Fig. 9.

Using the above stochastic model we have performed repetitive sampling of 1000 line integral measurements for each of 100 grain states while letting A_s and A_e successively increase between samples. The results of this analysis are presented in the histograms of Fig. 10, where each histogram corresponds to a total of 100 000 data points (100 × 1000) and a fixed maximum field variation (A_s, A_e). The average strain $\langle \boldsymbol{\epsilon}_\omega \rangle$ and diffraction vector $\langle \mathbf{G}_\omega \rangle$ involved in (59) were computed by first-order numerical integration using a total of 20 integration points along each domain $\mathcal{L}$. The reference orientation matrix, $\mathbf{U}_0$, was computed by averaging over $\sim$1000 equally spaced points of the sphere.

The results of Fig. 10 show that the error in (59) increases with the heterogeneity of both orientation and strain state. For small strains ($\leq 50 \times 10^{-4}$) and moderate mosaic spreads ($\leq 1^\circ$) the largest errors are a few times that of the experimental resolution limit (10^{-4}) and the bulk (>95%) of measurements are contained within [$\pm 10^{-4}$] units of strain. For samples featuring larger mosaicity (>1.0°) and strain variation ($>75 \times 10^{-4}$) the approximation starts to break down. At such elevated levels of deformation, however, one has to first consider if the small-strain approximation made in (7) is still valid.

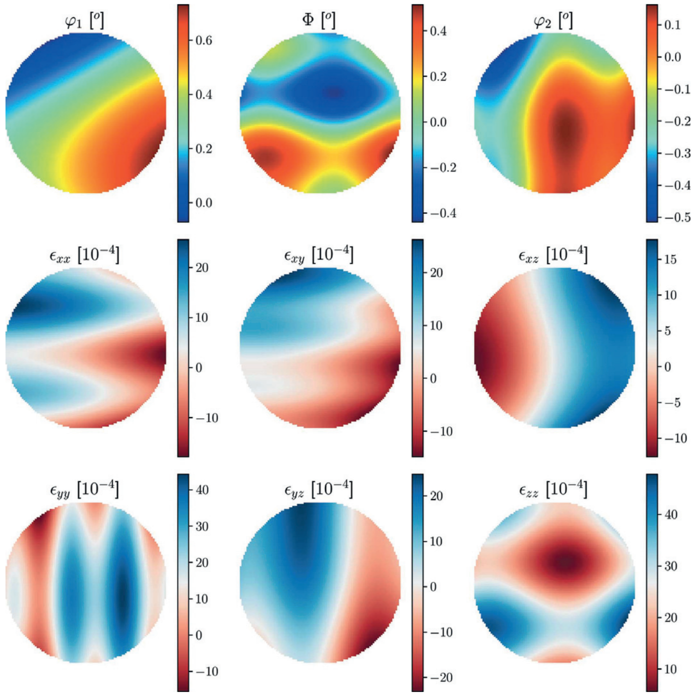

Figure 9
Typical Euler angle (top row) and strain (bottom and middle rows) fields generated by the stochastic model presented in equation (62). The presented fields exist on a spherical domain for which a central cut slice has been presented above ($z = 0$). The maximum difference parameters of the field were $A_\mathrm{e} = 1.4$ and $A_\mathrm{s} = 75 \times 10^{-4}$.

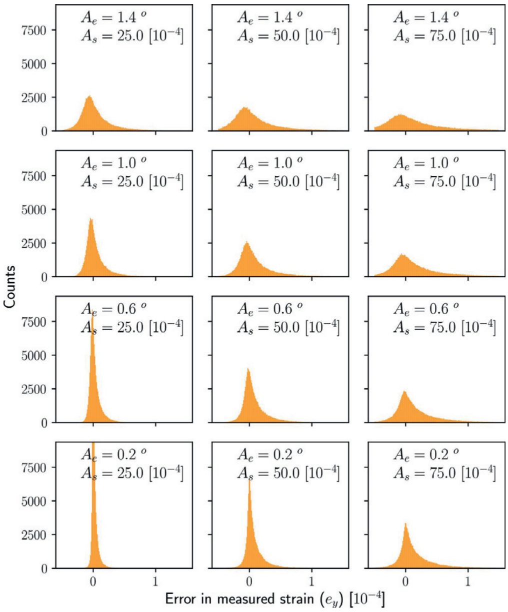

Figure 10
Absolute error (59) computed for the stochastic model defined through equations (60), (61) and (62). For each histogram 1000 random line integral measurements have been sampled from each of 100 spherical crystal states, resulting in a total of 100 000 data points per histogram. The maximum field difference in Euler angles and strain (A_e and A_s) increases from bottom to top and left to right, respectively, as indicated by the figure labels. (Note that the maximum counts of the bottom-left plot have been clipped in order to facilitate equal axes between subplots while maintaining good visibility of the histograms.)

Specifically, for the synthetic data set presented in this paper (Figs. 4 and 5) we conclude that the input strain and orientation fields will give rise to a negligible error, $e_y < 10^{-4}$. Likewise for the tin grain presented in Fig. 8, on the basis of the observed diffraction peak spread in ω, the mosaic spread is <1.0° and thus e_y is negligible.

Acknowledgements

The authors are grateful for the beamtime provided by the ESRF, beamline ID11, where the diffraction data were collected (Hektor *et al.*, 2019). The authors also thank Stephen Hall for valuable input on the manuscript during the final stages of writing the paper.

References

Alpers, A., Poulsen, H. F., Knudsen, E. & Herman, G. T. (2006). *J. Appl. Cryst.* **39**, 582–588.
Borbely, A., Renversade, L., Kenesei, P. & Wright, J. (2014). *J. Appl. Cryst.* **47**, 1042–1053.
Darbandi, P., Bieler, T., Pourboghrat, F. & Lee, T. (2013). *J. Electron. Mater.* **42**, 201–214.
Edmiston, J. K., Barton, N. R., Bernier, J. V., Johnson, G. C. & Steigmann, D. J. (2011). *J. Appl. Cryst.* **44**, 299–312.
Gregg, A., Hendriks, J., Wensrich, C. & O'Dell, N. (2020). *Nucl. Instrum. Methods Phys. Res. B*, **480**, 67–77.
Hayashi, Y., Hirose, Y. & Seno, Y. (2015). *J. Appl. Cryst.* **48**, 1094–1101.
Hayashi, Y., Setoyama, D., Hirose, Y., Yoshida, T. & Kimura, H. (2019). *Science*, **366**, 1492–1496.
Hayashi, Y., Setoyama, D. & Seno, Y. (2017). *Mater. Sci. Forum*, **905**, 157–164.
Hektor, J., Hall, S. A., Henningsson, N. A., Engqvist, J., Ristinmaa, M., Lenrick, F. & Wright, J. P. (2019). *Materials*, **12**, 446.
Hendriks, J., Gregg, A., Wensrich, C. & Wills, A. (2019). *Strain*, **55**, e12325.
Hendriks, J. N., Wensrich, C. M. & Wills, A. (2020). *Strain*, **56**, e12341.
Hendriks, J., Wensrich, C., Wills, A., Luzin, V. & Gregg, A. (2019). *Nucl. Instrum. Methods Phys. Res. B*, **444**, 80–90.
Henningsson, A. (2019). Student paper, Lund University, Sweden, http://lup.lub.lu.se/student-papers/record/8972668.
Henningsson, N. A., Hall, S. A., Wright, J. P. & Hektor, J. (2020). *J. Appl. Cryst.* **53**, 314–325.
Jidling, C., Hendriks, J., Wahlström, N., Gregg, A., Schön, T. B., Wensrich, C. & Wills, A. (2018). *Nucl. Instrum. Methods Phys. Res. B*, **436**, 141–155.
Jones, E., Oliphant, T., Peterson, P., *et al.* (2001). *SciPy*, http://www.scipy.org/.
Lauridsen, E. M., Schmidt, S., Suter, R. M. & Poulsen, H. F. (2001). *J. Appl. Cryst.* **34**, 744–750.
Lionheart, W. R. B. & Withers, P. J. (2015). *Inverse Probl.* **31**, 045005.
Margulies, L., Lorentzen, T., Poulsen, H. & Leffers, T. (2002). *Acta Mater.* **50**, 1771–1779.
Markussen, T., Fu, X., Margulies, L., Lauridsen, E. M., Nielsen, S. F., Schmidt, S. & Poulsen, H. F. (2004). *J. Appl. Cryst.* **37**, 96–102.
Moscicki, M., Kenesei, P., Wright, J., Pinto, H., Lippmann, T., Borbély, A. & Pyzalla, A. (2009). *Mater. Sci. Eng. A*, **524**, 64–68.
Nervo, L., King, A., Wright, J. P., Ludwig, W., Reischig, P., Quinta da Fonseca, J. & Preuss, M. (2014). *J. Appl. Cryst.* **47**, 1402–1416.
Oddershede, J., Schmidt, S., Poulsen, H. F., Sørensen, H. O., Wright, J. & Reimers, W. (2010). *J. Appl. Cryst.* **43**, 539–549.
Ottosen, N. S. & Ristinmaa, M. (2005). *The Mechanics of Constitutive Modeling.* Kidlington: Elsevier.
Paszke, A., Gross, S., Massa, F., Lerer, A., Bradbury, J., Chanan, G., Killeen, T., Lin, Z., Gimelshein, N., Antiga, L., Desmaison, A., Kopf, A., Yang, E., DeVito, Z., Raison, M., Tejani, A., Chilamkurthy, S., Steiner, B., Fang, L., Bai, J. & Chintala, S. (2019). *Advances in Neural Information Processing Systems 32*, edited by H. Wallach, H. Larochelle, A. Beygelzimer, F. dAlché-Buc, E. Fox & R. Garnett, pp. 8024–8035. Curran Associates. http://papers.neurips.cc/paper/9015-pytorch-an-imperative-style-high-performance-deep-learning-library.pdf.
Poulsen, H. (2004). PhD thesis, Risø National Laboratory, Roskilde, Denmark.
Poulsen, H. F. & Fu, X. (2003). *J. Appl. Cryst.* **36**, 1062–1068.
Poulsen, H. F., Nielsen, S. F., Lauridsen, E. M., Schmidt, S., Suter, R. M., Lienert, U., Margulies, L., Lorentzen, T. & Juul Jensen, D. (2001). *J. Appl. Cryst.* **34**, 751–756.
Poulsen, H. F. & Schmidt, S. (2003). *J. Appl. Cryst.* **36**, 319–325.
Rasmussen, C. E. (2003). *Advanced Lectures on Machine Learning*, Lecture Notes in Computer Science, Vol. 3176, pp. 63–71. Berlin, Heidelberg: Springer.
Reischig, P. & Ludwig, W. (2020). *Curr. Opin. Solid State Mater. Sci.* **24**, 100851.
Schmidt, S. (2014). *J. Appl. Cryst.* **47**, 276–284.
Sharma, H., Huizenga, R. M. & Offerman, S. E. (2012). *J. Appl. Cryst.* **45**, 693–704.
Solin, A. & Särkkä, S. (2020). *Stat. Comput.* **30**, 419–446.
Viganò, N., Tanguy, A., Hallais, S., Dimanov, A., Bornert, M., Batenburg, K. J. & Ludwig, W. (2016). *Sci. Rep.* **6**, 20618.
Wright, J. (2005). *ImageD11*, https://github.com/FABLE-3DXRD/ImageD11/.

Paper C

Axel Henningsson and Stephen A. Hall .

xrd_simulator: 3D X-ray diffraction simulation software supporting 3D polycrystalline microstructure morphology descriptions

In: Journal of Applied Crystallography 56, 282–292. (2023)

JOURNAL OF
APPLIED
CRYSTALLOGRAPHY

ISSN 1600-5767

xrd_simulator: 3D X-ray diffraction simulation software supporting 3D polycrystalline microstructure morphology descriptions

Axel Henningsson* and Stephen A. Hall

Div. Solid Mechanics, Lund University, Ole Römers väg 1, Lund, Sweden. *Correspondence e-mail: axel.henningsson@solid.lth.se

Received 14 June 2022
Accepted 16 November 2022

Edited by A. Borbély, Ecole National Supérieure des Mines, Saint-Etienne, France

Keywords: X-ray diffraction; 3DXRD; simulation tools; polycrystalline microstructure; computer programs.

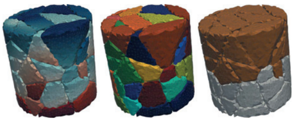

An open source Python package named *xrd_simulator*, capable of simulating geometrical interactions between a monochromatic X-ray beam and a polycrystalline microstructure, is described and demonstrated. The software can simulate arbitrary intragranular lattice variations of single crystals embedded within a multiphase 3D aggregate by making use of a tetrahedral mesh representation where each element holds an independent lattice. By approximating the X-ray beam as an arbitrary convex polyhedral region in space and letting the sample be moved continuously through arbitrary rigid motions, data from standard and non-standard measurement sequences can be simulated. This implementation is made possible through analytical solutions to a modified, time-dependent version of the Laue equations. The software, which primarily targets three-dimensional X-ray diffraction microscopy (high-energy X-ray diffraction microscopy) type experiments, enables the numerical exploration of which sample quantities can and cannot be reconstructed for a given acquisition scheme. Similarly, *xrd_simulator* targets investigations of different measurement sequences in relation to optimizing both experimental run times and sampling.

1. Introduction

Three-dimensional X-ray diffraction (3DXRD) covers a class of experimental techniques that facilitate the nondestructive study of polycrystalline materials on an inter- and intra-granular level. In its original form, 3DXRD, which is sometimes referred to as high-energy X-ray diffraction microscopy (HEDM) (Bernier *et al.*, 2020), was pioneered by Poulsen (2004) and co workers. The data for 3DXRD are acquired using monochromatic, parallel, hard X-ray beams (10–100 keV) and a 2D area detector that integrates the diffraction signal from a rotating polycrystalline sample. The samples typically studied using 3DXRD, in contrast to those studied with powder diffraction techniques, are polycrystals with a limited number of grains, allowing individual diffraction peaks to be resolved on the 2D detector image. The recorded diffraction peaks can be analysed using a plethora of methods to reconstruct, among other things, grain orientations (Lauridsen *et al.*, 2001; Sharma *et al.*, 2012*a*,*b*), grain topology (Poulsen & Schmidt, 2003; Poulsen & Fu, 2003; Alpers *et al.*, 2006; Batenburg *et al.*, 2010), and grain strain or stress tensors (Oddershede *et al.*, 2010). The beam cross section and angular step size in 3DXRD must be selected such that a limited number of grains are illuminated during detector readout, limiting spot overlap and revealing the individual diffraction peaks from grains within the aggregate in the 2D detector images. 3DXRD geometries using a narrow beam cross section, smaller than the grain diameter, are often referred to as scanning-3DXRD (Hayashi *et al.*, 2015). These methods allow for the study of intragranular effects (Hayashi *et al.*, 2017; Hektor *et al.*, 2019; Henningsson *et al.*, 2020) at the cost of having to scan the sample across the narrow beam to collect the full diffraction signal. Another branch of 3DXRD is diffraction contrast tomography (DCT) (Ludwig *et al.*, 2009), where the detector is placed close to the sample such that the projection of individual grain shapes can be seen in the recorded diffraction image. Using iterative reconstruction methods [*e.g.* Reischig & Ludwig (2020)] in conjunction with DCT methods, excellent resolution of the grain shapes can be achieved at the cost of strain resolution (Nervo *et al.*, 2014). For an in-depth summary of the state of the art in hard X-ray microscopy see Poulsen (2020).

In all of the aforementioned 3DXRD methods, to reconstruct the sample it is necessary to model the sample on a granular or even intragranular level, which stands in contrast to powder-like diffraction experiments where the sample is treated as a continuum. To produce a diffraction pattern of sufficient quality to reconstruct the desired sample details requires selection of experimental parameters such as sample rotation axis, sample translations, X-ray beam shape, detector geometry and sample rotation sequence adapted to the position, shape, orientation and strain of the individual crystals within the polycrystalline aggregate to be studied. The interactions between these acquisition and sample characteristics regulate the quality/resolution of the reconstructions of the sample microstructure as well as the total acquisition times, which can become unrealistically long. The question as to how measurements should be acquired and how many acquisitions are needed to recover a target quantity in a polycrystal are, thus, key in the field of 3DXRD. For instance, by analytical means, Lionheart & Withers (2015) showed that the full strain tensor could be recovered using direct methods if the diffracting sample was allowed to rotate consecutively around three orthogonal axes. On the other hand, using mechanical constraints, it was found that strain reconstructions could be achieved from single axis rotation data (Henningsson & Hendriks, 2021). On another note, recent advances in acquisition strategies for laboratory-based DCT (Oddershede *et al.*, 2022) suggest that more complex scan geometries could be used to improve sampling in 3DXRD experiments. From a practical point of view, considering scanning 3DXRD, the typical wall times to measure a single sample volume are often in the range of hours or even days [*e.g.* Hektor *et al.* (2019)], making efficient measurement schemes that can reduce the amount of data that need to be collected attractive.

As 3DXRD is a high-energy synchrotron technique, access to experiments is precious and the number of facilities in the world that offer 3DXRD controls the pace of the method development. An alternative route for development is the use of software simulation tools that can serve as a research primer, allowing ideas to be established or discarded at a theoretical stage. Many tools for simulating X-ray diffraction from individual crystals exist [*e.g.* Macrae *et al.* (2006), Momma & Izumi (2008), Soyer (1996), Campbell (1995), Huang (2010), Kanagasabapathy (2016), Weber (1997) and Laugier & Bochu (2001)]. Additional tools exist for simulating 2D diffraction patterns from arbitrarily textured samples (Poulsen, 2004; Le Page & Gabe, 1979; E *et al.*, 2018; Huang *et al.*, 2021*a*,*b*; Knudsen, 2009; Bernier *et al.*, 2011; Pagan *et al.*, 2020; Fang *et al.*, 2020; Sørensen *et al.*, 2012). However, for many questions related to 3DXRD techniques, the geometry of the polycrystal grains and the X-ray beam, together with intragranular lattice variations, must be accounted for. At the same time, the diffracting sample must be allowed to move along an arbitrary rigid body motion path, to explore different scan sequences.

Frameworks similar to those developed by Wong *et al.* (2013) and Song *et al.* (2008) provide important contributions in this direction, incorporating a spatial description of the sample microstructure by making use of a tetrahedral mesh representation. However, this previous work was limited to full-field illumination and sample motions derived from rotations about a fixed axis. Finite beam sizes, illuminating a subvolume of the samples during diffraction, is especially important to simulate scanning 3DXRD were the beam cross section is smaller than the sample.

In conclusion, no open source software exists with the set of capabilities needed to freely explore acquisition strategies in 3DXRD [see supplementary material of Huang *et al.* (2021*b*) for a useful summary of existing software capabilities].

We report on the development of new software, named *xrd_simulator*, that draws on concepts described by Fang *et al.* (2020) and extends the work of Wong *et al.* (2013), to take the beam geometry, the grain shapes and intragranular lattice variations into account using a tetrahedral mesh representation. Additionally, we derive analytical solutions to the Laue equations to calculate the diffraction volumes and vectors for arbitrary positions and orientations of the sample. This enables simulation of diffraction as the sample undergoes user-specified rigid body motion sequences during diffraction readout and can be viewed as a generalization of the equations provided by Wong *et al.* (2013) for single-axis rotation. By making *xrd_simulator* open source and easily accessible, we provide a means to accelerate the rate at which 3DXRD-type methodologies can evolve.

The paper is structured as follows. In Section 2 we present the diffraction approximations made in *xrd_simulator* and derive the analytical expressions needed for its implementation. In Sections 3 and 4 we comment on the software architecture and availability and provide references to external tutorials and documentation. In Section 5 we comment on the computational aspects of the software and provide sample benchmarks. Finally, in Section 6 we provide some concluding remarks. Additionally, we append a case study comparison of simulations performed with *xrd_simulator* and data collected at the ESRF ID11 beamline.

2. Diffraction approximations

X-ray diffraction is computed in *xrd_simulator* by defining a series of mathematical model components, including a polycrystal, an X-ray beam and a detector. In this section we describe the formulation of these models and discuss their interactions. In the following, any vector **v** is normalized by the inclusion of a symbol $\hat{}$ such that $\hat{\mathbf{v}} = \mathbf{v}/(\mathbf{v}^{\mathrm{T}}\mathbf{v})^{1/2}$.

Four Cartesian coordinate systems are used; the laboratory coordinate system, the sample coordinate system, the crystal coordinate system and the detector coordinate system (Fig. 1). The crystal, sample and detector coordinate systems are all fixed in relation to a lattice, a polycrystalline sample and a detector plane, respectively. Transformations of these three coordinates systems are tracked by the laboratory coordinate system, which serves as a global frame of reference.

The morphology of a polycrystalline sample is defined in the global laboratory reference frame with axes $\hat{\mathbf{x}}_{\mathrm{l}}, \hat{\mathbf{y}}_{\mathrm{l}}, \hat{\mathbf{z}}_{\mathrm{l}}$. As a starting point, the internal sample coordinate system, with axes $\hat{\mathbf{x}}_{\mathrm{s}}, \hat{\mathbf{y}}_{\mathrm{s}}, \hat{\mathbf{z}}_{\mathrm{s}}$, is aligned with the laboratory system. Once the sample has moved, to transform a point $\mathbf{p}_{\mathrm{l}}$ from laboratory to sample coordinates we apply a rigid body motion through a rotation matrix, **R**, and a translation vector, $\Delta\mathbf{x}$ as

$$\mathbf{p}_{\mathrm{s}} = \mathbf{R}\mathbf{p}_{\mathrm{l}} + \Delta\mathbf{x}. \tag{1}$$

The single crystal elements constituting a polycrystalline sample each have their own crystal coordinate reference frame with axes $\hat{\mathbf{x}}_{\mathrm{c}}, \hat{\mathbf{y}}_{\mathrm{c}}, \hat{\mathbf{z}}_{\mathrm{c}}$. A vector, $\mathbf{p}_{\mathrm{c}}$, described in crystal coordinates is transformed to the sample frame via the crystal orientation matrix, **U**, as

$$\mathbf{p}_{\mathrm{s}} = \mathbf{U}\mathbf{p}_{\mathrm{c}}. \tag{2}$$

The detector coordinate system, with in-plane axes $\hat{\mathbf{z}}_{\mathrm{d}}$, $\hat{\mathbf{y}}_{\mathrm{d}}$ and normal $\hat{\mathbf{n}}_{\mathrm{d}}$, defines the plane at which a diffraction pattern can be collected. A point on the detector surface, $\mathbf{p}_{\mathrm{l}}$, can be described by its projection onto the in-plane detector axes

$$\mathbf{p}_{\mathrm{d}} = \begin{bmatrix} \mathbf{p}_{\mathrm{l}}^{\mathrm{T}}\hat{\mathbf{z}}_{\mathrm{d}} \\ \mathbf{p}_{\mathrm{l}}^{\mathrm{T}}\hat{\mathbf{y}}_{\mathrm{d}} \end{bmatrix} = \begin{bmatrix} z_{\mathrm{d}} \\ y_{\mathrm{d}} \end{bmatrix}. \tag{3}$$

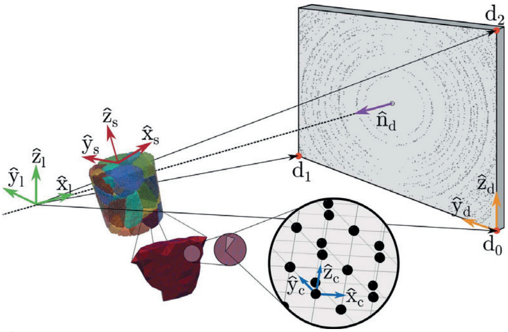

Figure 1
Illustration of *xrd_simulator* laboratory (subscript l), sample (subscript s), crystal (subscript c) and detector (subscript d) coordinates systems. The three corners of the detector $(\mathbf{d}_0, \mathbf{d}_1, \mathbf{d}_2)$ define its position and orientation in space.

2.1. Diffraction equations

We define an incident wavevector, **k**, to point in the propagation direction of a parallel monochromatic X-ray beam. The diffraction vector, **G**, is defined as

$$\mathbf{G} = \mathbf{k}' - \mathbf{k}, \tag{4}$$

where $\mathbf{k}'$ is an elastically scattered wavevector. The Euclidean norm, $||\cdot||$, of the wavevector is defined as

$$||\mathbf{k}'|| = ||\mathbf{k}|| = 2\pi/\lambda, \tag{5}$$

where λ is the X-ray wavelength.

From equation (4) and the elastic scattering condition it follows that

$$\mathbf{k}'^{\mathrm{T}}\hat{\mathbf{G}} = -\mathbf{k}^{\mathrm{T}}\hat{\mathbf{G}} = ||\mathbf{G}||/2. \tag{6}$$

Considering equation (6) together with equation (5), it follows that **k** and $-\mathbf{k}'$ form the same angle, $\pi/2 - \theta$, to **G**. The Bragg angle, θ, can be found as

$$\theta = \arccos\,(\hat{\mathbf{k}}'^{\mathrm{T}}\hat{\mathbf{k}})/2. \tag{7}$$

For diffraction to occur from a set of lattice planes the Laue equations require that

$$\begin{bmatrix} \mathbf{a}^{\mathrm{T}} \\ \mathbf{b}^{\mathrm{T}} \\ \mathbf{c}^{\mathrm{T}} \end{bmatrix} \mathbf{G} = \mathbf{G}_{hkl}, \tag{8}$$

where **a**, **b** and **c** define a unit cell and $\mathbf{G}_{hkl} = [h\ k\ l]^{\mathrm{T}}$ holds the integer Miller indices of the diffracting lattice plane family. Introducing the unique multiplicative decomposition of the inverse matrix $[\mathbf{a}\ \mathbf{b}\ \mathbf{c}]^{-\mathrm{T}}$ into a unitary rotation matrix, **U**, and an upper triangular matrix, **B**, with positive diagonal elements, we write equation (8) as

$$\mathbf{G} = \begin{bmatrix} \mathbf{a}^{\mathrm{T}} \\ \mathbf{b}^{\mathrm{T}} \\ \mathbf{c}^{\mathrm{T}} \end{bmatrix}^{-1} \mathbf{G}_{hkl} = \mathbf{U}\mathbf{B}\mathbf{G}_{hkl}. \tag{9}$$

In this description **U** is the crystal lattice orientation matrix while **B** is defined from the lattice unit cell.

2.2. Polycrystalline sample representation

A polycrystalline sample is represented by a tetrahedral mesh with each individual tetrahedron being modelled as a single crystal; grains are thus defined by adjacent cells with the same (or similar) unit-cell parameters (Fig. 2). The single crystal elements are defined through a reference unit cell, a phase, a symmetric infinitesimal strain tensor (laboratory coordinates), $\boldsymbol{\epsilon}_l$, and a crystal orientation matrix, **U**. Each of these four quantities remain constant over each element volume and spatial variations in the lattice structure are modelled by letting neighbouring elements hold different lattice states. The nodal vertices of a tetrahedron are denoted $(\mathbf{c}_0, \mathbf{c}_1, \mathbf{c}_2, \mathbf{c}_2)$, as illustrated in Fig. 2.

To compute the **B** matrix, given the quantities associated with a single tetrahedron for use in equation (9), we use *xfab*, which is part of the *3DXRD Fable* suite (Sørensen *et al.*, 2012).

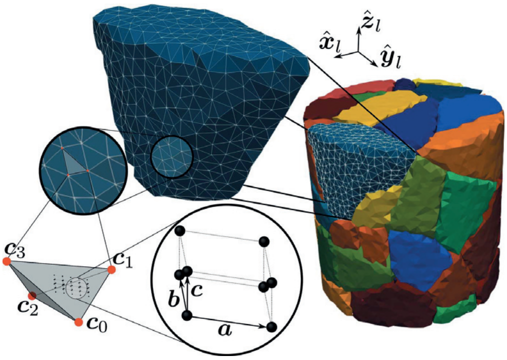

Figure 2
Illustration of a polycrystal representation in *xrd_simulator*. The tetrahedral single crystal elements form a mesh, representing a polycrystalline aggregate. Each individual tetrahedron can hold a unique lattice and phase.

2.3. Beam representation

A beam of X-rays is represented by a convex polyhedron with n vertices, $\mathbf{b}_i$, indexed as $i = 0, 1, \ldots, n$. The X-ray propagation direction is defined by the unit vector $\hat{\mathbf{n}}$. The photon density is taken to be uniform within the beam hull and the X-rays are assumed to be linearly polarized in the direction of a unit vector, $\hat{\boldsymbol{\varepsilon}}$. An example geometry of an X-ray beam is illustrated in Fig. 3.

The use of a convex polyhedron to represent the beam shape, as opposed to an axis-aligned box for instance, is motivated by the need for *xrd_simulator* to facilitate numerical investigations of scan sequences in far-field X-ray diffraction. Optimal selection of beam cross section shape and scan pattern remain open research questions in scanning 3DXRD experiments. Moreover, the use of a convex beam allows indirectly for simulations of variable beam intensity profiles. This can be achieved by repeatedly computing diffraction from sub regions of a composite beam, one diffraction pattern at a time, to produce a weighted sum of diffraction.

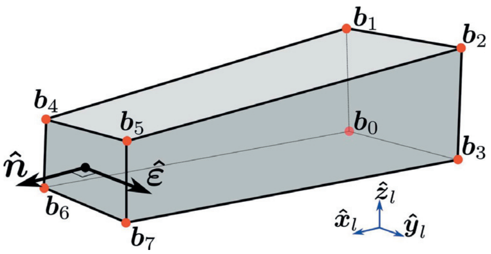

Figure 3
Example of a possible X-ray beam geometry with a total of eight nodes, $\mathbf{b}_i$, forming a convex hull in 3D space. Photons propagate in the direction of $\hat{\mathbf{n}}$ and are linearly polarized along $\hat{\boldsymbol{\varepsilon}}$. The photon intensity inside the beam hull is uniform.

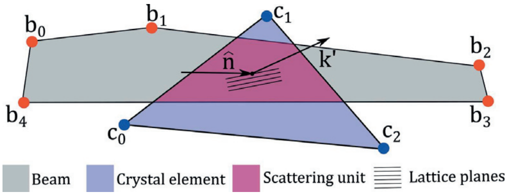

Figure 4
A simplified 2D example of a scattering unit formed as the intersection between the X-ray beam and a single crystal element. Note that *xrd_simulator* uses 3D representations for both beam and crystals.

2.4. Scattering unit

The volume intersection between an illuminated diffracting single crystal element and the beam is defined as a scattering unit. As both the beam and the single crystal tetrahedrons are convex, their intersections will also form convex polyhedrons. The scattering units each have a diffracted wavevector $\mathbf{k}'$ and serve as the basis for rendering diffraction patterns onto the detector area. A simplified 2D illustration of a scattering unit is given in Fig. 4

To compute the scattering unit polyhedron we use the *SciPy* (Virtanen *et al.*, 2020) wrapper for the *Qhull* (Barber *et al.*, 1996) library. The algorithm is seeded with an interior point of the scattering unit polyhedron, which can be found either by trial and error or by solving a linear program, as described in the `scipy.spatial.HalfspaceIntersection` documentation. Since the computation of the scattering unit polyhedron is expensive, *xrd_simulator* implements a collision detection algorithm that checks for intersections between element bounding spheres and the beam hull. This allows *xrd_simulator* to quickly exclude elements of the mesh that cannot take part in diffraction.

2.5. Detector representation

A detector is represented by an arbitrary rectangular plane segment holding a grid of rectangular pixels with user specified size $(p_{z_{\rm d}}, p_{y_{\rm d}})$. As depicted in Fig. 1, the detector can be parameterized by three vectors $(\mathbf{d}_0, \mathbf{d}_1, \mathbf{d}_2)$ extending from the laboratory origin to the detector corners. The three detector corners are arranged in clockwise order, with respect to the detector normal, and the detector coordinate system origin is taken as $\mathbf{d}_0$. Since the detector corners $\mathbf{d}_0$, $\mathbf{d}_1$ and $\mathbf{d}_2$ may be arbitrarily specified in 3D space it is possible to simulate arbitrary detector tilts and misalignments in *xrd_simulator*. The detector coordinate axes are defined as

$$\begin{aligned}\hat{\mathbf{y}}_{\rm d} &= (\mathbf{d}_1 - \mathbf{d}_0)/||\mathbf{d}_1 - \mathbf{d}_0||,\\ \hat{\mathbf{z}}_{\rm d} &= (\mathbf{d}_2 - \mathbf{d}_0)/||\mathbf{d}_2 - \mathbf{d}_0||.\end{aligned} \tag{10}$$

The detector normal is defined through the cross product,

$$\hat{\mathbf{n}}_{\rm d} = \hat{\mathbf{z}}_{\rm d} \times \hat{\mathbf{y}}_{\rm d} \tag{11}$$

Additionally, a point spread function, $\mathrm{PSF}(z_d, y_d)$, simulating blurring due to the detector optics can be specified. When computing the simulated diffraction data the point spread function is convoluted with the 2D diffraction image, as a final step.

2.6. Sample motion

Before the derivation of diffraction vectors can be considered, we must first describe the motion path of the sample during detector readout. An arbitrary rigid body motion of the sample is defined by a unit rotation axis, $\hat{\mathbf{r}} = \left[\hat{r}_x \, \hat{r}_y \, \hat{r}_z\right]^{\rm T}$, a rotation angle, $\Delta\omega \in (0, \pi)$, and a translation vector, $\Delta\mathbf{x}$. The motion is executed over the unitless time interval $t \in [0, 1]$ during which a single detector frame is collected. At the start of detector readout, before the sample has moved, $t = 0$, and at the end of readout, when the sample has translated by $\Delta\mathbf{x}$ and moved $\Delta\omega$ radians around $\hat{\mathbf{r}}$, $t = 1$. In this way, arbitrary scan sequences can be modelled using different sample motions for each detector frame readout.

The sample is modelled to move uniformly over $t \in [0, 1]$ such that at some intervening time, $0 < t < 1$, the coordinates of a node, $\mathbf{c}_i = \mathbf{c}_i(t)$, in the sample mesh can be found as

$$\mathbf{c}_i(t) = \mathbf{R}(t)\mathbf{c}_i(t = 0) + t\Delta\mathbf{x}_1, \tag{12}$$

$\mathbf{R}$ is a Rodriguez rotation matrix, defined as

$$\mathbf{R}(t) = (\mathbf{I} + \mathbf{K}^2) + \sin(t\Delta\omega)\mathbf{K} - \cos(t\Delta\omega)\mathbf{K}^2, \tag{13}$$

with unity matrix $\mathbf{I}$, and

$$\mathbf{K} = \begin{bmatrix} 0 & -\hat{r}_z & \hat{r}_y \\ \hat{r}_z & 0 & -\hat{r}_x \\ -\hat{r}_y & \hat{r}_x & 0 \end{bmatrix}. \tag{14}$$

With the motion path of the sample defined through equations (12), (13) and (14), we may now proceed to compute diffraction vectors.

2.7. Diffraction computation

By the introduction of arbitrary rigid body motions of the sample in equation (12), the Laue equation (9) becomes time dependent. Solutions to these equations for a fixed rotation axis and no sample translations have been derived by Wong *et al.* (2013). In the following we generalize these results to facilitate an arbitrary axis of rotation as well as an arbitrary sample translation.

Considering a single crystal element, equations (9) and (13) yield the scattering condition at time t as

$$\mathbf{G}(t) = \mathbf{R}(t)\mathbf{U}\mathbf{B}\mathbf{G}_{hkl}. \tag{15}$$

By finding solutions to equation (15) over $t \in [0, 1]$, the position of the crystal element nodes at the times when diffraction from the volume element can occur can be established through equation (12) together with the diffracted wavevector equation (4). This information defines the scattering unit. The lack of solutions to equation (15) over $t \in [0, 1]$ means that the crystal cannot diffract over the given sample motion.

To derive solutions to equation (12) in t we start by introducing a scalar form of the Laue condition. From equation (6) it follows that

$$\mathbf{k}^{\rm T}\mathbf{G}(t) + \frac{\mathbf{G}(t)^{\rm T}\mathbf{G}(t)}{2} = 0. \tag{16}$$

Introducing $\mathbf{G}_0 = \mathbf{U}\mathbf{B}\mathbf{G}_{hkl}$ and combining equation (13) with equation (16) we find

$$\begin{aligned} &\mathbf{k}^{\rm T}(\mathbf{I} + \mathbf{K}^2)\mathbf{G}_0 + \sin(t\Delta\omega)\mathbf{k}^{\rm T}\mathbf{K}\mathbf{G}_0 \\ &\quad - \cos(t\Delta\omega)\mathbf{k}^{\rm T}\mathbf{K}^2\mathbf{G}_0 + \mathbf{G}_0^{\rm T}\mathbf{G}_0/2 = 0, \end{aligned} \tag{17}$$

where we use the fact that $\mathbf{G}^{\rm T}(t)\mathbf{G}(t) = \mathbf{G}_0\mathbf{G}_0$ since $\mathbf{R}(t)$ is unitary. Introducing the scalars

$$\begin{aligned} \rho_0 &= -\mathbf{k}^{\rm T}\mathbf{K}^2\mathbf{G}_0, \\ \rho_1 &= \mathbf{k}^{\rm T}\mathbf{K}\mathbf{G}_0, \\ \rho_2 &= \mathbf{k}^{\rm T}(\mathbf{I} + \mathbf{K}^2)\mathbf{G}_0 + \mathbf{G}_0^{\rm T}\mathbf{G}_0/2, \end{aligned} \tag{18}$$

we may write equation (17) as

$$\rho_0 \cos(t\Delta\omega) + \rho_1 \sin(t\Delta\omega) + \rho_2 = 0. \tag{19}$$

Introducing the variable $s = \tan(t\Delta\omega/2)$ we find from the double-angle formula that

$$\rho_0 \frac{1 - s^2}{1 + s^2} + \rho_1 \frac{2s}{1 + s^2} + \rho_2 = 0. \tag{20}$$

Since equation (20) is a scalar quadratic equation, one, two or zero solutions must exist. Solving for s when $\rho_2 \neq \rho_0$ we find that

$$s = \frac{-\rho_1}{(\rho_2 - \rho_0)} \pm \left[\frac{\rho_1^2}{(\rho_2 - \rho_0)^2} - \frac{(\rho_0 + \rho_2)}{(\rho_2 - \rho_0)}\right]^{1/2}. \tag{21}$$

In the special case of $\rho_2 = \rho_0$ equation (20) reduces to

$$\rho_1 s + \rho_0 = 0, \tag{22}$$

such that a single solution, $s = -\rho_0/\rho_1$, can be found, given that $\rho_1 \neq 0$. Finally, the sought time, t, in equation (15) is found by reversing the tangent substitution,

$$t = \frac{2}{\Delta\omega}\arctan(s). \tag{23}$$

We remind the reader that the derived solutions, t, are the relative moments in time, during a frame acquisition, at which a single crystal element will diffract the incident X-rays. The position of the element nodes during diffraction can, thus, be computed through equation (12) and the geometry of the scattering unit is found by computing the intersection of the updated tetrahedral element and the X-ray beam. With this information available we may proceed to propagate the diffracted X-rays onto the 2D detector area.

2.8. Ray tracing

Once the scattering units have been established, the diffracted wavevectors, $\mathbf{k}'$, are traced onto the detector surface. Two options for ray tracing are available in *xrd_simulator*. Either rays are traced from the centroids of the individual scattering units or, alternatively, rays are traced from the detector pixel centroids back through the scattering units. The latter of the two models can be considered to produce a more accurate projection approximation while the former will be computationally faster. As illustrated in Fig. 5,

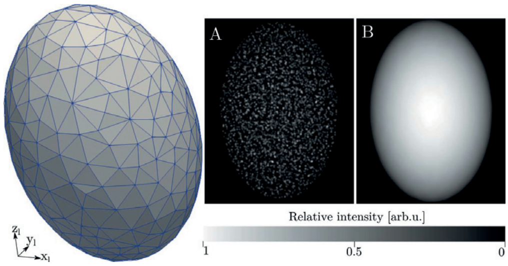

Figure 5
Illustration of a single simulated diffraction peak (right) for an elliptical grain meshed by 3283 elements (left). The difference between ray tracing driven by the scattering unit centroids (A) can be compared with ray tracing driven by the detector pixels grid (B).

ray tracing driven by the detector grid pixels will produce space-filling projections, while ray tracing driven by the scattering unit centroid will approximate a diffraction peak as a point cloud.

Considering a point $\mathbf{x}$ in the sample volume associated with a scattered wavevector $\mathbf{k}'$, we may parameterize a scattered ray through a scalar h as

$$\mathbf{p}(h) = \mathbf{x} + h\mathbf{k}'. \tag{24}$$

The point of intersection, $\mathbf{p}(h^*)$, between scattered ray and detector is found from

$$\hat{\mathbf{n}}_{\rm d}^{\rm T}(\mathbf{x} + h^*\mathbf{k}' - d_0) = 0. \tag{25}$$

Solving equation (25) for h^* yields

$$h^* = \frac{\hat{\mathbf{n}}_{\rm d}^{\rm T}(d_0 - \mathbf{x})}{\hat{\mathbf{n}}_{\rm d}^{\rm T}\mathbf{k}'}. \tag{26}$$

The detector coordinates of the intersection point can now be found through equation (10),

$$\begin{aligned} y_{\rm d} &= (\mathbf{x} + h^*\mathbf{k}' - d_0)^{\rm T}\hat{\mathbf{y}}_{\rm d}, \\ z_{\rm d} &= (\mathbf{x} + h^*\mathbf{k}' - d_0)^{\rm T}\hat{\mathbf{z}}_{\rm d}. \end{aligned} \tag{27}$$

By setting $\mathbf{x}$ in equation (27) as the scattering unit centroid, ray tracing can be performed. When ray tracing using the detector pixels as source points is considered instead, $\mathbf{x}$ in equation (24) must be taken as a point in the detector plane. By solving equation (24) for the intersections with the planes that define the facets of the scattering unit, an intersection length, l, between the ray and polyhedron can be established. To do so, we have implemented the clipping algorithm developed by Cyrus & Beck (1978). To speed up the computations, the vertices of a scattering unit are first projected onto the detector plane, establishing a feasible region on the detector where the projection may fall. In this way equation (24) is only solved for a sub-grid of the detector.

2.9. Intensity model

Once the diffracted rays of a scattering unit have been mapped to the pixels of the detector, the scattered intensity, I, can be computed and deposited. If ray tracing based on the scattering unit centroids is used, the intensity is modelled to be proportional to the scattering unit volume, V, polarization factor, P, Lorentz factor, L, and structure factor, F_{hkl}, as

$$I = VPLF_{hkl}. \tag{28}$$

If, instead, ray tracing is driven by the detector pixels, the intensity is modelled as

$$I = lPLF_{hkl}, \tag{29}$$

where l is the intersection length between the scattered ray and the scattering unit polyhedron.

The inclusion of the factors P, L and F_{hkl} in the intensity model of *xrd_simulator* can be toggled by the user. Since *xrd_simulator* is designed to separate the computation of scattering units from the diffraction pattern image rendering, several different intensity and ray tracing combinations can be tested without having to solve equation (15) repeatedly. It is also possible to access the scattering units directly in *xrd_simulator*, allowing for custom intensity and ray tracing models to be tested.

2.9.1. Structure factors. To compute structure factors we use the open source tool *xfab*, which is available as part of the *FABLE-3DXRD* software suite (Sørensen *et al.*, 2012; https:// github.com/FABLE-3DXRD/xfab). An introduction to structure factors is provided by, for example, Als-Nielsen & McMorrow (2011). To include structure factors in the intensity model the user is expected to provide a crystallographic information file (Hall *et al.*, 1991) to *xrd_simulator*, specifying the properties of the simulated material phases. If structure factors are not needed, the user may alternatively define the material phase by passing a set of unit-cell parameters.

2.9.2. Lorentz factors. As stated by Lauridsen *et al.* (2001), for a single axis rotation geometry, where the rotation axis is aligned with $\hat{\mathbf{z}}_{\rm d}$, the Lorentz factor can be approximated as

$$L(\theta, \eta) = \frac{1}{\sin(2\theta)\,|\sin\eta|}, \tag{30}$$

where η denotes the angle between the projection of the rotation axis, $\hat{\mathbf{r}}$, and scattered ray direction, $\hat{\mathbf{k}}'$, onto the $\hat{\mathbf{z}}_{\rm d}$–$\hat{\mathbf{y}}_{\rm d}$ plane. In *xrd_simulator* each detector frame has an arbitrary sample rotation axis and η can be found as

$$\begin{gathered} \eta = \arccos\big(\hat{\mathbf{r}}^{\rm T}\hat{\mathbf{w}}\big), \\ \mathbf{w} = \mathbf{k}' - \hat{\mathbf{k}}\mathbf{k}'^{\rm T}\hat{\mathbf{k}}. \end{gathered} \tag{31}$$

By additionally recovering θ from equation (7), the Lorentz factor can be computed from equation (30). Note that the expression for the Lorentz factor in equation (30) is approximate. Especially, for $\eta = 0$ or $\theta = 0$, the intensity will diverge, and *xrd_simulator* will insert `numpy.inf` values at the corresponding detector pixels.

2.9.3. Polarization factors. For linearly polarized X-rays (Als-Nielsen & McMorrow, 2011) the polarization factor takes the form

$$P(\hat{\boldsymbol{\varepsilon}}, \hat{\boldsymbol{\varepsilon}}') = |\hat{\boldsymbol{\varepsilon}}^{\mathrm{T}}\hat{\boldsymbol{\varepsilon}}'|^2, \tag{32}$$

where $\hat{\boldsymbol{\varepsilon}}$ and $\hat{\boldsymbol{\varepsilon}}'$ are the unit polarization vectors of the incident and scattered X-rays, respectively. An observer of an oscillating electron sitting on the scattered ray will only see oscillations that exist in the plane perpendicular to the propagation direction of the X-rays. Thus, we can describe $\hat{\boldsymbol{\varepsilon}}'$ by the projection

$$\hat{\boldsymbol{\varepsilon}}' = \frac{\hat{\boldsymbol{\varepsilon}} - \hat{\mathbf{k}}'\hat{\boldsymbol{\varepsilon}}^{\mathrm{T}}\hat{\mathbf{k}}'}{||\hat{\boldsymbol{\varepsilon}} - \hat{\mathbf{k}}'\hat{\boldsymbol{\varepsilon}}^{\mathrm{T}}\hat{\mathbf{k}}'||}. \tag{33}$$

Inserting equation (33) in equation (32) we find

$$P(\hat{\boldsymbol{\varepsilon}}, \hat{\mathbf{k}}') = 1 - (\hat{\boldsymbol{\varepsilon}}^{\mathrm{T}}\hat{\mathbf{k}}')^2. \tag{34}$$

3. Software architecture

xrd_simulator is a Python library organized around four Python objects: an X-ray beam, a polycrystalline sample, a detector and a sample motion. These four Python objects are implementations of the mathematical concepts previously outlined in Section 2 and define together a diffraction experiment simulator. The end user of *xrd_simulator* can define their own simulations through Python scripts, instantiating each of the four necessary objects as desired. By passing a motion object to the polycrystalline sample, together with a beam and detector, diffraction vectors can be computed. Scattering units are computed and stored in the detector object. The user may then call a detector rendering method to compute a diffraction pattern image.

A schematic overview of the *xrd_simulator* architecture can be found in Fig. 6. Detailed code samples and beginners tutorials on how to use *xrd_simulator* can be found both at GitHub (https://github.com/FABLE-3DXRD/xrd_simulator) as well as in the externally hosted documentation (https://fable-3dxrd.github.io/xrd_simulator/).

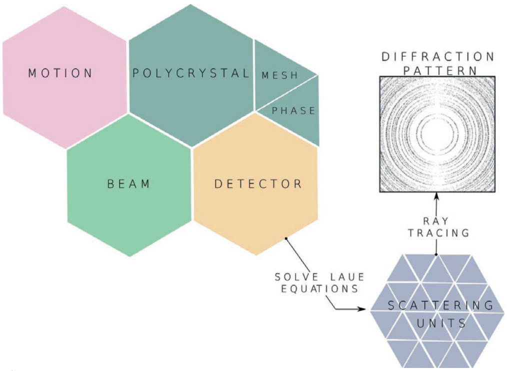

Figure 6
Four Python objects – an X-ray beam, a polycrystalline sample, a detector and a sample motion – define an experiment in *xrd_simulator*. Scattering units are computed and stored in the detector object. By selecting a ray tracing and intensity model a diffraction pattern image can be rendered.

4. Software availability

The source code of *xrd_simulator* is openly distributed with an MIT open source licence at GitHub (https://github.com/FABLE-3DXRD/xrd_simulator). *xrd_simulator* features cross-platform support and can be installed using the Python package installer, *pip*, or alternatively the *Anaconda* package manager. Documentation on installing *xrd_simulator* can be found at the GitHub source location or, alternatively, in the externally hosted documentation (https://fable-3dxrd.github.io/xrd_simulator/).

5. Computational tractability

The core computations of *xrd_simulator* can be summarized in three steps. Firstly, solutions to equation (17) are established. Secondly, polyhedral intersection regions between the X-ray beam and mesh elements are computed. Thirdly the diffraction signal is rendered into a diffraction pattern image. The total time needed to compute a diffraction pattern therefore scales with the number of elements within the mesh, the beam cross section and the angular range of the sample rotation. To enable computation of state-of-the-art data sets *xrd_simulator* implements a multiprocessing option using the Python native multiprocessing library. In Fig. 7 we provide some typical run times of *xrd_simulator* simulating a 10 × 10 pencil beam raster scan with 180 rendered frames in intervals of 1.0°. Considering the selected detector dimensions (2048 × 2048) the computed data consisted of, in total, $10 \times 10 \times 180 \times 2048 \times 2048 \sim 10^{11}$ floating point numbers. The timings presented in Fig. 7 were achieved on a Lenovo ThinkStation P330 MT deploying six Intel Core i7-8700K 3.70 GHz CPUs.

In conclusion, diffraction computations from samples with up to $\sim 10^6$ elements are feasible with *xrd_simulator* within 25 or 17 h, depending on what ray tracing model is selected.

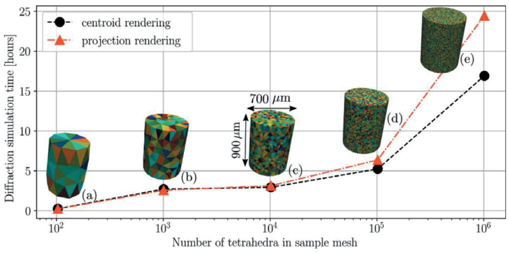

Figure 7
Typical compute times of *xrd_simulator* for a 10 ×10 × 180 × 2048 × 2048 pencil beam raster scan simulation. Diffraction was simulated from samples with random crystal orientations [coloured by one of their Bunge Euler angles in (*a*)–(*e*)]. For samples with many elements, a reduction in compute time is observed for the simplified ray tracing model described in Section 2.8.

6. Conclusions

An open source Python package for simulation of X-ray diffraction by polycrystals, named *xrd_simulator*, has been developed. By representing a polycrystalline sample as a tetrahedral mesh, an arbitrary sample morphology and microstructure can be modelled. Diffraction vectors are computed from the solutions of a time-dependent version of the Laue equations, enabling arbitrary rigid body motions of the sample. Diffraction peak intensities are computed as the product of scattering volumes and Lorentz, structure and polarization factors. Combining these features, *xrd_simulator* presents new opportunities to develop and understand the impact of different acquisition schemes for 3DXRD-type experiments such that optimal schemes can be defined in terms of acquisition time and resolution of the target parameters.

APPENDIX *A*
Experimental verification

To demonstrate the use of *xrd_simulator* we have simulated diffraction on the basis of measurements performed at the ESRF ID11 beamline. By comparing the results of *xrd_simulator* with the data from the experiment we explore the diffraction model limitations. The measured sample consisted of 12 quasi-spherical silica (SiO_2) grains confined within a cylindrical polyether ether ketone tube and subject to 20 N of uni-axial loading along the laboratory z-axis direction. The full 3D grain volume was scanned with a scanning 3DXRD geometry (Hayashi *et al.*, 2015) first using a 20 µm × 20 µm pencil beam and then a 20 µm-height letter-box beam (covering the full sample in the $\hat{\mathbf{x}}_l$–$\hat{\mathbf{y}}_l$ plane). The data from the pencil beam scan were used to perform tomographic reconstruction of the grain shapes, using a method similar to that reported by Poulsen & Schmidt (2003) [Fig. 8(*a*)]. The same pencil beam scan data were used to derive average crystallographic orientations and strain tensors of individual grains in the volume, using methods from *ImageD11* (Wright, 2005). A 20 µm-high slice (in the $\hat{\mathbf{x}}_l$–$\hat{\mathbf{y}}_l$ plane) was extracted from the 3D tomographic reconstruction, to provide an equivalent volume to one of the 20 µm letterbox 3DXRD acquisitions. This volume was used to derive a grain mesh that was input to *xrd_simulator* [Fig. 8(*b*)] together with a crystallographic information file corresponding to α-quartz. In this way the input microstructure for *xrd_simulator* was derived soley from the pencil beam scan data while any of the following comparisons between simulated and measured diffraction patterns are made with the independently measured letterbox beam data.

Diffraction was simulated for the 20 µm-high slice through the sample by integrating the diffraction signal over a 10° rotation. The resulting 2D diffraction patterns were log-normalized and compared with the corresponding measured log-normalized signal (Fig. 9) from an equivalent letterbox acquisition.

Visual comparison between columns A and C in Fig. 9 shows similar diffraction patterns. However, the subset of diffraction peaks in Figs. 9-A2 and 9-C2 show some discrepancy between simulated and measured peak shapes. This is not unexpected and several potential sources of errors can be listed. These include:

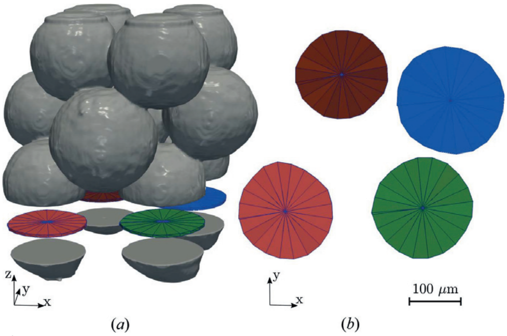

(*a*) (*b*)

Figure 8
Exploded view of 12 α-quartz grains measured at the ESRF ID11 beamline (*a*). A single 20 µm-thick slice featuring four distinct grains was extracted and considered for simulation (*b*).

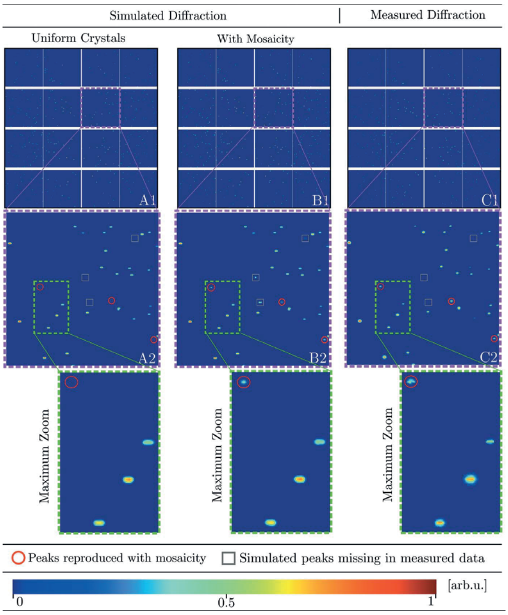

Figure 9
Simulated (A, B) and measured (C) log-normalized diffraction patterns from four 20 µm-thick $\hat{\mathbf{x}}_l$–$\hat{\mathbf{y}}_l$ grain slices of α-quartz (SiO_2). The diffraction pattern was integrated over a 10° sample rotation interval and is displayed with increasing levels of magnification in columns A, B and C, with the full tiled detector depicted in A1, B1 and C1. Diffraction peaks present in the true measured data which are only captured after the introduction of a random mosaicity are marked with circles. Diffraction peaks present in the simulated data but missing in the measurements are marked with squares.

(1) *Unknown detector point-spread function* will influence the peak shapes and maximal peak intensities.

(2) *Low signal-to-noise ratio* will influence low intensity scattering regions, which can lead to the removal of peaks or distortion of peak boundaries during background subtraction.

(3) *Unknown mosaicity and intragranular strain* will affect which peaks appear or not, as well as the peak shapes and intensities.

Turning our attention to the last of these error sources (3) we expect some, unknown, intragranular strain and orientation variations to be present within the individual grains. As a result the diffraction peak shapes will be deformed. Additionally, the set of possibly diffracting lattice plane families will be modified as the Bragg condition is shifted. To demonstrate these effects, modest, uniformly random mosaicity and strain variation were introduced into the simulation (Fig. 9 column B). First, each mesh element was seeded with the corresponding reconstructed grain average orientation matrix (derived from the pencil beam scan data). Next, the seeded orientation matrix was perturbed by a uniformly random rotation in the range 0.0–0.125°. Likewise, each component of strain was uniformly perturbed in the range 0–0.005. The magnitudes of the perturbations were chosen arbitrarily.

With the inclusion of random intragranular variations, we observe new, additional, diffraction peaks in Fig. 9-C as compared to Fig. 9-A. Although some diffraction events will now inevitably be erroneously pushed into their favourable Bragg conditions (marked with white squares in Figs. 9-A2, 9-B2 and 9-C2) several diffraction peaks originally missing in the simulation are now recovered (as marked with red circles in Figs. 9-A2, 9-B2 and 9-C2). This serves to illustrate how *xrd_simulator* captures the strong dependence between the measured diffraction signal and the underlying sample microstructure present in these types of experiments.

APPENDIX *B*
Highlights of software capability

xrd_simulator features space filling descriptions of polycrystals where each element of the tetrahedral mesh can have an individual phase, strain tensor and lattice orientation. To show how the spatial variation in a polycrystal can impact simulated diffraction patterns we provide far-field diffraction simulations from a multi-phase deformed polycrystal (Fig. 10) in this appendix section. As depicted in Fig. 10(*c*), a copper (Cu)–tin (Sn) aggregate composed of 64 grains with a combined total of 120282 individual tetrahedrons is considered. The individual grains were each seeded with a mean strain tensor and orientation matrix over which linear gradients in random directions were superimposed [Figs. 10(*a*) and 10(*b*)]. The aggregate was considered to be fully illuminated by 68.88 keV X-rays propagating along the x axis while the sample was rocked 1.0° around the z axis. To highlight the impact of the spatial deformation of the polycrystal, diffraction was simulated both with and without the prescribed strain and misorientations. The two resulting 2048 × 2048 pixelated diffraction patterns originating from a deformed and an undeformed

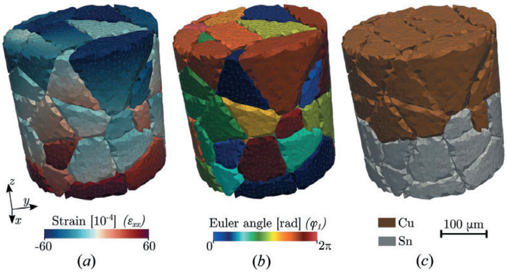

Figure 10
Phantom polycrystalline Cu–Sn aggregate composed of 120282 tetrahedral elements: (*a*) strain *xx* component, (*b*) Bunge Euler angle φ_1 and (*c*) Cu–Sn phase map.

Table 1
Simulation parameters used to render the diffraction patterns in Fig. 11 using the Cu–Sn phantom depicted in Fig. 10.

Detector distance (μm)	191023.9164
Detector centre pixel z	1024.2345
Detector centre pixel y	1023.1129
Pixel side length z (μm)	50.4234
Pixel side length y (μm)	48.2343
Number of detector pixels z	2048
Number of detector pixels y	2048
Wavelength (Å)	0.18
Beam side length z (μm)	400
Beam side length y (μm)	400
Rotation step (1.0°)	1.0
Rotation axis	[0 0 1]

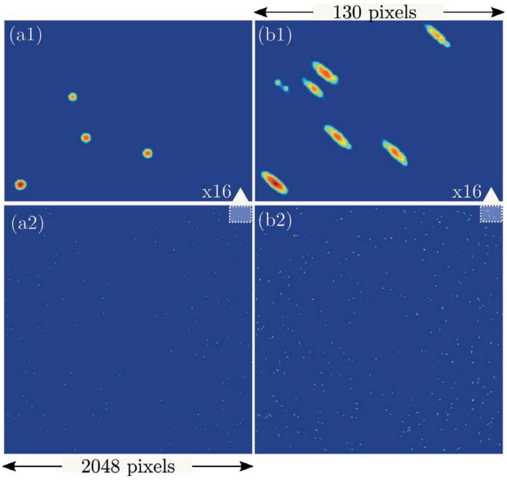

Figure 11
Simulated diffraction pattern from the phantom sample depicted in Fig. 10. Column (*a*) contains diffraction from an undeformed sample while column (*b*) depicts diffraction from a deformed version of the phantom. As a result, the diffraction peaks in the zoomed in area (*b*1) are distorted compared with the round diffraction peaks in (*a*1).

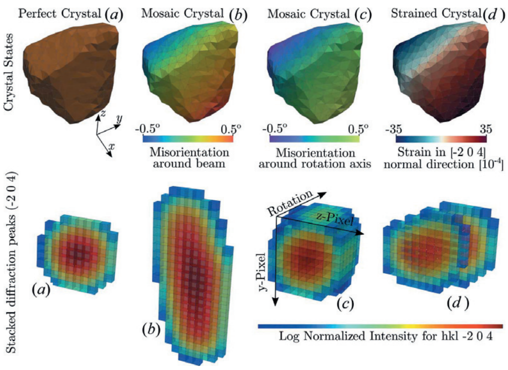

Figure 12
Single copper (Cu) grain extracted from the phantom in Fig. 10 composed of 4195 tetrahedral elements. The top row depicts induced deformation states while the bottom row shows the corresponding $\bar{2}04$ reflection rendered as a 3D peak, with sample rotational position as the third dimension.

sample can be viewed in Figs. 11(*a*2) and 11(*b*2), respectively. As depicted in Figs. 11(*a*1) and 11(*b*1) the impact of the lattice spatial variation is evident in the distorted diffraction peaks. Details of the experimental setup are presented in Table 1.

xrd_simulator offers a means to understand how the diffraction peak distortions relate to the internal grain deformation. To provide an example of how this can be utilized we have considered diffraction from a single Cu grain in the polycrystalline ensemble. The result of introducing a misorientation gradient around the beam direction and the axis of rotation are depicted in Figs. 12(*b*) and 12(*c*), respectively, where the resulting 3D peak shapes for the $\bar{2}04$ reflection have been rendered. Likewise, the effect of a strain gradient in the ($\bar{2}04$) crystal planes is depicted in Fig. 12(*d*). Comparing with a perfect crystal state [Fig. 12(*a*)], we see how the diffraction peak arcs over the detector for a misorientation around the beam axis while a misorientation around the rotation axis extends the angular range of diffraction. Finally, we can see the effect of a strain gradient in Fig. 12(*d*) resulting in a radially broadened and angularly extended diffraction peak.

Acknowledgements

We are grateful for the beam time provided at the ESRF ID11 beamline, where the data for evaluating the developed software tool were collected.

Funding information

Funding for this research was provided by Vetenskapsrådet (grant No. 2017-06719).

References

Alpers, A., Poulsen, H. F., Knudsen, E. & Herman, G. T. (2006). *J. Appl. Cryst.* **39**, 582–588.

Als-Nielsen, J. & McMorrow, D. (2011). *Elements of Modern X-ray Physics.* Chichester: John Wiley & Sons.

Barber, C. B., Dobkin, D. P. & Huhdanpaa, H. (1996). *ACM Trans. Math. Softw.* **22**, 469–483.

Batenburg, K. J., Sijbers, J., Poulsen, H. F. & Knudsen, E. (2010). *J. Appl. Cryst.* **43**, 1464–1473.

Bernier, J. V., Barton, N. R., Lienert, U. & Miller, M. P. (2011). *J. Strain Anal. Eng. Des.* **46**, 527–547.

Bernier, J. V., Suter, R. M., Rollett, A. D. & Almer, J. D. (2020). *Annu. Rev. Mater. Res.* **50**, 395–436.

Campbell, J. W. (1995). *J. Appl. Cryst.* **28**, 228–236.

Cyrus, M. & Beck, J. (1978). *Comput. Graph.* **3**, 23–28.

E, J. C., Wang, L., Chen, S., Zhang, Y. Y. & Luo, S. N. (2018). *J. Synchrotron Rad.* **25**, 604–611.

Fang, H., Juul Jensen, D. & Zhang, Y. (2020). *Acta Cryst.* A**76**, 652–663.

Hall, S. R., Allen, F. H. & Brown, I. D. (1991). *Acta Cryst.* A**47**, 655–685.

Hayashi, Y., Hirose, Y. & Seno, Y. (2015). *J. Appl. Cryst.* **48**, 1094–1101.

Hayashi, Y., Setoyama, D. & Seno, Y. (2017). *Mater. Sci. Forum*, **905**, 157–164.

Hektor, J., Hall, S. A., Henningsson, N. A., Engqvist, J., Ristinmaa, M., Lenrick, F. & Wright, J. P. (2019). *Materials*, **12**, 446.

Henningsson, A. & Hendriks, J. (2021). *J. Appl. Cryst.* **54**, 1057–1070.

Henningsson, N. A., Hall, S. A., Wright, J. P. & Hektor, J. (2020). *J. Appl. Cryst.* **53**, 314–325.

Huang, J. W., Cai, Y., Zhong, Z. Y. & Luo, S. N. (2021*a*). *Comput. Mater. Sci.* **186**, 109997.

Huang, J. W., Zhang, Y. Y., Hu, S. C., Cai, Y. & Luo, S. N. (2021*b*). *J. Appl. Cryst.* **54**, 686–696.

Huang, X. R. (2010). *J. Appl. Cryst.* **43**, 926–928.

Kanagasabapathy, M. (2016). *Crystalsim*, https://sourceforge.net/projects/crystalsim/.

Knudsen, E. B. (2009). *Quasi-Nearfield Simulation*, https://sourceforge.net/p/fable/wiki/nearfield%20simulation/.

Laugier, J. & Bochu, B. (2001). *LMGP Suite for Windows*, http://ccp14.cryst.bbk.ac.uk/tutorial/lmgp/index.html.

Lauridsen, E. M., Schmidt, S., Suter, R. M. & Poulsen, H. F. (2001). *J. Appl. Cryst.* **34**, 744–750.

Le Page, Y. & Gabe, E. J. (1979). *J. Appl. Cryst.* **12**, 464–466.

Lionheart, W. R. B. & Withers, P. J. (2015). *Inverse Probl.* **31**, 045005.

Ludwig, W., Reischig, P., King, A., Herbig, M., Lauridsen, E. M., Johnson, G., Marrow, T. J. & Buffière, J. Y. (2009). *Rev. Sci. Instrum.* **80**, 033905.

Macrae, C. F., Edgington, P. R., McCabe, P., Pidcock, E., Shields, G. P., Taylor, R., Towler, M. & van de Streek, J. (2006). *J. Appl. Cryst.* **39**, 453–457.

Momma, K. & Izumi, F. (2008). *J. Appl. Cryst.* **41**, 653–658.

Nervo, L., King, A., Wright, J. P., Ludwig, W., Reischig, P., Quinta da Fonseca, J. & Preuss, M. (2014). *J. Appl. Cryst.* **47**, 1402–1416.

Oddershede, J., Bachmann, F., Sun, J. & Lauridsen, E. (2022). *Integr. Mater. Manuf. Innov.* **11**, 1–12.

Oddershede, J., Schmidt, S., Poulsen, H. F., Sørensen, H. O., Wright, J. & Reimers, W. (2010). *J. Appl. Cryst.* **43**, 539–549.

Pagan, D. C., Jones, K. K., Bernier, J. V. & Phan, T. Q. (2020). *JOM*, **72**, 4539–4550.

Poulsen, H. F. (2004). *Three-Dimensional X-ray Diffraction Microscopy. Mapping Polycrystals and Their Dynamics*, Springer Tracts in Modern Physics, Vol. 205. Berlin: Springer.

Poulsen, H. F. (2020). *Curr. Opin. Solid State Mater. Sci.* **24**, 100820.

Poulsen, H. F. & Fu, X. (2003). *J. Appl. Cryst.* **36**, 1062–1068.

Poulsen, H. F. & Schmidt, S. (2003). *J. Appl. Cryst.* **36**, 319–325.

Reischig, P. & Ludwig, W. (2020). *Curr. Opin. Solid State Mater. Sci.* **24**, 100851.

Sharma, H., Huizenga, R. M. & Offerman, S. E. (2012*a*). *J. Appl. Cryst.* **45**, 693–704.

Sharma, H., Huizenga, R. M. & Offerman, S. E. (2012*b*). *J. Appl. Cryst.* **45**, 705–718.
Song, X., Zhang, S. Y., Dini, D. & Korsunsky, A. M. (2008). *Comput. Mater. Sci.* **44**, 131–137.
Sørensen, H. O., Schmidt, S., Wright, J. P., Vaughan, G. B. M., Techert, S., Garman, E. F., Oddershede, J., Davaasambuu, J., Paithankar, K. S., Gundlach, C. & Poulsen, H. F. (2012). *Z. Kristallogr.* **227**, 63–78.
Soyer, A. (1996). *J. Appl. Cryst.* **29**, 509.
Virtanen, P., Gommers, R., Oliphant, T. E., Haberland, M., Reddy, T., Cournapeau, D., Burovski, E., Peterson, P., Weckesser, W., Bright, J., van der Walt, S. J., Brett, M., Wilson, J., Millman, K. J., Mayorov, N., Nelson, A. R. J., Jones, E., Kern, R., Larson, E., Carey, C. J., Polat, İ., Feng, Y., Moore, E. W., VanderPlas, J., Laxalde, D., Perktold, J., Cimrman, R., Henriksen, I., Quintero, E. A., Harris, C. R., Archibald, A. M., Ribeiro, A. H., Pedregosa, F., van Mulbregt, P., Vijaykumar, A., Bardelli, A. P., Rothberg, A., Hilboll, A., Kloeckner, A., Scopatz, A., Lee, A., Rokem, A., Woods, C. N., Fulton, C., Masson, C., Häggström, C., Fitzgerald, C., Nicholson, D. A., Hagen, D. R., Pasechnik, D. V., Olivetti, E., Martin, E., Wieser, E., Silva, F., Lenders, F., Wilhelm, F., Young, G., Price, G. A., Ingold, G., Allen, G. E., Lee, G. R., Audren, H., Probst, I., Dietrich, J. P., Silterra, J., Webber, J. T., Slavič, J., Nothman, J., Buchner, J., Kulick, J., Schönberger, J. L., de Miranda Cardoso, J. V., Reimer, J., Harrington, J., Rodríguez, J. L. C., Nunez-Iglesias, J., Kuczynski, J., Tritz, K., Thoma, M., Newville, M., Kümmerer, M., Bolingbroke, M., Tartre, M., Pak, M., Smith, N. J., Nowaczyk, N., Shebanov, N., Pavlyk, O., Brodtkorb, P. A., Lee, P., McGibbon, R. T., Feldbauer, R., Lewis, S., Tygier, S., Sievert, S., Vigna, S., Peterson, S., More, S., Pudlik, T., Oshima, T., Pingel, T. J., Robitaille, T. P., Spura, T., Jones, T. R., Cera, T., Leslie, T., Zito, T., Krauss, T., Upadhyay, U., Halchenko, Y. O. & Vázquez-Baeza, Y. (2020). *Nat. Methods*, **17**, 261–272.
Weber, S. (1997). *J. Appl. Cryst.* **30**, 565–566.
Wong, S. L., Park, J.-S., Miller, M. P. & Dawson, P. R. (2013). *Comput. Mater. Sci.* **77**, 456–466.
Wright, J. (2005). *ImageD11*, https://github.com/FABLE-3DXRD/ImageD11/.

Paper D

Axel Henningsson and Stephen A. Hall

An efficient system matrix factorisation for strain tensor tomography

In: Acta Crystallographica Section A: Foundations and Advances, A79 (2023)

Acta Cryst A
FOUNDATIONS
ADVANCES

ISSN 2053-2733

Received 2 February 2023
Accepted 18 September 2023

Edited by D. A. Keen, STFC Rutherford Appleton Laboratory, United Kingdom

Keywords: X-ray diffraction; strain tensor; tomography; diffraction imaging.

An efficient system matrix factorization method for scanning diffraction based strain tensor tomography

Axel Henningsson* and Stephen A. Hall

Division of Solid Mechanics, Lund University, Ole Römersväg 1, Lund, Sweden. *Correspondence e-mail: axel.henningsson@solid.lth.se

Diffraction-based tomographic strain tensor reconstruction problems in which a strain tensor field is determined from measurements made in different crystallographic directions are considered in the context of sparse matrix algebra. Previous work has shown that the estimation of the crystal elastic strain field can be cast as a linear regression problem featuring a computationally involved assembly of a system matrix forward operator. This operator models the perturbation in diffraction signal as a function of spatial strain tensor state. The structure of this system matrix is analysed and a block-partitioned factorization is derived that reveals the forward operator as a sum of weighted scalar projection operators. Moreover, the factorization method is generalized for another diffraction model in which strain and orientation are coupled and can be reconstructed jointly. The proposed block-partitioned factorization method provides a bridge to classical absorption tomography and allows exploitation of standard tomographic ray-tracing libraries for implementation of the forward operator and its adjoint. Consequently, RAM-efficient, GPU-accelerated, on-the-fly strain/orientation tensor reconstruction is made possible, paving the way for higher spatial resolution studies of intragranular deformation.

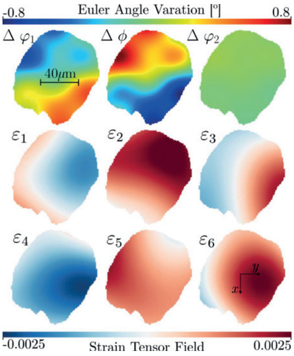

1. Introduction

Diffraction-based strain tomography is an experimental technique deployed for estimation of the six-component elastic strain tensor field, $\boldsymbol{\varepsilon}(\mathbf{x})$, within the bulk of polycrystalline aggregates. Whether used with X-rays (Hektor *et al.*, 2019; Korsunsky *et al.*, 2005; Lionheart & Withers, 2015) or neutrons (Hendriks *et al.*, 2020), the method offers a unique possibility to probe the internal heterogeneity of the strain in dense materials in a non-destructive way. In essence, the measured diffraction signal from the specimen can be reduced to average strains along line integral domains across a sample volume. Each of these scalar strain measures, γ_j, can be associated to a spatial sampling direction, $\boldsymbol{\kappa}_j$, which in general varies between measurements. Considering a set of $j = 1, \ldots, m$ such measurements, it is possible to construct a global linear system of equations,

$$\mathbf{A}\mathbf{s} = \boldsymbol{\gamma}, \tag{1}$$

where $\mathbf{s}$ holds the basis coefficients of a decomposed strain tensor field and $\boldsymbol{\gamma}$ is a vector with all measurements [the formation of $\boldsymbol{\gamma}$ from raw diffraction images and the decoupling of the crystal strain from orientation are discussed by Henningsson & Hendriks (2021)]. The rows of the system matrix, $\mathbf{A}$, are required to contain the integral weights of the strain tensor basis functions combined with non-linear combinations of the components of $\boldsymbol{\kappa}_j$. Using measurements only from a single axis of rotation, there exist no known, closed-form, direct back-projection algorithms to recover the strain tensor field $\mathbf{s}$. This motivates the need for iterative solvers, which may seem to require the assembly of $\mathbf{A}$. Unfortunately, the storage of $\mathbf{A}$ can be very RAM inefficient and the assembly routines needed to construct $\mathbf{A}$ involve ray-tracing through the strain tensor volume. Indeed, direct storage of the forward operator is unfeasible for high-resolution scalar, absorption-based, tomography. Considering a fixed resolution, strain tomography of symmetric strain tensor fields offers no relaxation in this respect as the number of non-zeros in the system matrix, $\mathbf{A}$, is a factor six greater compared with scalar tomography. As a result, several existing reconstruction methods have been cast in settings with few strain tensor basis functions limiting the achievable reconstruction resolution (Henningsson *et al.*, 2020; Henningsson & Hendriks, 2021; Hendriks *et al.*, 2020). Similarly, in scanning 3D X-ray diffraction (scanning-3DXRD) microscopy applications, it is common to collapse the rich 2D pixel intensity distribution of the recorded diffraction peaks to a single centre of gravity prior to the pursuit of strain reconstruction (Hayashi *et al.*, 2015).

We present a system matrix factorization for strain tensor tomography in which the forward operator, $\mathbf{A}$, can be implemented as a weighted sum of scalar forward projections as

$$\mathbf{A}\mathbf{s} = \sum_{i=1}^{i=6} \mathbf{S}_i \mathcal{P} \mathbf{a}_i, \tag{2}$$

where $\mathcal{P}$ is a scalar forward projection operator, $\mathbf{a}_1, \ldots, \mathbf{a}_6$ are the six individual components of the strain tensor field and $\mathbf{S}_1, \ldots, \mathbf{S}_6$ are diagonal weight matrices. This factorization allows for RAM-efficient, on-the-fly implementations to be easily achieved with existing tomographic libraries (for scalar projection). Additionally, our proposed factorization allows for access to GPU-accelerated implementations commonly deployed in scalar tomography to facilitate large sparse iterative solvers (Palenstijn *et al.*, 2011; van Aarle *et al.*, 2015, 2016).

For illustrative purposes we have selected to present our derivations in the context of strain reconstruction and for the experimental setup of scanning-3DXRD. The methodology is, however, also applicable for other neutron and X-ray scanning diffraction experiments given that a fixed axis of rotation is used and that the diffraction peak centre-of-mass positions can be accurately measured (typically in far-field geometry). The key ingredient in our derivation is the linearity of the diffraction model, which allows us to rearrange the order of the involved operators. In contrast to the far-field diffraction setting considered in this paper, near-field diffraction methods (Reischig & Ludwig, 2020) model the full detector intensity distribution of the diffraction peaks rather than the peak centroid positions. As a result, the forward operator in near-field diffraction models depends non-linearly on the intragranular strain and orientation. To highlight that our factorization method is applicable to multiple models, as long as they fall within the class of far-field diffraction, we derive and demonstrate (in Appendix *C*) a factorization similar to that of equation (2) for a previously suggested diffraction model that features coupling between the intragranular strain and orientation. This factorization enables efficient reconstruction of the full intragranular deformation field, including both strain and orientations.

2. Per-ray factorization

Given an unknown, symmetric, second-order strain tensor field,

$$\boldsymbol{\varepsilon}(\mathbf{x}) = \begin{bmatrix} \varepsilon_1(\mathbf{x}) & \varepsilon_4(\mathbf{x}) & \varepsilon_5(\mathbf{x}) \\ \varepsilon_4(\mathbf{x}) & \varepsilon_2(\mathbf{x}) & \varepsilon_6(\mathbf{x}) \\ \varepsilon_5(\mathbf{x}) & \varepsilon_6(\mathbf{x}) & \varepsilon_3(\mathbf{x}) \end{bmatrix}, \tag{3}$$

defined on a 3D spatial domain, $\mathbf{x} = [x\,y\,z]^{\mathrm{T}}$, we shall consider measurements of the average strain, γ_j, on the line integral domain $\mathcal{R}_j$ as

$$\gamma_j = \frac{1}{L_j} \int_{\mathcal{R}_j} \boldsymbol{\kappa}_j^{\mathrm{T}} \boldsymbol{\varepsilon}(\mathbf{x}) \boldsymbol{\kappa}_j \, \mathrm{d}\mathbf{x}, \tag{4}$$

where $\boldsymbol{\kappa}_j = [\kappa_1\,\kappa_2\,\kappa_3]^{\mathrm{T}}$ is a unit normal vector that describes the sampled strain direction and L_j is the ray intersection path length measured over the compact support of $\boldsymbol{\varepsilon}$. For scanning-3DXRD the formation of γ_j from the raw diffraction image data has been described elsewhere (Henningsson & Hendriks, 2021). Following a flattened vector format similar to that of Henningsson & Hendriks (2021) we find the alternative measurement model

$$\gamma_j = \int_{\mathcal{R}_j} \bar{\boldsymbol{\kappa}}_j^{\mathrm{T}} \bar{\boldsymbol{\varepsilon}}(\mathbf{x}) \, \mathrm{d}\mathbf{x}, \tag{5}$$

where

$$\bar{\boldsymbol{\varepsilon}}(\mathbf{x}) = \begin{bmatrix} \varepsilon_1(\mathbf{x}) \\ \varepsilon_3(\mathbf{x}) \\ \varepsilon_2(\mathbf{x}) \\ \varepsilon_4(\mathbf{x}) \\ \varepsilon_5(\mathbf{x}) \\ \varepsilon_6(\mathbf{x}) \end{bmatrix}, \quad \bar{\boldsymbol{\kappa}} = \frac{1}{L_j} \begin{bmatrix} \kappa_{1j}^2 \\ \kappa_{2j}^2 \\ \kappa_{3j}^2 \\ 2\kappa_{1j}\kappa_{2j} \\ 2\kappa_{1j}\kappa_{3j} \\ 2\kappa_{2j}\kappa_{3j} \end{bmatrix}. \tag{6}$$

Let $\bar{\boldsymbol{\varepsilon}}$ be decomposed on $\mathbf{x}$ with n basis functions $\varphi_l(\mathbf{x})$ as

$$\bar{\boldsymbol{\varepsilon}}(\mathbf{x}) = \sum_{l=1}^{n} \varphi_l(\mathbf{x}) \boldsymbol{\alpha}_l, \tag{7}$$

where the basis coefficients $\boldsymbol{\alpha}_l$ are defined as

$$\boldsymbol{\alpha}_l = \begin{bmatrix} \alpha_{1l} & \alpha_{2l} & \alpha_{3l} & \alpha_{4l} & \alpha_{5l} & \alpha_{6l} \end{bmatrix}^{\mathrm{T}}. \tag{8}$$

In the following we select φ_l to represent an equidistant grid of pixels such that $\varphi_l(\mathbf{x}) = 1$ when $\mathbf{x}$ is in pixel number l and $\varphi_l = 0$ otherwise. By insertion of (7) into (5) we have

$$\gamma_j = \int_{\mathcal{R}_j} \bar{\boldsymbol{\kappa}}_j^{\mathrm{T}} \sum_{l=1}^{n} \varphi_l(\mathbf{x}) \boldsymbol{\alpha}_l \, \mathrm{d}\mathbf{x}. \tag{9}$$

Reordering the integral and sum we can write

$$\gamma_j = \bar{\boldsymbol{\kappa}}_j^{\mathrm{T}} \sum_{l=1}^{n} \boldsymbol{\alpha}_l \int_{\mathcal{R}_j} \varphi_l(\mathbf{x})\,\mathrm{d}\mathbf{x}. \tag{10}$$

We now introduce the vector $\mathbf{w}_j$ which contains the scalar weights of the ray integral with respect to basis functions,

$$\mathbf{w}_j = \begin{bmatrix} \int_{\mathcal{R}_j} \varphi_1(\mathbf{x})\,\mathrm{d}\mathbf{x} \\ \int_{\mathcal{R}_j} \varphi_2(\mathbf{x})\,\mathrm{d}\mathbf{x} \\ \vdots \\ \int_{\mathcal{R}_j} \varphi_n(\mathbf{x})\,\mathrm{d}\mathbf{x} \end{bmatrix}. \tag{11}$$

Using the weights, $\mathbf{w}_j$, we may form a matrix projection operator that projects the six components of the strain field along a single ray path as

$$\mathbf{R}_j = \underbrace{\begin{bmatrix} \mathbf{w}_j^{\mathrm{T}} & \mathbf{0} & \mathbf{0} & \ldots & \mathbf{0} \\ \mathbf{0} & \mathbf{w}_j^{\mathrm{T}} & \mathbf{0} & \ldots & \mathbf{0} \\ \vdots & \ddots & \ddots & \ddots & \vdots \\ \mathbf{0} & \ldots & \mathbf{0} & \mathbf{0} & \mathbf{w}_j^{\mathrm{T}} \end{bmatrix}}_{6\times 6n}. \tag{12}$$

Additionally we introduce the vectors

$$\mathbf{a}_1 = \begin{bmatrix} \alpha_{11} \\ \alpha_{12} \\ \vdots \\ \alpha_{1n} \end{bmatrix}, \mathbf{a}_2 = \begin{bmatrix} \alpha_{21} \\ \alpha_{22} \\ \vdots \\ \alpha_{2n} \end{bmatrix} \ldots \mathbf{a}_6 = \begin{bmatrix} \alpha_{61} \\ \alpha_{62} \\ \vdots \\ \alpha_{6n} \end{bmatrix}, \tag{13}$$

and stack the basis coefficients of the unknown strain tensor field in a single column vector as

$$\mathbf{s} = \underbrace{\begin{bmatrix} \mathbf{a}_1 \\ \mathbf{a}_2 \\ \mathbf{a}_3 \\ \mathbf{a}_4 \\ \mathbf{a}_5 \\ \mathbf{a}_6 \end{bmatrix}}_{6n\times 1}. \tag{14}$$

We can now facilitate a fully vectorized and discretized format of the measurement model, equation (4), as

$$\gamma_j = \bar{\boldsymbol{\kappa}}_j^{\mathrm{T}} \mathbf{R}_j \mathbf{s}. \tag{15}$$

To arrive at a global format, in which several measurements, γ_j, are considered simultaneously, we introduce the vector

$$\boldsymbol{\gamma} = \begin{bmatrix} \gamma_1 & \gamma_2 & \ldots & \gamma_m \end{bmatrix}^{\mathrm{T}}. \tag{16}$$

Stacking the matrices $\bar{\boldsymbol{\kappa}}_j^{\mathrm{T}}$ and $\mathbf{R}_j$ in the same fashion,

$$\mathbf{K} = \underbrace{\begin{bmatrix} \bar{\boldsymbol{\kappa}}_1^{\mathrm{T}} & \mathbf{0} & \mathbf{0} & \ldots & \mathbf{0} \\ \mathbf{0} & \bar{\boldsymbol{\kappa}}_2^{\mathrm{T}} & \mathbf{0} & \ldots & \mathbf{0} \\ \vdots & \ddots & \ddots & \ddots & \vdots \\ \mathbf{0} & \ldots & \mathbf{0} & \mathbf{0} & \bar{\boldsymbol{\kappa}}_m^{\mathrm{T}} \end{bmatrix}}_{m\times 6m}, \quad \mathbf{V} = \underbrace{\begin{bmatrix} \mathbf{R}_1 \\ \mathbf{R}_2 \\ \vdots \\ \mathbf{R}_m \end{bmatrix}}_{6m\times 6n}, \tag{17}$$

we find the global matrix formulation as

$$\boldsymbol{\gamma} = \mathbf{K}\mathbf{V}\mathbf{s}. \tag{18}$$

We note that in equation (18) the matrix $\mathbf{A} = \mathbf{K}\mathbf{V}$ is factorized in two terms: $\mathbf{K}$, which contains information on the directional sampling of the strain field, and $\mathbf{V}$, which holds information on the projections of the sampled fields.

3. Hexa-block-diagonal form

In scalar tomography the forward projection operator, $\mathcal{P}$, is commonly block-partitioned over a series of projection views, $\mathcal{P}_i$, as

$$\mathcal{P} = \begin{bmatrix} \mathcal{P}_1 \\ \mathcal{P}_2 \\ \vdots \\ \mathcal{P}_k \end{bmatrix}, \tag{19}$$

where each projection view, $\mathcal{P}_i$, represents an ordered set of parallel line integrals defined over a single scalar field. In contrast, we note that the ray integrals contained in $\mathbf{V}$, as defined by equations (12) and (17), are neither ordered in complete views nor defined over a single scalar field. We therefore seek to reorder and partition the rays in $\mathbf{V}$ in a way that will allow our projection operator to be easily implemented using standard tomographic libraries. To this end, we note that the set of rows in $\mathbf{V}$ separated by a fixed multiple 6, with start at row number 1, forms the block-partitioned matrix

$$\underbrace{\begin{bmatrix} \mathbf{L} & \mathbf{0} & \mathbf{0} & \mathbf{0} & \mathbf{0} & \mathbf{0} \end{bmatrix}}_{m\times 6n}, \tag{20}$$

where $\mathbf{L}$ is now acting on the single scalar field $\mathbf{a}_1$. If the measurements in $\boldsymbol{\gamma}$ are selected to be stacked in complete projection views, we find that $\mathbf{L} = \mathcal{P}$. Since the initial selected ordering of measurements in $\boldsymbol{\gamma}$ is arbitrary, we shall assume that this ordering has been selected. Now, by simply repeating the row shifting operation with increasing row starting index, $1, 2, \ldots, 6$, it is possible to mutate $\mathbf{V}$ into the block-diagonal matrix form,

$$\mathbf{P} = \underbrace{\begin{bmatrix} \mathcal{P} & \mathbf{0} & \mathbf{0} & \mathbf{0} & \mathbf{0} & \mathbf{0} \\ \mathbf{0} & \mathcal{P} & \mathbf{0} & \mathbf{0} & \mathbf{0} & \mathbf{0} \\ \mathbf{0} & \mathbf{0} & \mathcal{P} & \mathbf{0} & \mathbf{0} & \mathbf{0} \\ \mathbf{0} & \mathbf{0} & \mathbf{0} & \mathcal{P} & \mathbf{0} & \mathbf{0} \\ \mathbf{0} & \mathbf{0} & \mathbf{0} & \mathbf{0} & \mathcal{P} & \mathbf{0} \\ \mathbf{0} & \mathbf{0} & \mathbf{0} & \mathbf{0} & \mathbf{0} & \mathcal{P} \end{bmatrix}}_{6m\times 6n}, \tag{21}$$

which contains the reordered rows of $\mathbf{V}$. Naturally, to maintain the global formulation in equation (17), we are required to now also modify $\mathbf{K}$. The shifting of the rows of $\mathbf{V}$, therefore, requires a corresponding shifting of columns in $\mathbf{K}$, leading to the block-partitioned matrix

$$\mathbf{S} = \underbrace{\begin{bmatrix} \mathbf{S}_1 & \mathbf{S}_2 & \mathbf{S}_3 & \mathbf{S}_4 & \mathbf{S}_5 & \mathbf{S}_6 \end{bmatrix}}_{m\times 6m}, \tag{22}$$

with diagonal blocks

$$\mathbf{S}_1 = \mathrm{Diag}\left(\frac{\kappa_{1j}^2}{L_j}\right), \quad \mathbf{S}_2 = \mathrm{Diag}\left(\frac{\kappa_{2j}^2}{L_j}\right), \tag{23}$$

$$\mathbf{S}_3 = \mathrm{Diag}\left(\frac{\kappa_{3j}^2}{L_j}\right), \quad \mathbf{S}_4 = \mathrm{Diag}\left(\frac{2\kappa_{1j}\kappa_{2j}}{L_j}\right), \tag{24}$$

$$\mathbf{S}_5 = \mathrm{Diag}\left(\frac{2\kappa_{1j}\kappa_{3j}}{L_j}\right), \quad \mathbf{S}_6 = \mathrm{Diag}\left(\frac{2\kappa_{2j}\kappa_{3j}}{L_j}\right). \tag{25}$$

It is now possible to write

$$\gamma = \mathbf{SPs} = \sum_{i=1}^{i=6} \mathbf{S}_i \mathcal{P} \mathbf{a}_i. \tag{26}$$

In this factorization the execution of the forward operator, $\mathbf{A} = \mathbf{SP}$, corresponds to six scalar forward projections followed by the application of $\mathbf{S}$, which, due to its diagonal form, presents a modest $6m$ multiplications and additions. The implementation of $\mathcal{P}$ can be directly achieved by any ray-tracing library, *e.g.* the *ASTRA-toolbox* (Palenstijn *et al.*, 2011; van Aarle *et al.*, 2015, 2016). The implementation of $\mathbf{S}$ is trivial and, owing to its diagonal form, there is no need to assemble the matrix, as it suffices to store the six vectors of diagonal weights. Since the six projections being executed in $\mathbf{P}$ are independent, we note that the resulting arrays, $\mathbf{a}_1, \ldots, \mathbf{a}_6$, may be stacked and projected in parallel on a GPU. To service the diffraction imaging community, and to illustrate how equation (26) can be put to use to achieve an easily implementable GPU-accelerated diffraction model, we provide an open-source demo Python code at https://github.com/AxelHenningsson/flyxdm.

4. Generalizations

For the sake of clarity, we derived equation (26) in the setting of strain reconstruction. This setting features scalar measurements, γ_j, which simplifies the exposition and allows us to focus on the core rearrangement of equations necessary to arrive at our block-partitioned factorized format. The same algebraic manipulations can be used to factorize a wider class of linear far-field diffraction models. We demonstrate the generality of our matrix factorization method in Appendix *C* where we have pursued an extended diffraction model originally suggested by Henningsson *et al.* (2020). In this alternative setting the intragranular orientation field is jointly reconstructed with the strain tensor field and the measurement associated to the ray integral is vector valued rather than scalar.

To reconstruct a target field, $\mathbf{s}$, in practice, it is often desirable to introduce a measurement weight matrix, $\mathbf{W}$, that describes the measurement precision. For instance, in the work of Henningsson *et al.* (2020) a diagonal weight matrix was used to reconstruct strain in a weighted least-squares sense. We note that our factorization is indifferent to the introduction of $\mathbf{W}$ and the global equation system would in practical application be extended as

$$\mathbf{W}\gamma = \mathbf{WSPs}, \tag{27}$$

where $\mathbf{W}^2 = \boldsymbol{\Sigma}_\gamma^{-1}$ is the covariance of the measurements, γ.

Another practical concern is the incorporation of constraints on the solution vector, $\mathbf{s}$. One popular approach is to modify the basis of the unknown target field to encode the prior knowledge. To exploit our factorized format in these settings, we suggest introducing a rendering matrix, $\mathbf{N}$, that maps the basis coefficients, $\mathbf{q}$, from the constrained basis set back to the pixel basis coefficients, $\mathbf{s}$, as

$$\mathbf{s} = \mathbf{Nq}. \tag{28}$$

The resulting global equations now become

$$\mathbf{W}\gamma = \mathbf{WSPNq}, \tag{29}$$

where the columns of $\mathbf{N}$ can be interpreted as pixel images of the selected basis set. As the forward operator, $\mathbf{WSPN}$, and the adjoint operator, $\mathbf{N}^\mathrm{T}\mathbf{P}^\mathrm{T}\mathbf{S}^\mathrm{T}\mathbf{W}^\mathrm{T}$, still feature the desired multiplicative block-partitioned split between $\mathbf{P}$ and $\mathbf{S}$, we conclude that the results in equation (26) can be exploited in a wide range of applications.

As a final note, on the topic of generalizations, we would like to mention that, just as the tensor components of the target field can be stacked into a 3D volume and projected in parallel on a GPU card, one may instead consider stacking grain slices into a volume and projecting each tensor component separately. This modification, reconstructing a full grain volume rather than a grain slice, has no impact on the algebraic format of equation (26). The rendering matrix, $\mathbf{N}$, is then computing the coefficients of a set of voxels that are projected as a 3D volume by $\mathbf{P}$.

5. Demonstration

To demonstrate the memory benefits that can be achieved using equation (26) compared with assembling and storing the sparse matrix, $\mathbf{A}$, we consider a single-crystal diffraction simulation case study. The simulation is described in detail in Appendix *A*, together with illustrations of the reconstructions achieved when exploiting the format of equation (26) during regression (Appendices *B* and *C*). The supplementary code used to generate the simulation data as well as the recon-

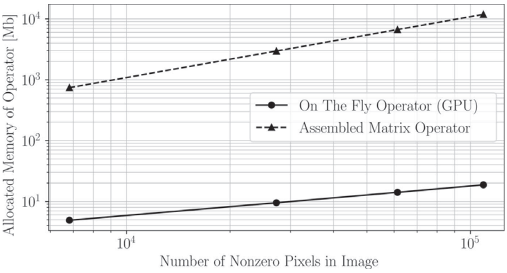

Figure 1
Number of megabytes of computer RAM necessary to compute $\gamma = \mathbf{As}$ using either an assembled sparse matrix (dashed line) or, alternatively, the discussed factorization in conjunction with an on-the-fly projection operator, $\mathbf{P}$ (solid line). Note that the benchmarks correspond to a single-crystal grain slice and 500 diffraction peaks (projection views) as described in Appendix *A*.

structions is openly available at https://github.com/AxelHenningsson/flyxdm.

In Fig. 1 we present the number of megabytes of computer RAM necessary to compute $\boldsymbol{\gamma} = \mathbf{As}$ using either a fully assembled sparse matrix $\mathbf{A}$ or, alternatively, the factorization $\mathbf{A} = \mathbf{SP}$, where $\mathbf{P}$ is represented using pre-existing, on-the-fly, projection operators, available in the *ASTRA-toolbox* (van Aarle *et al.*, 2015). Considering that the results presented in Fig. 1 represent the reconstruction of a single grain slice using 500 projection views (each corresponding to a diffraction event), it is evident that parallel, high-resolution, full volume/sample reconstructions are unfeasible using an assembled format of $\mathbf{A}$. For instance, reconstructing, in parallel, a single, cubic-shaped grain volume, with a cross-sectional resolution of 256 × 256 pixels from ~300 unique (with respect to Miller index) diffraction peaks would require ~1 TB of computer RAM storage.

6. Conclusion

We have presented a system matrix factorization for strain tensor tomography in which the directional sampling of the strain tensor field is separated from the tomographic projection operator. The proposed format allows for the exploitation of standard tomographic ray-tracing libraries in the implementation of the forward operator. We have also shown how our factorization method can be generalized for other diffraction models, for example one in which strain and orientation are coupled. We have provided an openly available GPU implementation of the approach and demonstrated the computational efficiency of our factorization method through application to a model example. By enabling RAM-efficient, GPU-accelerated, on-the-fly strain/orientation tensor reconstruction, our results facilitate higher spatial resolution studies of intragranular deformation.

APPENDIX *A*
Demonstration example

To demonstrate the discussed matrix factorization in a practical application we have included a single-crystal X-ray diffraction simulation case study. Diffraction data were forward modelled from a 2D grain slice of α-quartz (SiO$_2$) subject to a spatially varying strain tensor field, $\boldsymbol{\varepsilon}(\mathbf{x})$, as well as a misorientation field, $\mathbf{U}(\mathbf{x})$, where $\mathbf{U}(\mathbf{x})$ is the local crystal orientation matrix. The synthetic strain tensor field can be viewed in Fig. 2 together with the Bunge Euler angle variation, which was defined as

$$\begin{aligned}\Delta\varphi_1 &= \varphi_1 - \langle\varphi_1\rangle,\\ \Delta\phi &= \phi - \langle\phi\rangle,\\ \Delta\varphi_2 &= \varphi_2 - \langle\varphi_2\rangle,\end{aligned} \tag{30}$$

where $\langle\cdot\rangle$ denotes volume average.

Using the space group of quartz (P3221) together with an X-ray wavelength of λ = 0.2846 Å, a total of 500 reflections were randomly (uniformly) selected in the Bragg angle interval $\theta = [4^\circ, 13^\circ]$ to be included in the simulation. Using the Laue equations,

$$\mathbf{G} = \mathbf{UBG}_{hkl}, \tag{31}$$

where the matrix $\mathbf{B}$ maps from the integer reciprocal-space Miller indices, $\mathbf{G}_{hkl} = [h\,k\,l]^{\rm T} \in \mathbb{Z}^{3\times1}$, to crystal coordinates, diffraction vectors $\mathbf{G} = [G_1\,G_2\,G_3]^{\rm T}$ were formed. The theoretical diffraction vectors were then corrupted with zero mean Gaussian noise as

$$\begin{aligned}G_{1j} &\leftarrow G_{1j} + n_{1j}, & n_{1j} &\sim \mathcal{N}(0, \sigma_{1j}^2)\\ G_{2j} &\leftarrow G_{2j} + n_{2j}, & n_{2j} &\sim \mathcal{N}(0, \sigma_{2j}^2)\\ G_{3j} &\leftarrow G_{3j} + n_{3j}, & n_{3j} &\sim \mathcal{N}(0, \sigma_{3j}^2),\end{aligned} \tag{32}$$

where $\sigma_{1j} = \sigma_{2j} = \sigma_{3j} = 10^{-3}$ for 90% of the measurements while $\sigma_{1j} = \sigma_{2j} = \sigma_{3j} = 10^{-2}$ for the remaining 10%, emulating the presence of outliers. The 10% selected for outlier noising was selected randomly uniformly from the full diffraction data set.

Using the *ASTRA-toolbox* we have implemented the matrix factorization derived in this paper in operator format. This means that we never need to form the explicit sparse matrices involved in the forward model, but, instead, implement an on-the-fly operator that operates on an input vector to produce the system matrix vector dot product (and the corresponding adjoint product). This operator implementation is only possible thanks to the algebraic results that constitute the contribution of this paper. The code used to implement our matrix factorization (on an NVIDIA GPU architecture), produce the simulated data and reconstruct the strain (and later orientation) field is openly available as a demo Python library https://github.com/AxelHenningsson/flyxdm. In the same supplementary demo code, we provide

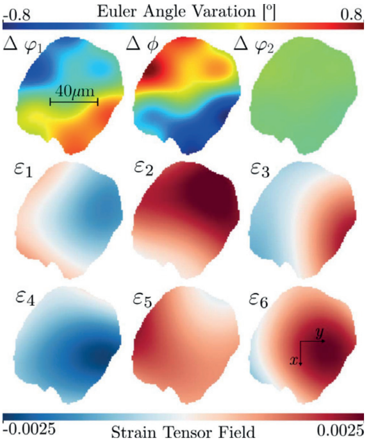

Figure 2
Strain (bottom) and mosaicity (top) in a simulated 2D grain slice of α-quartz (SiO$_2$). The Bunge Euler angles are displayed as variations around their respective mean values.

detailed comments on the simulation and reconstruction setup and provide the code used to generate all figures found in these Appendices (including the generalizations to orientation fields made in Appendix *C*).

APPENDIX *B*
Strain reconstruction

In this Appendix, we use the simulation data in conjunction with the Taylor expansion described by Henningsson & Hendriks (2021) and convert the diffraction vectors, **G**, into measurements of directional strain with the aim of reconstructing the intragranular strain field. In Appendix *C* we describe how the diffraction vectors can be used without transform to reconstruct strain and intragranular orientation variations jointly, again exploiting our matrix factorization method. Note that while the aim in Appendix *B* is to demonstrate our matrix factorization method for the case of strain reconstruction, the simulated data still originate from a grain that features both intragranular strain and orientation variation. As discussed elsewhere (Henningsson *et al.*, 2020; Henningsson & Hendriks, 2021), this is not a problem as long as the mosaicity of the grain is moderate.

In Fig. 3, the result of strain tensor reconstruction can be viewed. Here a radial basis expansion was used to construct **N** [in equation (29)]. The true noise covariance of the diffraction vectors was propagated through the Taylor expansion to construct the directional strain covariance yielding **W**. The small residuals and root-mean-squared errors (RMSEs) found in the bottom row of Fig. 3 are expected as a consequence of noise and model mismatch. For further details we refer the reader to the supplementary code.

APPENDIX *C*
Generalization to coupled orientation–strain models

We shall now consider generalizing our matrix factorization method to a diffraction model discussed by Henningsson *et al.* (2020, Section 6 equation 10-16). Considering the Laue equations (31) in integral form, we find

$$\langle \mathbf{G}_j \rangle = \frac{1}{L_j} \int\limits_{\mathcal{R}_j} \mathbf{U}\mathbf{B}\mathbf{G}^{(j)}_{hkl}\,\mathrm{d}\mathbf{x}, \tag{33}$$

where $\langle \cdot \rangle$ denotes volume average. The target intragranular field of deformation is now generalized to include the local rigid-body rotations as

$$\mathbf{U}\mathbf{B} = \mathbf{U}(\mathbf{x})\mathbf{B}(\mathbf{x}) = \mathbf{f}(\mathbf{x}) \in \mathbb{R}^{3\times 3}. \tag{34}$$

In contrast to the small strain tensor, $\boldsymbol{\varepsilon}$, $\mathbf{f}$ is not symmetric and the number of unknowns per point, $\mathbf{x}$, in the grain is now increased to 9 (compared with six strain tensor components). To reach a similar factorization as that of (26), we start by introducing a flattened format of (33) as

$$\langle \mathbf{G}_j \rangle = \mathbf{H}_j \int\limits_{\mathcal{R}_j} \bar{\mathbf{f}}(\mathbf{x})\,\mathrm{d}\mathbf{x}, \tag{35}$$

where

$$\bar{\mathbf{f}} = \begin{bmatrix} f_{11}(\mathbf{x}) \\ f_{21}(\mathbf{x}) \\ f_{31}(\mathbf{x}) \\ f_{12}(\mathbf{x}) \\ f_{22}(\mathbf{x}) \\ f_{32}(\mathbf{x}) \\ f_{13}(\mathbf{x}) \\ f_{23}(\mathbf{x}) \\ f_{33}(\mathbf{x}) \end{bmatrix} \tag{36}$$

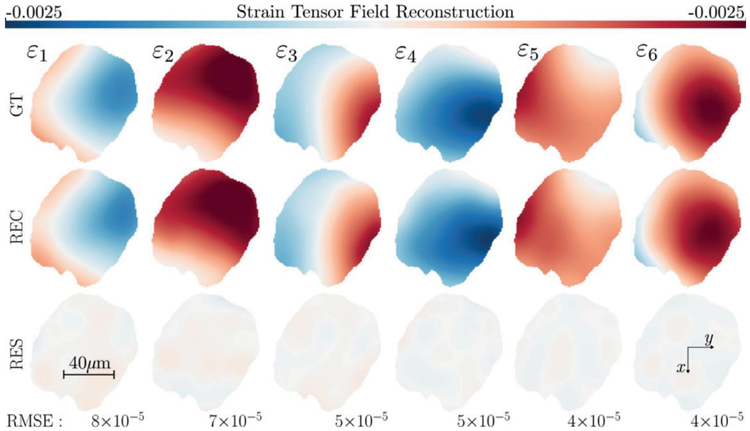

Figure 3
Strain tensor reconstruction (REC) of a single-crystal α-quartz grain slice. The matrix factorization in equation (29) has been used to reconstruct the strain field without the need to assemble the global system matrix. The top row ground-truth simulation input (GT) is to be compared with the middle row reconstructed strain field (REC). The bottom row shows the residual between reconstructed and true strain fields (RES).

and

$$\mathbf{H}_j = \frac{1}{L_j}\left[\,\mathbf{I}h_j \quad \mathbf{I}k_j \quad \mathbf{I}l_j\,\right], \tag{37}$$

and $\mathbf{I}$ is the 3×3 identity matrix. Let us now decompose the target field, $\bar{\mathbf{f}}(\mathbf{x})$, on a finite basis as

$$\bar{\mathbf{f}}(\mathbf{x}) = \sum_{l=1}^{n} \boldsymbol{\beta}_l \varphi_l(\mathbf{x}), \tag{38}$$

where $\varphi_l \in \mathbb{R}$ are the scalar (pixel/voxel) basis functions and

$$\boldsymbol{\beta}_l = \begin{bmatrix} \beta_{1l} \\ \beta_{2l} \\ \beta_{3l} \\ \beta_{4l} \\ \beta_{5l} \\ \beta_{6l} \\ \beta_{7l} \\ \beta_{8l} \\ \beta_{9l} \end{bmatrix}. \tag{39}$$

Insertion of equation (38) into equation (35) yields after rearrangement that

$$\langle \mathbf{G}_j \rangle = \mathbf{H}_j \sum_{l=1}^{n} \boldsymbol{\beta}_l \int_{\mathcal{R}_j} \varphi_l(\mathbf{x})\,\mathrm{d}\mathbf{x}, \tag{40}$$

where the linearity of the involved operators was used. We now note that equation (40) is a higher-dimensional copy of equation (10). Defining $\mathbf{w}_j$ according to equation (11), we find in analogy with equation (12) that

$$\mathbf{Q}_j = \underbrace{\begin{bmatrix} \mathbf{w}_j^{\mathrm{T}} & \mathbf{0} & \mathbf{0} & \ldots & \mathbf{0} \\ \mathbf{0} & \mathbf{w}_j^{\mathrm{T}} & \mathbf{0} & \ldots & \mathbf{0} \\ \vdots & \ddots & \ddots & \ddots & \vdots \\ \mathbf{0} & \ldots & \mathbf{0} & \mathbf{0} & \mathbf{w}_j^{\mathrm{T}} \end{bmatrix}}_{9\times 9n}. \tag{41}$$

We now introduce a set of coefficient vectors,

$$\mathbf{b}_1 = \begin{bmatrix} \beta_{11} \\ \beta_{12} \\ \vdots \\ \beta_{1n} \end{bmatrix}, \mathbf{b}_2 = \begin{bmatrix} \beta_{21} \\ \beta_{22} \\ \vdots \\ \beta_{2n} \end{bmatrix}, \ldots, \mathbf{b}_9 = \begin{bmatrix} \beta_{91} \\ \beta_{92} \\ \vdots \\ \beta_{9n} \end{bmatrix}, \tag{42}$$

and define a partitioned global coefficient vector as

$$\boldsymbol{\tau} = \begin{bmatrix} \mathbf{b}_1 \\ \mathbf{b}_2 \\ \vdots \\ \mathbf{b}_9 \end{bmatrix}. \tag{43}$$

The ray integral equation (40) can now be cast as

$$\langle \mathbf{G}_j \rangle = \mathbf{H}_j \mathbf{Q}_j \boldsymbol{\tau}. \tag{44}$$

We now note that each row in equation (44) has an identical algebraic format compared with equation (15). Splitting the diffraction vector measurements into three separate vectors as

$$\mathbf{d}_1 = \begin{bmatrix} \langle \mathbf{G}_{11} \rangle \\ \langle \mathbf{G}_{12} \rangle \\ \vdots \\ \langle \mathbf{G}_{1m} \rangle \end{bmatrix}, \quad \mathbf{d}_2 = \begin{bmatrix} \langle \mathbf{G}_{21} \rangle \\ \langle \mathbf{G}_{22} \rangle \\ \vdots \\ \langle \mathbf{G}_{2m} \rangle \end{bmatrix}, \quad \mathbf{d}_3 = \begin{bmatrix} \langle \mathbf{G}_{31} \rangle \\ \langle \mathbf{G}_{32} \rangle \\ \vdots \\ \langle \mathbf{G}_{3m} \rangle \end{bmatrix}, \tag{45}$$

we are free to use the same arguments of row and column permutation as described in Section 3 to arrive at

$$\mathbf{d}_1 = \mathbf{M}_1 \mathbf{P}' \boldsymbol{\tau}, \tag{46}$$

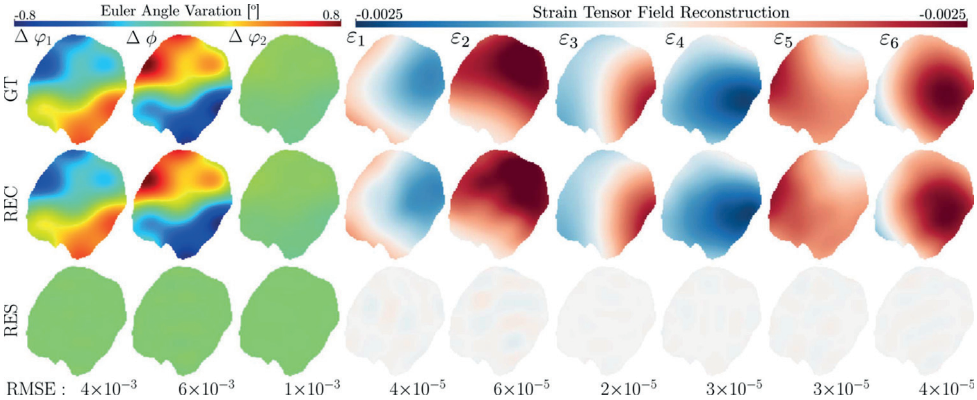

Figure 4
Coupled strain–orientation reconstruction (middle row) in a single slice of α-quartz. The simulated ground-truth (GT) field and corresponding data are described in Appendix *A*. The residual field (RES) can be viewed in the bottom row. Note that the Bunge Euler angles (left) are displayed as a deviation from their respective mean values, allowing for a shared colorbar.

where $\mathbf{P}'$ now is a $9m \times 9n$ block-diagonal projection matrix in direct analogy to equation (21) and the block-diagonal matrix $\mathbf{M}_1$ holds the Miller indices weighted by path length as

$$\mathbf{M}_1 = \underbrace{\begin{bmatrix} \mathbf{h} & \mathbf{0} & \mathbf{0} & \mathbf{k} & \mathbf{0} & \mathbf{0} & \mathbf{l} & \mathbf{0} & \mathbf{0} \end{bmatrix}}_{m\times 9m}, \tag{47}$$

with

$$\mathbf{h} = \mathrm{Diag}\left(\frac{h_j}{L_j}\right),$$
$$\mathbf{k} = \mathrm{Diag}\left(\frac{k_j}{L_j}\right),$$
$$\mathbf{l} = \mathrm{Diag}\left(\frac{l_j}{L_j}\right). \tag{48}$$

The global system of equations can now be written as

$$\begin{bmatrix} \mathbf{d}_1 \\ \mathbf{d}_2 \\ \mathbf{d}_3 \end{bmatrix} = \begin{bmatrix} \mathbf{M}_1 \\ \mathbf{M}_2 \\ \mathbf{M}_3 \end{bmatrix} \mathbf{P}'\boldsymbol{\tau}, \tag{49}$$

with

$$\mathbf{M}_2 = \begin{bmatrix} \mathbf{0} & \mathbf{h} & \mathbf{0} & \mathbf{0} & \mathbf{k} & \mathbf{0} & \mathbf{0} & \mathbf{l} & \mathbf{0} \end{bmatrix},$$
$$\mathbf{M}_3 = \begin{bmatrix} \mathbf{0} & \mathbf{0} & \mathbf{h} & \mathbf{0} & \mathbf{0} & \mathbf{k} & \mathbf{0} & \mathbf{0} & \mathbf{l} \end{bmatrix}. \tag{50}$$

Alternatively, denoting the measurement vector as

$$\mathbf{d} = \underbrace{\begin{bmatrix} \mathbf{d}_1 \\ \mathbf{d}_2 \\ \mathbf{d}_3 \end{bmatrix}}_{3m\times 1} \tag{51}$$

and the Miller sampling matrix as

$$\mathbf{M} = \underbrace{\begin{bmatrix} \mathbf{M}_1 \\ \mathbf{M}_2 \\ \mathbf{M}_3 \end{bmatrix}}_{3m\times 9m}, \tag{52}$$

we arrive at our final factorized diffraction model,

$$\mathbf{d} = \mathbf{M}\mathbf{P}'\boldsymbol{\tau}. \tag{53}$$

The forward pass in equation (53) is defined by nine separate (scalar) projection operations followed by nine multiplications with the diagonal blocks $(\mathbf{h}, \mathbf{k}, \mathbf{l})$ of $\mathbf{M}$. This factorization therefore admits the same computational benefits that are discussed for the decoupled strain model in the main paper. The discussion on generalizations held in Section 4, introducing a weight matrix $\mathbf{W}$ and a change of basis matrix $\mathbf{N}$, is likewise applicable to equation (53). To verify that our derivations are correct we dedicate the following section to applying equation (53) to our demonstration example presented in Appendix *A*.

C1. Application to demonstration example

For completeness we have implemented and solved equation (53) in our demo supplementary code for the same demonstration example that was considered in Appendices *A* and *B*. The same radial basis expansion as described in Appendix *B* was used during regression. Likewise, the true noise covariance matrix was used to solve for the unknown radial basis coefficients in a weighted least-squares sense. The resulting maximum likelihood reconstruction (REC) can be viewed in the middle row of Fig. 4 together with the ground truth (GT) and residual (RES).

Funding information

This work was funded by Vetenskapsrådet – Röntgen Ångström Cluster, project No. 2017-06719.

References

Aarle, W. van, Palenstijn, W. J., Cant, J., Janssens, E., Bleichrodt, F., Dabravolski, A., De Beenhouwer, J., Joost Batenburg, K. & Sijbers, J. (2016). *Opt. Express*, **24**, 25129–25147.

Aarle, W. van, Palenstijn, W. J., De Beenhouwer, J., Altantzis, T., Bals, S., Batenburg, K. J. & Sijbers, J. (2015). *Ultramicroscopy*, **157**, 35–47.

Hayashi, Y., Hirose, Y. & Seno, Y. (2015). *J. Appl. Cryst.* **48**, 1094–1101.

Hektor, J., Hall, S. A., Henningsson, N. A., Engqvist, J., Ristinmaa, M., Lenrick, F. & Wright, J. P. (2019). *Materials*, **12**, 446.

Hendriks, J. N., Wensrich, C. M. & Wills, A. (2020). *Strain*, **56**, e12341.

Henningsson, A. & Hendriks, J. (2021). *J. Appl. Cryst.* **54**, 1057–1070.

Henningsson, N. A., Hall, S. A., Wright, J. P. & Hektor, J. (2020). *J. Appl. Cryst.* **53**, 314–325.

Korsunsky, A. M., Vorster, W. J. J., Zhang, S. Y., Dini, D., Latham, D., Golshan, M., Liu, J., Kyriakoglou, Y. & Walsh, M. J. (2006). *Acta Mater.* **54**, 2101–2108.

Lionheart, W. R. B. & Withers, P. J. (2015). *Inverse Probl.* **31**, 045005.

Palenstijn, W. J., Batenburg, K. J. & Sijbers, J. (2011). *J. Struct. Biol.* **176**, 250–253.

Reischig, P. & Ludwig, W. (2020). *Curr. Opin. Solid State Mater. Sci.* **24**, 100851.

Paper E

Axel Henningsson, Adrian G. Wills, Stephen A. Hall, Johannes Hendriks,
Jonathan P. Wright, Thomas B. Schön, Henning F. Poulsen

Inferring the probability distribution over strain tensors in polycrystals from diffraction based measurements

In: Computer methods in Applied Mechanics and Engineering,
Volume 417, Part A. (2023)

Available online at www.sciencedirect.com
ScienceDirect

Comput. Methods Appl. Mech. Engrg. 417 (2023) 116417

Computer methods in applied mechanics and engineering
www.elsevier.com/locate/cma

Inferring the probability distribution over strain tensors in polycrystals from diffraction based measurements[☆]

Axel Henningsson[a,*], Adrian G. Wills[b], Stephen A. Hall[a], Johannes Hendriks[c,d], Jonathan P. Wright[c,d], Thomas B. Schön[e], Henning F. Poulsen[f]

[a] *Lund University, Division of Solid Mechanics, Ole Römersväg 1, Lund, 221 00, Sweden*
[b] *School of Engineering, University of Newcastle, Newcastle, Australia*
[c] *Australian National University, Canberra, Australia*
[d] *ESRF-The European Synchrotron, Grenoble, France*
[e] *Department of Information Technology, Uppsala University, Uppsala, Sweden*
[f] *Department of Physics, Technical University of Denmark, Kongens Lyngby, Denmark*

Received 17 May 2023; received in revised form 28 August 2023; accepted 29 August 2023
Available online xxxx

Graphical Abstract

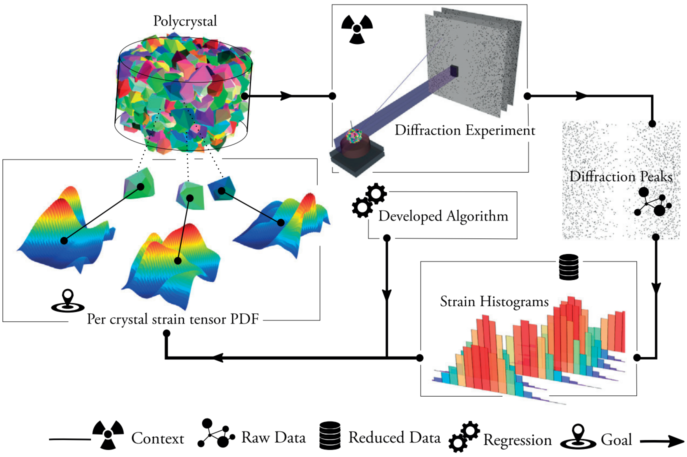

Abstract

Polycrystals illuminated by high-energy X-rays or neutrons produce diffraction patterns in which the measured diffraction peaks encode the individual single crystal strain states. While state of the art X-ray and neutron diffraction approaches can be

---

[☆] This work was funded by Vetenskapsrådet - Röntgen Ångström Cluster, project no. 2017-06719.

[*] Corresponding author.

E-mail address: axel.henningsson@solid.lth.se (A. Henningsson).

https://doi.org/10.1016/j.cma.2023.116417

used to routinely recover per grain mean strain tensors, less work has been produced on the recovery of higher order statistics of the strain distributions across the individual grains. In the setting of small deformations, we consider the problem of estimating the crystal elastic strain tensor probability distribution from diffraction data. For the special case of multivariate Gaussian strain tensor probability distributions, we show that while the mean of the distribution is well defined from measurements, the covariance of strain has a null-space. We show that there exist exactly 6 orthogonal perturbations to this covariance matrix under which the measured strain signal is invariant. In particular, we provide analytical parametrisations of these perturbations together with the set of possible maximum-likelihood estimates for a multivariate Gaussian fit to data. The parametric description of the null-space provides insights into the strain PDF modes that cannot be accurately estimated from the diffraction data. Understanding these modes prevents erroneous conclusions from being drawn based on the data. Beyond Gaussian strain tensor probability densities, we derive an iterative radial basis regression scheme in which the strain tensor probability density is estimated by a sparse finite basis expansion. This is made possible by showing that the operator mapping the strain tensor probability density onto the measured histograms of directional strain is linear, without approximation. The utility of the proposed algorithm is demonstrated by numerical simulations in the setting of single crystal monochromatic X-ray scattering. The proposed regression methods were found to robustly reject outliers and accurately predict the strain tensor probability distributions in the presence of Gaussian measurement noise.

Keywords: Diffraction; Estimation; Strain tensor; X-rays; Polycrystals; Probability distributions

1. Introduction

Neutrons and high energy X-rays are key tools for non-destructive testing in the materials research community (e.g., [1,2]). Today, large scale synchrotron, reactor and spallation facilities offer a wide range of material characterisation possibilities where in-situ 3D volume measurements in the bulk of dense materials can be achieved, e.g., [3,4]. Coupled with modern statistical regression tools and high performance computing, a plethora of physical quantities, embedded into first principle mathematical material models, can be characterised, e.g., [5,6]. Such estimations are important for successful calibration and validation of advanced numerical materials models. Importantly, the non-destructive nature of neutrons and X-rays enables measurements on the same test specimens to be repeated, decreasing uncertainty in the estimation and unlocking the possibility for monitoring of changes during in-situ testing, e.g., loading [7] or heating [8].

Three Dimensional X-ray Diffraction Microscopy (3DXRD) [9] and the High Energy Diffraction Microscopy (HEDM) [10] are becoming established as workhorses for the diffraction microscopy imaging community. Using hard X-rays (∼10–100 keV), these microscopy techniques enable per-grain characterisation of polycrystalline aggregates featuring thousands of grains [11–14]. With a penetration depth in the range of mm for dense materials, 3DXRD/HEDM has developed into a popular tool for non destructive testing of metals, alloys, rocks and granular media. The technique relies on the measurement of 2D mono-channel digital images of spotty diffraction patterns to estimate per-grain position, volume, average strain [15], average stress [16,17] and orientation [18].

Beyond the average grain state, accessible by standard 3DXRD and in pursuit of intragranular variation, Scanning Three Dimensional X-ray Diffraction Microscopy (s3DXRD) [19] and point focused High Energy Diffraction Microscopy (pf-HEDM) [20] have developed under the 3DXRD and HEDM umbrellas. The key difference in s3DXRD is the focusing of the X-ray beam such that only sub-volumes of the crystals are illuminated at any given time. By carefully scanning the sample across the beam, bundles of 2D diffraction pattern images are acquired. From these images, tomography-like reconstruction methods can be used to estimate the grain shapes as well as the intragranular strain tensor fields [21–24]. In addition to achieving sub-grain resolution, narrowing the beam helps alleviate the issue of diffraction spot overlap due to abundant scattering [25]. Unfortunately, despite recent progress in beam brilliance and detector technology, the scanning type methods are time consuming, with state of the art experiments often requiring tens of hours for a full 3D scan of a sample, e.g., [26]. On the other hand, classical (full-field) 3DXRD/HEDM microscopy, using a wide beam, offers a 10–100 times speedup.

For polycrystal samples with a moderate number of grains (100–1000), with minimal diffraction spot overlap, efficient algorithms for mapping the individual crystal orientations exist [27]. The main drawback of full-field 3DXRD/HEDM, in relation to its scanning mode, is the loss of information on the spatial origin of diffraction within the grains. This makes reconstruction of orientation and strain maps over the grain volume very challenging, especially for highly deformed samples [28]. However, valuable intragranular information can still be attained in terms of probability density distributions over the underlying spatial fields. For example, in the work of Poulsen et al. [29] and Hansen et al. [30] the probability density of orientation states within the individual crystals where shown to be recoverable. In similar spirit [31], inspired by Behnken [32], showed how the mean strain tensor state for each intragranular orientation state can be efficiently baked into the inverse problem, enriching the capabilities of the 3DXRD/HEDM microscope. The latter of these methods recovers a lattice strain density function (LSDF), sometimes also refereed to as a strain orientation density function (SODF). As explained by Bernier and Miller [33], the variation in the micromechanical state is not fully captured by the SODF. To illustrate we may consider a near-perfect crystal, such that the orientation distribution function approaches a Dirac delta, the resulting SODF will then only provide information on the mean strain tensor in the grain. None the less, the diffracting grains can possess spatially varying elastic strain fields, even if the grain orientation is close to constant. More generally, considering an orientation spread within the grain, each individual orientation state in the grain can exist on a spatially extended sub-volume of the grain over which the strain tensor is unlikely to be constant.

Just as the grain orientation variation unlocks a new type of material parameter estimation [34], higher order statistics on the distribution of the elastic strain tensors can be used to calibrate micro-mechanical material models. Motivated by this, we decouple the problem of orientation reconstruction from that of strain and develop a regression framework capable of estimating the strain tensor probability distribution (strain PDF) inside the individual crystals within a polycrystalline sample. The aim is to recover the 6-dimensional strain PDF that describes the scalar likelihood of encountering any one particular strain tensor at any randomly (uniformly) selected point within the given grain. We emphasise that our method recovers the strain PDF in a single crystal diffraction setting.

Our method is primarily aimed at upgrading the full-field mode of the 3DXRD/HEDM microscope, where peak strain broadening is a known phenomena (c.f [35]). However, our results can be cast abstractly as a regression from sets of histograms of directional strains attached to an unknown spatial volume. Other neutron and X-ray microscopy methods where such data can reliably be made available will, therefore, be applicable for a similar upgrade. For instance [36] recently showed that the second moment of such directional strain histograms can be reliably recovered from neutron Bragg edge transmission measurements on polycrystals.

The structure of the paper is as follows. In Section 2, we describe how the considered diffraction measurements relate to the strain state of the crystals and introduce the concept of histograms of directional strain. In Section 3 we define our target reconstruction quantity – the strain PDF – and present the inverse problem we are solving. In Section 4, we discuss some of the benefits and limitations of recovering the strain PDF. In Section 5, we derive the mapping between measured and reconstructed quantities. Using the established measurement model we describe our solution to the inversion problem in Section 6. In Section 7, we discuss the observability of the inverse problem for the special case of a multivariate Gaussian strain PDF and provide a closed form solution for its estimation. To verify our mathematical results we devote Section 8 to a numerical simulation study of a spherical iron (Fe) grain with a cubic crystal structure in mechanical self-equilibrium. We summarise our findings in Section 9, and give an outlook for future research in Section 10. Finally, we conclude our paper in Section 11.

2. Crystal strains in diffraction measurements

The conditions for diffraction to occur from a crystal can be described by the Laue equations. Under elastic scattering conditions, letting the incident wavevector, $\boldsymbol{k}$, be aligned with the incident photon propagation direction and denoting the scattered wavevector by, $\boldsymbol{k}'$, the Laue equations state that

$$\boldsymbol{C}^T(\boldsymbol{k}'-\boldsymbol{k}) = 2\pi\begin{bmatrix} h \\ k \\ l \end{bmatrix}, \quad \boldsymbol{k}^T\boldsymbol{k} = \boldsymbol{k}'^T\boldsymbol{k}' = \frac{4\pi^2}{\lambda^2}, \tag{1}$$

where h, k and l are Miller indices and the columns of the matrix $\boldsymbol{C}$ are the crystal unit cell vectors in direct space. Eq. (1) represents a geometrical relation between the X-ray wavelength, λ, and the lattice plane separation, d_{hkl}, resulting in alignment of the outgoing scattered wave crests. Reducing the Laue equations (1) to 2D results in the well known Bragg's law,

$$2d_{hkl}\sin(\theta) = m\lambda, \quad m = 1, 2, 3, .. \tag{2}$$

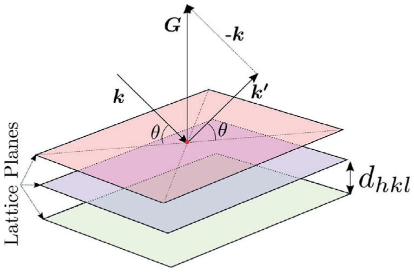

Fig. 1. Conceptual drawing of scattering from a set of crystal lattice planes. The difference between incident, $\boldsymbol{k}$, and scattered, $\boldsymbol{k}'$, wavevector forms the diffraction vector $\boldsymbol{G}$, which is orthogonal to the scattering planes. A perturbation to the lattice plane distance d_{hkl} will be observed as a change in Bragg angle θ.

where θ is the Bragg angle formed between $\boldsymbol{k}$ and the diffracting crystal planes. Considering a small scalar strain, s, acting on the lattice planes we find from Bragg's law (2) that

$$2(1+s)d_{hkl}\sin(\theta) = m\lambda \quad \rightarrow \quad \sin(\theta) = \frac{m\lambda}{2(1+s)d_{hkl}}, \tag{3}$$

i.e, the scattering angle, θ, is sensitive to directional strain. Given some reference angle of scattering, θ_0, corresponding to a strain free crystal, we find that the directional strain, s, existing along the diffraction vector, $\boldsymbol{G} = \boldsymbol{k}' - \boldsymbol{k}$, can be expressed as

$$s = \frac{d_{hkl} - d_{hkl}^{(0)}}{d_{hkl}^{(0)}} = \frac{\sin(\theta_0) - \sin(\theta)}{\sin(\theta)}, \tag{4}$$

where d_{hkl} and $d_{hkl}^{(0)}$ are the strained and strain free lattice plane separations respectively. The geometrical context of the above discussed quantities is presented in Fig. 1.

For a more in depth explanation of the fundamental concepts of X-ray scattering see, for example, Als-Nielsen and McMorrow [37].

2.1. The 3DXRD/HEDM framework

The experimental 3DXRD/HEDM techniques exploit the Laue equations (1) to find the crystal lattices of the individual grains in a diffracting polycrystalline aggregate. The typical experimental setup is depicted in Fig. 2 where the sample, in this case, rotates about a single (vertical) axis throughout the measurement sequence. When the angle between the lattice planes and $\boldsymbol{k}$ fulfil Bragg's law (2) diffraction spots are measured with the 2D detector placed behind the sample. The Laue equations (1) constrain $\boldsymbol{k}'$ to fall on cones of increasingly larger opening angles. As a result, the diffraction pattern seen in Fig. 2 is characterised by non-zero intensity falling on rings centred around the detector and beam intersection point.

Commonly in the 3DXRD/HEDM type of diffraction applications, the unit cell matrix, $\boldsymbol{C}$, is given in a multiplicative form as

$$\boldsymbol{C} = \boldsymbol{U}\boldsymbol{C}_c, \tag{5}$$

where the crystal rotation matrix, $\boldsymbol{U}$, acts to rotate the unit cell vector, now contained in crystal coordinates in $\boldsymbol{C}_c$, into the sample coordinate system. This multiplicative split is motivated by the fact that, while the matrix $\boldsymbol{C}_c$ is fairly constant between crystals sharing a phase in the sample, the orientation of the crystals, $\boldsymbol{U}$, can vary drastically between grains. The primary task in 3DXRD/HEDM is to find a set of crystal orientations, $\boldsymbol{U}$, such that the measured data can be explained. This procedure is denoted as grain mapping or grain indexing.

Introducing $\boldsymbol{B} = 2\pi\boldsymbol{C}_c^{-T}$ and $\boldsymbol{G}_{hkl} = \begin{bmatrix} h & k & l \end{bmatrix}^T$, we write

$$\boldsymbol{G}_s = \boldsymbol{U}\boldsymbol{B}\boldsymbol{G}_{hkl}, \tag{6}$$

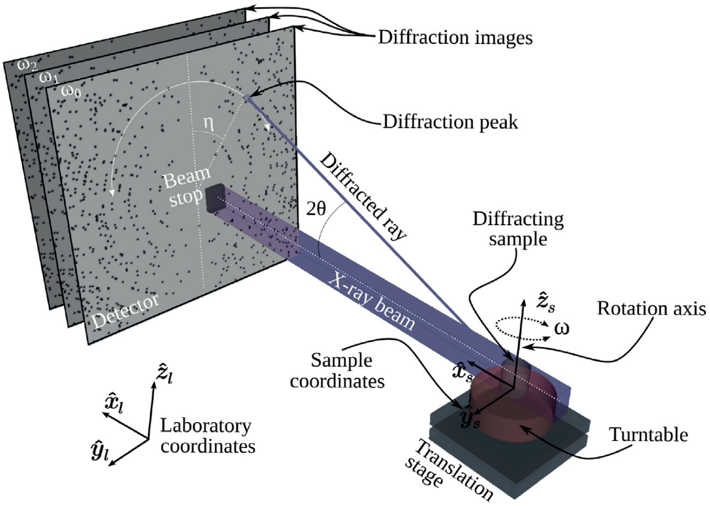

Fig. 2. A polycrystalline aggregate is rotated about a single axis, $\hat{z}_s = \hat{z}_l$, while fully illuminated by a beam of high energy X-rays with wavevector along $\hat{\boldsymbol{x}}$. The recorded digital images of spotty diffraction data (black dots) can be used to infer the grain positions and orientations. The Cartesian sample coordinates follow the turntable while the Cartesian laboratory frame is fixed with respect to sample motion. A diffraction image is recorded at each turntable rotation ($\omega_0, \omega_1, \omega_2 ..$).

where subscript s has been used to denote that $\boldsymbol{G}_s$ is given in sample coordinates. As the sample is rotated by an angle ω around $\hat{z}_s$ the corresponding rotation matrix, $\boldsymbol{\Omega}$, provides the map between laboratory and sample coordinates. The central equation for 3DXRD/HEDM is, therefore,

$$\boldsymbol{G}_l = \boldsymbol{\Omega}\boldsymbol{U}\boldsymbol{B}\boldsymbol{G}_{hkl}, \tag{7}$$

where $\boldsymbol{G}_l$ can be computed from observations of $\boldsymbol{k}_l'$. Thus, given a set of unit cell parameters (defining $\boldsymbol{B}$), a selected lattice plane (defining $\boldsymbol{G}_{hkl}$), a crystal orientation ($\boldsymbol{U}$) and a sample rotation ($\boldsymbol{\Omega}$), Eq. (7), can be used to predict $\boldsymbol{G}_l = \boldsymbol{k}_l' - \boldsymbol{k}_l$. Given experimental parameters, such as detector size and position, these equations provide a model connecting the measured diffraction patterns and the properties of the polycrystalline aggregate. Indeed, sophisticated algorithms have been developed, and refined over years, to reconstruct the set of $\boldsymbol{U}$ and $\boldsymbol{B}$ matrices that correspond to the individual grains within the aggregate, e.g., [11,12,27]. Once estimated, any proceeding analysis can operate on a per grain basis, separating out the parts of the diffraction images that are associated to any given crystal.

2.2. Histograms of directional strain

The recording on the detector of diffraction peaks generated by a crystal with known orientation, $\boldsymbol{U}$, are digital images representing a discrete rendering of an underlying 2D photon intensity distribution. The formation of this intensity distribution is a nontrivial process involving, among other things; the crystal shape, the crystal deformation, the beam coherence, the energy bandwidth of beam, the detector point spread function and the detector pixel size [38,39]. To recover the strain tensor probability density associated to the given crystal, we are interested in modelling the impact of the crystal strain to the peak shape. To this end we shall denote the spatial coordinate with $\boldsymbol{x} \in \mathbb{R}^3$ and let the deformation gradient tensor $\boldsymbol{F} \in \mathbb{R}^{3\times3}$ map from reference, $\boldsymbol{x}_0$, to current deformed configuration as

$$\boldsymbol{F}\boldsymbol{x}_0 = \boldsymbol{x}. \tag{8}$$

We denote the undeformed reference unit cell, $\boldsymbol{C}_0$, and the current deformed unit cell matrix as $\boldsymbol{C}_{cur}$. Let $\mathcal{G}[\cdot]$ be the diffraction operator that, given an input unit cell matrix, returns the corresponding set of diffraction vectors,

$\{\boldsymbol{G}^1, \boldsymbol{G}^2, \dots, \boldsymbol{G}^m\}$, observed in 3DXRD/HEDM. Clearly, the measured set of diffraction vectors originates from the deformed configuration as

$$\mathcal{G}[\boldsymbol{C}_{cur}] = \{\boldsymbol{G}^1, \boldsymbol{G}^2, \dots, \boldsymbol{G}^m\}. \tag{9}$$

However, there exist modes of deformation, which we, here, denote by $\boldsymbol{F}_p$, to which the diffraction set is immutable, such that

$$\mathcal{G}[\boldsymbol{F}_p\boldsymbol{C}_0] = \mathcal{G}[\boldsymbol{C}_0]. \tag{10}$$

For instance, dislocation glide that results in a constant-volume plastic deformation and leaves the crystal lattice unchanged, has no measurable effect on the diffraction patterns in 3DXRD/HEDM. This motivates the use of a multiplicative split of the deformation gradient tensor similar to that used in crystal plasticity [40–44],

$$\boldsymbol{F} = \boldsymbol{F}_e\boldsymbol{F}_p, \tag{11}$$

where the elastic deformation, $\boldsymbol{F}_e$, is defined, here, as any deformation to the crystal that will cause a nonzero perturbation in the measured set of diffraction vectors,

$$\mathcal{G}[\boldsymbol{F}_e\boldsymbol{C}_0] \neq \mathcal{G}[\boldsymbol{C}_0]. \tag{12}$$

The plastic contribution, $\boldsymbol{F}_p$, here maps from the reference state to an intermediate stress-free configuration while $\boldsymbol{F}_e$ maps from the intermediate configuration to the current deformed configuration. See Appendix A Fig. 13 for a summary of the discussed configurations.

Building on the above arguments, we define a fictive configuration, $\boldsymbol{C}$, that would result from the application of the elastic deformation to the reference unit cell,

$$\boldsymbol{C} = \boldsymbol{F}_e\boldsymbol{C}_0, \tag{13}$$

with the special property,

$$\mathcal{G}[\boldsymbol{C}] = \mathcal{G}[\boldsymbol{C}_{cur}]; \tag{14}$$

i.e the fictive unit cell matrix, $\boldsymbol{C}$, is diffraction equivalent to the true deformed unit cell matrix, $\boldsymbol{C}_{curr}$. To relate the elastic, diffraction observable, deformation, $\boldsymbol{F}_e$, to the crystal strain tensor field, we define the total Green–Lagrange strain in the intermediate stress free configuration [43] as

$$\boldsymbol{e} = \frac{1}{2}\boldsymbol{F}_p^{-T}(\boldsymbol{F}^T\boldsymbol{F} - \boldsymbol{I})\boldsymbol{F}_p^{-1} = \underbrace{\frac{1}{2}(\boldsymbol{F}_e^T\boldsymbol{F}_e - \boldsymbol{I})}_{\boldsymbol{e}_e} + \underbrace{\frac{1}{2}(\boldsymbol{I} - \boldsymbol{F}_p^{-T}\boldsymbol{F}_p^{-1})}_{\boldsymbol{e}_p}, \tag{15}$$

where the total strain, $\boldsymbol{e}$, is decomposed into an elastic part, $\boldsymbol{e}_e$, and a plastic part, $\boldsymbol{e}_p$. Working in the limit of small strains, we are now ready to define our ultimate goal that is to reconstruct the probability density distribution of the elastic strain tensor field, $\boldsymbol{e}_e$. By Taylor expansion we find

$$\boldsymbol{e}_e = \boldsymbol{e}_e(\boldsymbol{x}) = \begin{bmatrix} e_{11}(\boldsymbol{x}) & e_{12}(\boldsymbol{x}) & e_{13}(\boldsymbol{x}) \\ e_{12}(\boldsymbol{x}) & e_{22}(\boldsymbol{x}) & e_{23}(\boldsymbol{x}) \\ e_{13}(\boldsymbol{x}) & e_{23}(\boldsymbol{x}) & e_{33}(\boldsymbol{x}) \end{bmatrix} \approx \frac{1}{2}(\boldsymbol{F}_e^T + \boldsymbol{F}_e) - \boldsymbol{I}, \tag{16}$$

(see e.g., [45] for an introduction to continuum-mechanics). Since all unit cell matrices are invertible, by definition, it follows from Eq. (13) that

$$\boldsymbol{F}_e = \boldsymbol{C}\boldsymbol{C}_0^{-1}. \tag{17}$$

Using the Laue Equations (1), we find a reference diffraction vector, $\boldsymbol{G}_0$, and a measured diffraction vector, $\boldsymbol{G}$, as

$$\boldsymbol{G}_0 = 2\pi\boldsymbol{C}_0^{-T}\boldsymbol{G}_{hkl}, \quad \boldsymbol{G} = 2\pi\boldsymbol{C}^{-T}\boldsymbol{G}_{hkl}. \tag{18}$$

Combining Eqs. (17) and (18) we find that

$$\boldsymbol{G} = \boldsymbol{F}_e^{-T}\boldsymbol{G}_0. \tag{19}$$

Multiplying Eq. (16) from left and right by $\boldsymbol{G}$ and making use of Eq. (19), we find

$$\boldsymbol{G}^T\boldsymbol{e}_e\boldsymbol{G} = \frac{1}{2}(\boldsymbol{G}^T\boldsymbol{G}_0 + \boldsymbol{G}_0^T\boldsymbol{G}) - \boldsymbol{G}^T\boldsymbol{G}, \tag{20}$$

Normalising Eq. (20) by $\boldsymbol{G}^T\boldsymbol{G}$, we now arrive at a scalar directional strain measure, $s_{hkl} = \hat{\boldsymbol{\kappa}}^T \boldsymbol{e}_e \hat{\boldsymbol{\kappa}}$, as

$$s_{hkl} = \hat{\boldsymbol{\kappa}}^T \boldsymbol{e}_e \hat{\boldsymbol{\kappa}} = \frac{\boldsymbol{G}^T\boldsymbol{G}_0}{\boldsymbol{G}^T\boldsymbol{G}} - 1, \tag{21}$$

where

$$\hat{\boldsymbol{\kappa}} = \frac{\boldsymbol{G}}{\sqrt{\boldsymbol{G}^T\boldsymbol{G}}}. \tag{22}$$

Note that for small elastic deformations the approximation

$$\hat{\boldsymbol{\kappa}} = \frac{\boldsymbol{G}}{\sqrt{\boldsymbol{G}^T\boldsymbol{G}}} \approx \frac{\boldsymbol{G}_0}{\sqrt{\boldsymbol{G}_0^T\boldsymbol{G}_0}}, \tag{23}$$

is also valid. Likewise, from Eq. (21), it follows that the directional strain, s_{hkl}, is only weakly dependent on lattice rotations, as $\boldsymbol{G}^T\boldsymbol{G} = \boldsymbol{B}^T\boldsymbol{U}^T\boldsymbol{U}\boldsymbol{B} = \boldsymbol{B}^T\boldsymbol{B}$ and $\boldsymbol{G}_0^T\boldsymbol{G} = \boldsymbol{B}_0^T\boldsymbol{U}_0^T\boldsymbol{U}\boldsymbol{B}$ where $\boldsymbol{U}_0^T\boldsymbol{U} \approx 1$ for moderate deformations. This motivates the decoupling of strain reconstruction from that of lattice rotations in the presence of small deformations. While it may be possible to extend the derivations presented above, and in the following, to a large deformation setting we limit the scope of this paper to that of small elastic strains.

Considering that each of the detector pixels composing a single diffraction peak is associated to a distinct diffraction vector, $\boldsymbol{G}$, we see from Eq. (21) that also s_{hkl} will vary over the diffraction peak. As the pixel intensity values of the diffraction peak are proportional to the diffracting sub volumes of the grain we have access to a histogram, $h(s_{hkl})$, over directional strains in the crystal. To form this histogram each normalised pixel intensity weight is to be added to the corresponding bin-count for the associated directional strain value, s_{hkl}. Note that this procedure reduces the information contained in the diffraction peak to a one dimensional function in s_{hkl}. Importantly, these histograms of directional strain are directly linked to the underlying spatial strain tensor field as

$$h(s_{hkl}) = \frac{1}{V_\Omega} \int_{s_{hkl}-w/2}^{s_{hkl}+w/2} \int_{\mathbb{R}^3} \mathcal{I}(\hat{\boldsymbol{\kappa}}^T \boldsymbol{e}_e(\boldsymbol{x})\hat{\boldsymbol{\kappa}} - s') d\boldsymbol{x} ds', \quad V_\Omega = \int_\Omega d\boldsymbol{x}, \tag{24}$$

where $\mathcal{I}$ is an indicator function supported on the crystal grain domain Ω, V_Ω is the volume of the grain and w is the histogram bin width. To simplify our following analysis we introduce a flattened vector notation similar to Henningsson and Hendriks [24]. Utilising the symmetry of the strain tensor we write

$$\boldsymbol{E} = \begin{bmatrix} e_{11} \\ e_{22} \\ e_{33} \\ e_{12} \\ e_{13} \\ e_{23} \end{bmatrix}, \quad \bar{\boldsymbol{\kappa}} = \begin{bmatrix} \kappa_x^2 \\ \kappa_y^2 \\ \kappa_z^2 \\ 2\kappa_x\kappa_y \\ 2\kappa_x\kappa_z \\ 2\kappa_y\kappa_z \end{bmatrix}, \tag{25}$$

and find that the inner product in Eqs. (21) and (24) become

$$s = \hat{\boldsymbol{\kappa}}^T \boldsymbol{e}_e(\boldsymbol{x})\hat{\boldsymbol{\kappa}} = \bar{\boldsymbol{\kappa}}^T \boldsymbol{E}. \tag{26}$$

With the introduction of the histograms of directional strains we are now ready to formally define our sought quantity; the strain PDF. Once this additional definition is made we can state our full inverse problem formulation.

3. Problem formulation

We seek to estimate the probability density function over strain tensors (strain PDF), $p_{\boldsymbol{E}}(\boldsymbol{\epsilon})$, that describes the scalar probability of encountering any one particular strain tensor, $\boldsymbol{\epsilon}$, at a randomly (uniformly) selected point, $\boldsymbol{x}$, in the grain. Formally, we define the strain PDF, $p_{\boldsymbol{E}} : \mathbb{R}^6 \to \mathbb{R}^1$, associated to a spatial strain tensor field, $\boldsymbol{E}(\boldsymbol{x})$, as

$$p_{\boldsymbol{E}}(\boldsymbol{\epsilon}) = \frac{1}{V_\Omega} \int_{\mathbb{R}^3} \mathcal{I}(\boldsymbol{E}(\boldsymbol{x}) - \boldsymbol{\epsilon}) d\boldsymbol{x}, \quad V_\Omega = \int_\Omega d\boldsymbol{x}, \tag{27}$$

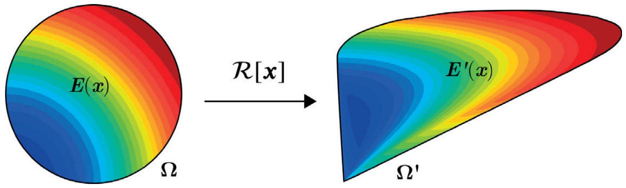

Fig. 3. The mapping of a spatial field, $\boldsymbol{E}$, supported on the unit disc, centred at $\boldsymbol{x} = [0.5, 0.5]$, results in a new spatial field, $\boldsymbol{E}'(\boldsymbol{x}) = \boldsymbol{E}(\mathcal{R}[\boldsymbol{x}])$, such that $\boldsymbol{E}(\boldsymbol{x}) \neq \boldsymbol{E}'(\boldsymbol{x})$. Nevertheless, the two corresponding strain PDFs remain identical, $p_{\boldsymbol{E}}(\boldsymbol{\epsilon}) = p_{\boldsymbol{E}'}(\boldsymbol{\epsilon})$, as long as the map, $\mathcal{R}[\boldsymbol{x}]$, is area preserving.

and state the inverse problem: *Given a set of histograms,* $h_1(s_{hkl}), h_2(s_{hkl}), .., h_m(s_{hkl})$*, all of which are associated with a single grain, we seek an estimation of the strain PDF,* $p_{\boldsymbol{E}}(\boldsymbol{\epsilon})$*, of the given grain, such that the measured histograms can be plausibly explained.*

We emphasise that each histogram, $h_i(s_{hkl})$, corresponds to a single diffraction peak and measures directional strain in a known distinct direction, $\bar{\boldsymbol{\kappa}}_i$, in the indexed crystal. The task is therefore to find a parametric expression for $p_{\boldsymbol{E}}(\boldsymbol{\epsilon})$ such that the measured histograms, $h_1(s_{hkl}), h_2(s_{hkl}), .., h_m(s_{hkl})$, are well modelled. To achieve this we will need to establish the transformation from strain PDF to directional histograms of strains. Before pursuing this task, however, we shall discuss some general properties and limitations of the strain PDF. Especially, we emphasise how the strain PDF provides richer information about the grain deformation state compared to the grain average strain tensor.

4. Properties of the strain probability density function

We note that while the strain PDF exists for any one spatial strain field $\boldsymbol{E}(\boldsymbol{x})$, the mapping is not necessarily unique. As an example, let $\mathcal{R} : \mathbb{R}^3 \rightarrow \mathbb{R}^3$ be an area preserving function such that $\det(\mathcal{R}') = 1, \forall \boldsymbol{x}$, where $\mathcal{R}'$ is the Jacobian of $\mathcal{R}$. Making use of this map we define a modified spatial strain field as $\boldsymbol{E}'(\boldsymbol{x}) = \boldsymbol{E}(\mathcal{R}[\boldsymbol{x}])$ with $\boldsymbol{y} = \mathcal{R}[\boldsymbol{x}]$. From the definition of the strain PDF it now follows that

$$\begin{aligned} p_{\boldsymbol{E}}(\boldsymbol{\epsilon}) &= \frac{1}{V_\Omega}\int_{\mathbb{R}^3} \mathcal{I}(\boldsymbol{E}(\boldsymbol{y}) - \boldsymbol{\epsilon}) d\boldsymbol{y} = \frac{1}{V_\Omega}\int_{\mathbb{R}^3} \mathcal{I}(\boldsymbol{E}(\mathcal{R}[\boldsymbol{x}]) - \boldsymbol{\epsilon}) d\mathcal{R}[\boldsymbol{x}] = \\ &\frac{1}{V_\Omega}\int_{\mathbb{R}^3} \mathcal{I}(\boldsymbol{E}'(\boldsymbol{x}) - \boldsymbol{\epsilon}) \det(\mathcal{R}') d\boldsymbol{x} = \frac{1}{V_\Omega}\int_{\mathbb{R}^3} \mathcal{I}(\boldsymbol{E}'(\boldsymbol{x}) - \boldsymbol{\epsilon}) d\boldsymbol{x} = p_{\boldsymbol{E}'}(\boldsymbol{\epsilon}). \end{aligned} \tag{28}$$

Simple examples of $\mathcal{R}$ on $\mathbb{R}^3$ includes combinations of rigid body rotations and translations. In Fig. 3 we give a nonlinear example on $\mathbb{R}^2$, mapping the unit disc centred at $\boldsymbol{x} = [0.5, 0.5]$ through the area preserving map

$$\mathcal{R}[\boldsymbol{x}] = \begin{bmatrix} \sqrt{x_1} \\ 2x_2\sqrt{x_1} \end{bmatrix}, \quad \boldsymbol{x} > 0. \tag{29}$$

The strain PDF provides weaker information on the deformation of the domain compared to the spatial strain tensor field itself. Nevertheless, in relation to only knowing the mean value of a spatial strain tensor field, the strain PDF is a rich quantity. We provide an illustration of the concept of a strain PDF in Fig. 4. In this example a Finite Element solver was used to solve for the equilibrium strain field given a symmetric (across y) geometry and boundary load. The body was considered linear elastic with width and height both set to 1 μm, while the out of $x-y$ thickness was set to 100 μm such that plane strain conditions prevailed. Owing to the symmetry, a perturbation in Young's modulus, E, will correspond to a simple scaling of the strain field. As illustrated in the projections of the corresponding strain PDFs in Fig. 4 (left column), the mean of the distribution is immutable to such a scaling of the spatial strain field (the cerise dot marking the mean does not move). The topology of the strain PDF does, however, change as a result of the perturbation in material stiffness, E. This motivates the value of retaining deeper statistics on the strain PDF, beyond the commonly derived mean value. Similar examples can be constructed with respect to perturbations in boundary load, object topology, Poisson ratio, etc.

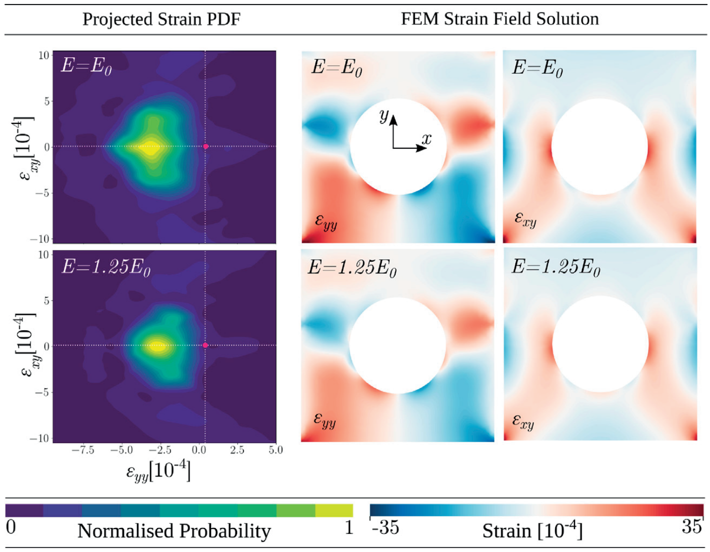

Fig. 4. Example of the topological shape of a strain PDF (left) revealed in part by its projection onto one of the 15 Cartesian planes in strain space (zoomed in around the mean strain which is marked out by a cerise dot and a dashed cross). The spatial strain field (right) is the linear elastic Finite Element solution of a symmetric plane strain boundary value problem using 4944 triangular constant strain elements. Changing the stiffness of the material (top row vs. bottom row) results in a scaled FEM solution. While the mean of the strain PDF is invariant to a change in stiffness, the full topology of the strain PDF mutates with the change in material stiffness, E (compare left top and left bottom). This illustrates that the strain PDF is a richer quantity than the mean of the spatial strain tensor field.

5. Measurement model

To solve the inverse problem defined in Section 3 we establish a measurement model that can map the strain PDF to a set of histograms of directional strain. Let us therefore consider a single histogram, $h_j[s_j]$, and let us inquire for the bin count at the bin centre, $s_j = s_j^*$, such that $h_j^* = h_j[s_j^*]$, where s_j^* is the directional strain at the bin centre, $s_j^* = \bar{\boldsymbol{\kappa}}^T \boldsymbol{E}^*$. The subdomain on strain space holding the strain tensors, $\boldsymbol{E}^*$, that fulfil this equality is then defined by

$$\frac{1}{\|\bar{\boldsymbol{\kappa}}\|_2} \bar{\boldsymbol{\kappa}}^T \boldsymbol{E}^* = \frac{s}{\|\bar{\boldsymbol{\kappa}}\|_2}. \tag{30}$$

Eq. (30) defines a hyperplane on $\mathbb{R}^6$ with unit normal $\hat{\boldsymbol{n}} = \bar{\boldsymbol{\kappa}}/\|\bar{\boldsymbol{\kappa}}\|_2$ and scalar origin offset $t = s/\|\bar{\boldsymbol{\kappa}}\|_2$. It follows that the histogram bin count, h_j^*, is given by the integral across all planes with normal $\hat{\boldsymbol{n}}$ and origin of-sets $t \in [s_j^* - w/2, s_j^* + w/2]$ where w is the histogram bin width. Thus,

$$h_j^*[s_j^*] = \int_{s_j^* - w/2}^{s_j^* + w/2} \int_{\boldsymbol{\epsilon} \in \Pi(t, \hat{\boldsymbol{n}}_j)} p_{\boldsymbol{E}}(\boldsymbol{\epsilon}) d\boldsymbol{\epsilon} dt, \tag{31}$$

where $\Pi(t, \hat{\boldsymbol{n}}_j)$ is the hyperplane with normal $\hat{\boldsymbol{n}}_j$ and scalar origin offset $t = s/\|\bar{\boldsymbol{\kappa}}\|_2$. This represents a linear measurement model and requires the computation of a single volume integral per measured histogram bin. Let us now define the linear operator $\mathcal{M}_j$ which maps any function, $f(\boldsymbol{\epsilon})$, to k histogram bins modelling all histogram bin counts for the j:th histogram as

$$\mathcal{M}_j[f(\boldsymbol{\epsilon})] = \begin{bmatrix} \int_{s_j^1-w/2}^{s_j^1+w/2} \int_{\boldsymbol{\epsilon}\in\Pi(t,\hat{\boldsymbol{n}}_j)} p_{\boldsymbol{E}}(\boldsymbol{\epsilon}) d\boldsymbol{\epsilon} dt \\ \vdots \\ \vdots \\ \int_{s_j^k-w/2}^{s_j^k+w/2} \int_{\boldsymbol{\epsilon}\in\Pi(t,\hat{\boldsymbol{n}}_j)} p_{\boldsymbol{E}}(\boldsymbol{\epsilon}) d\boldsymbol{\epsilon} dt \end{bmatrix} = \begin{bmatrix} h_j[s_j^1] \\ \vdots \\ \vdots \\ h_j[s_j^k] \end{bmatrix}, \tag{32}$$

where s_j^k denotes the k:th bin centre of the j:th histogram. A closed form expression for the inverse operator, $\mathcal{M}_j^{-1}$, is not known. However, by selecting a parametric expression for the strain PDF and a cost function, measuring the difference between model and measured histograms of directional strain, gradient based optimisation techniques can be used to recover the parameters defining the strain PDF. We therefore proceed to introduce a finite basis expansion of the strain PDF.

6. Reconstruction approach

6.1. Finite basis strain PDF expansion

Decomposing the strain PDF into a linear combination of n basis functions, φ_i, as

$$p_{\boldsymbol{E}}(\boldsymbol{\epsilon}) = \sum_i^n c_i \varphi_i(\boldsymbol{\epsilon}), \quad c_i, \varphi_i \in \mathbb{R}^1, \tag{33}$$

we find the maximum-likelihood estimator in the presence of Gaussian noise as

$$\underset{c_i}{\operatorname{argmin}} \sum_j^m \| h_j - \mathcal{M}_j[p_{\boldsymbol{E}}] \|_2^2, \quad \texttt{s.t.} \quad p_{\boldsymbol{E}} = \sum_i^n c_i \varphi_i(\boldsymbol{\epsilon}) > 0. \tag{34}$$

where c_i are the basis coefficients to be optimised with respect to the scalar cost function. Since $\mathcal{M}_j$ is a linear operator it suffices to compute $\mathcal{M}_j[\varphi_i(\boldsymbol{\epsilon})]$ to evaluate the cost function and its gradient with respect to c_i. To achieve this we shall adopt a radial basis function as

$$\varphi_i(\boldsymbol{\epsilon}) = \exp\left(- \frac{(\boldsymbol{\epsilon} - \boldsymbol{p}_i)^T(\boldsymbol{\epsilon} - \boldsymbol{p}_i)}{2\sigma^2} \right). \tag{35}$$

The benefit of this selection is twofold. Firstly, using the error function, we will be able to derive a closed form solution to Eq. (31) as a sum of error functions. Retaining analytical expressions for the forward model is paramount as the alternative of numerical integration scales poorly with the number of dimensions (which is $\mathbb{R}^6$ for our application). Secondly, the selection in (35) simplifies the requirement $p_{\boldsymbol{E}} > 0$ to a linear constraint in the unknowns $c_i > 0$. The optimisation problem given in (34) is therefore rendered convex.

6.2. Basis function integration

To execute our forward model, $\mathcal{M}_j[\varphi_i]$, we seek the solution of the integral of the form

$$\int_{s_j^*-w/2}^{s_j^*+w/2} \int_{\boldsymbol{\epsilon}\in\Pi(t,\hat{\boldsymbol{n}}_j)} \exp\left(- \frac{(\boldsymbol{\epsilon} - \boldsymbol{p}_i)^T(\boldsymbol{\epsilon} - \boldsymbol{p}_i)}{2\sigma^2} \right) d\boldsymbol{\epsilon} dt. \tag{36}$$

Analysis of Eq. (36) (see Appendix C) leads to a bounded Gaussian integral which can be solved using the error function, erf, as

$$I_t = 4\pi^3\sigma^6 \left| \operatorname{erf}\left(\frac{b}{\sigma\sqrt{2}} \right) - \operatorname{erf}\left(\frac{a}{\sigma\sqrt{2}} \right) \right|, \tag{37}$$

where $a = (s_j^* - w/2)\boldsymbol{p}_i^T \hat{\boldsymbol{n}}_j$ and $b = (s_j^* + w/2)\boldsymbol{p}_i^T \hat{\boldsymbol{n}}_j$ respectively.

6.3. Maximum-likelihood estimate

In the presence of additive Gaussian noise to the measured histogram bin counts we find the maximum-likelihood estimator of c_i as

$$\underset{c_i}{\operatorname{argmin}} \quad \|\boldsymbol{h} - \boldsymbol{L}\boldsymbol{c}\|_2^2, \quad \texttt{s.t} \quad \boldsymbol{c} > \boldsymbol{0}, \tag{38}$$

where $\boldsymbol{c} \in \mathbb{R}^n$ is a column vector holding the basis coefficients, c_i, the matrix $\boldsymbol{L} \in \mathbb{R}^{M\times n}$ contains the model integral over each individual basis function and $\boldsymbol{h} \in \mathbb{R}^M$ is a column vector stacking all histogram bin values for $j = 1, 2, \dots, m$ in accordance with $\boldsymbol{L}$. Specifically,

$$\boldsymbol{L} = \begin{bmatrix} \mathcal{M}_1[\varphi_1] & \dots & \mathcal{M}_1[\varphi_n] \\ \mathcal{M}_2[\varphi_1] & \dots & \mathcal{M}_2[\varphi_n] \\ \vdots & \ddots & \vdots \\ \mathcal{M}_m[\varphi_1] & \dots & \mathcal{M}_m[\varphi_n] \end{bmatrix}, \quad \boldsymbol{c} = \begin{bmatrix} c_1 \\ c_2 \\ \vdots \\ c_n \end{bmatrix}, \quad \boldsymbol{h} = \begin{bmatrix} h_1(s^1) \\ h_1(s^2) \\ \vdots \\ h_1(s^k) \\ \vdots \\ \vdots \\ h_m(s^1) \\ h_m(s^2) \\ \vdots \\ h_m(s^k) \end{bmatrix}. \tag{39}$$

To solve for $\boldsymbol{c}$ in Eq. (38) we use the active set method described by Lawson and Hanson [46] and implemented in `scipy.optimize.nnls` [47].

6.4. Basis placement

Selecting basis function positions, $\boldsymbol{p}_i$, over a uniform rectangular grid in $\mathbb{R}^6$ and letting $n \to \infty$ while $\sigma \to 0$ there exist $c_i > 0$ such that any positive function $p_{\boldsymbol{E}}$ can be approximated. While this is technically true, for any practical application we have to use a finite number of basis functions, n, each with some finite, nonzero, radius σ. One could imagine that a grid type approach to basis placement will maintain a good performance as long as n is some large finite number. However, owing to the number of dimensions of the problem, this approach scales poorly. To illustrate, consider a target strain PDF which is believed to hold relevant information in a neighbourhood of $\pm 25 \times 10^{-4}$ units of strain around some known mean value. Targeting an approximate resolution of $\pm 1 \times 10^{-4}$ units of strain and producing an equidistant grid over strain space centred around the mean strain, we find that we need a total of $\sim 10^8$ basis functions. The corresponding computation of $\boldsymbol{L} \in \mathbb{R}^{M\times 10^8}$ is impractical, if not altogether unfeasible. Moreover, considering the underlying physics, $p_{\boldsymbol{E}}$ may be narrowly supported on $\mathbb{R}^6$. For instance, in the case when the underlying spatial strain tensor field is in a state of plane stain, as is the case in Fig. 4, $p_{\boldsymbol{E}}$ will be fully contained by a 3-dimensional hyperplane on $\mathbb{R}^6$. In a more general case, the mechanical equilibrium equations constrain the support of the strain PDF. This means that the placement of basis functions on a rectangular grid runs the risk of wasting a large portion of the basis set. As an example, in the case of plane strain, only $\approx 25^3 (\approx 10^4)$ out of the 10^8 previously mentioned basis function would be active in approximating $p_{\boldsymbol{E}}$, effectively wasting $\approx 99.9936\%$ of the basis function set. Thus, we are presented with the challenge of distributing a sparse set of basis functions on $\mathbb{R}^6$ such that the final approximation of $p_{\boldsymbol{E}}$ can explain the observed histograms.

6.4.1. Sequential sampling approach

To address the above described sampling issue, we present a class of stochastic basis placement algorithms that are heuristically expected to perform well for mapping out the support of smooth, simply connected, positive functions. The central idea evolves around producing a sparse sequence of basis sets such that the explanatory value of the basis sets with respect to measured data increases with iteration. The approach is, in part, similar to sequential Monte Carlo methods [48] as the proposal distribution, from which new basis locations are drawn, is allowed to

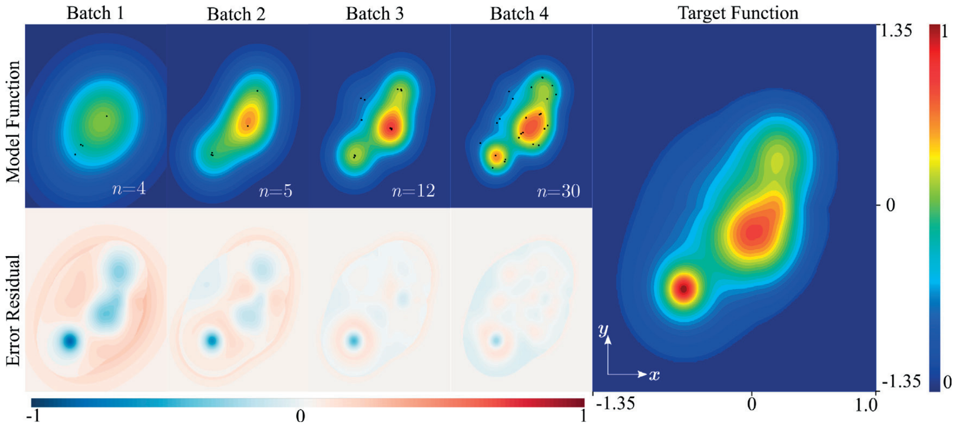

Fig. 5. Illustration of increasingly good basis approximations retrieved from the iteration of Algorithm 1. The current model function and the residual field are plotted at the end of each batch. The black circles correspond to basis function locations. The radius of the basis function was relaxed as $\sigma = [0.25, 0.1, 0.06, 0.03]$ with $B = 20$ and $J = 20$.

mutate between iterations. However, to the best of the authors knowledge, the method we use has not been reported on previously. We summarise our approach in Algorithm 1. The procedure can be summarised as follows. First a single basis function is placed at a location, $\boldsymbol{\epsilon}$, at which the target function $p_{\boldsymbol{E}}$ is believed to be supported. For instance, we have found that putting the initial basis function at the mean strain of the grain performs well. Next a basis coefficient c_1 for our single basis function is selected such that $p_{\boldsymbol{E}}$ becomes a probability distribution. From this probability distribution B samples, $\boldsymbol{\epsilon}_1, \boldsymbol{\epsilon}_2, \dots, \boldsymbol{\epsilon}_B$, are randomly drawn. At each sampled location, $\boldsymbol{\epsilon}_i$, a basis function is now placed such that the approximation of $p_{\boldsymbol{E}}$ is expanded to contain $B + 1$ basis functions. The coefficients of the basis set is now recomputed such that the likelihood of observing the strain histogram data is maximised, i.e a least squares problem is solved. Any basis functions that appears to have a small explanatory value, i.e a small fitted coefficient, $c_i \leq \xi$, are now removed from the basis expansion. The value of ξ is selected arbitrarily with higher values resulting in a sparser number of basis functions and less freedom for the algorithm to match the measured data, while a smaller value of ξ will result in a more dense basis set and more freedom for the algorithm to match the measured data. For instance, we found that setting $\xi = 0$, and thus keeping all basis functions that are on the support of $p_{\boldsymbol{E}}$, performed well in our strain estimation problem. After the basis set has been pruned of any unwanted basis functions the resulting function $p_{\boldsymbol{E}}$ is again normalised to represent a probability distribution. A new sample of B locations, $\boldsymbol{\epsilon}_1, \boldsymbol{\epsilon}_2, \dots, \boldsymbol{\epsilon}_B$, is drawn from the updated distribution and the procedure of basis coefficient fitting is repeated. This iteration is allowed to continue for a fixed number of redraw iterations J. For large selections of J the root mean squared error between of the maximum likelihood fit is seen to plateau, i.e a large selection of J will in general perform better than a small selection of J, with diminishing returns as J grows. So far we have summarised the inner most sub-iteration of Algorithm 1 which we denote as a batch run. After this sub-iteration/batch comes to an end the standard deviation (or radius) of the radial basis functions, σ, is decreased and the entire procedure is repeated, carrying forward all basis functions accumulated in the previous sub-iteration. Note that while the radius, σ, varies globally between iteration it does not vary between the individual basis functions in the same basis expansion set. Basis locations are now again randomly drawn using the new, smaller, σ value in the basis expansion of $p_{\boldsymbol{E}}$ and both old and new basis functions are marked for pruning as previously. After K sub-iterations of the algorithm, each featuring J basis location draws of size B, the algorithm terminates at the final smallest length-scale, σ_K. By decreasing σ slowly, in many fine steps, better results were found in general, at the expense of computational complexity. For instance, in the result presented in 8 we used $(\sigma_1, \sigma_2, \sigma_3, \sigma_4, \sigma_5) = (10.0, 8.4, 7.1, 5.9, 5.0)$ and $B = J = 25$. As σ is gradually diminished the algorithm refines the approximation of $p_{\boldsymbol{E}}$ and is able to make use of an increasingly larger set of basis functions.

Algorithm 1: A Stochastic Radial Basis Placement Strategy

```
Result: $n$, $\sigma$, $\boldsymbol{p}_i$ $\forall, i = 1, .., n$,
Select batch size, $B$, and number of batch iterations, $J$;
Select a relaxation sequence $[\sigma_1, .., \sigma_K]$, with $\sigma_{k+1} < \sigma_k$;
Select $\boldsymbol{p}_1$ on the support of $p_{\boldsymbol{E}}$;
Set $p_{\boldsymbol{E}}^{(11)}(\boldsymbol{\epsilon}) = c_1\varphi_1(\boldsymbol{\epsilon})$;
Fit $c_1$ with respect to data (solve Equation (38));
for $\sigma_k$ in $[\sigma_1, .., \sigma_K]$ do
    Set $\sigma = \sigma_k$;
    for $j = 1, .., J$ do
        Draw $B$ new basis locations, $\boldsymbol{p}_i$, from $p_{\boldsymbol{E}}^{(kj)}$;
        Let $n \leftarrow n + B$;
        Extend expansion $p_{\boldsymbol{E}}^{(kj)}(\boldsymbol{\epsilon}) = \sum_{i=1}^{i=n} c_i\varphi_i(\boldsymbol{\epsilon})$;
        Fit $c_i$ with respect to data (solve Equation (38));
        Set prune count, $p = 0$;
        for $i = 1, .., n$ do
            if $c_i \leq \xi$ then
                Mark $\varphi_i$ for pruning;
                Increment prune count $p \leftarrow p + 1$
            end
        end
        Prune marked $\varphi_i$ from expansion $p_{\boldsymbol{E}}^{(kj)}(\boldsymbol{\epsilon}) = \sum_{i=1}^{i=n} c_i\varphi_i(\boldsymbol{\epsilon})$;
        Decrement basis set count $n \leftarrow n - p$ ;
    end
end
Accept $p_{\boldsymbol{E}} = p_{\boldsymbol{E}}^{(KJ)} = \sum_{i=1}^{i=n} c_i\varphi_i(\boldsymbol{\epsilon})$ ;
```

We illustrate the evolving basis expansion produced by our Algorithm 1 in Fig. 5. For illustrative purposes the example case takes place on $\mathbb{R}^2$ with the target data selected as a direct observation of the underlying target function (rightmost plot in Fig. 5). The residual between the current model function and the target function is seen to decrease as the algorithm produces a sequence of customised basis sets. The algorithm parameters where set to $B = 20$, $J = 20$ and $\sigma = [0.25, 0.1, 0.06, 0.03]$. This means that the algorithm can theoretically attain a maximum of $20 \times 20 \times 4 = 1600$ basis functions over the four batch runs. We note that the final number of accumulated basis functions produced by our algorithm is much sparser ($n = 30$). This means that although we have to solve the inverse problem of fitting c_i 80 times throughout the run, each inversion is fast owing to the low number of basis functions. This property is especially beneficial when the algorithm used to solve for c_i scales super-linearly with n. A concise python implementation of Algorithm 1 in the setting of Fig. 5 is openly available at https://gist.github.com/AxelHenningsson/8a9179f859751634859eb7e051ebd804.

7. Observability and reduced models

It is well known that the mean of the strain PDF can be recovered from 6 measured diffraction peaks [15]. This does however not indicate whether or not the strain PDF itself is well defined from measurements of directional strain. To answer this question one needs to investigate under what perturbations the strain PDF generates identical histograms of directional strains through the model, $\mathcal{M}[p_{\boldsymbol{E}}]$. For an arbitrary functional form of the strain PDF a complete description of this null-space is challenging. However, a feasible generalisation of a mean value analysis is to let the strain PDF be a multivariate Gaussian.

In the following we shall derive a class of perturbations to multivariate Gaussian strain PDFs that leave the measured histograms unchanged. From this analysis we will also find a closed form estimator of the strain PDF. We start our analysis by reiterating why the mean value of the strain PDF is well defined.

7.1. First moments

By definition, the expected value of the strain PDF is

$$\mathbb{E}[\boldsymbol{E}] = \int \boldsymbol{E} p_{\boldsymbol{E}}(\boldsymbol{\epsilon}) d\boldsymbol{\epsilon}, \tag{40}$$

where $\mathbb{E}[\cdot]$ denotes the expectation operator. Considering the expected value of any one single measured directional strain histogram, $h_j(s_j)$, and using the linearity of expectation, we have

$$\mathbb{E}[s_j] = \mathbb{E}[\bar{\boldsymbol{\kappa}}_j^T \bar{\boldsymbol{E}}] = \bar{\boldsymbol{\kappa}}_j^T \mathbb{E}[\boldsymbol{E}], \tag{41}$$

where the index j denotes association to a fixed direction, $\bar{\boldsymbol{\kappa}}_j$. We note that (41) holds true regardless of the functional form of $p_{\boldsymbol{E}}(\boldsymbol{\epsilon})$. Denoting $\boldsymbol{\mu}_{\boldsymbol{E}} = \mathbb{E}[\boldsymbol{E}]$ and collecting a set of $\bar{\boldsymbol{\kappa}}_j$ and $\mathbb{E}[s_j]$, with $j = 1, \dots, m$, in the matrices $\boldsymbol{K}$ and $\boldsymbol{\mu}_s$, as

$$\boldsymbol{K} = \begin{bmatrix} \bar{\boldsymbol{\kappa}}_1^T \\ \bar{\boldsymbol{\kappa}}_2^T \\ \vdots \\ \bar{\boldsymbol{\kappa}}_m^T \end{bmatrix}, \quad \boldsymbol{\mu}_s = \begin{bmatrix} \mathbb{E}[s_1] \\ \mathbb{E}[s_2] \\ \vdots \\ \mathbb{E}[s_m] \end{bmatrix}, \tag{42}$$

we may produce a linear system of equations,

$$\boldsymbol{K} \boldsymbol{\mu}_{\boldsymbol{E}} = \boldsymbol{\mu}_s. \tag{43}$$

From Eq. (43) we conclude that $\boldsymbol{\mu}_{\boldsymbol{E}}$ is well defined if and only if $\boldsymbol{K}$ is full column rank. This requires the collection of a minimum of 6 linearly independent $\bar{\boldsymbol{\kappa}}$ vectors. As an illustration, the choice

$$\begin{aligned} &\hat{\boldsymbol{\kappa}}_1 = \begin{bmatrix} 1 & 0 & 0 \end{bmatrix}, && \hat{\boldsymbol{\kappa}}_2 = \begin{bmatrix} 0 & 1 & 0 \end{bmatrix}, && \hat{\boldsymbol{\kappa}}_3 = \begin{bmatrix} 1 & 1 & 1 \end{bmatrix}/\sqrt{3} \\ &\hat{\boldsymbol{\kappa}}_4 = \begin{bmatrix} 1 & 1 & 0 \end{bmatrix}/\sqrt{2}, && \hat{\boldsymbol{\kappa}}_5 = \begin{bmatrix} 1 & 0 & 1 \end{bmatrix}/\sqrt{2}, && \hat{\boldsymbol{\kappa}}_6 = \begin{bmatrix} 0 & 1 & 1 \end{bmatrix}/\sqrt{2}, \end{aligned} \tag{44}$$

produces the fully ranked $\boldsymbol{K}$ matrix as

$$\boldsymbol{K} = \frac{1}{3} \begin{bmatrix} 3 & 0 & 0 & 0 & 0 & 0 \\ 0 & 3 & 0 & 0 & 0 & 0 \\ 1 & 1 & 1 & 2 & 2 & 2 \\ 3/2 & 3/2 & 0 & 3 & 0 & 0 \\ 3/2 & 0 & 3/2 & 0 & 3 & 0 \\ 0 & 3/2 & 3/2 & 0 & 0 & 3 \end{bmatrix}. \tag{45}$$

We note that in this example no $\bar{\boldsymbol{\kappa}}$ vector is closer than 45° to the $\hat{z}_s = [0, 0, 1]$ axis. This explains why it is possible to reconstruct mean crystal grains strains in 3DXRD/HEDM using only a single axis of rotation. We note that in practice, to reduce experimental error, it is common to solve an overdetermined system, using more than 6 observations [15].

7.2. The multivariate Gaussian case

Let the strain PDF be a multivariate Gaussian as

$$p_{\boldsymbol{E}}(\bar{\boldsymbol{\epsilon}}) = n \exp\left(-\frac{1}{2}(\bar{\boldsymbol{\epsilon}} - \mu_{\bar{\epsilon}})^T \boldsymbol{\Sigma}^{-1} (\bar{\boldsymbol{\epsilon}} - \mu_{\bar{\epsilon}})\right), \quad n = \frac{1}{\sqrt{(2\pi)^6 \mathtt{det}[\boldsymbol{\Sigma}]}}, \quad \boldsymbol{\Sigma} = \boldsymbol{\Sigma}^T \in \mathbb{R}^{6\times6}, \quad \bar{\boldsymbol{\epsilon}} \in \mathbb{R}^{6\times1}, \tag{46}$$

such that $p_{\boldsymbol{E}}(\bar{\boldsymbol{\epsilon}})$ describes the scalar probability of encountering any one particular strain tensor, $\bar{\boldsymbol{\epsilon}}$. Considering $\boldsymbol{E} \sim p_{\boldsymbol{E}}(\bar{\boldsymbol{\epsilon}})$ as a stochastic variable, we can then form a set of scalar stochastic variables (directional strains) as

$$S_j = \bar{\boldsymbol{\kappa}}_j^T \boldsymbol{E}, \quad j = 1, 2, 3..m. \tag{47}$$

Since the transformation from $\boldsymbol{E}$ to S_j is linear, it follows that $S_j \sim p_{S_j}(s)$ is Gaussian with PDF

$$p_{S_j}(s) = a \exp\left(-\frac{1}{2}(s - \bar{\boldsymbol{\kappa}}_j^T \mu_{\bar{\epsilon}})(\bar{\boldsymbol{\kappa}}_j^T \boldsymbol{\Sigma} \bar{\boldsymbol{\kappa}}_j)^{-1}(s - \bar{\boldsymbol{\kappa}}_j^T \mu_{\bar{\epsilon}})\right), \quad a = \frac{1}{\sqrt{2\pi \mathtt{det}[\bar{\boldsymbol{\kappa}}_j^T \boldsymbol{\Sigma} \bar{\boldsymbol{\kappa}}_j]}}, \quad j = 1, 2, 3..m. \tag{48}$$

Now, considering that the measurements, $h_j(s_j)$, are the histograms formed through the binning of the PDFs, $p_{S_j}(s)$, it follows that, if $p_{S_j}(s)$ is invariant under a perturbation of $p_{\boldsymbol{E}}(\bar{\boldsymbol{\epsilon}})$, so are the measurements, $h_j(s_j)$. The task of characterising the null-space is, therefore, reduced to that of finding perturbations to $p_{\boldsymbol{E}}(\bar{\boldsymbol{\epsilon}})$ such that $p_{S_j}(s)$ remains unaltered.

7.2.1. *Measurement invariant perturbations*

To permute $p_{\boldsymbol{E}}(\bar{\boldsymbol{\epsilon}})$ inside the class of multivariate Gaussians, we can change either the mean or the covariance of the distribution. Our preceding analysis has already shown that the mean of $p_{\boldsymbol{E}}(\bar{\boldsymbol{\epsilon}})$ is well defined, regardless of the functional form. Thus, we can immediately turn our analysis to perturbations in $\boldsymbol{\Sigma}$. To this end, we introduce $\boldsymbol{\Sigma}^* = \boldsymbol{\Sigma} + \boldsymbol{N}$, where $\boldsymbol{N}$ is some perturbation that preserves symmetry and positive definiteness, i.e.,

$$\boldsymbol{N} = \boldsymbol{N}^T, \quad \boldsymbol{z}^T(\boldsymbol{\Sigma} + \boldsymbol{N})\boldsymbol{z} \geq 0, \quad \forall \boldsymbol{z} \neq \boldsymbol{0}. \tag{49}$$

We find the modified PDF over directional strains as

$$p^*_{S_j}(s) = a \exp\left(-\frac{1}{2}(s - \bar{\boldsymbol{\kappa}}_j^T \mu_{\bar{\epsilon}})(\bar{\boldsymbol{\kappa}}_j^T(\boldsymbol{\Sigma} + \boldsymbol{N})\bar{\boldsymbol{\kappa}}_j)^{-1}(s - \bar{\boldsymbol{\kappa}}_j^T \mu_{\bar{\epsilon}})\right), \quad a = \frac{1}{\sqrt{2\pi \mathtt{det}[\bar{\boldsymbol{\kappa}}_j^T(\boldsymbol{\Sigma} + \boldsymbol{N})\bar{\boldsymbol{\kappa}}_j]}}. \tag{50}$$

Clearly

$$p^*_{S_j}(s) = p_{S_j}(s) \quad \textit{iff} \quad \bar{\boldsymbol{\kappa}}_j^T(\boldsymbol{\Sigma} + \boldsymbol{N})\bar{\boldsymbol{\kappa}}_j = (\bar{\boldsymbol{\kappa}}_j^T \boldsymbol{\Sigma} \bar{\boldsymbol{\kappa}}_j), \tag{51}$$

and it follows that the null-space requires the existence of $\boldsymbol{N}$ such that

$$\bar{\boldsymbol{\kappa}}_j^T \boldsymbol{N} \bar{\boldsymbol{\kappa}}_j = 0, \quad \forall j. \tag{52}$$

A thorough analysis of Eq. (52) will reveal 6 possible selections of $\boldsymbol{N}$. The somewhat lengthy derivations of these 6 covariance perturbations are presented in Appendix B and we proceed here immediately to summarise the result of these calculations.

7.2.2. *Parametric null-space*

In conclusion, if the strain PDF is a Gaussian on $\mathbb{R}^6$, with positive definite covariance $\boldsymbol{\Sigma}$, the null-space of the strain PDF on this function class is described by the addition of a non-positive-semi-definite symmetric matrix to the strain PDF Gaussian covariance matrix

$$\boldsymbol{\Sigma}^* = \boldsymbol{\Sigma} + \boldsymbol{N}(\alpha, \beta, \gamma, \xi, \eta, \rho), \quad \mathtt{s.t} \quad \boldsymbol{z}^T \boldsymbol{\Sigma} \boldsymbol{z} + \boldsymbol{z}^T \boldsymbol{N} \boldsymbol{z} > 0, \quad \forall \boldsymbol{z} \in \mathbb{R}^6, \quad \boldsymbol{z} \neq \boldsymbol{0}, \tag{53}$$

where the class of matrices $\boldsymbol{N} = \boldsymbol{N}(\alpha, \beta, \gamma, \xi, \eta, \rho)$ is parameterised as

$$\boldsymbol{N} = \begin{bmatrix} 0 & 2\alpha & 2\beta & 0 & 0 & 2\gamma \\ 2\alpha & 0 & 2\eta & 0 & 2\xi & 0 \\ 2\beta & 2\eta & 0 & 2\rho & 0 & 0 \\ 0 & 0 & 2\rho & -\alpha & -\gamma & -\xi \\ 0 & 2\xi & 0 & -\gamma & -\beta & -\rho \\ 2\gamma & 0 & 0 & -\xi & -\rho & -\eta \end{bmatrix}, \quad \alpha, \beta, \gamma, \xi, \eta, \rho \in \mathbb{R}. \tag{54}$$

Since the scalars $\alpha, \beta, \gamma, \xi, \eta, \rho$ can be chosen arbitrarily small it will, in general, be possible to construct such perturbations while maintaining positive definite $\boldsymbol{\Sigma}^*$.

7.2.3. *Null-space verification*

To verify that the null-space leaves the measured histograms unaltered, in Fig. 6 we show the distribution of the directional strain in the $\hat{\boldsymbol{\kappa}}^T = \sqrt{50/27}[1/2, 1/2, 1/5]$ direction for a series of perturbations to an underlying simulated strain tensor probability density.

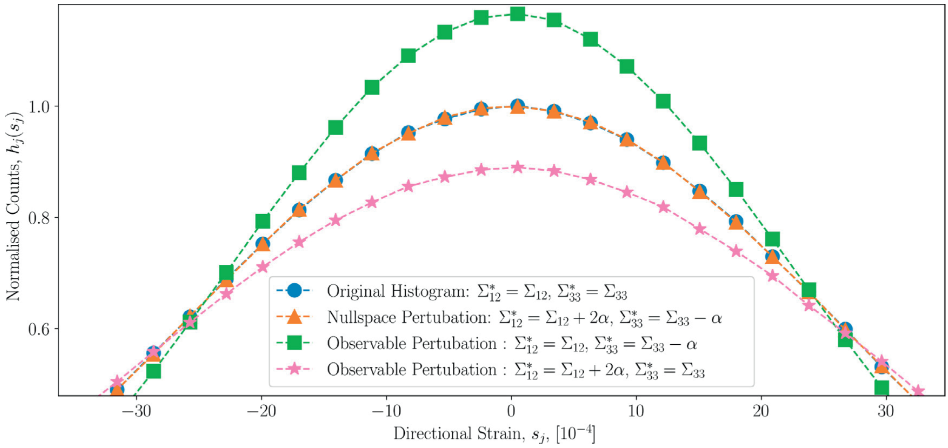

Fig. 6. Zoom in on histograms of directional strain in the $\hat{\boldsymbol{\kappa}}^T = [1/2, 1/2, 1/5]/\sqrt{27/50}$ direction corresponding to four realisations of each 20 000 000 strain tensors drawn from four distinct Gaussian strain PDFs. The covariance components of the four Gaussian strain PDFs, Σ^*_{ij}, were modified according to the legend. It is clear to see that when the modification to the covariance is in the null-space (triangles) the original (circles) histogram is recovered. Other perturbations of the covariance (squares and stars) result in observable changes in the histogram.

Each histogram in Fig. 6 was constructed by drawing 20 000 000 strain tensors at random from a multivariate Gaussian, where the unperturbed covariance matrix was selected as

$$\boldsymbol{\Sigma} = \begin{bmatrix} 63 & 0 & 0 & 0 & 0 & 0 \\ 0 & 34 & 0 & 0 & 0 & 0 \\ 0 & 0 & 3 & 0 & 0 & 0 \\ 0 & 0 & 0 & 49 & 0 & 0 \\ 0 & 0 & 0 & 0 & 25 & 0 \\ 0 & 0 & 0 & 0 & 0 & 25 \end{bmatrix} \times 10^{-7}. \tag{55}$$

As expected, the two histograms in Fig. 6 that are in the null-space described in Section 7.2.2 look identical (triangles and circles). Similarly, we see in Fig. 6 that perturbations to the strain distribution that are not in the null-space leads to changes in the histogram (squares and stars).

7.2.4. *Maximum-likelihood estimator for a Gaussian strain PDF*

The relationship between the first moment of the strain PDF and the histograms of directional strain was established in Eq. (43). To fully describe the Gaussian strain PDF we are, therefore, left with the estimation of the covariance matrix $\boldsymbol{\Sigma}$. Letting $\mathbb{V}[\cdot]$ be the variance operator and denoting the (scalar) variance associated to a single histogram of directional strain by σ_j^2 we find with the use of Eq. (47) that

$$\sigma_j^2 = \mathbb{V}[S_j] = \mathbb{V}[\bar{\boldsymbol{\kappa}}_j^T \boldsymbol{E}] = \bar{\boldsymbol{\kappa}}_j^T \mathbb{V}[\boldsymbol{E}] \bar{\boldsymbol{\kappa}}_j = \bar{\boldsymbol{\kappa}}_j^T \boldsymbol{\Sigma} \bar{\boldsymbol{\kappa}}_j. \tag{56}$$

Thus, by collecting the variance of each histogram in a column vector, $\boldsymbol{\sigma}_s^2 = [\sigma_1^2, \sigma_2^2, \dots]^T$, a system of equations linear in the components of $\boldsymbol{\Sigma}$ can be established. To express $\boldsymbol{\Sigma}$ as a function of $\boldsymbol{\sigma}_s^2$ in a least squares sense we introduce in Appendix B a flattening of Eq. (56) (in analogy with $\bar{\boldsymbol{\kappa}}$ and $\boldsymbol{E}$ in Eq. (26)). Letting the column vector $\bar{\boldsymbol{\Sigma}}^* \in \mathbb{R}^{21\times 1}$ hold the unique components of the strain PDF covariance matrix $\boldsymbol{\Sigma}^* \in \mathbb{R}^{6\times 6}$ and letting the matrix $\boldsymbol{V} \in \mathbb{R}^{m\times 21}$ operate the outer product maps defined in Eq. (56) we find that

$$\begin{aligned} \boldsymbol{\mu}_E &= (\boldsymbol{K}^T\boldsymbol{K})^{-1}\boldsymbol{K}^T\boldsymbol{\mu}_s, \\ \bar{\boldsymbol{\Sigma}}^* &= (\boldsymbol{V}^T\boldsymbol{V})^{-1}\boldsymbol{V}^T\boldsymbol{\sigma}_s^2 + \boldsymbol{u}(\alpha, \beta, \gamma, \eta, \xi, \rho), \end{aligned} \tag{57}$$

where the null-space of the covariance is described by the vector $\boldsymbol{u} \in \mathbb{R}^{21\times 1}$ which is the flattening of $\boldsymbol{N}$ in Eq. (54). The rows of $\boldsymbol{V}$ are explicitly described in Eq. (80) in Appendix B. Without any further information we set $\boldsymbol{u} = \boldsymbol{u}(0,0,0,0,0,0) = \boldsymbol{0}$ and find in conclusion that

$$\begin{aligned} \boldsymbol{\mu}_E &= (\boldsymbol{K}^T\boldsymbol{K})^{-1}\boldsymbol{K}^T\boldsymbol{\mu}_s, \\ \bar{\boldsymbol{\Sigma}}^* &= (\boldsymbol{V}^T\boldsymbol{V})^{-1}\boldsymbol{V}^T\boldsymbol{\sigma}_s^2. \end{aligned} \tag{58}$$

Eq. (58) can be thought of as an approximation to the strain PDF which, in general, does not need to be a Gaussian. The main benefits of the Gaussian approximation compared to the finite basis expansion solution presented in Section 6 is its simplicity and low computational complexity.

8. Simulation study

To test the derived framework we reconstruct the strain PDF for a synthetically generated data set. Importantly, the simulation framework described in this section operates directly on the spatial domain ($\boldsymbol{x} \in \mathbb{R}^3$) for data generation. This ensures that we are not committing the inverse crime of using one and the same mapping for both regression and data generation. Additionally, as described in Section 8.4, we introduce challenging levels of noise and outliers to test the robustness of the proposed methods.

8.1. Strain field generation

Since the underlying spatial strain tensor field is expected to be in equilibrium on the unknown domain Ω, we generate a strain tensor field that satisfies the point-wise equilibrium equations,

$$\begin{aligned} &\frac{\partial \sigma_{11}}{\partial x} + \frac{\partial \sigma_{21}}{\partial y} + \frac{\partial \sigma_{31}}{\partial z} = 0 \\ &\frac{\partial \sigma_{12}}{\partial x} + \frac{\partial \sigma_{22}}{\partial y} + \frac{\partial \sigma_{32}}{\partial z} = 0, \qquad \bar{\boldsymbol{\sigma}} = \begin{bmatrix} \sigma_{11} \\ \sigma_{22} \\ \sigma_{33} \\ \sigma_{12} \\ \sigma_{13} \\ \sigma_{23} \end{bmatrix} = \boldsymbol{D}\boldsymbol{E}, \\ &\frac{\partial \sigma_{31}}{\partial x} + \frac{\partial \sigma_{32}}{\partial y} + \frac{\partial \sigma_{33}}{\partial z} = 0 \end{aligned} \tag{59}$$

where $\boldsymbol{D}$ is a 6 × 6 isotropic material stiffness matrix,

$$\boldsymbol{D} = \frac{E}{(1+\nu)(1-2\nu)} \begin{bmatrix} 1-\nu & \nu & \nu & 0 & 0 & 0 \\ \nu & 1-\nu & \nu & 0 & 0 & 0 \\ \nu & \nu & 1-\nu & 0 & 0 & 0 \\ 0 & 0 & 0 & (1-2\nu) & 0 & 0 \\ 0 & 0 & 0 & 0 & (1-2\nu) & 0 \\ 0 & 0 & 0 & 0 & 0 & (1-2\nu) \end{bmatrix}. \tag{60}$$

To generate a random strain field satisfying (60), we constructed a zero mean Gaussian process, similar to Hendriks et al. [23], using a squared exponential kernel that we mapped through the partial differential operator that encodes the Maxwell equilibrium stress solutions [49]. We used iron (Fe) like materials parameters, $E = 200$ GPa, $\nu = 0.3$, and sampled a strain field at random on a spherical domain with radius 5 μm. The length-scale of the kernel was set to the radius of the sphere and the amplitude of the kernel was set to 60. An interpolation of the resulting strain tensor field can be visualised in Fig. 7. For strain tensor sampling ∼50 000 spatial coordinates, $\boldsymbol{x}$, where selected over the spherical domain on an equidistant grid.

8.2. Crystal generation

With samples from the spatial strain tensor field defined, we are left with the generation of $\hat{\boldsymbol{\kappa}}$ before histograms of directional strains can be formed. To mimic a 3DXRD/HEDM experiment we generate $\hat{\boldsymbol{\kappa}}$ based on a crystal lattice structure. Adopting the cubic symmetry of iron (Fe) with unit cell parameters,

$$a = 2.8665\ \text{Å}, \quad b = 2.8665\ \text{Å}, \quad c = 2.8665\ \text{Å}, \quad \alpha = 90^\circ, \quad \beta = 90^\circ, \quad \gamma = 90^\circ, \tag{61}$$

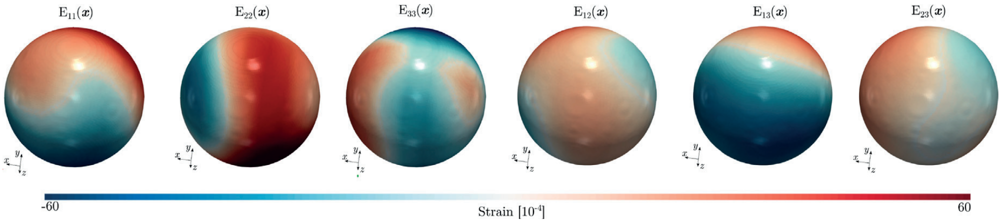

Fig. 7. Volume rendering of spatial strain tensor field in units of $[10^{-4}]$ sampled over a spherical domain using an equilibrium encoded Gaussian process. The strain tensor field is used to construct synthetic histograms of directional strains considering a cubic crystal structure (space group Im-3m).

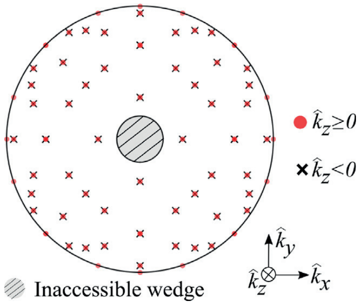

Fig. 8. A total of $j = 1, \ldots, 134$ directions, $\hat{\boldsymbol{\kappa}}_j$, generated from a cubic iron (Fe) crystal structure are displayed by projecting the unit ball unto the $\kappa_x - \kappa_y$-plane (sample coordinate system). The sampling is seen to be both non-uniform as well as incomplete as a result of the crystal structure and experimental limitations.

and a wavelength of 0.19 Å, we consider all reflections that fall on a 2048 × 2048 flat area detector with a 50 μm pixel size. The resulting diffraction events where confined to fall in the range $\theta = [5^\circ, 15^\circ]$. Without loss of generality, we set the crystal orientation as $\boldsymbol{U} = \boldsymbol{I}$ and solve the Laue equations (1) for $\boldsymbol{G}$. The corresponding $\hat{\boldsymbol{\kappa}}$ directions where computed by normalising the $\boldsymbol{G}$ vectors, which, by definition, are orthogonal to the diffracting lattice planes. To simulate the limitations imposed by the finite energy of the X-rays and the single axis of rotation we remove all $\hat{\boldsymbol{\kappa}}$ that fall within 10° of the rotation $\pm\hat{z}$-axis. This procedure generated a total $j = 1, \ldots, 132$ directions, $\hat{\boldsymbol{\kappa}}_j$. The spread of the generated directions on the unit ball can be viewed in Fig. 8.

8.3. Histogram formation

To form the final histograms of directional strains we must select a histogram bin size. The practical achievable resolution in terms of bin size depends on the instrument, material, geometry and detector parameters. In this work we select to use 6 bins spaced equidistantly throughout histogram formation. We select the range of the bins to cover fully the directional strains generated by multiplying through the sample strain tensors with the generated $\hat{\boldsymbol{\kappa}}$ directions. Additionally, for visual purposes, we pad the histogram with an additional bin on each side of this range to illustrate that no strain is falling outside our interval. Note that the proposed regression method can equally be deployed in the presence of fewer or more histogram bins. Naturally, the number of accessible bins will regulate what resolution can be expected of the recovered strain PDF.

Given the spatial strain tensor sample, $\boldsymbol{E}(\boldsymbol{x}_1), \boldsymbol{E}(\boldsymbol{x}_2), \ldots, \boldsymbol{E}(\boldsymbol{x}_m)$, we generate samples of directional strains as

$$\boldsymbol{s}_j = (s_1, s_2, ..s_m) = (\bar{\boldsymbol{\kappa}}_j^T \boldsymbol{E}(\boldsymbol{x}_1), \bar{\boldsymbol{\kappa}}_j^T \boldsymbol{E}(\boldsymbol{x}_2), \ldots, \bar{\boldsymbol{\kappa}}_j^T \boldsymbol{E}(\boldsymbol{x}_m)), \quad \forall j. \tag{62}$$

For each j the corresponding sample of $\boldsymbol{s}_j$ was used to form a histogram. The histograms were normalised to represent probability densities.

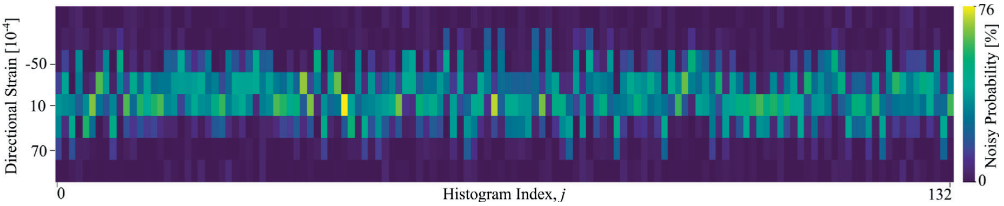

Fig. 9. Synthetic histograms used as input to the derived regression framework. Each column in the image is a histogram of directional strain in the direction of a fixed $\hat{\boldsymbol{\kappa}}_j$. The pixel colour values represent the (noisy) probability that the directional strain will fall into the respective bin.

8.4. Noise model

Before deploying our regression framework, we introduce noise on the measured histogram bin values, h_{ij}, where h_{ij} denotes the i:th bin in the j:th histogram. We add independent, identically distributed, Gaussian noise to all bins as

$$h_{ij} \leftarrow h_{ij} + e_{ij}, \quad e_{ij} \sim \mathcal{N}(0, \sigma_{ij}^{\text{noise}}), \quad \forall i, j, \tag{63}$$

where

$$\sigma_{ij}^{\text{noise}} = 10^{-4} + h_{ij}/SNR_1. \tag{64}$$

The signal to noise ratio was set to $SNR_1 = 50$ representing a few percent of noise per bin with the constant 10^{-4} ensuring that noise is added to bins featuring zero counts. We simulate outliers in the data by adding an additional larger Gaussian noise to a randomly (uniformly) selected subset as

$$h_{ij} \leftarrow h_{ij} + e_{ij}^{\text{outlier}}, \quad e_{ij}^{\text{outlier}} \sim \mathcal{N}(0, \sigma_{ij}^{\text{outlier}}), \forall i, j \in \mathcal{O}, \tag{65}$$

where

$$\sigma_{ij}^{\text{outlier}} = 10\sigma_{ij}^{\text{noise}} \tag{66}$$

and ∼20% of the data histogram bins were selected for outlier corruption. The final step of our noise model is a re-normalisation, ensuring that the histogram bin data are positive. We subtract the minimal bin-count,

$$h_{ij} \leftarrow h_{ij} - \underset{i}{\texttt{min}}(h_{ij}), \quad \forall j, \tag{67}$$

and normalise,

$$h_{ij} \leftarrow h_{ij} \left(\sum_i w h_{ij} \right)^{-1} \quad \forall j. \tag{68}$$

Collecting all generated histograms, one for each direction $\hat{\boldsymbol{\kappa}}_j$, the total available data can be visualised as an image. In Fig. 9 the noisy histogram data used for regression is displayed. Each pixel corresponds to a single histogram bin and each column to a single histogram. The colourmap reveals the bin-count as the probability of encountering a particular directional strain in the crystal.

8.5. Results

We deployed the generic radial basis regression framework derived in Section 6 to the synthetic histogram data described in Section 8. Additionally, using the closed form solution given in Eq. (58), we provide estimates based on a sparsely parameterised multivariate Gaussian strain PDF model, as described in Section 7.2.4.

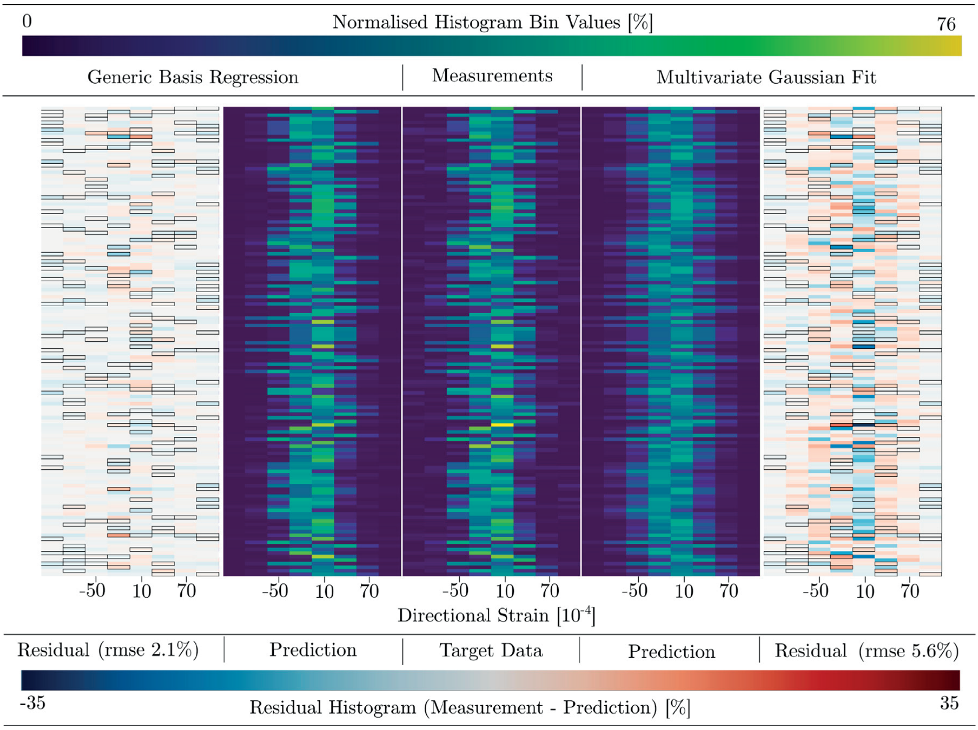

Fig. 10. Predicted histograms using a sparsely parameterised multivariate Gaussian model (right) and a generic radial basis regression model (left) compared to the ground truth noisy histograms (central column). The respective residual fields are shown in the outermost columns. Histogram bins that were randomly selected to be corrupted into outliers are marked in the residual plots with a black border.

8.5.1. Data prediction quality

To assess the quality of reconstruction we present a comparison between predicted and measured histograms of directional strains in Fig. 10. A good regression model should reject noise while at the same time predict directional strain histogram data in agreement with the measurements. The root mean squared error between predicted and measured data was defined as

$$\text{rmse} = \sqrt{\frac{\sum_i \sum_j (h_{ij}^{\text{predicted}} - h_{ij}^{\text{true}})^2}{8m}}, \tag{69}$$

where $8m$ is the total number of measured bin values across all $m = 132$ histograms.

8.5.2. Convergence

The parameters for Algorithm 1 were selected as $B = J = 25$ and $(\sigma_1, \sigma_2, \sigma_3, \sigma_4, \sigma_5) = (10.0, 8.4, 7.1, 5.9, 5.0)$. The convergence of the algorithm is shown in Fig. 11.

8.5.3. Strain PDF reconstruction quality

To further assess our two models, in Fig. 12 we present a comparison between the predicted strain PDFs and the ground truth strain PDF (originating from the strain field in Fig. 7). Since the strain PDF is supported on 6-dimensions we present 2-dimensional projections onto the 15 unique Cartesian planes that can be formed by combining components of the strain tensor. As the directional strain histogram data resolution is limited, we must expect arbitrary oscillations in the reconstructed strain PDF to occur at length-scales smaller than the directional

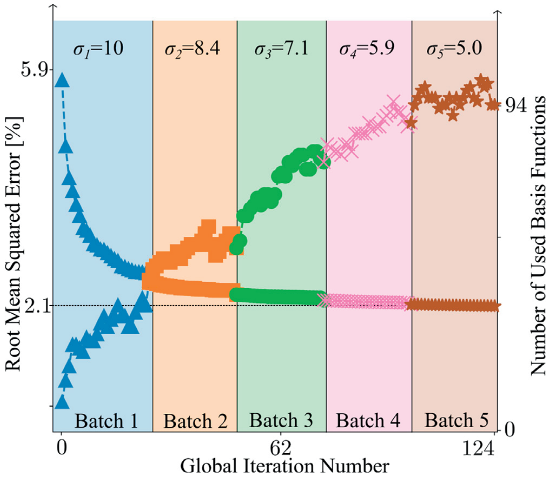

Fig. 11. Convergence of Algorithm 1 applied to the data generated through the procedure described in Section 8. Each batch represents a fixed radial basis radius, σ. The number of basis functions used in the expansion of the strain PDF (right axis) is seen to increase with iteration. Likewise, the root mean squared error (rmse) is seen to decrease (left axis) with iteration. The minimal obtainable rmse is bounded by the standard deviation of the noise model described in Section 8.4.

strain histogram bin width. Any meaningful comparison should, therefore, be made on a grid with similar resolution. To this end we have binned the projected strain PDFs into histograms in Fig. 12.

9. Discussion

Comparing the multivariate Gaussian prediction fit in Fig. 10 with the generic radial basis expansion model we observe a reduction in the residual error using the generic model. This is expected considering that the underlying strain PDF visualised in Fig. 12 is non-Gaussian. In fact, already from visual inspection of the histograms of directional strains, we may expect that the strain PDF is non-Gaussian. Nevertheless, despite the strain PDF being non-Gaussian, we observe from Fig. 12 that the Gaussian model captures multiple features of the strain PDF. Further inspection of Fig. 12 confirms that the full radial basis model offers additional improvements in terms of predicting the strain PDF shape. Considering the noise introduced into the data, as described in Section 8.4, these results imply that both regression models are robust in the presence of multiple outliers, limited and non-uniform $\hat{\boldsymbol{\kappa}}$ sampling and elevated levels of Gaussian measurement noise.

In terms of compute time, using a non-optimised python implementation, the estimation for the sparsely parameterised multivariate Gaussian model was in the range of ~20 ms, while the stochastic radial basis placement algorithm finished in ~6 s. These results were achieved with a Dell XPS 15 9560 laptop using a single Intel(R) Core(TM) i7-7700HQ CPU @ 2.80 GHz. Low compute times are important features of the proposed algorithms, effectively enabling the analysis of polycrystals with large number of grains (~1000) without the need for high performance computing resources. On the other hand, if an optimised multi-threaded implementation is pursued, these benchmarks are reasonable to permit online reconstruction at the same pace as data are being collected.

The final number of free parameters used by the radial basis regression is observed to be $94 \times 6 = 564$ from Fig. 11. We note that the total number of nonzero data bins in the measured histograms are $6 \times 132 = 792$, which is greater than the 564 parameters, avoiding over parametrisation of the model. In contrast to the 564 parameters used by the radial basis model, the sparsely parameterised multivariate Gaussian fit uses a mere total of $6+21 = 27$ model parameters (estimating the mean and symmetric covariance respectively). This could motivate the use of the Gaussian model in situations when the available data are scarce.

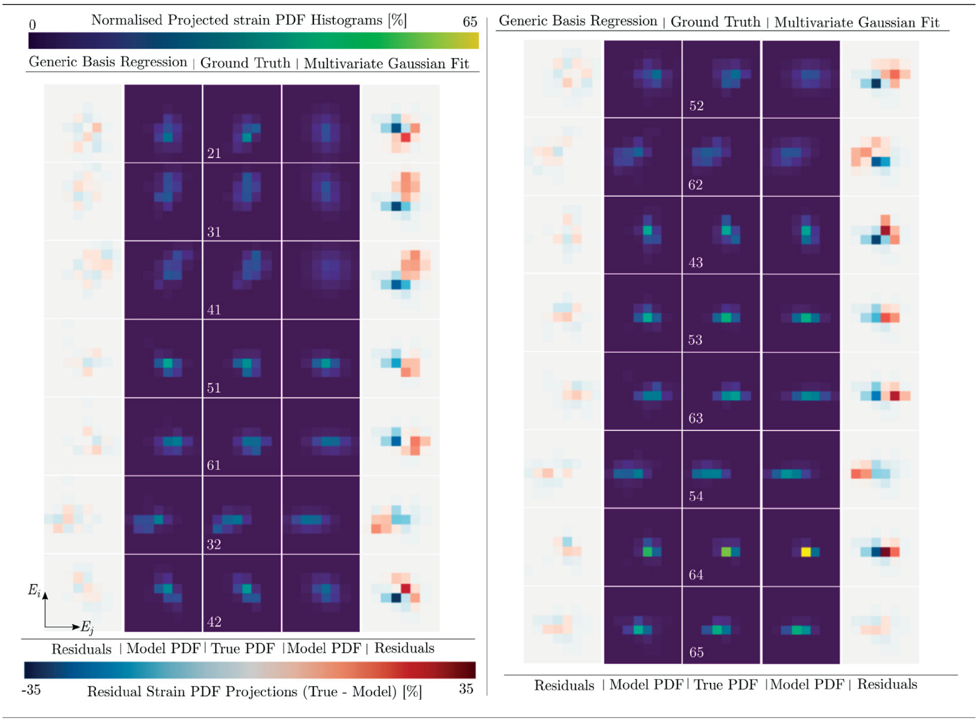

Fig. 12. Binned projections of the strain PDF unto the 15 possible unique Cartesian planes on $\mathbb{R}^6$ (the $E_2 - E_1$-plane, the $E_3 - E_1$-plane, …etc.). The ground truth strain PDF (central column) originated from the spatial strain tensor field in Fig. 7. The reconstructed strain PDFs, using both the sparsely parameterised multivariate Gaussian model (right) and the generic radial basis regression method (left) are to be compared to the ground truth strain PDF (central column). The respective residual fields are shown in the outermost columns.

10. Outlook

The convergence properties of the proposed Algorithm 1 are an ongoing research topic and future research should focus on parameter selection for B, J, σ and ξ. We believe the algorithm outlined in 1 has potential applications for a wider class of estimation problems, going beyond the estimation of strain PDFs, where a smooth, positive, simply connected scalar function needs to be approximated using a sparse basis. One such possible application is (X-ray or neutron) tomographic reconstruction, where a positive scalar attenuation function is to be estimated from noisy lower dimensional projections.

In terms of designing pilot experiments for the verification of the proposed regression methods, we suggest to perform time consuming s3DXRD in conjunction with fast full-field 3DXRD. Using the s3DXRD data the spatial strain tensor field can be estimated. By transforming the reconstructed spatial strain tensor field into a strain PDF and using the methods presented in this paper to recover the strain PDF from the full-field 3DXRD data independently, experimental validation could be achieved.

The research presented in this paper shows that approximation of the strain PDF, beyond a single mean value, is possible even with noisy distributions of directional strains. As such, we have provided a catalyst for pursuing algorithms that can optimally transform raw diffraction images into strain histograms. Since the number of achievable bins in such histograms is strongly related to the resolution of the detector, we anticipate the histogram resolution will increase with time, following the general trend in 3DXRD/HEDM type experiments. Alternatively, keeping the pixel density unchanged, the detector may be moved further away from the sample, leading to diffraction spot magnification. This is similar to the high angular resolution 3DXRD method, developed by Jakobsen et al. [50] (see also [51,52]).

The framework developed within this paper is not strictly limited to 3DXRD/HEDM applications. Other diffraction based techniques capable of producing histograms of directional strains, such that at least 2 bins can be resolved, will benefit from our results. As such we foresee a broader application of our findings in the context of non-destructive diffraction based materials research using both neutrons and X-rays.

11. Conclusions

In the context of high energy X-ray diffraction measurement from polycrystals, we have discussed the estimation of the strain tensor probability density function from noisy histograms of directional strains. Working in the limit of small strains, we derive a generic, iterative framework for strain PDF regression using a radial basis expansion as well as a sparsely parameterised multivariate Gaussian fit to which we provide a closed form solution. For the latter Gaussian class of strain tensor probability density functions, we give an exact description to the null-space of the inverse problem. The parametric description of the null-space provides insights into the strain PDF modes that cannot be accurately estimated from the diffraction data. Understanding these modes prevents erroneous conclusions from being drawn based on the data. The radial basis expansion method was shown to provide more accurate strain PDF estimations, at the expense of being mathematically involved, compared to the multivariate Gaussian fit which, on the other hand, represents a conceptually simple first order approximation to the strain PDF. We demonstrate our findings by numerical simulation considering a cubic iron (Fe) crystal in self-equilibrium. The simulation results imply that the proposed method performs well in the presence of Gaussian noise, outliers and non-uniform strain sampling. Overall, our findings represent an upgrade to the full-field 3DXRD/HEDM microscope methodology with the potential of broader application to other diffraction based methods.

Declaration of competing interest

The authors declare that they have no known competing financial interests or personal relationships that could have appeared to influence the work reported in this paper.

Data availability

Data will be made available on request

Acknowledgements

This work was funded by Vetenskapsrådet - Röntgen Ångström Cluster, project no. 2017-06719. The authors are grateful for the grants provided by The Fund of the Walter Gyllenberg Foundation, Sweden (no. 43096) as well as the Travel Grants for Young Researchers (no. 43000) granted by the Royal Physiographic Society of Lund, Sweden. These grants made necessary international collaboration between the authors possible.

Appendix A. Deformation configurations

In Fig. 13 we illustrate that the deformed unit cell matrix is reached from the undeformed state by applying the deformation gradient tensor as

$$\boldsymbol{C}_{cur} = \boldsymbol{F}\boldsymbol{C}_0 = \boldsymbol{F}_e\boldsymbol{F}_p\boldsymbol{C}_0. \tag{70}$$

The set of diffraction vectors measured from the current deformed state is denoted $\mathcal{G}[\boldsymbol{C}_{cur}] = \{\boldsymbol{G}^1, \boldsymbol{G}^2, \dots, \boldsymbol{G}^m\}$ and could equally have originated from a crystal with unit cell matrix

$$\boldsymbol{C} = \boldsymbol{F}_e\boldsymbol{C}_0, \tag{71}$$

as indicated to the right of Fig. 13. Similarly the unit cell matrices $\boldsymbol{C}_0$ and $\boldsymbol{C}_p = \boldsymbol{F}_p\boldsymbol{C}_0$ are diffraction equivalent, which is illustrated to the left in Fig. 13. We note that while we call $\boldsymbol{F}_e$ an *elastic* deformation and $\boldsymbol{F}_p$ a *plastic* deformation the technical definition is here that $\boldsymbol{F}_e$ is any deformation such that

$$\mathcal{G}[\boldsymbol{F}_e\boldsymbol{C}_0] \neq \mathcal{G}[\boldsymbol{C}_0], \tag{72}$$

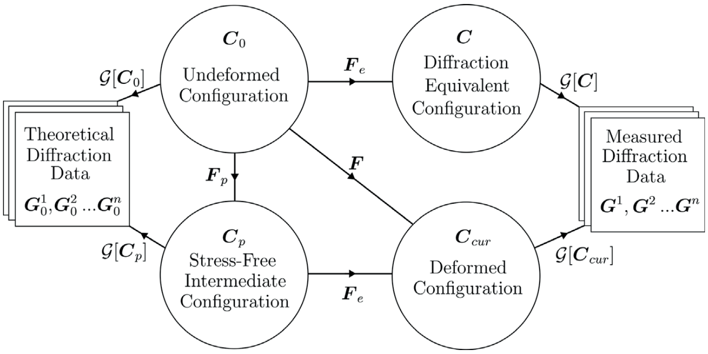

Fig. 13. Connection between single crystal deformation configurations associated with a multiplicative decomposition of the deformation gradient tensor, $\boldsymbol{F} = \boldsymbol{F}_e\boldsymbol{F}_p$. The physical process that yields diffraction from a crystal configuration is denoted by the operator $\mathcal{G}$. The fact that the diffraction data in 3DXRD/HEDM is independent of the plastic deformation, $\boldsymbol{F}_p$, is illustrated to the right and left.

while $\boldsymbol{F}_p$ is any deformation such that

$$\mathcal{G}[\boldsymbol{F}_p\boldsymbol{C}_0] = \mathcal{G}[\boldsymbol{C}_0]. \tag{73}$$

This means that, in our formulation, $\boldsymbol{F}_e$ can embody deformations that persist in the crystal when the boundary tractions are revoked.

Appendix B. Covariance perturbations

We seek solutions to Eq. (52) which we reiterate here as

$$\bar{\boldsymbol{\kappa}}_j^T \boldsymbol{N} \bar{\boldsymbol{\kappa}}_j = 0, \quad \forall j. \tag{74}$$

We divide our analysis into two cases; one where $\boldsymbol{N}$ is symmetric-positive-definite and one where $\boldsymbol{N}$ is symmetric-non-positive-definite.

B.1. Symmetric positive-definite covariance perturbations

Let us start by analysing the case when $\boldsymbol{z}^T\boldsymbol{N}\boldsymbol{z} \geq 0$, which can be parameterised by the matrix outer product $\boldsymbol{N} = \boldsymbol{A}\boldsymbol{A}^T, \quad \boldsymbol{A} \in \mathbb{R}^{6\times k}$. Adopting our previous matrix format we have

$$\boldsymbol{K}\boldsymbol{A}\boldsymbol{A}^T\boldsymbol{K} = \boldsymbol{0}, \tag{75}$$

and it follows from the quadratic format that we must require

$$\boldsymbol{K}\boldsymbol{A} = \boldsymbol{0}, \tag{76}$$

i.e., we must require $\boldsymbol{K}$ to have a null-space. This is in contradiction with our previous results in Section 7.1 were we showed that $\boldsymbol{K}$ can be fully ranked in general. Thus, no positive semi-definite perturbations to the covariance of the strain PDF exists in general, such that the measurements remain invariant.

B.2. General symmetric covariance perturbations

We are left with the analysis of perturbations, $\boldsymbol{N}$, that are not positive semi-definite, i.e we shall search over a more general class of perturbations, requiring only that

$$\boldsymbol{z}^T\boldsymbol{\Sigma}\boldsymbol{z} + \boldsymbol{z}^T\boldsymbol{N}\boldsymbol{z} \geq 0, \quad \forall \boldsymbol{z} \neq 0, \tag{77}$$

ensuring that $\boldsymbol{\Sigma}^*$ is a valid covariance matrix. This requirement effectively puts a bound on the norm of $\boldsymbol{N}$. To proceed with our analysis we shall vectorise the scalar product equation $\bar{\boldsymbol{\kappa}}_j^T \boldsymbol{N} \bar{\boldsymbol{\kappa}}_j$ as

$$\bar{\boldsymbol{\kappa}}_j^T \boldsymbol{N} \bar{\boldsymbol{\kappa}}_j = \boldsymbol{v}_j^T \boldsymbol{u}, \quad \boldsymbol{v}_j, \boldsymbol{u} \in \mathbb{R}^{21}, \tag{78}$$

where $\boldsymbol{u}$ stacks the 21 unique components of $\boldsymbol{N}$

$$\begin{array}{llllll}
\boldsymbol{u} = [N_{11} & N_{21} & N_{31} & N_{41} & N_{51} & N_{61} \\
 & \dots N_{22} & N_{32} & N_{42} & N_{52} & N_{62} \\
 & & \dots N_{33} & N_{43} & N_{53} & N_{63} \\
 & & & \dots N_{44} & N_{54} & N_{64} \\
 & & & & \dots N_{55} & N_{65} \\
 & & & & & \dots N_{66}],
\end{array} \tag{79}$$

and $\boldsymbol{v}_j$ is arranged accordingly,

$$\begin{array}{llllll}
\boldsymbol{v}_j = [\kappa_x^4 & 2\kappa_x^2\kappa_y^2 & 2\kappa_x^2\kappa_z^2 & 4\kappa_x^3\kappa_y & 4\kappa_x^3\kappa_z & 4\kappa_x^2\kappa_y\kappa_z \\
 & \dots \kappa_y^4 & 2\kappa_y^2\kappa_z^2 & 4\kappa_x\kappa_y^3 & 4\kappa_y^2\kappa_x\kappa_z & 4\kappa_y^3\kappa_z \\
 & & \dots \kappa_z^4 & 4\kappa_z^2\kappa_x\kappa_y & 4\kappa_x\kappa_z^3 & 4\kappa_y\kappa_z^3 \\
 & & & \dots 4\kappa_x^2\kappa_y^2 & 8\kappa_y\kappa_x^2\kappa_z & 8\kappa_x\kappa_y^2\kappa_z \\
 & & & & \dots 4\kappa_x^2\kappa_z^2 & 8\kappa_x\kappa_y\kappa_z^2 \\
 & & & & & 4\kappa_y^2\kappa_z^2].
\end{array} \tag{80}$$

The task is now to provide $\boldsymbol{u}$ orthogonal to $\boldsymbol{v}_j$ independently of the selection of j. Interestingly, the symmetry of $\boldsymbol{v}_j$ allows for the following selection

$$\begin{array}{llllll}
\boldsymbol{u} = [0 & 2\alpha & 2\beta & 0 & 0 & 2\gamma \\
 & \dots 0 & 2\eta & 0 & 2\xi & 0 \\
 & & \dots 0 & 2\rho & 0 & 0 \\
 & & & \dots -\alpha & -\gamma & -\xi \\
 & & & & \dots -\beta & -\rho \\
 & & & & & \dots -\eta],
\end{array} \tag{81}$$

with $(\alpha, \beta, \gamma, \eta, \xi, \rho) \in \mathbb{R}^1$ arbitrary. This class of $\boldsymbol{u}$ can be though of as a six dimensional subspace of $\mathbb{R}^{21}$ spanned by the columns of a matrix $\boldsymbol{U} \in \mathbb{R}^{21\times 6}$ as

$$\boldsymbol{U} = \begin{bmatrix}
0 & 0 & 0 & 0 & 0 & 0 \\
2\alpha & 0 & 0 & 0 & 0 & 0 \\
0 & 2\beta & 0 & 0 & 0 & 0 \\
0 & 0 & 0 & 0 & 0 & 0 \\
0 & 0 & 0 & 0 & 0 & 0 \\
0 & 0 & 2\gamma & 0 & 0 & 0 \\
0 & 0 & 0 & 0 & 0 & 0 \\
0 & 0 & 0 & 2\eta & 0 & 0 \\
0 & 0 & 0 & 0 & 0 & 0 \\
0 & 0 & 0 & 0 & 2\xi & 0 \\
0 & 0 & 0 & 0 & 0 & 0 \\
0 & 0 & 0 & 0 & 0 & 0 \\
0 & 0 & 0 & 0 & 0 & 2\rho \\
0 & 0 & 0 & 0 & 0 & 0 \\
0 & 0 & 0 & 0 & 0 & 0 \\
-\alpha & 0 & 0 & 0 & 0 & 0 \\
0 & 0 & -\gamma & 0 & 0 & 0 \\
0 & 0 & 0 & 0 & -\xi & 0 \\
0 & -\beta & 0 & 0 & 0 & 0 \\
0 & 0 & 0 & 0 & 0 & -\rho \\
0 & 0 & 0 & -\eta & 0 & 0
\end{bmatrix}. \tag{82}$$

It follows that if we can give example of a rank $21 - 6 = 15$ matrix, $\boldsymbol{R}$, such that

$$(\boldsymbol{R} + \boldsymbol{U}^T)\boldsymbol{v}_j = \boldsymbol{R}^T \boldsymbol{v}_j, \tag{83}$$

the column space of $\boldsymbol{U}$ depletes the sought null-space. Numerous examples of such $\boldsymbol{R}$ can be generated with computer aid. One possible selection, with all kappa forming angles >26° to the z-axis, is, for example,

$$\begin{aligned}
&\hat{\boldsymbol{\kappa}}_1 = \frac{1}{\sqrt{3}}\begin{bmatrix}1\\1\\1\end{bmatrix}, \quad \hat{\boldsymbol{\kappa}}_2 = \frac{1}{\sqrt{2}}\begin{bmatrix}1\\1\\0\end{bmatrix}, \quad \hat{\boldsymbol{\kappa}}_3 = \frac{1}{\sqrt{3}}\begin{bmatrix}1\\1\\-1\end{bmatrix}, \quad \hat{\boldsymbol{\kappa}}_4 = \frac{1}{\sqrt{6}}\begin{bmatrix}1\\1\\2\end{bmatrix}, \quad \hat{\boldsymbol{\kappa}}_5 = \frac{1}{\sqrt{6}}\begin{bmatrix}1\\1\\-2\end{bmatrix}, \\
&\hat{\boldsymbol{\kappa}}_6 = \frac{1}{\sqrt{2}}\begin{bmatrix}1\\0\\1\end{bmatrix}, \quad \hat{\boldsymbol{\kappa}}_7 = \begin{bmatrix}1\\0\\0\end{bmatrix}, \quad \hat{\boldsymbol{\kappa}}_8 = \frac{1}{\sqrt{2}}\begin{bmatrix}1\\0\\-1\end{bmatrix}, \quad \hat{\boldsymbol{\kappa}}_9 = \frac{1}{\sqrt{5}}\begin{bmatrix}1\\0\\2\end{bmatrix}, \quad \hat{\boldsymbol{\kappa}}_{10} = \frac{1}{\sqrt{3}}\begin{bmatrix}1\\-1\\1\end{bmatrix}, \\
&\hat{\boldsymbol{\kappa}}_{11} = \frac{1}{\sqrt{2}}\begin{bmatrix}1\\-1\\0\end{bmatrix}, \quad \hat{\boldsymbol{\kappa}}_{12} = \frac{1}{\sqrt{3}}\begin{bmatrix}1\\-1\\-1\end{bmatrix}, \quad \hat{\boldsymbol{\kappa}}_{13} = \frac{1}{\sqrt{6}}\begin{bmatrix}1\\2\\1\end{bmatrix}, \quad \hat{\boldsymbol{\kappa}}_{14} = \frac{1}{\sqrt{5}}\begin{bmatrix}1\\2\\0\end{bmatrix}, \quad \hat{\boldsymbol{\kappa}}_{15} = \frac{1}{\sqrt{6}}\begin{bmatrix}1\\-2\\1\end{bmatrix}.
\end{aligned} \tag{84}$$

Appendix C. Basis integration

We seek to solve the integral given in Eq. (36) which we reiterate here as

$$\int_{s_j^*-w/2}^{s_j^*+w/2} \int_{\boldsymbol{\epsilon} \in \Pi(t,\hat{\boldsymbol{n}}_j)} \exp\left(-\frac{(\boldsymbol{\epsilon} - \boldsymbol{p}_i)^T(\boldsymbol{\epsilon} - \boldsymbol{p}_i)}{2\sigma^2}\right) d\boldsymbol{\epsilon} dt. \tag{85}$$

We denote the inner integral $I_{\boldsymbol{\epsilon}}$ and the outer integral I_t and initiate our analysis with $I_{\boldsymbol{\epsilon}}$. To solve the integral we start by parameterising all points on Π by the range of $\boldsymbol{P} \in \mathbb{R}^{6\times 5}$ such that the columns of $\boldsymbol{P}$ forms a basis for Π. For reasons that will become apparent later we select the parametrisation

$$\boldsymbol{\epsilon} = \boldsymbol{\epsilon}(\boldsymbol{y}) = \boldsymbol{P}\boldsymbol{y} + t\hat{\boldsymbol{n}}_j + \boldsymbol{P}\boldsymbol{P}^T\boldsymbol{p}_i \in \Pi(t, \hat{\boldsymbol{n}}_j), \quad \boldsymbol{y} \in \mathbb{R}^5. \tag{86}$$

This simplifies our problem to an unbounded integral over $\mathbb{R}^5$ as

$$I_{\boldsymbol{\epsilon}} = \int_{\mathbb{R}^5} \exp\left(-\frac{(\boldsymbol{\epsilon}(\boldsymbol{y}) - \boldsymbol{p}_i)^T(\boldsymbol{\epsilon}(\boldsymbol{y}) - \boldsymbol{p}_i)}{2\sigma^2}\right) d\boldsymbol{y}. \tag{87}$$

Without loss of generality, we now select the columns of $\boldsymbol{P}$ to be orthonormal, such that $\boldsymbol{P}^T\boldsymbol{P} = \boldsymbol{I}$. Expanding the square in (87) we find that

$$I_{\boldsymbol{\epsilon}} = \int_{\mathbb{R}^5} \exp\left(-\frac{(\boldsymbol{y}^T\boldsymbol{y} - 2t\boldsymbol{p}_i^T\hat{\boldsymbol{n}}_j + t^2 - \boldsymbol{p}_i^T\boldsymbol{P}\boldsymbol{P}^T\boldsymbol{p}_i + \boldsymbol{p}_i^T\boldsymbol{p}_i)}{2\sigma^2}\right) d\boldsymbol{y}, \tag{88}$$

where it was used that $\boldsymbol{P}\hat{\boldsymbol{n}}_j = \boldsymbol{0}$. Introducing the scalar minimum squared distance, d^2, between Π and $\boldsymbol{p}_i$ as

$$d^2 = (\boldsymbol{p}_i - \boldsymbol{P}\boldsymbol{P}^T\boldsymbol{p}_i - t\hat{\boldsymbol{n}}_j)^T(\boldsymbol{p}_i - \boldsymbol{P}\boldsymbol{P}^T\boldsymbol{p}_i - t\hat{\boldsymbol{n}}_j) = \boldsymbol{p}_i^T\boldsymbol{p}_i - 2t\boldsymbol{p}_i^T\hat{\boldsymbol{n}}_j + t^2 - \boldsymbol{p}_i^T\boldsymbol{P}\boldsymbol{P}^T\boldsymbol{p}_i, \tag{89}$$

we find by insertion into (87) that

$$I_{\boldsymbol{\epsilon}} = \int_{\mathbb{R}^5} \exp\left(-\frac{(\boldsymbol{y}^T\boldsymbol{y} + d^2)}{2\sigma^2}\right) d\boldsymbol{y}. \tag{90}$$

The benefits of the specific parametric selection of Π is now evident from the cancelled terms. Factoring out the part that is independent of $\boldsymbol{y}$, we have

$$I_{\boldsymbol{\epsilon}} = \exp\left(\frac{-d^2}{2\sigma^2}\right) \int_{\mathbb{R}^5} \exp\left(-\frac{\boldsymbol{y}^T\boldsymbol{y}}{2\sigma^2}\right) d\boldsymbol{y}, \tag{91}$$

where the rightmost integral features an non-normalised Gaussian with covariance $\boldsymbol{I}\sigma^2$. We solve this Gaussian integral by normalisation as

$$\int_{\mathbb{R}^5} \exp\left(-\frac{\boldsymbol{y}^T\boldsymbol{y}}{2\sigma^2}\right) d\boldsymbol{y} = \sigma^5\sqrt{(2\pi)^5} \int_{\mathbb{R}^5} \frac{1}{\sigma^5\sqrt{(2\pi)^5}} \exp\left(-\frac{\boldsymbol{y}^T\boldsymbol{y}}{2\sigma^2}\right) d\boldsymbol{y} = \sigma^5\sqrt{(2\pi)^5}. \tag{92}$$

Inserting (92) into (91) we find

$$I_{\epsilon} = \sigma^5 \sqrt{(2\pi)^5} \exp\left(\frac{-d^2}{2\sigma^2}\right). \tag{93}$$

We proceed to solve for the outer integral in (36). Using the result in (93) we have

$$I_t = \int_{s_j^* - w/2}^{s_j^* + w/2} I_{\epsilon} dt = \sigma^5 \sqrt{(2\pi)^5} \int_{s_j^* - w/2}^{s_j^* + w/2} \exp\left(\frac{-d^2}{2\sigma^2}\right) dt. \tag{94}$$

Since the distance d is linear in t and the increments, $dd = dt$, are one to one, we now find a bounded Gaussian integral that can be solved using the error function, erf, as

$$I_t = \sigma^5 \sqrt{(2\pi)^5} \left| \int_a^b \exp\left(\frac{-d^2}{2\sigma^2}\right) dd \right| = 4\pi^3 \sigma^6 \left| \operatorname{erf}\left(\frac{b}{\sigma\sqrt{2}}\right) - \operatorname{erf}\left(\frac{a}{\sigma\sqrt{2}}\right) \right|, \tag{95}$$

where the transformed bounds, a and b, can be computed as $a = (s_j^* - w/2)\boldsymbol{p}_i^T \hat{\boldsymbol{n}}_j$ and $b = (s_j^* + w/2)\boldsymbol{p}_i^T \hat{\boldsymbol{n}}_j$, respectively. This concludes our integration analysis.

References

[1] H. Poulsen, Multi scale hard x-ray microscopy, Curr. Opin. Solid State Mater. Sci. 24 (2) (2020) 100820.

[2] V. Santoro, K.H. Andersen, M. Bernasconi, M. Bertelsen, Y.B. ler, D. Campi, V. Czamler, D.D.D. Julio, E. Diane, K. Dunne, P. Fierlinger, A. Gaye, G. Gorini, C. Happe, T. Kittelmann, E.B. Klinkby, Z. Kokai, R. Kolevatov, B. Lauritzen, R. Linander, J.I.M. Damian, B. Meirose, F. Mezei, D. Milstead, G. Muhrer, K. Ramic, B. Rataj, N. Rizzi, S. Samothrakitis, J.R. Selknaes, S. Silverstein, M. Strobl, M. Strothmann, A. Takibayev, R. Wagner, P. Willendrup, S.C. Yiu, L. Zanini, O. Zimmer, Development of a high intensity neutron source at the European Spallation source: The HighNESS project, 2022.

[3] A. Cereser, M. Strobl, S.A. Hall, A. Steuwer, R. Kiyanagi, A.S. Tremsin, E.B. Knudsen, T. Shinohara, P.K. Willendrup, A.B. da Silva Fanta, S. Iyengar, P.M. Larsen, T. Hanashima, T. Moyoshi, P.M. Kadletz, P. Krooß, T. Niendorf, M. Sales, W.W. Schmahl, S. Schmidt, Time-of-flight three dimensional neutron diffraction in transmission mode for mapping crystal grain structures, Sci. Rep. 7 (1) (2017) 9561.

[4] Y. Hayashi, D. Setoyama, Y. Hirose, T. Yoshida, H. Kimura, Intragranular three-dimensional stress tensor fields in plastically deformed polycrystals, Science 366 (6472) (2019) 1492–1496.

[5] E. Demir, J.-S. Park, M. Miller, P. Dawson, A computational framework for evaluating residual stress distributions from diffraction-based lattice strain data, Comput. Methods Appl. Mech. Engrg. 265 (2013) 120–135.

[6] R. Quey, L. Renversade, Optimal polyhedral description of 3D polycrystals: Method and application to statistical and synchrotron X-ray diffraction data, Comput. Methods Appl. Mech. Engrg. 330 (2018) 308–333.

[7] M.M. Thakur, N.A. Henningsson, J. Engqvist, P.-O. Autran, J.P. Wright, R.C. Hurley, On mesoscale modeling of concrete: Role of heterogeneities on local stresses, strains, and representative volume element, Cem. Concr. Res. 163 (2023) 107031.

[8] J.M. Dake, J. Oddershede, H.O. Sørensen, T. Werz, J.C. Shatto, K. Uesugi, S. Schmidt, C.E. Krill, Direct observation of grain rotations during coarsening of a semisolid Al–Cu alloy, Proc. Natl. Acad. Sci. 113 (41) (2016) E5998–E6006.

[9] H. Poulsen, 3DXRD – A New Probe for Materials Science (Ph.D. thesis), Risø National Laboratory, 2004.

[10] J.V. Bernier, R.M. Suter, A.D. Rollett, J.D. Almer, High-energy X-Ray diffraction microscopy in materials science, Annu. Rev. Mater. Res. 50 (1) (2020) 395–436.

[11] E.M. Lauridsen, S. Schmidt, R.M. Suter, H.F. Poulsen, Tracking: a method for structural characterization of grains in powders or polycrystals, J. Appl. Crystallogr. 34 (6) (2001) 744–750.

[12] H. Sørensen, S. Schmidt, J. Wright, G. Vaughan, S. Techert, E. Garman, J. Oddershede, J. Davaasambuu, K. Paithankar, C. Gundlach, H. Poulsen, Multigrain crystallography, Z. Kristallogr.–Cryst. Mater. 227 (1) (2012) 63–78.

[13] H. Sharma, R.M. Huizenga, S.E. Offerman, A fast methodology to determine the characteristics of thousands of grains using three-dimensional X-ray diffraction. I. Overlapping diffraction peaks and parameters of the experimental setup, J. Appl. Crystallogr. 45 (4) (2012) 693–704.

[14] J.M. Wozniak, H. Sharma, T.G. Armstrong, M. Wilde, J.D. Almer, I. Foster, Big data staging with MPI-IO for interactive X-ray science, in: 2014 IEEE/ACM International Symposium on Big Data Computing, 2014, pp. 26–34.

[15] L. Margulies, T. Lorentzen, H. Poulsen, T. Leffers, Strain tensor development in a single grain in the bulk of a polycrystal under loading, Acta Mater. 50 (7) (2002) 1771–1779.

[16] H.F. Poulsen, S.F. Nielsen, E.M. Lauridsen, S. Schmidt, R.M. Suter, U. Lienert, L. Margulies, T. Lorentzen, D. Juul Jensen, Three-dimensional maps of grain boundaries and the stress state of individual grains in polycrystals and powders, J. Appl. Crystallogr. 34 (6) (2001) 751–756.

[17] J. Oddershede, S. Schmidt, H.F. Poulsen, H.O. Sørensen, J. Wright, W. Reimers, Determining grain resolved stresses in polycrystalline materials using three-dimensional X-ray diffraction, J. Appl. Crystallogr. 43 (3) (2010) 539–549.

[18] J.V. Bernier, N.R. Barton, U. Lienert, M.P. Miller, Far-field high-energy diffraction microscopy: a tool for intergranular orientation and strain analysis, J. Strain Anal. Eng. Des. 46 (7) (2011) 527–547.

- [19] Y. Hayashi, D. Setoyama, Y. Seno, Scanning three-dimensional X-Ray diffraction microscopy with a high-energy microbeam at spring-8, Mater. Sci. Forum 905 (2017) 157–164.
- [20] W. Li, H. Sharma, K. Peter, S. Ravi, H. Sehitoglu, A. Bucsek, Resolving intragranular stress fields in plastically deformed titanium using point-focused high-energy diffraction microscopy, J. Mater. Res. 38 (1) (2023) 165–178.
- [21] J. Hendriks, C. Wensrich, A. Wills, V. Luzin, A. Gregg, Robust inference of two-dimensional strain fields from diffraction-based measurements, Nucl. Instrum. Methods Phys. Res. B 444 (2019) 80–90.
- [22] N.A. Henningsson, S.A. Hall, J.P. Wright, J. Hektor, Reconstructing intragranular strain fields in polycrystalline materials from scanning 3Dxrd data, J. Appl. Crystallogr. 53 (2) (2020) 314–325.
- [23] J.N. Hendriks, C.M. Wensrich, A. Wills, A Bayesian approach to triaxial strain tomography from high-energy X-ray diffraction, Strain 56 (3) (2020) e12341, e12341 10.1111/str.12341.
- [24] A. Henningsson, J. Hendriks, Intragranular strain estimation in far-field scanning X-ray diffraction using a Gaussian process, J. Appl. Crystallogr. 54 (4) (2021) 1057–1070.
- [25] Y. Hayashi, Y. Hirose, Y. Seno, Polycrystal orientation mapping using scanning three-dimensional X-ray diffraction microscopy, J. Appl. Crystallogr. 48 (4) (2015) 1094–1101.
- [26] J. Hektor, S.A. Hall, N.A. Henningsson, J. Engqvist, M. Ristinmaa, F. Lenrick, J.P. Wright, Scanning 3Dxrd measurement of grain growth, stress, and formation of Cu6Sn5 around a tin whisker during heat treatment, Materials 12 (3) (2019).
- [27] S. Schmidt, GrainSpotter: a fast and robust polycrystalline indexing algorithm, J. Appl. Crystallogr. 47 (1) (2014) 276–284.
- [28] S. West, S. Schmidt, H. Sørensen, G. Winther, H. Poulsen, L. Margulies, C. Gundlach, D. Juul Jensen, Direct non-destructive observation of bulk nucleation in 30% deformed aluminum, Scr. Mater. 61 (9) (2009) 875–878.
- [29] H.F. Poulsen, U. Lienert, W. Pantleon, Characterisation of orientation distributions of individual grains within deformed metals, Mater. Sci. Technol. 21 (12) (2005) 1397–1400.
- [30] P.C. Hansen, H.O. Sørensen, Z. Sükösd, H.F. Poulsen, Reconstruction of single-grain orientation distribution functions for crystalline materials, SIAM J. Imaging Sci. 2 (2) (2009) 593–613.
- [31] N.R. Barton, J.V. Bernier, A method for intragranular orientation and lattice strain distribution determination, J. Appl. Crystallogr. 45 (6) (2012) 1145–1155.
- [32] H. Behnken, Strain-function method for the direct evaluation of intergranular strains and stresses, Phys. Status Solidi (A) 177 (2) (2000) 401–418.
- [33] J.V. Bernier, M.P. Miller, A direct method for the determination of the mean orientation-dependent elastic strains and stresses in polycrystalline materials from strain pole figures, J. Appl. Crystallogr. 39 (3) (2006) 358–368.
- [34] D. Boyce, P. Shade, W. Musinski, M. Obstalecki, D. Pagan, J. Bernier, T. Turner, Estimation of anisotropic elastic moduli from high energy X-Ray data and finite element simulations, Materialia 12 (2020) 100795.
- [35] W. Pantleon, H. Poulsen, J. Almer, U. Lienert, In situ X-ray peak shape analysis of embedded individual grains during plastic deformation of metals, Mater. Sci. Eng. A 387–389 (2004) 339–342, 13th International Conference on the Strength of Materials.
- [36] K. Fogarty, E. Ametova, G. Burca, A.M. Korsunsky, S. Schmidt, P.J. Withers, W.R.B. Lionheart, Recovering the second moment of the strain distribution from neutron bragg edge data, Appl. Phys. Lett. 120 (16) (2022) 164102.
- [37] J. Als-Nielsen, D. McMorrow, Elements of Modern X-ray Physics, John Wiley & Sons, Ltd, 2011.
- [38] S.L. Wong, J.-S. Park, M.P. Miller, P.R. Dawson, A framework for generating synthetic diffraction images from deforming polycrystals using crystal-based finite element formulations, Comput. Mater. Sci. 77 (2013) 456–466.
- [39] P.R. Dawson, M.P. Miller, A virtual diffractometer for creating synthetic HEDM images of tessellated and meshed finite element polycrystals, 2023.
- [40] E. Kröner, Allgemeine kontinuumstheorie der versetzungen und eigenspannungen, Arch. Ration. Mech. Anal. 4 (1959) 273–334.
- [41] E.H. Lee, D.T. Liu, Finite-strain elastic—Plastic theory with application to plane-wave analysis, J. Appl. Phys. 38 (1) (1967) 19–27.
- [42] R.J. Clifton, On the equivalence of FeFp and FpFe, J. Appl. Mech. 39 (1) (1972) 287–289.
- [43] J. Clayton, D. McDowell, A multiscale multiplicative decomposition for elastoplasticity of polycrystals, Int. J. Plast. 19 (9) (2003) 1401–1444.
- [44] Y. Jiao, J. Fish, On the equivalence between the multiplicative hyper-elasto-plasticity and the additive hypo-elasto-plasticity based on the modified kinetic logarithmic stress rate, Comput. Methods Appl. Mech. Engrg. 340 (2018) 824–863.
- [45] N.S. Ottosen, M. Ristinmaa, The Mechanics of Constitutive Modeling, Elsevier, 2005.
- [46] C.L. Lawson, R.J. Hanson, Solving Least Squares Problems, SIAM, 1995.
- [47] P. Virtanen, R. Gommers, T.E. Oliphant, M. Haberland, T. Reddy, D. Cournapeau, E. Burovski, P. Peterson, W. Weckesser, J. Bright, S.J. van der Walt, M. Brett, J. Wilson, K.J. Millman, N. Mayorov, A.R.J. Nelson, E. Jones, R. Kern, E. Larson, C.J. Carey, İ. Polat, Y. Feng, E.W. Moore, J. VanderPlas, D. Laxalde, J. Perktold, R. Cimrman, I. Henriksen, E.A. Quintero, C.R. Harris, A.M. Archibald, A.H. Ribeiro, F. Pedregosa, P. van Mulbregt, SciPy 1.0 Contributors, Scipy 1.0: Fundamental algorithms for scientific computing in python, Nature Methods 17 (2020) 261–272.
- [48] A.G. Wills, T.B. Schön, Sequential Monte Carlo: A unified review, Annu. Rev. Control Robot. Auton. Syst. 6 (1) (2023) null.
- [49] R. Rostamian, The completeness of Maxwell's stress function representation, J. Elasticity 9 (4) (1979) 349–356.
- [50] B. Jakobsen, H.F. Poulsen, U. Lienert, J. Almer, S.D. Shastri, H.O. Sørensen, C. Gundlach, W. Pantleon, Formation and subdivision of deformation structures during plastic deformation, Science 312 (5775) (2006) 889–892.
- [51] T. Ungár, G. Ribárik, L. Balogh, A.A. Salem, S.L. Semiatin, G.B. Vaughan, Burgers vector population, dislocation types and dislocation densities in single grains extracted from a polycrystalline commercial-purity Ti specimen by X-ray line-profile analysis, Scr. Mater. 63 (1) (2010) 69–72.
- [52] C. Nisr, G. Ribárik, T. Ungár, G.B.M. Vaughan, P. Cordier, S. Merkel, High resolution three-dimensional X-ray diffraction study of dislocations in grains of MgGeO3 post-perovskite at 90 GPa, J. Geophys. Res.: Solid Earth 117 (B3) (2012).